DEVELOPMENT AND CHARACTERIZATION OF PLASMA-BASED SOURCES FOR AMBIENT DESORPTION/IONIZATION MASS SPECTROMETRY

Jacob T. Shelley

Submitted to the faculty of the University Graduate School
in partial fulfillment of the requirements
for the degree
Doctor of Philosophy
in the Department of Chemistry
Indiana University
June, 2011

Accepted by the Graduate Faculty, Indiana University, in partial fulfillment of the requirements for the degree of Doctor of Philosophy.

Doctoral Committee

Gary M. Hieftje, Ph.D.

Dennis G. Peters, Ph.D.

Stephen C. Jacobson, Ph.D.

Bogdan Dragnea, Ph.D.

Date of Oral Examination
May 31, 2011

Acknowledgements

The work presented hereafter would not have been possible without the motivation, guidance, and support of numerous people, both personally and professionally. I am forever indebted to these people for helping me grow as a scientist and as a person.

I would first like to thank my parents, Fred and Mindy, and my brother, Keith, for all the love and support they have provided throughout my life. It is comforting to know that no matter how difficult or trying life is, I can always turn to these three people. I would certainly not have made it this far without them. The ever optimistic and encouraging attitude provided by my grandparents, Fred and Lilly Shelley as well as Jane and the late Chuck Baldridge, has always given me motivation and put a smile on my face. I am extremely thankful to my aunt and uncle, Allie and Jerry Hoskins, for providing a home away from home in Phoenix during my undergraduate and graduate studies.

I have also been lucky enough to have some truly amazing friends in my life that have provided sanity as well as open ears and hearts during the many difficult times over the past six years. On the top of the list are my classmates Dr. Matt Foley, Soca "Danger" Wibowo, and Nichole Stewart as well as lifelong comrade Brian Spall.

Professionally, I owe everything I am and will become as a scientist to my research advisor, Prof. Gary M. Hieftje. He certainly deserves thanks for providing the support and the means to perform this research and earn this degree. But more

importantly, he has provided me, and the rest of his research group, with a wealth of freedom, opportunities, and experiences that would have not have been had in any other setting. His love of science and education has created a research group that more closely resembles a family. Through this family atmosphere I have made some lifelong friends and colleagues; in particular Dr. Greg Schilling, Josh Wiley, Dr. Carsten Engelhard and the whole Bioionomics Bowling team. In addition to them, I have had the privilege and honor to have great post-doctoral mentors throughout the years in Dr. George Chan, Dr. Steve Ray, and Dr. Francisco Andrade. Their passion for science and knowledge is on par with Prof. Hieftje and I am excited to see the superb work to come from them in the future. I also have to thank the rest of the past and present Hieftje "family" that has made graduate school so much fun: Prof. José Broekaert, Yan Cheung, Elise Dennis, Dr. Eyal Elish, Jeremy Felton, Dr. Gerardo Gamez, Ana Gonzalvez, Alex Graham, Meghan McCormick, Kevin Pfeuffer, Dr. Radislav Potyrailo, Dr. Duane Rogers, Arnon Rubinshtein, Andy Schwartz, Dan Shelby, Andrew Storey, Dr. Mike Webb, Dr. Bill Wetzel, Cori Weinel, Prof. Zhenli Zhu, and, surrogate group member from Prosolia Inc., Dr. Justin Wiseman. Last but not least, many things would not have been accomplished without the administrative assistance of LeeAnn Mobley, Selina Williams, Misty Boteler, and Susan Hieftje.

There are several other support groups at Indiana University that deserve special thanks. These include Gary Fleener, Brian Ferguson, Doug Garvin, Rick Moore, and Bruce Frye in the Edward J. Bair Mechanical Instrument Services; John Poehlman and Andy Alexander in the Electrical Instrument Services group; Susie DuMond, Jackie Drake, and Rick Hackler in the Requisitioning office and Chemical Storeroom.

During my time in graduate school I was also fortunate enough to spend half a year doing work in the research group of Prof. R. Graham Cooks at Purdue University through the Center for Analytical Instrumentation Development Fellowship. It certainly is an experience I will never forget. It also led to one of the most productive and fun collaborations I have ever been a part of with Dr. Carsten Engelhard, Dr. George Chan, and myself from Indiana and Dr. Ayanna Jackson and Josh Wiley from Purdue; some of that work is presented below. In addition to the insightful conversations with Prof. Cooks, I must thank Dr. Ewa Sokol, Dr. Fatkhulla Tadjimukhamedov, Dr. Rob Noll, Dr. Demian Ifa, and Paul Hendricks from Aston Labs for sharing their wealth of knowledge on mass spectrometry and giving me a new perspective on scientific research.

I would not have pursued chemistry without the teachings and guidance of my high school chemistry teachers, Dr. Meg Cox and the late David Thurston. They showed me how exciting and rewarding science can be. I would not have made it into graduate school or even applied to Indiana University without the urgings of Dr. Chris Hassell, Dr. Cris Lewis, and Dr. James Barnes during my time at Los Alamos National Laboratory. In addition, Dr. Srinivas Iyer and Dr. Andy Koppisch from the Bioscience Division of Los Alamos National Laboratory and Prof. Diane Stearns at Northern Arizona University gave me my first opportunities to pursue scientific research and let me so with almost total freedom.

These projects were supported by Award Number 1R41RR025718 from the National Center for Research Resources (NCRR) in collaboration with Prosolia, Inc., Indianapolis, IN. The content is solely the responsibility of the authors and does not necessarily represent the official views of the NCRR or the NIH.

Additional funding was provided by NSWC Crane through federal grant number N00164-08-C-JQ11, the US Department of Energy through federal grant number DE-FG02-98ER14890, the Lilly Endowment-Indiana MetaCyt Initiative, by the Department of Homeland Security through grant HSHQDC-09-9-00008, and by the Center for Analytical Instrumentation Development at Purdue University. The authors would also like to thank Leco, Horiba Jobin-Yvon, and Prosolia for the loan of equipment used in these studies.

DEVELOPMENT AND CHARACTERIZATION OF PLASMA-BASED SOURCES FOR AMBIENT DESORPTION/IONIZATION MASS SPECTROMETRY

Jacob T. Shelley

A number of atmospheric-pressure ionization sources for mass spectrometry has recently appeared in the literature to yield a field that is collectively referred to as Ambient Desorption/Ionization-Mass Spectrometry (ADI-MS). These sources include, among others, Desorption ElectroSpray Ionization (DESI), Direct Analysis in Real Time (DART), the Flowing Atmospheric-Pressure Afterglow (FAPA), and the Low-Temperature Plasma (LTP) probe. Collectively, these ADI-MS sources offer numerous advantages over conventional ionization sources, including direct analysis of solid, liquid, and gaseous samples, high ionization efficiency, and soft ionization. Additionally, their ability to analyze samples directly with no pretreatment dramatically reduces analysis times.

The ultimate ambient ionization source would be one that is capable of desorbing and ionizing a broad range of analytes (polar, non-polar, small molecules, biopolymers, etc.) while being minimally influenced by matrix effects. While the plasma-based ADI-MS sources, such as FAPA, DART, and LTP, have been shown to be capable of efficiently ionizing a range of small molecules, few investigations have been aimed at understanding desorption and ionization processes or matrix effects that occur with them.

At present, the performance and fundamental characteristics of the FAPA source, developed in our research group, and the LTP probe, developed at Purdue University, are being evaluated through optical and mass-spectrometric methods. The FAPA source consists of a direct-current, atmospheric-pressure glow discharge in a pin-to-plate configuration. A hole in the plate allows ionized and excited plasma species to interact directly with a sample, while physically and electrically isolating the discharge from the sample-introduction region. Conversely, the LTP probe is a high-voltage, alternating-current, dielectric-barrier discharge that interacts directly with a sample. While the

fundamental processes governing these discharges are quite different, mass spectra produced with both sources are very similar. The major differences are in achievable detection limits and susceptibility to matrix effects, with the FAPA sources routinely performing better. Direct, fundamental comparisons among the FAPA source, the LTP probe, and DART are made.

Gary M. Hieftje, Ph.D.

Dennis G. Peters, Ph.D.

Stephen C. Jacobson, Ph.D.

Bogdan Dragnea, Ph.D.

Table of Contents

Chapter 3 —

Fast Transient Analysis and First-Stage Collision-Induced Dissociation with the Flowing Atmospheric-Pressure Afterglow Ionization Source to Improve Analyte Detection and Identification

Chapter 4 —

Characterization of Direct-Current Atmospheric-Pressure Discharges Useful for Ambient Desorption/Ionization Mass Spectrometry

Chapter 6 —

Spectroscopic Plasma Diagnostics on a Low-Temperature Plasma Probe for Ambient Mass Spectrometry

Chapter 7 —

Elucidation of Reaction Mechanisms Responsible for Afterglow and Reagent-Ion Formation in the Low-Temperature Plasma Probe Ambient Ionization Source

Chapter 8 —

Understanding the Flowing Atmospheric-Pressure Afterglow Ambient Ionization Source Through Optical Means

Chapter 9 —

Ultrasensitive Ambient Mass Spectrometric Analysis with a Pin-to-Capillary Flowing Atmospheric-Pressure Afterglow Source

List of Tables

List of Figures

Chapter 1

Ambient Mass Spectrometry: Approaching the Chemical Analysis of Things as They Are

1.1 The Chemical Analysis of Things as They Are

In an article entitled "The Chemical Analysis of Things as They Are," G. E. F. Lundell[1] describes the current state of the analytical sciences and the role of scientists working in that field. He asserts that too much emphasis is placed on specialized analyses, which often leads to more time and effort being placed on the end result of an analysis (a quick number) than on understanding the analytical measurement within the context of the sample (an accurate value). The assumption of many users is that only one or a few constituents of a sample, usually the analyte(s) of interest, play a role in the measurement that is obtained, which is often not the case. Too frequently, reports in analytical journals describe a new method of analysis in which analyte X is measured in sample Y through method Z, but there is little concern about what, if any, other species in the sample might yield a false response or if this method could be applied to other sample

types. As a result, the technique will likely see little use aside from that envisioned by the developers. Lundell refers to this type of approach as "The Chemical Analysis of Things as They Are Not", which he attributes to a steady loss of the analytical viewpoint. An increasing number of scientists involved in or entering the analytical field have an additional scientific focus (e.g. materials development, synthesis, chemical biology, etc.) that often leads to decreased interest in or focus on the analytical viewpoint. While these multidisciplinary chemists were and are certainly important to the scientific community, many can be classified as, in Lundell's terms, "Determinators," while more traditional analytical chemists can be categorized as "Analysts." Determinators' primary interest is how the analytical result pertains to a particular system; thus, the analytical technique used by Determinators should be as sensitive and selective as possible to ensure a correct answer.

Interestingly, the "current" state of analytical chemistry described by G. E. F. Lundell is that of the early 1930s, with the article being published in 1933. While many modern analytical techniques were not even developed at that time, let alone commercialized, the "chemical analysis of things as they are not" is still a prevalent theme in present-day analytical literature. However, a recently conceived field in mass spectrometry strives to reduce this problem through direct sample analysis. Ambient desorption/ionization mass spectrometry (or "ambient mass spectrometry," for short), as it is called, combines the benefits of recent advances in vacuum and ionization-source technology with the high selectivity and sensitivity inherent to mass-spectrometric analyses.

1.2 Concept of Ambient Mass Spectrometry

A conceptual diagram of the ambient mass spectrometry approach is shown in Figure 1.1. The approach requires three components: the source, the sample, and an atmospheric-sampling mass spectrometer. The source is responsible for both the removal of analyte from the sample surface (e.g. desorption or extraction) and ionization of the analyte, a requisite of mass-spectrometric detection. Generally, the source is comprised of a power source, an ion-generation region, and a sweep liquid and/or gas. Lastly, the source must be operated at atmospheric pressure such that the sample can be probed in the ambient air.

A clear distinction must be made between ambient desorption/ionization mass spectrometry and atmospheric-pressure ionization mass spectrometry (API-MS). The latter, which includes electrospray ionization (ESI), atmospheric-pressure chemical ionization (APCI), and atmospheric-pressure photoionization (APPI), is incapable of directly volatilizing molecules from samples and, as a result, complex sample introduction methods, such as heated nebulizers, as often needed. Additionally, as Harris et al.[2] explain, ambient desorption/ionization mass spectrometry analyses should be performed in the open, ambient environment without sample pretreatment (e.g. dissolution, extraction, or separation) and on nearly any atmospheric-pressure inlet mass spectrometer. That is, the desorption/ionization source should be simple and versatile enough to be interfaced to many instruments without modification.

The sample, which has undergone little or no pretreatment, is placed within the desorption/ionization beam of the source where molecules, denoted by different-colored

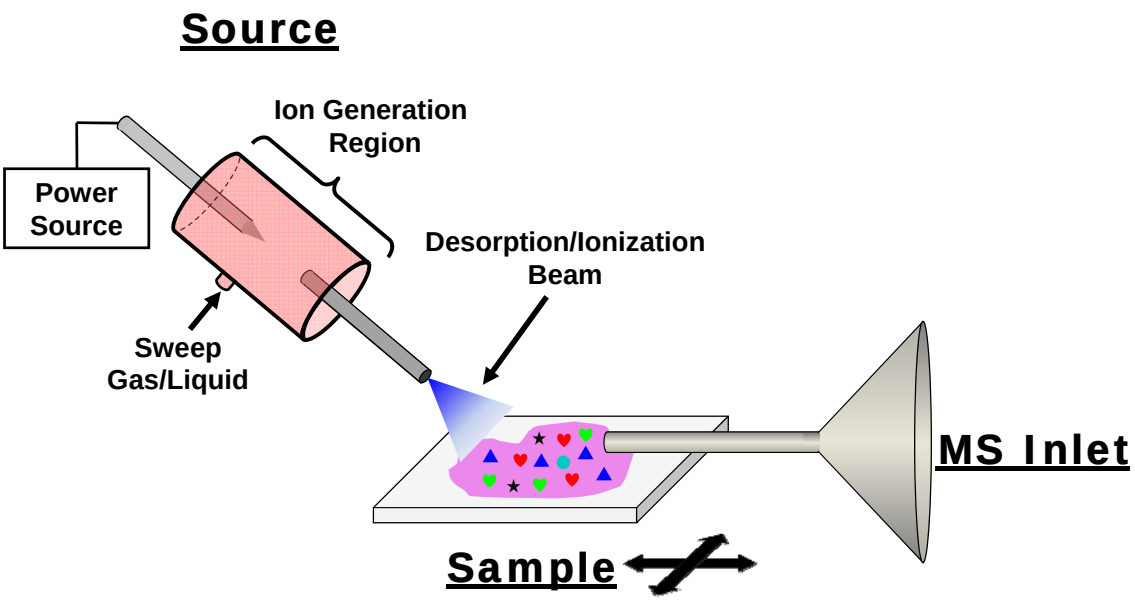

Figure 1.1 General diagram of an ambient mass spectrometry experiment. Ions from the ion generation region are carried to the untreated sample with a sweep gas and/or liquid. This desorption/ionization beam releases analytes (identified by different colored symbols) into the gas phase and subsequently ionizes them. Ions are drawn into the mass spectrometer inlet, separated by m/z, and detected.

symbols in Figure 1.1, are lofted into the gas phase and ionized. These ionized molecules are transferred into the mass spectrometer with the aid of the sweep gas/aerosol from the source and the vacuum inlet of the MS, separated according to their mass-to-charge (m/z) values, and detected.

Often, but not necessarily, the mass spectra generated during ambient desorption/ionization MS are very simple and uncluttered. Figure 1.2 shows an ideal ambient mass spectrum of the sample in Figure 1.1. Each species present in the sample gives rise to only a single mass-spectral peak indicative of the molecular mass. This spectral simplicity arises because the ionization processes used by the sources are typically based on electrospray or chemical-ionization mechanisms, which typically produce few fragment ions. Also, because the ionization process occurs at atmospheric pressure, collisional cooling aids in the dissipation of excess energy, further reducing fragmentation of analyte ions. Consequently, even though samples might be very complex and contain numerous constituents, those species are separated by the mass spectrometer on a very fast timescale, potentially obviating the need for lengthy sample preprocessing or separation methods. Further, because mass spectrometry allows individual ions to be detected, the relative peak heights in the spectrum should ideally be the same as the relative abundance of the corresponding analyte species in the sample (cf. Figure 1.1 and Figure 1.2a).

1.3 The Hype

Clearly there is a need in the scientific community, as well as in society in general, for a fast, sensitive, and selective method for the chemical analysis of things as

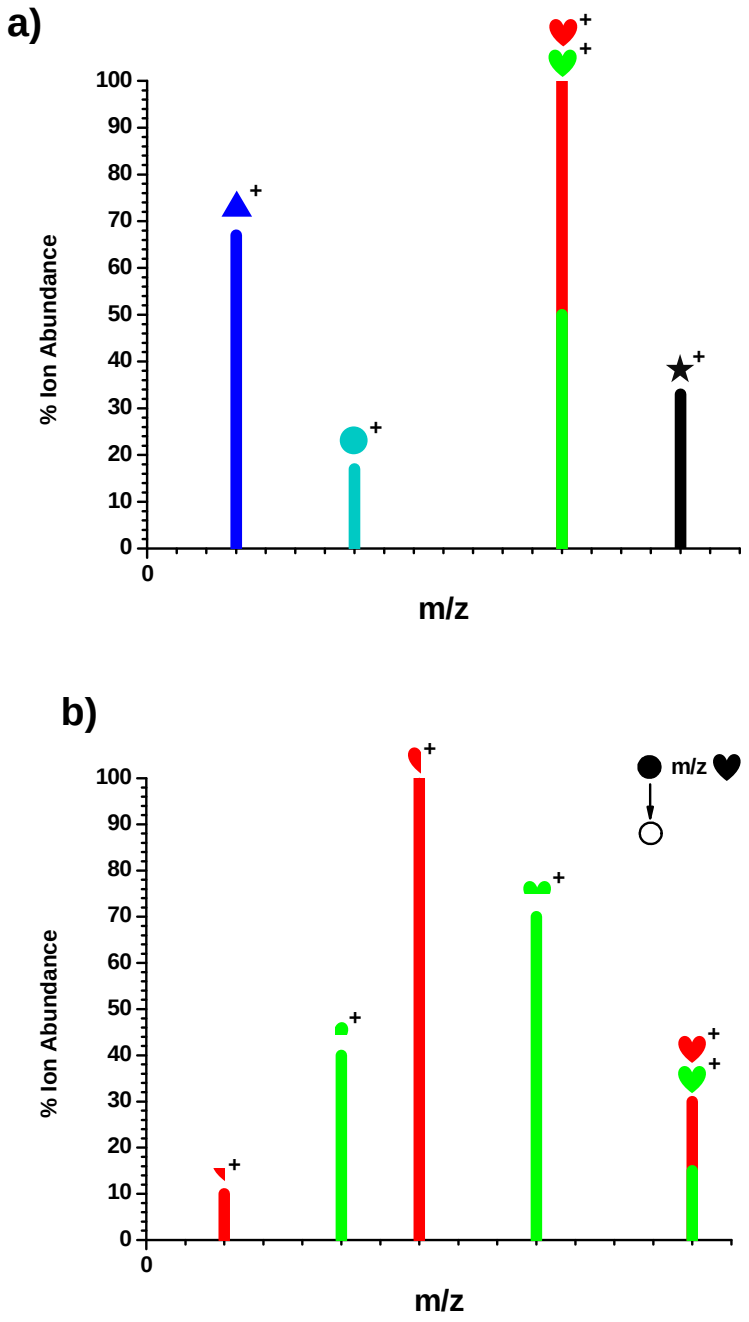

Figure 1.2 a) Ideal ambient mass spectrum of the sample in Figure 1 with one mass spectral peak per analyte. The different colored ♥ symbols represent isobars that cannot be resolved. b) Tandem mass spectrum of the ♥ peak in (a). Based on fragmentation pattern, the two species can be resolved and identified.

they are. When the concept of ambient mass spectrometry was proposed in 2004 by Prof. R. Graham Cooks at Purdue University,[3-4] it seemed to fit this need quite well. The introduction of ambient mass spectrometry as a field was accompanied by introduction of two desorption/ionization sources, desorption electrospray ionization (DESI)[4] and direct analysis in real time (DART),[5] which are commercially available from Prosolia and IonSense, respectively. So, at the same time the conceptual groundwork was laid out for this field, the practical implementation was also demonstrated. The combination of these events led to unbridled optimism and enthusiasm (i.e. hype) regarding this field and, consequently, to the rapid introduction of over 30 different desorption/ionization sources,[2, 6] publication of almost 300 manuscripts in a two-year window,[2] and even references in popular media such as television shows.[7-8] While not necessarily of the same magnitude, this trend in hype and expectations is common to the introduction of nearly any new technology. This trend is so common that Gartner, an information technology research and advisory company, developed the Hype Cycle Model to describe a society's response to the initiation of a new technology or field.[9]

1.4 Ambient Mass Spectrometry Hype Cycle

A diagram of the time-dependent hype cycle as it pertains to ambient mass spectrometry is shown in Figure 1.3a. There are five general regions of the hype cycle: the technology trigger, the peak of inflated expectations, the trough of disillusionment, the slope of enlightenment, and the plateau of productivity. The technology trigger in the case of ambient mass spectrometry was the introduction of DESI and DART in 2004 and early 2005, respectively. Interest in the analytical community grew rapidly, especially

for Determinators, who wished to exploit the new technology. The positive hype was generated through a range of applications, including the detection of illicit drugs and metabolites in bodily fluids,[10-11] direct explosives screening,[5, 12] imaging of biological molecules in tissues,[13] and rapid categorizing of counterfeit pharmaceuticals.[14] At the same time, numerous research groups developed alternative desorption/ionization sources, with as many as seven introduced in the literature in a single year (cf. Figure 1.3a). Since 2007, however, the number of new sources described per year has gradually declined, with more attention being focused on applications of ambient mass spectrometry; this shift is a sign of maturation of the field and an indicator that the Peak of Inflated Expectations might be near. For most technologies, it is at this point in the hype cycle when it is realized that the initial and usually unrealistic goals or promises have not been met, which yields negative hype. The true shortcomings of the technology become evident and many people lose interest, creating the Trough of Disillusionment. Many inventions do not recover from this trough, ultimately causing collapse of the product or field of interest.

If ambient mass spectrometry is at or near the Peak of Inflated Expectations, it begs the question: "Where does the field go from here?" To formulate an answer to this question, it is necessary to understand what causes the hype-cycle behavior. The hype cycle arises from two unfortunately independent processes: the initial hype and research-driven interest (cf. Figure 1.3b). The initial hype is caused by human interest and a bandwagon effect. The people that drive the initial excitement are almost never the same as those who develop the technology trigger. In the case of the analytical sciences, the hype is propagated and escalated by Determinators because they do not necessarily

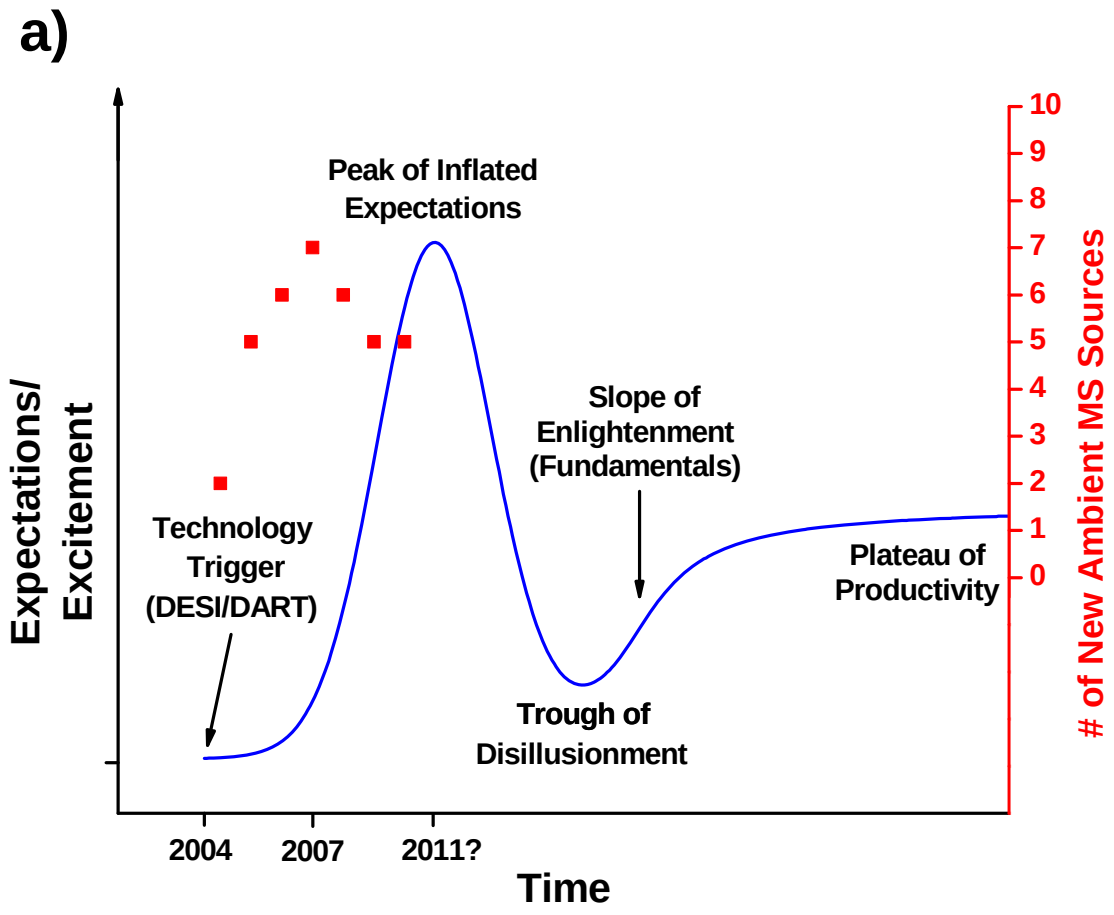

Figure 1.3a Gartner Hype Cycle Model (blue trace) showing the five phases of a newly described technology formatted in the context of ambient mass spectrometry. The technology trigger was the introduction of DESI and DART in 2004 and early 2005. As a reference, the red symbols show the number of new ambient mass spectrometry sources introduced each year, compiled from References 2 and 6, with a maximum of seven in 2007.

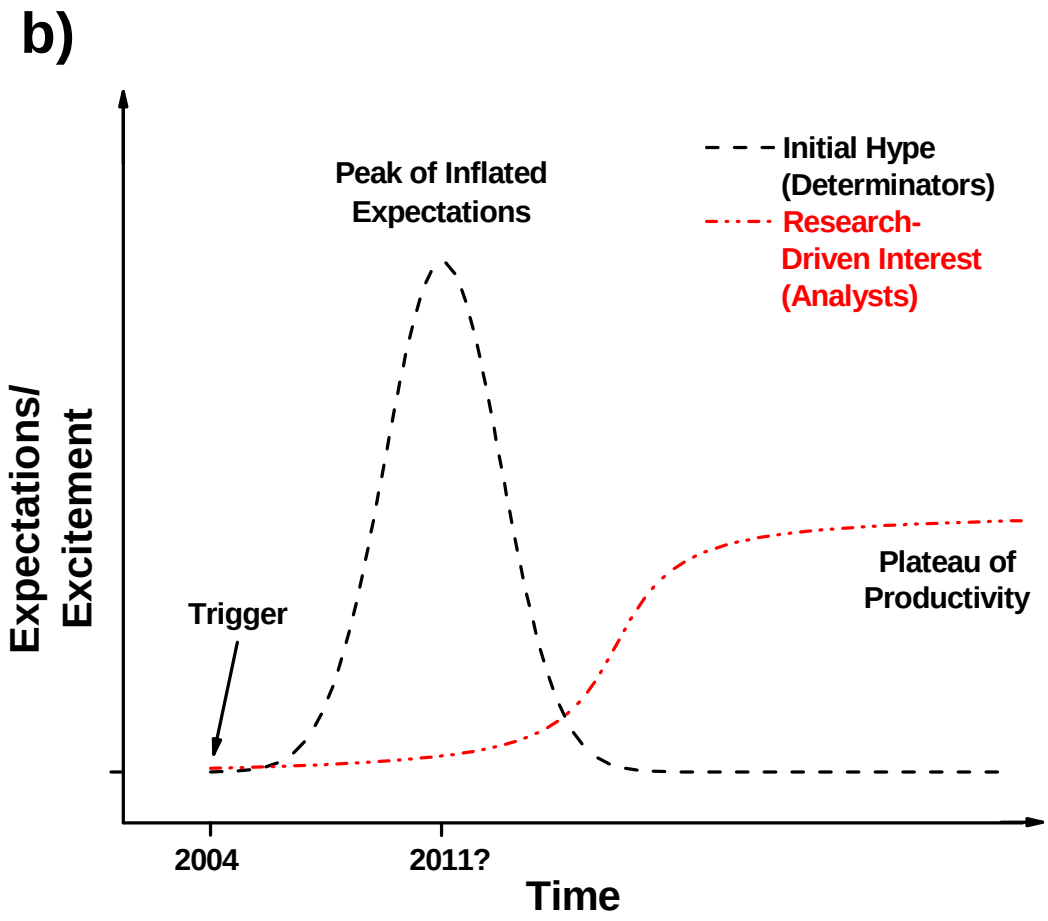

Figure 1.3b Two factors that led to the formation of the hype cycle. Initial hype (black trace) is caused by immediate human reaction to a new technology and is often proliferated by those who do not yet understand the fundamental limitations of the technology (i.e. Determinators). Research-driven interest occurs independently of the initial hype and is guided by fundamental research and development of the technology, typically by Analysts. Absence of overlap in these processes can lead to complete abandonment of the technology/field. Figures adapted and reprinted with permission from "Mastering the Hype Cycle: How to Choose the Right Innovation at the Right Time" by Jackie Fenn and Mark Raskino. Harvard Business Press, 2008.

understand the fundamental limitations of the technique. As a result, when the analytical method does not meet the Determinators' initial, inflated expectations, negative hype is expressed through the literature and other presentations.

The other component of the hype cycle is the natural maturation of the invention where the initial description of the technology does not have much inherent value; rather, the gradual culmination of fundamental research and development over time leads to rapid interest in the invention (i.e. the Slope of Enlightenment). For the analytical sciences, this research-driven interest is nearly always initiated and propagated by Analysts, those who have a good understanding of the technique's fundamental strengths and weaknesses and who wish to delineate its boundaries. If these curves are separated too much in time, the Trough of Disillusionment becomes deeper and wider, which can lead to the death of the technology through various means, including societal loss of interest, lack of funding opportunities, and others. The earlier the Slope of Enlightenment is realized, the less likely the invention will fail or suffer irreparable damage from negative hype. Accordingly, for ambient mass spectrometry to thrive as a method for the chemical analysis of things as they are, more fundamental studies are needed to address inherent problems and shortcomings. Some of these issues as well as methods to understand and overcome them will be presented in the following sections.

1.5 Ambient Mass Spectrometry In Practice

While the concept of ambient mass spectrometry is relatively straightforward, numerous practical issues must be considered in its application. As an example, ambient mass spectra of navel orange peels obtained with the plasma-based flowing atmospheric-

pressure afterglow (FAPA) source[15] are shown in Figure 1.3. Both oranges were purchased at a local commercial market and appear to be similar; however one was labeled as "organic" (cf. Figure 1.4a) and the other was not (cf. Figure 1.4b). The orange fruit was manually positioned between the source and mass spectrometer for 5 seconds. In this short analysis time, the spectra reveal that these oranges carry different molecules on their surfaces. The major peaks for the organic orange (cf. Figure 1.4a) are between 325 and 450 Da, with minor peaks in the range of 100 and 150 Da. The same peaks were observed for the non-organic orange (cf. Figure 1.4b), indicating that they are likely native to the fruit. A few mass-spectral peaks, however, were present only in the spectrum of the non-organic orange, including the base peak at 297.05 Da. So, even with the most limited understanding of ambient mass spectrometry and no *a priori* knowledge of the two samples other than visual inspection, it can be determined that something has likely been added to the orange peel whose spectrum is in Figure 1.3b. However, that information alone will not suffice. It is essential to know *what* was added and, ideally, *how much* is present. Furthermore, it is important to determine the identity of the species corresponding to the peaks common to both spectra.

Although generating only a single mass-spectral peak per analyte is advantageous in the analysis of complex samples, identification of each component in the spectrum can then be difficult. This point is emphasized in Figure 1.1 where heart symbols of two different colors exist in the sample; in the corresponding mass spectrum (cf. Figure 1.2a), the two species cannot be resolved and appear as one peak with a higher relative abundance than is actually present. Additionally, it is possible that two different molecules have either a similar enough molecular weight that they cannot be resolved by

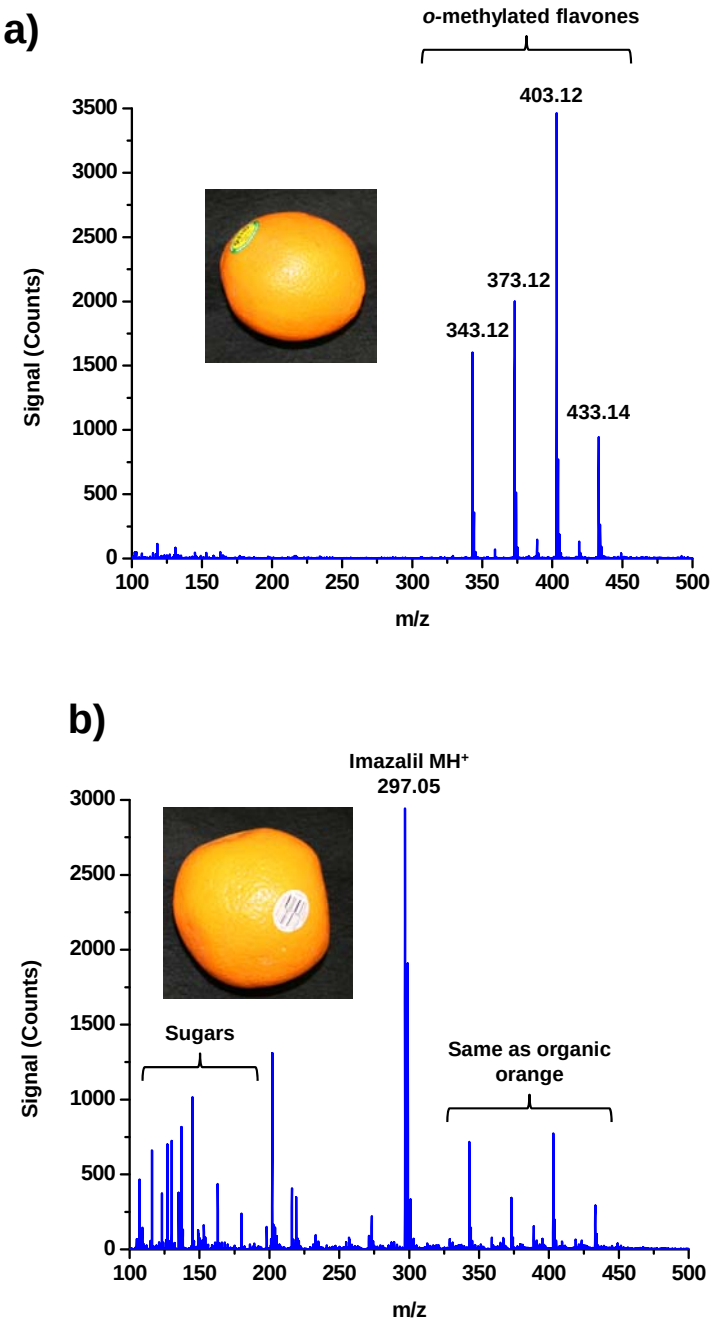

Figure 1.4 Direct, ambient mass spectra of organic (a) and non-organic (b) navel orange peels obtained with the FAPA desorption/ionization source. The peaks in the high-mass and low-mass range for both oranges correspond to o-methylated flavones and sugars/sugar fragments, respectively. The peak at 297.05 Da in (b) is indicative of the fungicide imazalil.

the mass spectrometer (isobars) or have the same elemental composition, but different chemical structures (isomers) such that their molecular weights are exactly the same. High-resolution mass spectrometers (e.g. Fourier transform ion-cyclotron resonance, Orbitrap, or time-of-flight) can help distinguish isobars and, with sufficient mass accuracy, reveal the exact elemental composition of each molecule. Unfortunately, these instruments are often more expensive than their lower-resolution counterparts, such as quadrupole mass filters or ion traps, and it is impossible to obtain structural information with them. Tandem mass spectrometry (MS/MS), often obtained through collision-induced dissociation in an ion trap, enables fragmentation of molecules within a mass window prior to mass analysis so isobars or isomers can be differentiated (cf. Figure 1.1c). Also, the fragment ions in the MS/MS spectrum can reveal structural information and lead to unambiguous analyte identification.

In the case of the orange-peel analysis in Figure 1.4, the peak at m/z 297.05 was found to have an empirical formula of $C_{14}H_{14}Cl_2N_2O$ based on accurate-mass information as well as from the isotopic distribution. A literature search, in conjunction with MS/MS data, revealed the identity of this molecule as imazalil, a common fungicide used to treat citrus fruits. This identity would explain the absence of the peak in the spectrum of the organic orange peel. The set of high- and low-mass peaks in both spectra were identified, through similar methods as above, as various o-methylated flavones and sugars/sugar fragments, respectively.

Remaining is the question of *how much* of each constituent is present; this point is one of the biggest fundamental challenges remaining in this field. The ability to relate

mass-spectral signal amplitude to the amount of analyte in the sample is dependent on a number of factors, including the desorption process, the ionization event, and the transport of the resulting analyte ions into the mass spectrometer. Moreover, matrix effects can occur in both the desorption and ionization processes, suggesting a need for matrix-matched standards, which is often not practical for the complex samples probed in ambient mass spectrometry. Internal standards can be used to correct for some of these issues,[16-17] but because of variances in desorption and ionization efficiency for different molecules, isotopically labeled standards of an analyte of interest should be used. Regrettably, they are often difficult to find, expensive, or problematic to synthesize. Therefore, fundamentally characterizing and understanding ambient mass spectrometry in the context of desorption/ionization processes and analyte transport is essential for this field to overcome the trough of disillusionment.

1.6 The Future: Seeking Enlightenment

Ambient mass spectrometry has been shown to be a powerful tool for the chemical analysis of things as they are in a variety of applications. However, several major hurdles must be addressed by Analysts before this method of analysis can become commonplace. The sources that particularly are not well understood are those based on electrical discharges, such as DART,[5] FAPA,[15] and the low-temperature plasma (LTP) probe;[18] many of the suggested desorption or ionization mechanisms for these plasma-based sources have been only hypothesized, and supported by little experimental evidence. This fact is quite surprising, considering that plasma-based sources constitute nearly half of those described for ambient mass spectrometry. In addition, a wealth of

knowledge and expertise on the fundamental properties and characteristics of plasmas already exists in the analytical sciences within the atomic spectroscopy community.

The desorption mechanism for most plasma-based sources is often claimed to be essentially thermal, where the elevated temperature of the discharge gas serves to volatilize organic molecules from surfaces.[19-20] This assertion is supported by the fact that elevated plasma-gas temperatures enhance analyte signals.[17-19] Although thermal effects can certainly influence the desorption process, other factors, such as chemical sputtering or photo-induced desorption, could contribute and should be specifically studied. Furthermore, how these processes are altered for different substrates will yield insights into the role of desorption matrix effects, which are probably the biggest present unknown in this field.

Ionization mechanisms of plasma-based sources have received greater study, but are often suggested on the basis of background ions in the mass spectra,[5, 18, 21] analyte ions, and mechanisms believed to exist in APCI.[22-23] Protonated water clusters $[(H_2O)_nH^+]$ and ions from other atmospheric gases (e.g. N_2^+ and O_2^+) are commonly detected and are known to be involved in proton transfer or charge transfer, respectively, with a gas-phase molecule to yield a softly formed ion. However, the mechanism of formation of these reagent species is not yet clear.

The identity of the discharge gas has been shown to greatly affect sensitivity and reagent-ion formation, with helium providing the best performance. In the initial description of DART, it was proposed that helium metastable atoms (He^m) were responsible for reagent-ion formation through Penning ionization of atmospheric gases.

Such metastables have long lifetimes, high internal energy (>19 eV), and are neutral, which is a necessary trait in the case of DART because filter grids are used to remove charged species ahead of the sample introduction region.[5] Without published validation, this same mechanism has been suggested for many of the plasma-based sources, even those that do not filter ions.[18, 24]

Several research groups have initiated work to determine how these different plasmas can operate as desorption/ionization sources for molecular mass spectrometry. Good examples were presented in a session at the most recent Federation of Analytical Chemistry and Spectroscopy Societies (FACSS) Conference in Raleigh, North Carolina. Matthew Heywood from the research group of Prof. Paul Farnsworth at Brigham Young University demonstrated the ability to directly map He^m densities in the afterglow of a helium dielectric-barrier discharge, similar to the LTP probe, with collisionally assisted laser-induced fluorescence.[25] He found that plasma power affected spatial emission profiles of high-energy helium atoms, even though profiles of He^m were unchanged. When a glass microscope slide was introduced into the afterglow, to mimic an ambient mass spectrometry analysis, the He^m concentration nearly doubled, demonstrating that sample introduction and sample or substrate morphology could alter the ion chemistry. This finding suggests another potential form of matrix effect that can occur with these sources. Lastly, the effect of a mixed discharge gas on the He^m density and mass spectral performance was explored by the addition of 1% H_2 to the plasma gas. Surprisingly, even though the concentration of He^m was strongly reduced by the addition of hydrogen, an enhancement in the mass spectral signal of a model analyte occurred. These data

show that He^m is not essential for a plasma-based ambient mass spectrometry source to perform well and that the use of mixed gases should be explored in greater detail.

Joshua Wiley, from the research group of Prof. R. Graham Cooks at Purdue University, presented some collaborative research performed with the Hieftje laboratory at Indiana University, on imaging the afterglow of the LTP probe with optical spectroscopy and relating these findings to mass spectrometric results.[26] It was found that the afterglow from the LTP probe is reproducibly transient and consists of plasma "bullets" that propagate at supersonic velocities (~3,000 m/s). Furthermore, various emitting species had different plasma bullet starting times and durations. In particular, emission from N_2 preceded that from N_2^+ and He* in space and time, while N_2^+ and He* were closely correlated. These plasma bullets, and presumably reagent-ion formation, had a duty cycle of less than 1% with respect to the input-voltage waveform, but could be increased to ~18% when a grounded needle was placed into the afterglow; improved mass spectral performance was also reported when the sample was applied to a grounded needle.

In this work, the close spatial and temporal correlation of N_2^+ and He was found to be a result of the presence of helium dimer ion, He_2^+, which generates at least 30% of the N_2^+ reagent ions.[27] These spectroscopic investigations helped reveal a set of reactions that occur in the afterglow of the LTP, and likely in other plasma-based source, that had not been shown before (cf. Figure 1.5). The source of atmospheric gases (N_2, O_2, H_2O) in the LTP was also determined through optical spectroscopy[28] and has ultimately led to re-designed LTP[26] and FAPA[29] sources.

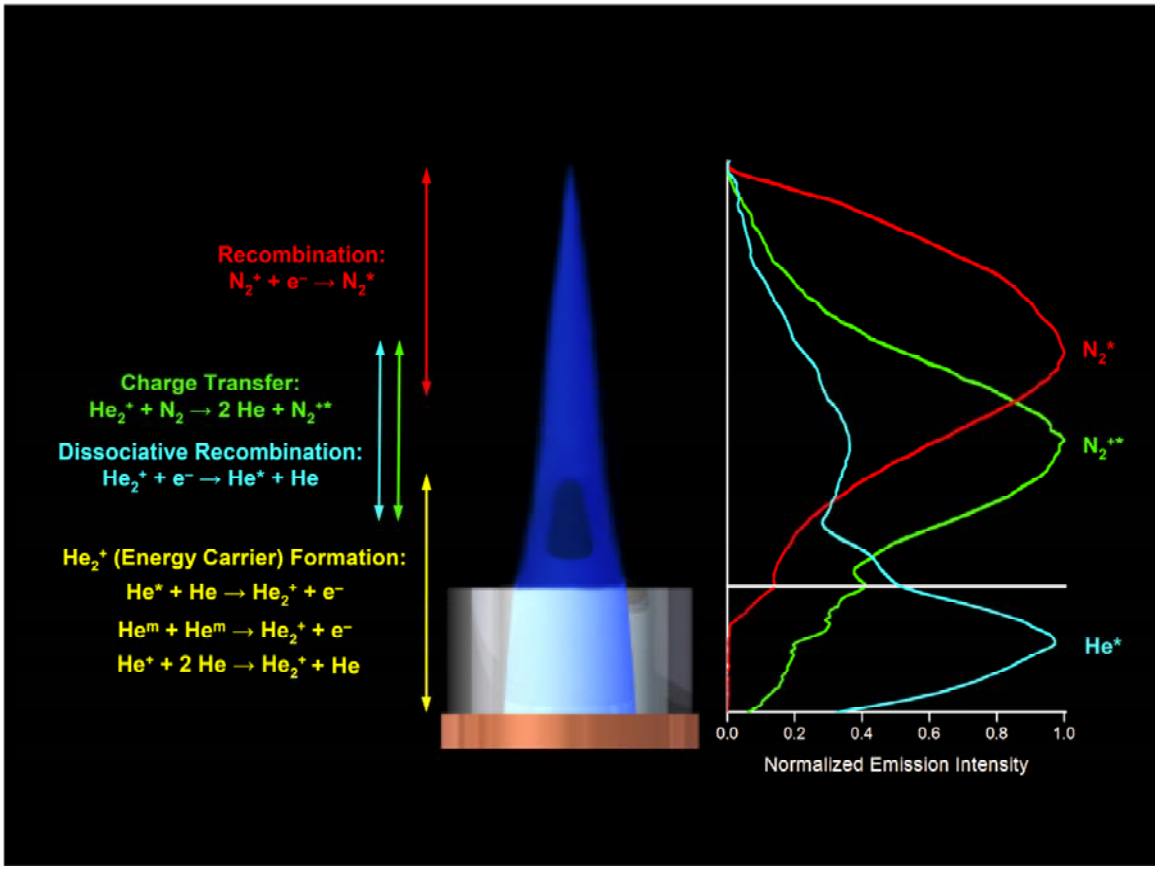

Figure 1.5 Proposed sequence of reagent-ion-forming reactions in the afterglow of the LTP probe (cf. Ref. 27). The reactions were revealed through optical-spectroscopic measurements of the LTP discharge and afterglow.

As mentioned previously, matrix effects are of large concern in ambient mass spectrometry analyses because of the complex samples that are examined. Furthermore because a single source is used for both desorption and ionization, which means that a second, orthogonal dimension of matrix effects are possible. While not explicitly studied yet, desorption matrix effects for plasma-based sources could be caused by differences volatility of sample species or thermal conductivity of the sample substrate. Our group has recently examined the degree of ionization matrix effects that occur with FAPA, DART, and LTP sources.[30] The most common form of ionization matrix effect is through ion suppression where a gas-phase matrix molecule has a lower ionization energy and is then capable of being preferentially ionized over an analyte molecule. Figure 1.6 shows the level of acetophenone signal suppression when a matrix with higher proton affinity, triethyl phosphate, is present in the ionization region at different concentrations. In this case all three exhibited a matrix effect even at a matrix-to-mole ratio of 10^{-3}, with analyte signal entirely suppressed for DART and LTP at a mole ratio of 10. Similar results were obtained when the proton affinities of the matrix and analyte were more closely matched. Methods to lessen these effects certainly need to be pursued in the future.

These examples show that some effort is being expended to understand and overcome fundamental limitations of plasma-based ambient mass spectrometry sources. However to avoid the trough of disillusionment in this field, many more issues need to be addressed. Improving methods of sample introduction and quantification are still a substantial concern, and it is important to further clarify physical processes that govern analyte desorption and ionization. Given the expertise in plasma processes in the atomic

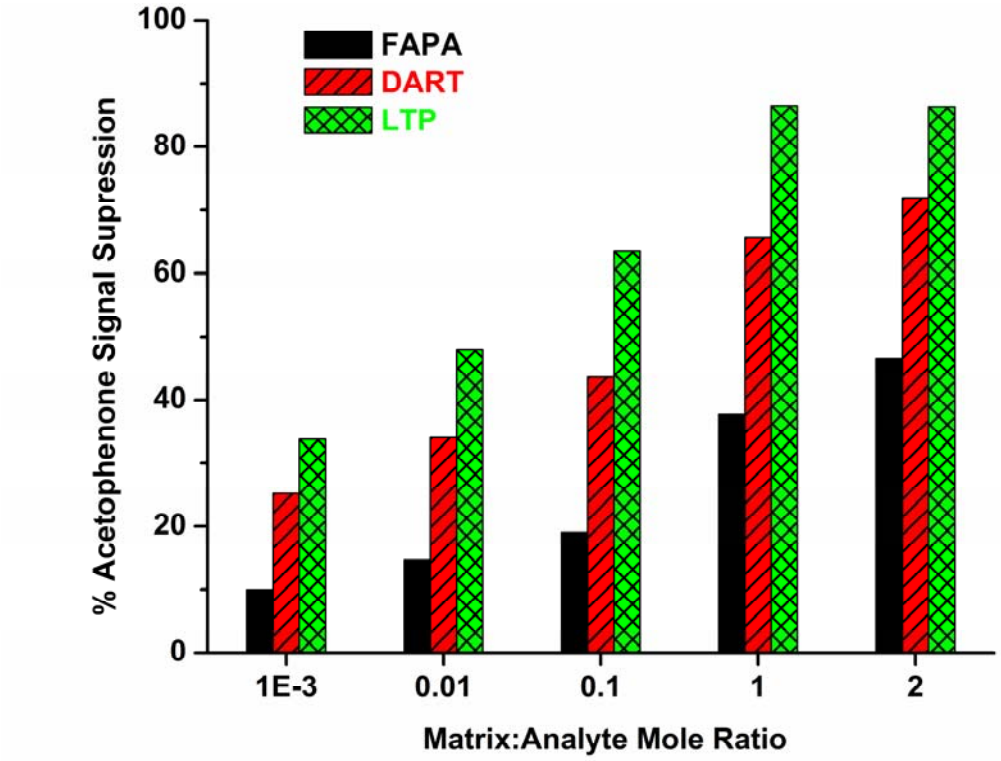

Figure 1.5 Mass-spectral signal suppression for acetophenone with FAPA, DART, and LTP ionization sources when a matrix with a higher proton affinity, triethyl phosphate, is present in the ionization region (cf. Ref. 30).

spectrometry field, it makes sense for these research groups to become heavily involved in the ambient mass spectrometry field. These types of studies will ensure that ambient mass spectrometric methods can truly perform the chemical analysis of things as they are.

References

1. Lundell, G. E. F. *Industrial & Engineering Chemistry Analytical Edition* **1933**, *5*, 221-225.
2. Harris, G. A.; Galhena, A. S.; Fernández, F. M. *Anal. Chem.* **2011**, null-null.
3. Cooks, R. G.; Ouyang, Z.; Takats, Z.; Wiseman, J. M. *Science* **2006**, *311*, 1566-1570.
4. Takats, Z.; Wiseman, J. M.; Gologan, B.; Cooks, R. G. *Science* **2004**, *306*, 471-473.
5. Cody, R. B.; Laramee, J. A.; Durst, H. D. *Anal. Chem.* **2005**, *77*, 2297-2302.
6. Weston, D. J. *Analyst* **2010**, *135*, 661-668.
7. Jamieson, J., in *The Salem News*. Salem, MA, 2005.
8. Gardner, E., in *Purdue University News*. West Lafayette, IN, 2008, vol. 2011.
9. Fenn, J.; Raskino, M., *Mastering the Hype Cycle: How to Choose the Right Innovation at the Right Time*. Harvard Business Press: 2008.
10. Kauppila, T. J.; Talaty, N.; Kuuranne, T.; Kotiaho, T.; Kostiainen, R.; Cooks, R. G. *Analyst* **2007**, *132*, 868-875.
11. Zhao, Y. P.; Lam, M.; Wu, D. L.; Mak, R. *Rapid Commun. Mass Spectrom.* **2008**, *22*, 3217-3224.
12. Cotte-Rodriguez, I.; Takats, Z.; Talaty, N.; Chen, H. W.; Cooks, R. G. *Anal. Chem.* **2005**, *77*, 6755-6764.
13. Wiseman, J. M.; Ifa, D. R.; Song, Q. Y.; Cooks, R. G. *Angewandte Chemie-International Edition* **2006**, *45*, 7188-7192.

14. Fernandez, F. M.; Cody, R. B.; Green, M. D.; Hampton, C. Y.; McGready, R.; Sengaloundeth, S.; White, N. J.; Newton, P. N. *ChemMedChem* **2006**, *1*, 702-+.

15. Andrade, F. J.; Shelley, J. T.; Wetzel, W. C.; Webb, M. R.; Gamez, G.; Ray, S. J.; Hieftje, G. M. *Anal. Chem.* **2008**, *80*, 2654-2663.

16. Jackson, A. U.; Garcia-Reyes, J. F.; Harper, J. D.; Wiley, J. S.; Molina-Diaz, A.; Ouyang, Z.; Cooks, R. G. *Analyst* **2010**, *135*, 927-933.

17. Wiley, J. S.; Garcia-Reyes, J. F.; Harper, J. D.; Charipar, N. A.; Ouyang, Z.; Cooks, R. G. *Analyst* **2010**, *135*, 971-979.

18. Harper, J. D.; Charipar, N. A.; Mulligan, C. C.; Zhang, X. R.; Cooks, R. G.; Ouyang, Z. *Anal. Chem.* **2008**, *80*, 9097-9104.

19. Nilles, J. M.; Connell, T. R.; Durst, H. D. *Analyst* **2010**, *135*, 883-886.

20. Shelley, J. T.; Wiley, J. S.; Chan, G. C. Y.; Schilling, G. D.; Ray, S. J.; Hieftje, G. M. *J. Am. Soc. Mass. Spectrom.* **2009**, *20*, 837-844.

21. Andrade, F. J.; Shelley, J. T.; Wetzel, W. C.; Webb, M. R.; Gamez, G.; Ray, S. J.; Hieftje, G. M. *Anal. Chem.* **2008**, *80*, 2646-2653.

22. Horning, E. C.; Horning, M. G.; Carroll, D. I.; Dzidic, I.; Stillwel, R. N. *Anal. Chem.* **1973**, *45*, 936-943.

23. Good, A.; Durden, D. A.; Kebarle, P. *J. Chem. Phys.* **1970**, *52*, 212-&.

24. Ratcliffe, L. V.; Rutten, F. J. M.; Barrett, D. A.; Whitmore, T.; Seymour, D.; Greenwood, C.; Aranda-Gonzalvo, Y.; Robinson, S.; McCoustra, M. *Anal. Chem.* **2007**, *79*, 6094-6101.

25. Heywood, M. S.; Wright, J.; Farnsworth, P. B., presented in part at Federation of Analytical Chemistry and Spectroscopy Societies Conference, Raleigh, North Carolina, October 21, 2010, Yea.

26. Wiley, J. S.; Shelley, J. T.; Jackson, A. U.; Hieftje, G. M.; Cooks, R. G., presented in part at Federation of Analytical Chemistry and Spectroscopy Societies Conference, Raleigh, North Carolina, October 21, 2010, Yea.

27. Chan, G. C. Y.; Shelley, J. T.; Wiley, J. S.; Engelhard, C.; Jackson, A. U.; Cooks, R. G.; Hieftje, G. M. *Anal. Chem.* **2011**, null-null.

28. Chan, G. C. Y.; Shelley, J. T.; Jackson, A. U.; Wiley, J. S.; Engelhard, C.; Cooks, R. G.; Hieftje, G. M. *J. Anal. At. Spectrom.* **2011**.

29. Shelley, J. T.; Wiley, J. S.; Hieftje, G. M. *Anal. Chem.* **2011**, Submitted.

30. Shelley, J. T.; Hieftje, G. M. *J. Anal. At. Spectrom.* **2010**, *25*, 345-350.

Chapter 2

Laser Ablation Coupled to a Flowing Atmospheric-Pressure Afterglow for Ambient Mass Spectral Imaging

2.1 Introduction

Mass spectral imaging (MSI) has been growing in importance, especially for the analysis of tissues and other biological samples. Conventionally, MSI is performed with an ionization source under vacuum, such as matrix-assisted laser desorption/ionization (MALDI) or secondary ion mass spectrometry (SIMS).[1] To date, two methods for performing MSI with MALDI have been demonstrated. The most common, termed MALDI probe imaging, involves scanning a pulsed UV laser across a sample surface that has been evenly coated with a UV-absorbing matrix.[2] The resulting time trace can be converted into a distance plot from which the chemical image can be extracted.

An alternative method, termed MALDI microscope imaging, employs a defocused UV laser that envelops a large area on a matrix-covered sample.[3] Special ion optics preserve and magnify the shape of the resulting ion packet. The ions are then detected with an intensified charged coupled device (iCCD) after traveling through a conventional time-of-flight (TOF) mass analyzer for mass-to-charge (m/z) separation. Obviously, the latter technique is complicated by the need for specialized ion optics, fast electronics/detectors, and complex computing to generate chemical images. Further, very few m/z values can be detected with each run because of the detector response time and the size of the data files that are generated.[4] There are other problems that plague MALDI for use in MSI. For instance, samples are analyzed under vacuum, so biological or wet samples must be dried and mounted prior to analysis. In addition, the matrix solution must be applied to the sample evenly and in small enough droplets to preserve spatial resolution while maintaining an optimal matrix-to-analyte ratio.

One way to avoid the aforementioned complications is to use an ionization source that operates at atmospheric pressure. Li et al.[5] proposed using atmospheric-pressure infrared MALDI (AP-IR-MALDI) for MSI. In this case, an IR laser tuned to a vibrational band of water was used for the desorption/ionization process, so water serves as the matrix. However, AP-IR-MALDI was limited heavily by the diffraction-limited spot size of the laser (~250 μm); also, signal-to-noise ratios were disappointing and resulted in mediocre analyte distribution maps.[5]

The use of a recent class of atmospheric-pressure ionization sources with mass spectrometry, collectively termed ambient desorption/ionization mass spectrometry (ADI-MS), would seem well suited to MSI. One possibility is desorption electrospray

ionization (DESI).[6] In DESI, developed by Cooks et al.,[7] a high-velocity gas stream directs solvent droplets from an electrospray ionization (ESI) source onto a surface. When the large solvent droplets impact the sample surface, they break up into smaller droplets and pick up analyte molecules. The smaller droplets, which have a scatter angle of ~10° under incidence angles between 55-75°, are drawn into the capillary interface of a mass spectrometer.[8-11] As the analyte-containing solvent droplets evaporate, the charges originally on a droplet are transferred to analyte molecules. To perform MSI, the sample stage was scanned underneath the DESI tip and mass spectrometer capillary interface.[6, 12] Spatial resolution was limited by droplet scatter, sample smearing, and DESI tip diameter (~200 μm).[6, 12]

Nemes et al.[13-14] used ablation by a mid-IR laser to remove material from a surface and employed ESI to ionize molecules from the ablation plume. This technique, termed laser ablation electrospray ionization (LAESI), requires no sample pretreatment, can operate at atmospheric pressure, and offers the potential of depth information. Good detection limits were achieved (5 fmol for verapamil), with a broad detectable mass range (up to 66 kDa). Images of a leaf yielded a spatial resolution worse than 400 μm, with a theoretical, instrumental limit of 350 μm.[13] It is important to note that LAESI and DESI have similar biological resolution capabilities.

The use of plasma-based ADI-MS sources for MSI has not been explored in much detail. Plasma-based sources include direct analysis in real time (DART),[15] dielectric barrier discharge ionization (DBDI),[16] plasma-assisted desorption/ionization (PADI),[17] and the flowing atmospheric-pressure afterglow (FAPA).[18-19] These ADI-MS sources have a distinct advantage over ESI and MALDI-based techniques in that there are little or

no solvent considerations. The plasma sources use either gaseous reagent ions or metastables for ionization, resulting in a wider variety of compounds that can be ionized under a fixed set of operating conditions. Early attempts in our laboratory to obtain spatial information of samples directly with the FAPA source resulted in poor spatial resolution (~0.5 mm) and yielded only one-dimensional images.[19] In the present study, high-resolution chemical images of solid samples were produced by coupling UV laser ablation with the FAPA ionization source (LA-FAPA). Besides chemical images, LA-FAPA was used for depth profiling and as a reproducible method for sample introduction into the ADI-MS source.

2.2 Experimental

2.2.1 Chemical Reagents and Materials

All reagents used were analytical grade. Ultra high-purity helium (99.999% ultra-high purity helium, Airgas, Radnor, PA) was used in all experiments. Dry nitrogen for transport of the ablation aerosol was supplied from boil-off of a local liquid-nitrogen storage facility.

2.2.2 Instrumentation

A schematic diagram of the FAPA ionization source is given in Figure 2.1a. The APGD was formed between a tungsten pin (cathode) and a brass plate (anode). The electrodes were held in a fixed position by a Teflon® bodied cell with a typical electrode gap of ~5 mm (cf. photo in Figure 2.1b). Helium was fed into the discharge chamber through a small orifice in the cell body. All parts of the discharge were sealed within the

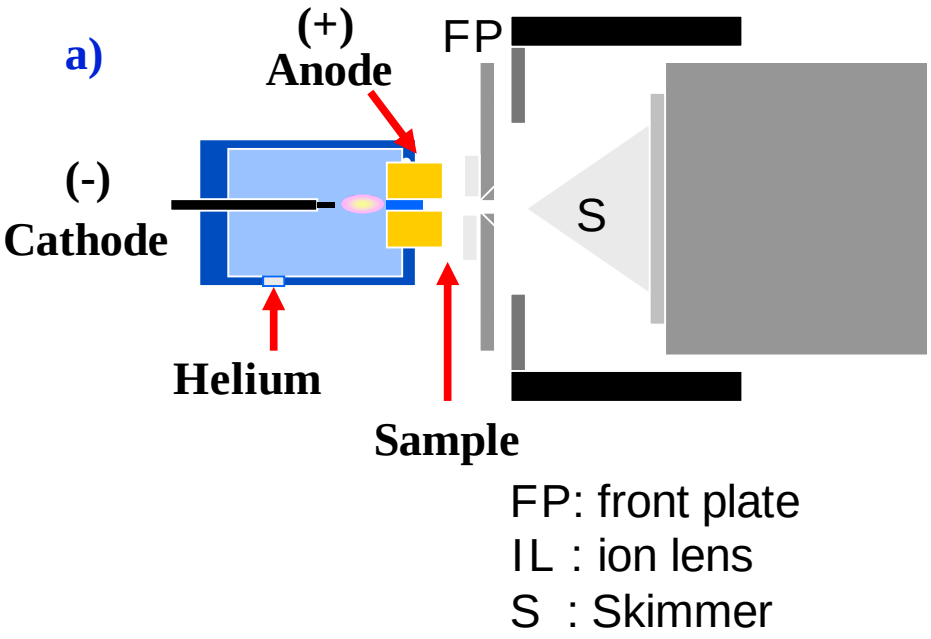

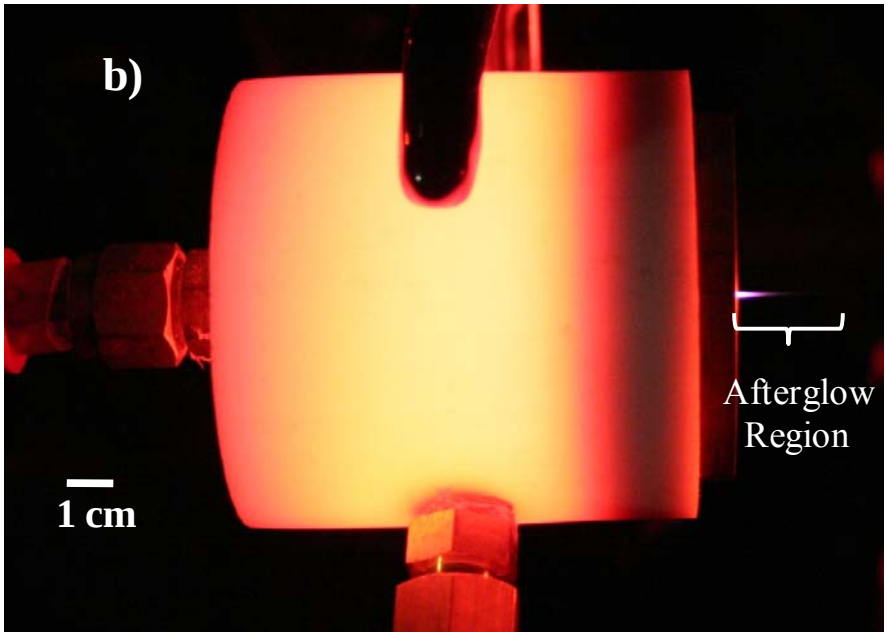

Figure 2.1 a) Schematic diagram of the FAPA ionization source. A glow discharge is created between a tungsten pin cathode and a brass anode plate. A hole in the anode allows the excited discharge gases to exit and interact with a sample outside the chamber. b) Photograph of FAPA cell with a neon discharge to emphasize the afterglow region.

cell to ensure that helium could exit only through a hole in the anode. The cell was positioned ~10 mm from the front plate of the mass spectrometer. Based on the velocity of gas exiting the discharge cell, it is estimated that the residence time of analyte species in the afterglow is roughly one millisecond. A diagram of the entire setup is given in Figure 2.2.

A helium flow of 0.5 to 1.5 L/min through the cell was maintained by a mass flow controller (Model FC-280-SAV, Tylan General, Carson, CA). A negative DC potential was applied to the cathode in a current-controlled mode through a 2.5 kΩ ballast resistor by means of a high-voltage power supply (Model DRC-5-400R, Universal Voltronics, Mount Kisco, NY). The anode plate was connected to a DC low-voltage power supply (Model 6299A, Hewlett Packard-Harrison Division, Berkley Heights, NJ) to create a field-free region between the anode and mass spectrometer interface. The FAPA was mounted on a 3D translation stage (home built) for proper alignment with the mass spectrometer.

Ions were detected by a LECO HT Unique® (LECO Corp. St. Joseph, MI) time-of-flight (TOF) mass spectrometer (MS). No adjustments were made to the Unique® spectrometer; however, the instrument was designed for conventional APCI and ESI sources, so its vacuum system could not properly cope with the helium flow. As a result, the discharge was operated at lower He flow rates (~0.8 L/min), resulting in lower gas temperatures and decreased reagent ion production. This change ultimately reduced the sensitivity somewhat.

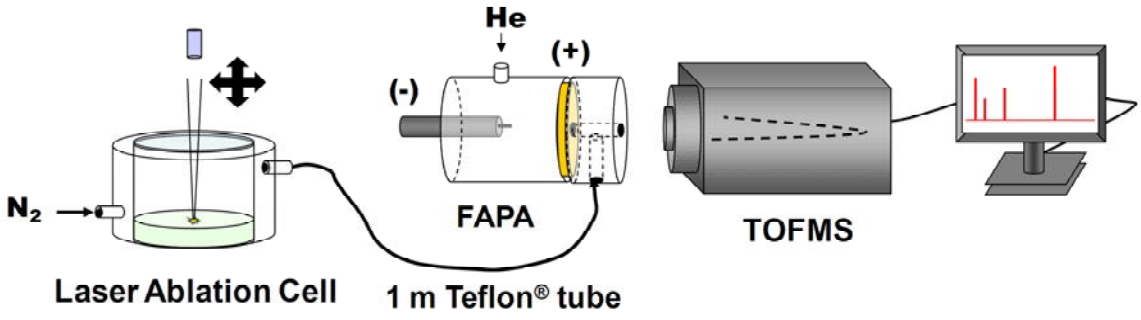

Figure 2.2 Schematic diagram of the LA-FAPA setup. A small amount of sample is ablated with 266 nm laser light. The resulting aerosol is transferred in a stream of N_2 through a 1 m Teflon tube to the afterglow region for desorption/ionization and detection.

2.2.3 Thermal Images

Temperature maps of the afterglow were generated with a Fluke Ti40 IR Flexcam (Fluke Corporation, Everett, WA) infrared camera by positioning a glass microscope slide either parallel or perpendicular to the helium flow for horizontal or vertical cross-sections, respectively (cf. Figure 2.3a). The temperatures obtained from the images were adjusted by using the emissivity of the glass slide (0.92).

2.2.4 Laser Ablation-FAPA

A Nd:YAG laser ablation system (LSX-200, CETAC, Inc., Omaha, NE) operating at 20 Hz was used to ablate material from selected points on a sample surface by employing 266 nm radiation focused to spot sizes between 10 μm and 300 μm in diameter. Aerosol generated by the ablation event was carried in a stream of N_2 at 0.3 L/min through a 1 m Teflon® tube into a second chamber where the aerosol was mixed with the afterglow from the discharge (cf. Figure 2.2). Molecules were then desorbed from the particles, ionized, and sampled by the TOFMS.

2.2.5 Analyte Printing

In order to generate chemical images of known shape and size, an inkjet printer cartridge was emptied and filled with a 2 M solution of caffeine (analyte) and food coloring (for visualization). The cartridge was used with an HP DeskJet 5740 printer (Hewlett-Packard Company, Palo Alto, CA) to print images doped with caffeine. The

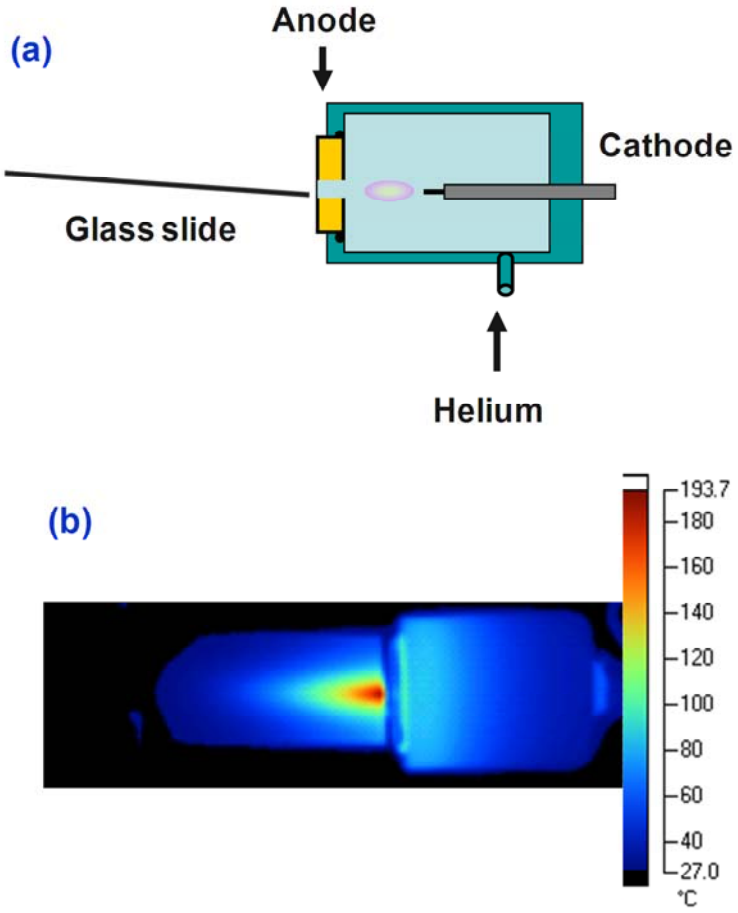

Figure 2.3 a) Arrangement of glass slide with respect to FAPA source for afterglow temperature imaging by Fluke Ti40 IR Flexcam. b) Temperature map of afterglow under standard operating conditions. The thermal image reveals that the afterglow region occupies an area of ~2.2 mm^2.

printer with a doped ink cartridge was used also to deposit single droplets (~5 pL) onto a glass slide to perform a calibration. The feed-through mechanism of the print head was disabled and single droplets were dispensed at 300 dpi. Single dots were produced by means of a commercial image processing program which enabled printing of single droplets.

2.3 Results and Discussion

The FAPA has ordinarily been employed for direct surface analysis by desorption/ionization. In this mode, molecules are desorbed and ionized in a single step from the surface of a sample placed in the flowing afterglow. Because the interaction area of the FAPA plume is relatively large (cf. Figure 2.1b), the lateral spatial resolution is coarse (~1 mm).[19] An infrared thermal image of the flowing afterglow (obtained with a Fluke Ti40 IR Flexcam), shown in Figure 2.3b, reveals surface temperatures that reach 185˚C and cover an area of 2.2 mm^2. Employing laser ablation as a means of sampling for FAPA ionization, while more costly and complex than direct analyses, provides a number of advantages: significantly improved spatial resolution due to the small laser spot size, possible depth profiling of samples, and reduced thermal stress on the sample because it is no longer positioned in the afterglow.

Representative mass spectra obtained with the LA-FAPA combination are shown in Figure 2.4. Mass resolution obtained with this configuration is the same as that seen with conventional ionization sources (~2000). The dominant ion is typically the protonated parent molecule, with slight fragmentation observed in some cases. The degree of fragmentation was found to be independent of laser irradiance, suggesting it

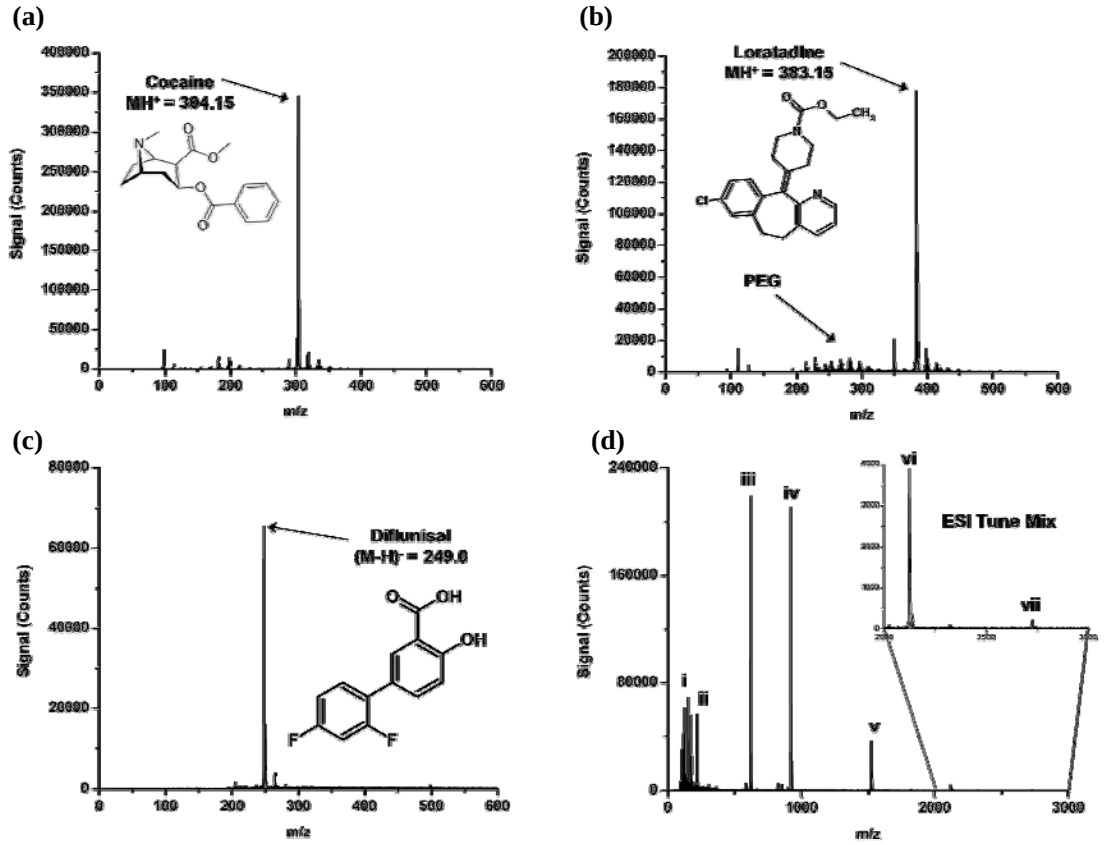

Figure 2.4 Representative mass spectra obtained by LA-FAPA. (a) Cocaine standard, (b) Claritin tablet, (c) diflunisal tablet, (d) commercial tuning mixture containing betaine (m/z = 117.08), and various phosphazines (m/z = 621.02; 921.00; 1520.96; 2120.93; 2720.88).

arises in either the FAPA source or within the mass spectrometer rather than in the ablation process. Spectra observed with LA introduction were identical to those observed using direct analysis of the same substance, including dimerization and adduct formation.

Each laser ablation event creates a distribution of fine particles that are carried into the afterglow where desorption and ionization take place. Figure 2.5a shows an example of repeated single-pulse laser analyses of a two-component spin-coated film of caffeine (MH^+ = 195) and acetaminophen (MH^+ = 152). Peak widths from each laser pulse were ~1.2 s full-width at half maximum (FWHM), and were limited by the washout time of the ablation chamber. By reducing the volume of the chamber by half, the peak widths were narrowed to <0.3 s FWHM. Pulse-to-pulse laser power variations caused single-pulse analyses to exhibit substantial variability, with an RSD of 13%. The same precision has been demonstrated with different ionization sources and samples;[20] suggesting that the major variance of the system arises from the laser ablation unit. Yet, this precision is much better than is commonly exhibited by other ADI-MS sources (generally ~40%). Furthermore, when one analyte was used as an internal standard for the other, precision was improved here to 3.1% RSD, which is the equivalent to the stability of the FAPA source by itself.

Accurate quantification of spatially heterogeneous surface features can be challenging in the absence of appropriate standards. Here, a calibration curve was generated for caffeine by using a modified inkjet printer to deposit 5 pL droplets of solution onto a glass slide. The calibration curve shows good linearity (R^2 = 0.992) with ~5% RSD shot-to-shot variation and a limit of detection of 5 fmol. This finding shows that not only is quantification possible with this ADI-MS method, but also sampling

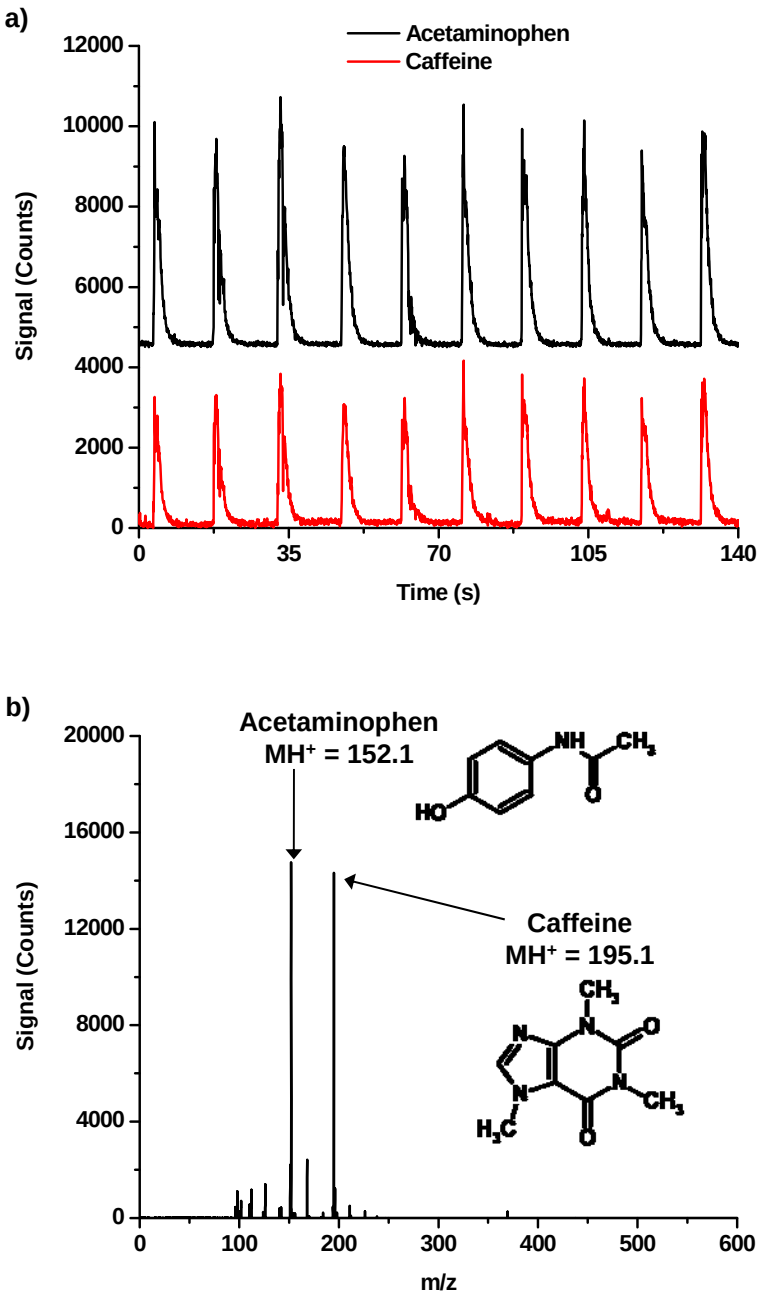

Figure 2.5 Single-shot LA-FAPA analysis of a two-component film, spin-coated on glass. a) Signal trace representing 10 single-shot laser ablation events from different positions along a sample film containing acetaminophen (red) and caffeine (black). b) Typical mass spectrum of a single laser ablation event.

reproducibility is dramatically improved over direct sample introduction. Of course, all ADI-MS sources suffer greatly from matrix effects, usually in the form of competitive ionization. In order to obtain a valid calibration curve for a sample, it is important to matrix match the standards. It will be essential in future studies on ADI-MS sources to examine the extent, and potential cures, of matrix effects.

One of the strongest advantages of laser ablation over conventional desorption is its ability to produce depth information about a sample. The depth profile of an Excedrin® Migraine pharmaceutical tablet was obtained by successive laser pulses that removed an average of 36 μm with each burst (Figure 2.6a). Each signal spike in Figure 2.6a represents the removal of a layer of material. The active ingredients, caffeine and acetaminophen, were monitored along with an unknown analyte at m/z 110, which was found to be a constituent also of the protective coating of the tablet. This mass was used to determine when the coating had been drilled through and the average thickness of material removed per burst. As illustrated in Figure 2.6a, the coating layer was deficient in both active ingredients. In addition, both caffeine and acetaminophen were heterogeneously distributed in the bulk composition, which would be expected because the tablet is a heterogeneously pressed powder. With 75 consecutive laser pulses, the total analysis depth was 2.7 mm, significantly deeper than in any published MSI configuration.[14] Of course, the attainable depth resolution depends on the material being analyzed, laser power, and laser spot size. However, a depth resolution of less than 1 μm has been achieved with a similar laser ablation system.[21]

Finally, LA-FAPA was used to perform chemical imaging of solid samples. Figure 2.7 demonstrates the process that was used to image a sample. In this case, ink

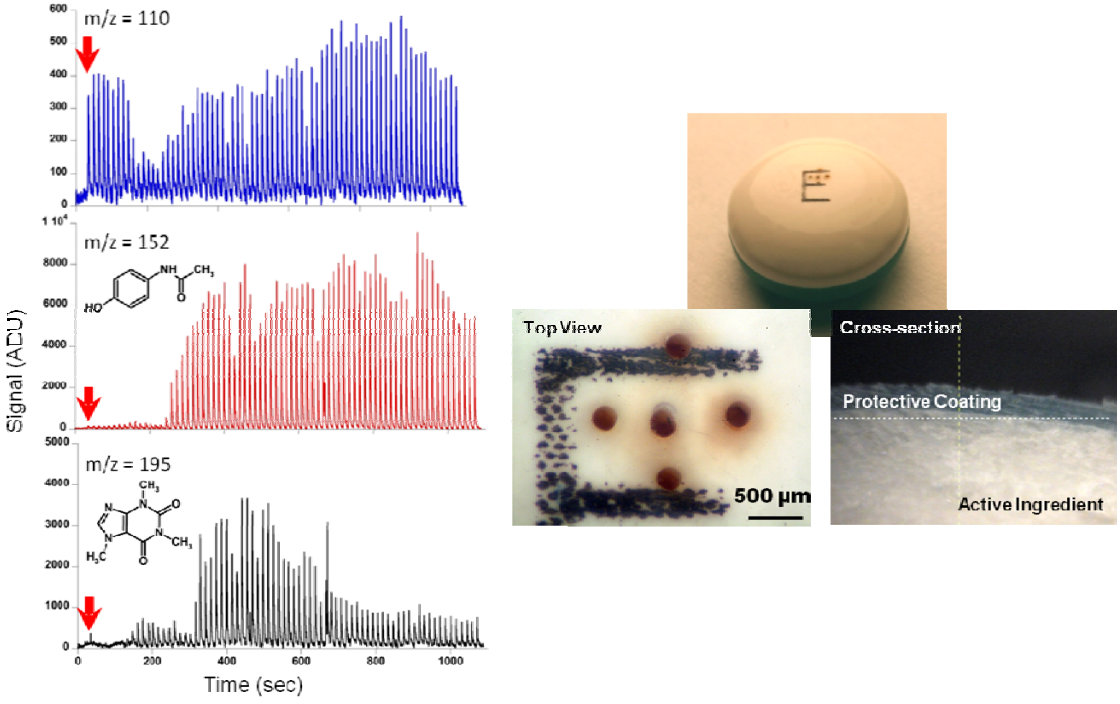

Figure 2.6 Depth profiling an Excedrin tablet. a) Analyte distribution as a function of successive laser shots of mass marker (m/z = 110, blue), acetaminophen (m/z = 152, red), and caffeine (m/z = 195, black). The arrows depict the start of the laser drilling process. b) Photograph of ablated tablet with top view and cross section.

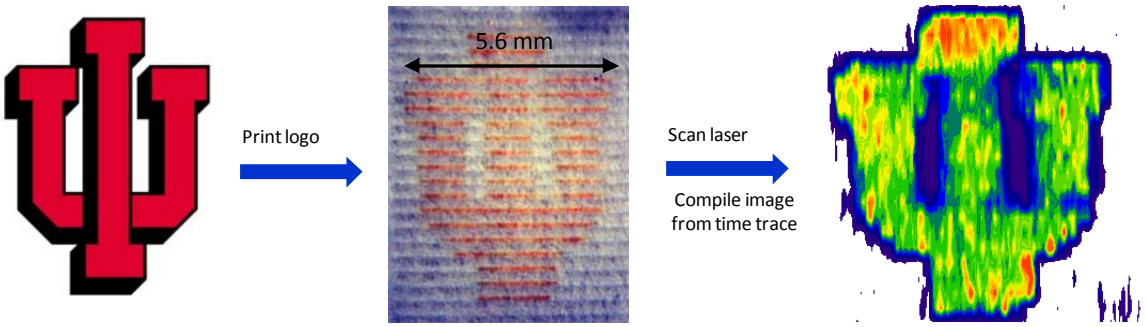

Figure 2.7 Steps in generating a chemical image of the Indiana University logo printed on paper with caffeine-doped ink. This logo is a registered trademark of Indiana University. The center image shows the logo (left) after it was laser-ablated. The path of the repetitively pulsed laser is clearly apparent. The reconstructed logo is at right.

doped with caffeine was introduced into the modified inkjet printer and used to print the Indiana University logo, which was 5.6 mm wide. Next the laser was scanned across the print, resulting in a time trace. Lastly, the time trace for m/z 195 was deconvoluted and plotted as a contour map by means of a commercial data analysis package. The total analysis time for this sample was less than 30 min.

To evaluate the attainable spatial resolution of the imaging setup, a 1951 USAF spatial-resolution target was printed with the same analyte-doped ink with a printing resolution of 1200 dpi (cf. Figure 2.8). The print was scanned with a 200 μm laser spot at 80 μm/s with a line spacing of 150 μm. In this case, the horizontal and vertical spatial resolution was 63 μm and 178 μm, respectively. Horizontal spatial resolution was limited by the scan speed and washout time of the LA cell, whereas the vertical resolution was limited by the spacing between the scan lines. However, a spatial resolution better than 20 μm was obtained when a 20 μm laser spot was scanned across a 20-μm wide line of caffeine at 5 μm/s (data not shown).

In an attempt to determine the usefulness of this MSI technique with real tissue samples, 50 ng of lidocaine, containing a blue dye for visualization, was spotted onto a slice of wet turkey tissue (luncheon meat) and imaged (cf. Figure 2.9a). The lidocaine was clearly identified in the mass spectrum and the chemical image matches the white-light image.

Figure 2.9b demonstrates imaging of celery veins that contained caffeine. A section of celery stock was immersed in an aqueous solution of caffeine and blue dye (for visualization). The celery was then sliced perpendicular to the stock and imaged. The total analysis and data processing time was less than 30 min. The celery veins can very

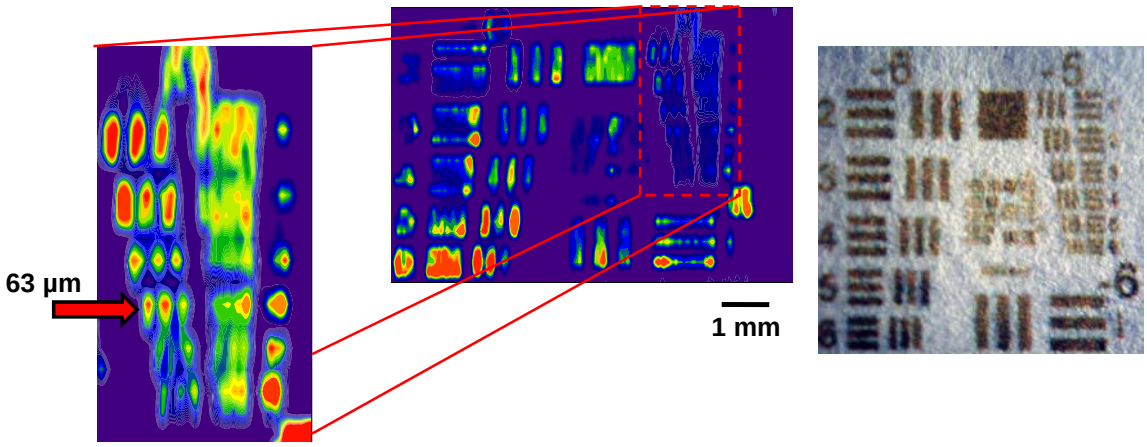

Figure 2.8 Chemical images of the 1951 USAF resolution target (shown on right) printed with caffeine at 1200 dpi onto paper. Vertical and horizontal resolution is 178 and 63 µm, respectively. Vertical and horizontal resolution are limited by spacing of scan lines and scan speed, respectively. The central image is an enlarged rendition of the one at left.

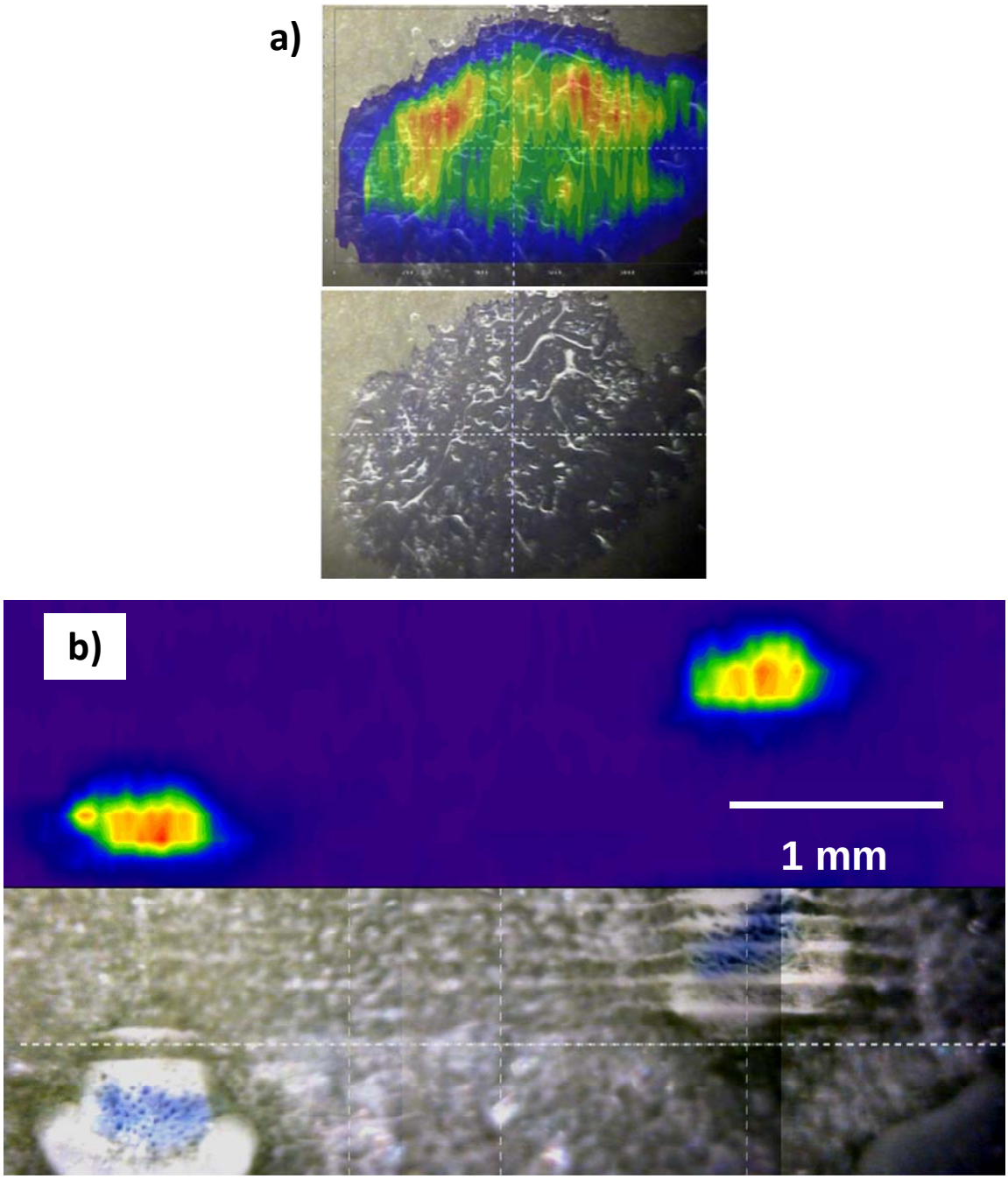

Figure 2.9 a) Chemical (top) and white-light (bottom) images of 50 ng of lidocaine spotted manually onto turkey tissue. b) Chemical (top) and white light (bottom) images of celery veins doped with caffeine. Celery was sliced perpendicular to the direction of the stock. Both solutions contained a blue dye for visualization.

clearly be identified as can the sheath surrounding the vein. To date, attempts to image tissue samples containing drugs/drug metabolites have not been made, but this preliminary work shows that MSI of tissue samples by LA-FAPA is promising.

These results demonstrate that coupling laser ablation with a plasma-based ADI-MS source, such as FAPA, can be very effective in performing molecular MSI. While imaging with LA-FAPA is currently limited to small molecules (<1000 u), a much broader range of chemical species can be imaged than in MALDI imaging or DESI. In addition to imaging, laser ablation permits depth profiling of samples. The combination has been shown not only to be highly sensitive (LOD of 5 fmol for caffeine), but also to offer better spatial resolution (~20 μm) than has been achieved previously with ADI-MSI systems. Significantly, the FAPA source could not be operated under optimized conditions in this study because of mass spectrometer vacuum-pumping limitations. Therefore, it is likely that LODs and S/N (and consequently spatial resolution) could be improved by modifying the mass spectrometer vacuum system. Lastly, this study demonstrates that the problem of precision in ADI-MS sources caused by sampling can be overcome by using laser ablation as a means to introduce small amounts of sample reproducibly.

References

1. McDonnell, L. A. H., R. M. *Mass Spectrom. Rev.* **2007**, *26*, 606-643.
2. Caprioli, R. M.; Farmer, T. B.; Gile, J. *Anal. Chem.* **1997**, *69*, 4751-4760.
3. Luxembourg, S. L.; Mize, T. H.; McDonnell, L. A.; Heeren, R. M. A. *Anal. Chem.* **2004**, *76*, 5339-5344.
4. Klinkert, I.; McDonnell, L. A.; Luxembourg, S. L.; Altelaar, A. F. M.; Amstalden, E. R.; Piersma, S. R.; Heeren, R. M. A. *Rev. Sci. Instrum.* **2007**, *78*.
5. Li, Y.; Shrestha, B.; Vertes, A. *Anal. Chem.* **2007**, *79*, 523-532.
6. Wiseman, J. M.; Ifa, D. R.; Song, Q. Y.; Cooks, R. G. *Angewandte Chemie-International Edition* **2006**, *45*, 7188-7192.
7. Takats, Z.; Wiseman, J. M.; Gologan, B.; Cooks, R. G. *Science (Washington, DC, United States)* **2004**, *306*, 471-473.
8. Cooks, R. G.; Ouyang, Z.; Takats, Z.; Wiseman, J. M. *Science* **2006**, *311*, 1566-1570.
9. Costa, A. B.; Cooks, R. G. *Chem. Commun.* **2007**, 3915-3917.
10. Takats, Z.; Wiseman, J. M.; Cooks, R. G. *J. Mass Spectrom.* **2005**, *40*, 1261-1275.
11. Venter, A.; Sojka, P. E.; Cooks, R. G. *Anal. Chem.* **2006**, *78*, 8549-8555.
12. Ifa, D. R.; Gumaelius, L. M.; Eberlin, L. S.; Manicke, N. E.; Cooks, R. G. *Analyst* **2007**, *132*, 461-467.
13. Nemes, P.; Barton, A. A.; Li, Y.; Vertes, A. *Anal. Chem.* **2008**, *80*, 4575-4582.
14. Nemes, P.; Vertes, A. *Anal. Chem.* **2007**, *79*, 8098-8106.
15. Cody, R. B.; Laramee, J. A.; Durst, H. D. *Anal. Chem.* **2005**, *77*, 2297-2302.

16. Na, N.; Zhao, M. X.; Zhang, S. C.; Yang, C. D.; Zhang, X. R. *J. Am. Soc. Mass. Spectrom.* **2007**, *18*, 1859-1862.

17. Ratcliffe, L. V.; Rutten, F. J. M.; Barrett, D. A.; Whitmore, T.; Seymour, D.; Greenwood, C.; Aranda-Gonzalvo, Y.; Robinson, S.; McCoustrat, M. *Anal. Chem.* **2007**, *79*, 6094-6101.

18. Andrade, F. J.; Shelley, J. T.; Wetzel, W. C.; Webb, M. R.; Gamez, G.; Ray, S. J.; Hieftje, G. M. *Anal. Chem.* **2008**.

19. Andrade, F. J.; Shelley, J. T.; Wetzel, W. C.; Webb, M. R.; Gamez, G.; Ray, S. J.; Hieftje, G. M. *Anal. Chem.* **2008**.

20. Barnes, J. H.; Schilling, G. D.; Hieftje, G. M.; Sperline, R. P.; Denton, M. B.; Barinaga, C. J.; Koppenaal, D. W. *J. Am. Soc. Mass. Spectrom.* **2004**, *15*, 769-776.

21. Bleiner, D.; Plotnikov, A.; Vogt, C.; Wetzig, K.; Gunther, D. *Fresenius J. Anal. Chem.* **2000**, *368*, 221-226.

Chapter 3

Fast Transient Analysis and First-Stage Collision-Induced Dissociation with the Flowing Atmospheric-Pressure Afterglow Ionization Source to Improve Analyte Detection and Identification

---

3.1 Introduction

The recent development of a wide variety of atmospheric-pressure ionization sources for mass spectrometry, termed ambient desorption/ionization mass spectrometry (ADI-MS), has allowed fast, simple analysis of many different sample types. To date, over 25 ADI-MS ionization sources have been described in the literature.[1] These sources

offer numerous advantages, including little or no sample pre-treatment, simple mass spectra, and direct analysis of solids and liquids.[2] For these reasons, ADI-MS has become an important tool in cleaning validation,[3] forensic analyses,[4-5] and drug discovery.[6-8]

However, two major problems with ADI-MS sources have prevented them from becoming more widely used. First, quantification is difficult to achieve because of matrix-dependent changes in analyte desorption and the necessity of precisely positioning the sample with respect to the source and mass spectrometer.[9-10] Internal standardization (IS) is typically performed to account for incomplete desorption/ionization. However, in many cases IS is not feasible for quantification of unknown species and analyses of complex sample matrices. Second, preferential ionization of easily ionizable analytes or more abundant analytes creates problems when mixtures containing a broad range of analyte concentrations must be analyzed.[11] For complex samples, the latter problem can be overcome by separating the desorption or sampling step from the ionization process. Some examples where this technique has been employed include extractive electrospray ionization (EESI),[12-13] laser ablation-electrospray ionization (LAESI),[14] and laser ablation-flowing atmospheric-pressure afterglow (LA-FAPA).[15] These methods also lessen ionization matrix effects by limiting the amount of sample that is introduced into the ionization source. However, to maintain the fast analysis times inherent to ADI-MS, the sample must often be introduced as a transient pulse (less than 10 ms), which is faster than the response time of most mass analyzers. Therefore, these fast transient signals are detected with a time-of-flight mass spectrometer (TOF-MS), which is capable of a high

spectral acquisition rate (greater than 1 kHz) and simultaneous detection of a broad mass range.

Another problem of ADI-MS can arise from isobaric mass spectral overlaps of analyte species. This case is often encountered because of the simple mass spectra that are produced, which consist almost exclusively of the molecular or protonated molecular ion. It has been shown that in these cases, tandem mass spectrometry (MS/MS), through collision-induced dissociation (CID) within an ion trap mass spectrometer (IT-MS), can be used to successfully identify analytes in complex matrices.[16-17] Unfortunately, the spectral acquisition rate of IT-MS is much lower, which precludes detection of fast transient signals.[18-19] In addition, space charge effects within the ion trap limit the dynamic range to two or three orders of magnitude,[19-20] limiting the quantitative abilities of the technique.

It has long been known that ions formed from electrospray ionization can be fragmented through CID within the orifice-skimmer region (the first stage) of the mass spectrometer.[21-24] More recently, the utility of this technique was demonstrated for the determination of analytes in atmospheric-pressure chemical ionization (APCI).[25-26] While this method enables a large majority of mass spectrometers to perform MS/MS, a pre-separation step with liquid or gas chromatography is needed to yield simple fragmentation spectra.

Conventional liquid chromatography requires complex pumps and solvent systems and results in separation times of tens of minutes to hours, which runs counter to the philosophy of ADI-MS: rapid, portable, and direct analyses. While ultra high performance liquid chromatography has reduced separation times to less than one

minute,[27] there is an even greater need for expensive, bulky solvent pumps.[28] On the other hand for many analytes, gas chromatography (GC) requires only a heated capillary column and can easily result in transient signals on the millisecond timescale. The use of GC in ADI-MS should reduce ionization matrix effects, through limited analyte introduction and external sampling, and improve analyte identification through first-stage CID, while minimally compromising ADI-MS analysis times.

Ionization of GC effluents under ambient conditions with traditional atmospheric-pressure sources, such as atmospheric-pressure chemical ionization and electrospray ionization, is a well-established technique.[29-32] However, of the large number of described ADI-MS sources, only direct analysis in real time (DART)[33] and the flowing atmospheric-pressure afterglow (FAPA)[34] have been used for the analysis of gaseous samples from a GC column. In both cases, the gas chromatograph was used as merely a sample introduction method. Indeed, integration of a separation step, and all associated sample preparation procedures, with this type of analysis seems to defy the traditional mantra of ADI-MS. However, the overall improvement in matrix-effect related measurement errors, and ultimately sensitivity, often outweighs the additional separation step, as has been demonstrated in coupling thin-layer chromatography with other ADI-MS sources.[35-36] Regarding ADI-MS analyses, gas chromatography has the distinct advantage, over most ADI-MS sources and other separation methods, that the desorption and ionization processes can be physically and energetically separated.

In the current study, the ability to reduce matrix effects experienced with the FAPA[34, 37] ionization source was was investigated by coupling an external sampling, separation technique, gas chromatography (GC), to minimize ionization matrix effects,

while maintaining fast analysis times (less than 5 min). In addition, the possibility of obtaining structural information of analytes with a TOF-MS via first-stage CID was also explored.

3.2 Experimental

3.2.1 Reagents

All reagents were analytical grade. High-purity helium (99.999% ultra-high purity helium, Airgas, Radnor, PA) was used as the GC carrier gas and the FAPA discharge gas in all experiments. A standard mixture of 13 herbicides in ethyl acetate was purchased from Supelco (Bellefonte, PA). All other reagents were purchased from Sigma Aldrich (St. Louis, MO).

3.2.2 Instrumentation

The details of FAPA-MS have previously been described,[15] but a brief account will be given here. A helium atmospheric-pressure glow discharge was formed between a 5 mm sharpened tungsten pin (cathode) and a brass plate (anode). An air-tight, Teflon® discharge chamber was used to hold the electrodes at a spacing of 7 mm. A 1.5-mm hole was drilled in the anode plate to enable species generated in the discharge to flow into the atmosphere and interact with the sample. A helium flow rate of 0.8 L/min was used for all experiments and maintained with a mass flow controller (MKS Instruments, Andover, MA). The discharge was sustained at a fixed current of -25 mA at a voltage of approximately -500 V with a high-voltage power supply (Model BHK 1000-0.2MG, Kepco, Inc., Flushing, NY). Ions were sampled by positioning the FAPA source ~1 cm

from the inlet cone (nozzle) of a LECO HT Unique® (LECO Corp., St. Joseph, MI) TOF-MS. A field-free region between the FAPA source and the TOF-MS was achieved by applying a potential to the brass anode with a low-voltage power supply (Model 6299A, Hewlett Packard-Harrison Division, Berkley Heights, NJ).

All chromatographic separations were carried out with an Agilent 6890 gas chromatograph equipped with a 10 m Rtx®-5 column (Restek, Bellefont, PA, 180 µm i.d., 0.2 µm film) with a He carrier flow rate of 2 mL/min. To interface the gas chromatograph with the FAPA-MS, approximately 0.5 m of the column was fed through a 200 °C transfer line and positioned in the afterglow of the FAPA source by means of a 3D translational stage. The GC effluent was ionized by the FAPA source and ions were detected with the TOF-MS. TOF-MS has the distinct advantage of producing full mass spectra for each extraction event, eliminating any problems of spectral skew. In addition, the Unique® spectrometer has a very high spectral acquisition rate (100 Hz), allowing multiple, full mass spectra to be collected across a fast transient signal.

First-stage CID with the TOF-MS was performed by increasing the potential difference between the inlet, nozzle cone and the skimmer cone by means of the software provided with the Unique® spectrometer. Even across fast transient signals, CID was performed by modulating the nozzle cone potential with an optically isolated MOSFET relay (Model AQV258, Digi-key Corp., Thief River Falls, MN) driven with a TTL pulse from a function generator (Model 8003A, Hewlett Packard-Harrison Division, Berkley Heights, NJ).

3.3 Results and Discussion

3.3.1 GC-FAPA-MS

Utilizing gas chromatography (GC) as a separation method before ionization with the FAPA source offers many benefits. The fast separation speeds of GC (100s of seconds) and high sensitivity of the FAPA source (1 to 50 fmol for most gaseous analytes)[34, 38] combine to yield a detection system that maintains the advantages of typical ADI-MS, but overcomes the issues of quantification, consistent sample introduction, and matrix effects cause by competitive ionization.

An example of a GC-FAPA-MS analysis is shown in Figure 3.1. In this case, dried soil was doped with 20 ppm, by mass, of six chemical warfare agent (CWA) simulants. The six mimics, each with its abbreviation and corresponding CWA in parentheses, were dipropylene glycol monomethyl ether (DPGME, GA), dimethyl methylphosphonate (DMMP, GB), triethyl phosphate (TEP, GB), 2-chloroethyl ethyl sulfide (2-CEES, HD), butyl sulfide (HD), and methyl salicylate (HD), where GA, GB, and HD, are the abbreviations for tabun, sarin, and mustard gas, respectively.

The CWA surrogates were extracted with ethanol and filtered. One microliter of extract was injected into the GC at a split ratio of 100:1 at an injection temperature of 160 °C. The oven temperature was held at 90 °C for 0.2 min and then ramped to 210 °C at a rate of 40 °C/min. The total analysis time, from extraction to detection, was less than five minutes.

The plot in Figure 3.1 displays the extracted-ion chromatograms for the protonated forms of each analyte, MH^+, with the exception of 2-CEES in which only the odd-electron species, $M^{+\cdot}$, was detected. While neither the extraction process nor the

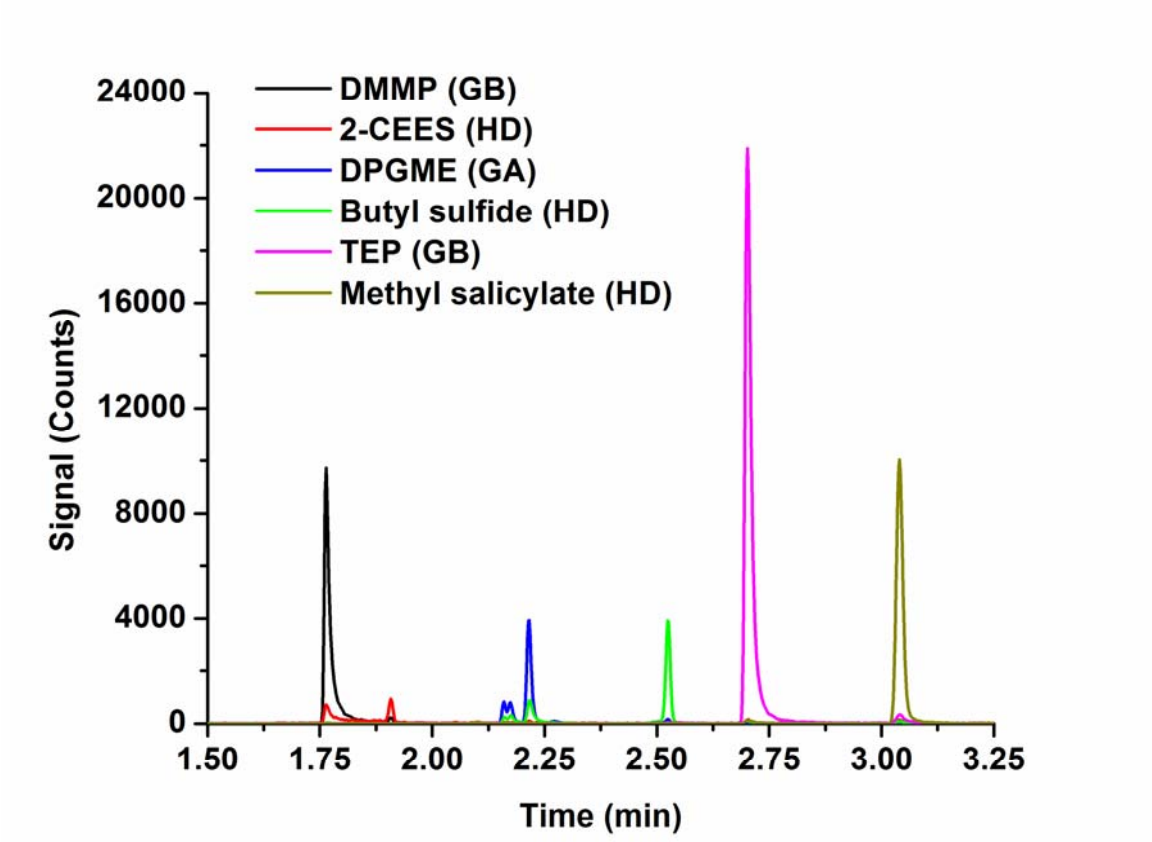

Figure 3.1 Chromatogram of the GC-FAPA-MS analysis of six CWA simulants extracted from dirt. Each colored trace corresponds to the extracted ion chromatogram for the MH^+ ion for the analyte listed in the legend. The CWA corresponding to each simulant is given in parentheses: GB, sarin; HD, mustard gas; GA, tabun.

chromatographic separation was fully optimized, the six CWA simulants were clearly separated and detected in approximately 3 min. This method resulted in detection limits of approximately 1 ppb in the soil for all CWA surrogates except 2-CEES. Although the reason for the disappointing sensitivity to 2-CEES is not known, it is likely that it would be more readily detected in negative ionization mode. Regrettably, this hypothesis could not readily be verified because of the difficulty of operating this particular instrument in negative-ion mode.

The use of GC-FAPA-TOF-MS was investigated also for the detection of herbicides. Figure 3.2 shows the extracted-ion chromatogram for the injection of 1 ng each of a neat mixture of 13 herbicides. In this case, the oven temperature was held at 35 °C for 0.2 min and ramped to 300 °C at a rate of 30 °C/min. Each colored trace in Figure 3.2 corresponds to the MH^+ ion for 9 of the 13 compounds. Four of the analytes were not included due to their incomplete separation under the conditions used. Even without a fully optimized temperature program, the 9 monitored analytes were easily separated and detected in less than ten minutes. Furthermore, the analytical working curve for each analyte was found to be linear over at least three orders of magnitude with limits of detection between 2 and 6 fmol for the nine analytes.

Additionally, ten manual injections of the herbicide mixture yielded relative standard deviations (RSDs) of less than 5%, which underscores the utility of using GC as a sample introduction method for FAPA. One of the largest drawbacks with ADI-MS analyses is precise analyte quantification due to irreproducible sample positioning and matrix effects. In earlier FAPA analyses, RSDs as high as 43% have been reported for the direct analysis of pharmaceutical agents from tablets.[38] Laser ablation coupled to

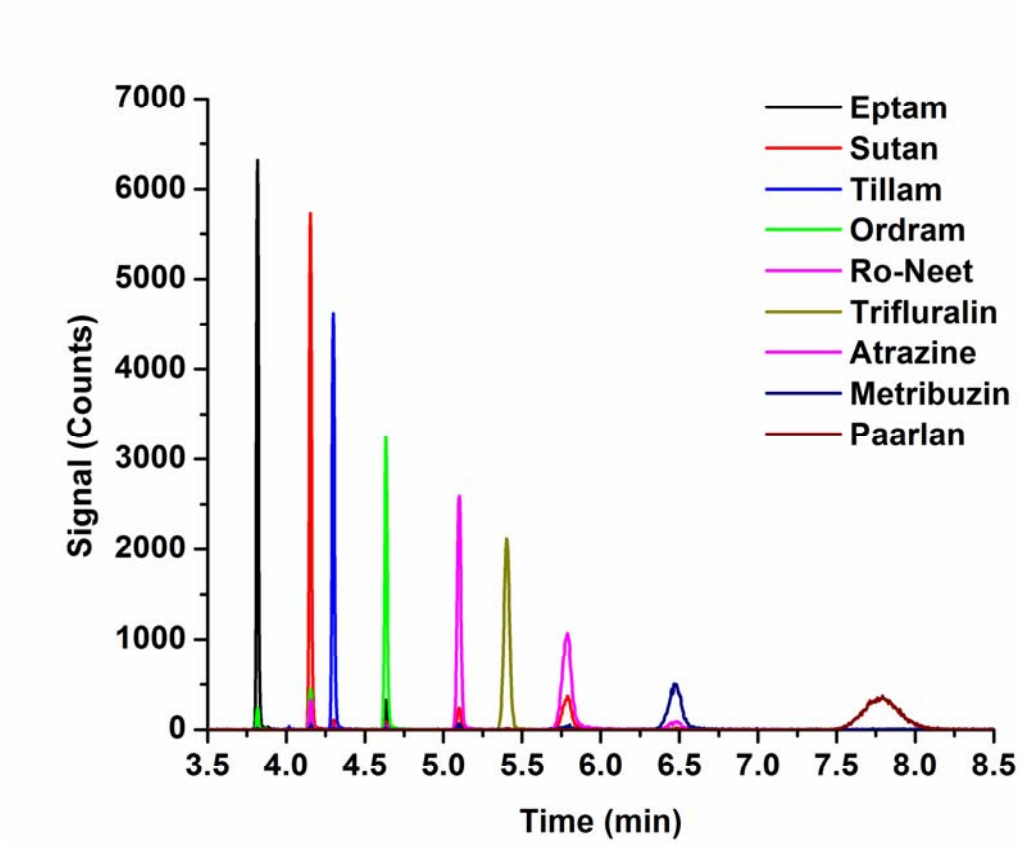

Figure 3.2 Chromatogram of the GC-FAPA-MS analysis of a mixture of 13 herbicides. Each colored trace corresponds to the extracted ion chromatogram of the MH^+ ion for the analytes listed in the legend. The limit of detection for every analyte was less than 6 fmol.

FAPA has also been used to improve sample introduction precision;[15] however GC would be a much more cost-effective approach to reproducible sample introduction.

Using GC as a sampling method for FAPA ionization could also reduce measurement errors caused by matrix effects. It is believed that the most prevalent type of matrix effect encountered in FAPA-MS involves competitive ionization with more easily ionizable species present in the sample.[11] A fast, pre-separation step would limit the number of species exposed to the ionization region at a given time, thereby reducing matrix effects.

A mass spectrum from the direct (non-separated) FAPA analysis of the same herbicide mixture is shown in Figure 3.3a. For comparison, Figure 3.3b shows the overlaid mass spectra corresponding to seven of the non-interfered chromatographic peaks in Figure 3.2. A severe matrix effect is clearly observed in the direct analysis mass spectrum. The dashed boxes in Figure 3.3 emphasize ions that were detected with GC-FAPA, but were heavily or completely suppressed in the direct FAPA desorption/ionization of the non-separated mixture.

By introducing each analyte individually into the FAPA source, it was noted that the sensitivity was very similar for the different herbicides. However, this feature was completely lost with the direct herbicide analysis because of competitive desorption and ionization. This example demonstrates the serious role matrix effects play in ADI-MS analyses. In future studies of ADI-MS sources it will be important to investigate methods to overcome these matrix effects, which can hamper quantification or even prevent detection.

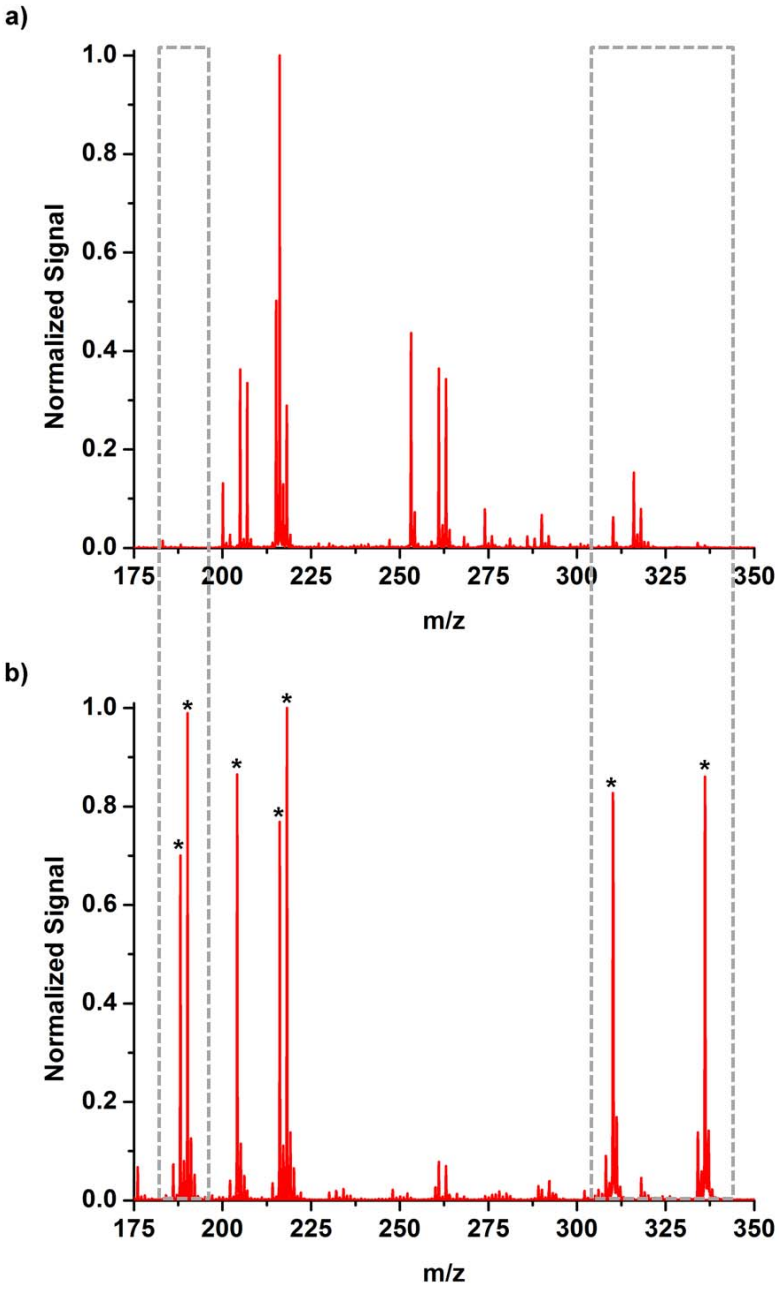

Figure 3.3 a) Mass spectrum of the direct FAPA-MS analysis of the herbicide mixture used in Figure 3.2. b) Overlaid mass spectra from seven of the chromatographic peaks in Figure 3.2. Only seven peaks were included due to isobaric overlap of some analytes. The * denotes the MH^+ ion of each analyte. The gray boxes are to emphasize analytes that were partially or entirely suppressed by competitive ionization in the direct analysis.

3.3.2 First-stage Collision-Induced Dissociation

Another common problem in ADI-MS analyses is shown in Figure 3.3b. Only seven of the analytes were included in the superimposed mass spectra because of isobaric overlaps of MH^+ ions. Generally, obtaining simple mass spectra in the analysis of complex samples can aid in the identification of many analytes. However if two analytes have the same nominal mass and cannot be spectrally resolved, identification becomes impossible. For situations where analytes have differing elemental compositions, this problem can be overcome by using high mass accuracy instruments.[33, 39] However, this solution is quite costly and is difficult to implement in field-portable instruments. Often, a more attractive alternative is to obtain structural information through MS/MS analyses.

It was found that analyte fragmentation with FAPA-TOF-MS could be performed by increasing the potential difference between the MS nozzle and skimmer cones. An example of the spectra obtained for benzophenone at two different nozzle cone potentials is shown in Figure 3.4. At a nozzle potential of 60 V, the predominant peak at m/z 183 corresponds to the protonated form of benzophenone (cf. Figure 3.4a). By increasing the nozzle potential to 95 V, the most abundant ion, at m/z 105, corresponds to the loss of a phenyl ring.

As ions pass through the electric field gradient between the two cones, they are accelerated within the first vacuum region of the MS. When the ionized analytes collide with other gases, the energy imparted to the ion from the collision is converted to vibrational motion, which can result in the fragmentation of weak chemical bonds. An

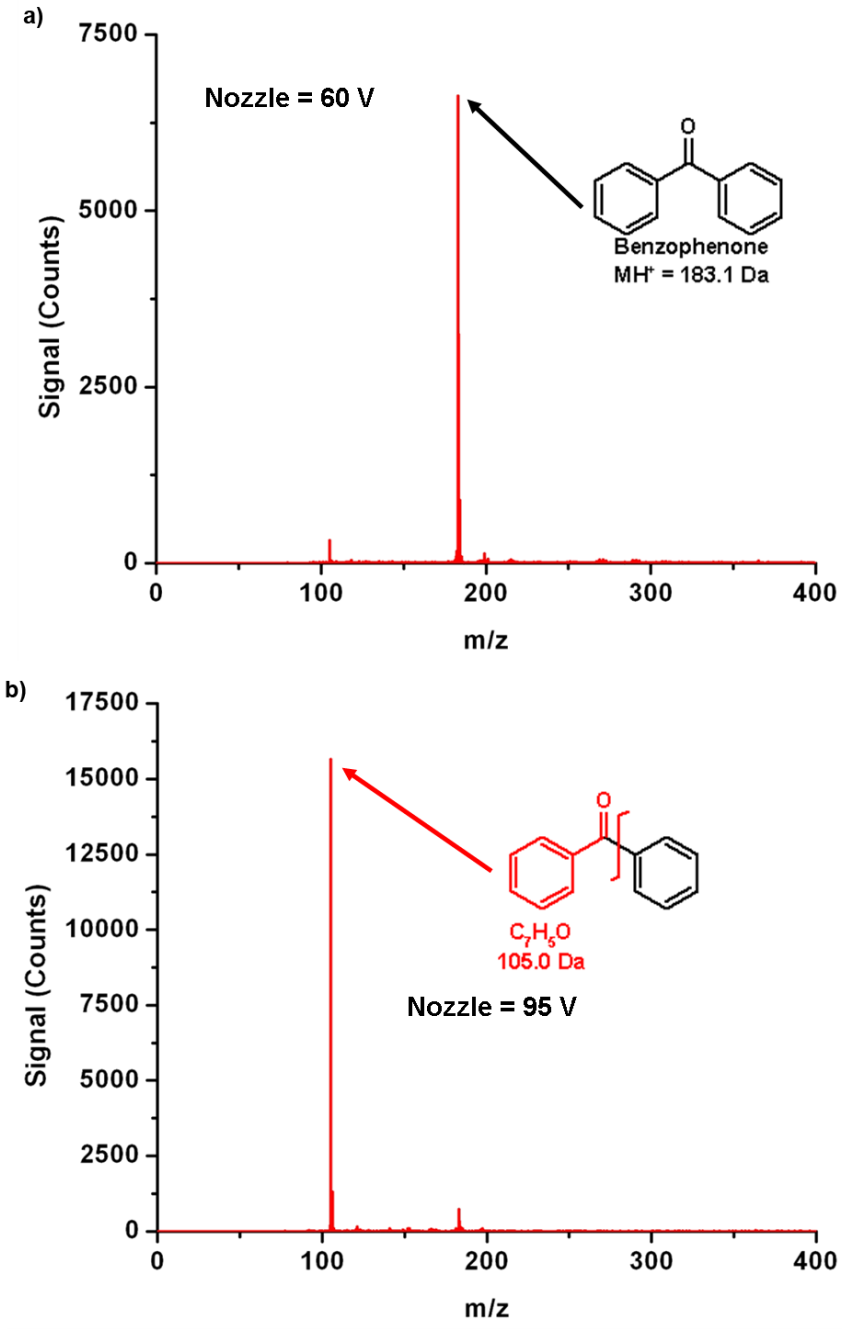

Figure 3.4 FAPA-MS spectra of benzophenone at a nozzle cone potential of (a) 60 V and (b) 95 V. A larger potential difference between the nozzle and skimmer resulted in greater fragmentation of the analyte.

increase in the potential difference between the cones causes greater ion acceleration and, thus, a greater amount of fragmentation.

To demonstrate this behavior, the nozzle cone potential was gradually increased while a constant stream of acetaminophen was introduced into the FAPA source by means of laser ablation. The normalized signals of three ions detected, as a function of the nozzle potential, are shown in Figure 3.5. The three ions detected at m/z 152, 110, and 93 correspond to the MH^+ ion, a loss of acetaldehyde, and the phenol cation, respectively. The increasing nozzle potential resulted in a greater abundance of higher energy fragments. Interestingly, the analyte fragmentation patterns observed with first-stage CID were identical to those achieved with conventional MS/MS with an ion trap mass spectrometer (data not shown). These findings demonstrate that first-stage CID can be used for analyte identification in FAPA-MS analyses. However, if more than one substance is ionized by the FAPA and subsequently fragmented through first-stage CID, the mass spectral interpretation can become extremely complicated. Therefore, it would be most advantageous to perform first-stage CID after a fast separation by GC.

In order to obtain both molecular ion and fragmentation spectra across a GC transient, the nozzle potential was modulated at a frequency lower than the spectral acquisition rate of 100 Hz. A chromatographic peak of methyl salicylate with a modulated nozzle potential is shown in Figure 3.6a. The black and red time traces correspond to the protonated molecular ion and a loss of methanol, respectively. In this case, the nozzle cone was pulsed from 57 V to 105 V for 50 ms at a repetition rate of 1.7 Hz. The result was a fragmentation duty cycle of ~8%. Low duty factors were used to

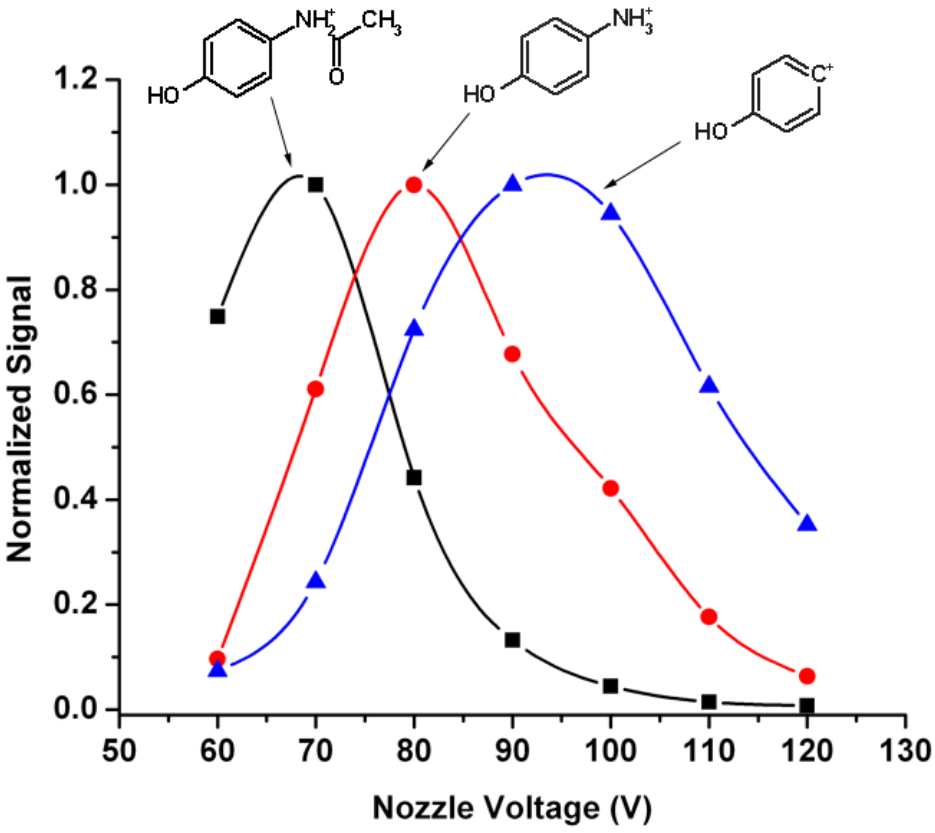

Figure 3.5 Normalized ion signals for the FAPA-MS analysis of acetaminophen at different nozzle potentials. Higher nozzle cone voltages resulted in a greater abundance of higher energy fragments.

preserve original chromatographic peak shape, which enabled proper peak identification and integration. The mass spectra corresponding to the low and high nozzle potentials are shown in Figures 6b and c, respectively. When the nozzle was pulsed to the higher potential, fragment ions corresponding to the losses of a methoxy or a methyl group from the parent molecule were readily detected. Because the modulated CID was performed on such a short time scale to preserve the chromatographic peak shape, the only type of mass analyzer capable of acquiring these molecular and fragmentation spectra was a time-of-flight unit.

3.4 Conclusions

Although FAPA-MS, as well as ADI-MS in general, can be used as a very sensitive and rapid analysis method, reproducible sample introduction along with matrix effects and unknown analyte identification limit its more widespread use. Coupling GC with FAPA improved sampling precision to better than 5% and heavily reduced matrix effects by minimizing the amount and number of analytes introduced into the ionization region of the FAPA at a time. This combination of methods maintained the high sensitivity inherent to FAPA-MS, but did extend analysis times from seconds to minutes. This extra analysis time could be recovered by using a micro GC system, which would also preserve the compact nature of the FAPA source, which could be used for field portable analyses. Additionally, modulated, first-stage CID with GC-FAPA-MS enabled analyte identification within the timescale of a chromatographic peak. While the presented methods overcome some of the problems with ADI-MS, they are not universal.

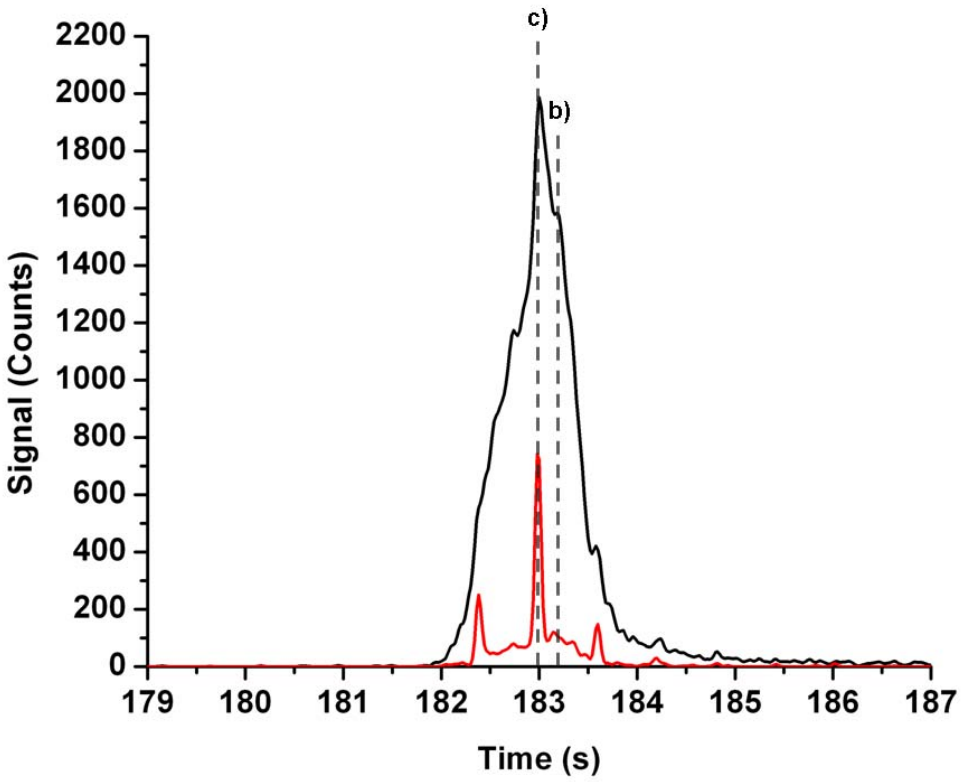

Figure 3.6a Extracted ion chromatograms for *m*/*z* 153 (black) and *m*/*z* 121 (red) from the GC-FAPA-MS analysis of methyl salicylate with a modulated nozzle potential. A low fragmentation duty cycle of *ca*. 8% was used to preserve the chromatographic peak shape, which resulted in the pulsed behavior exhibited in the red trace.

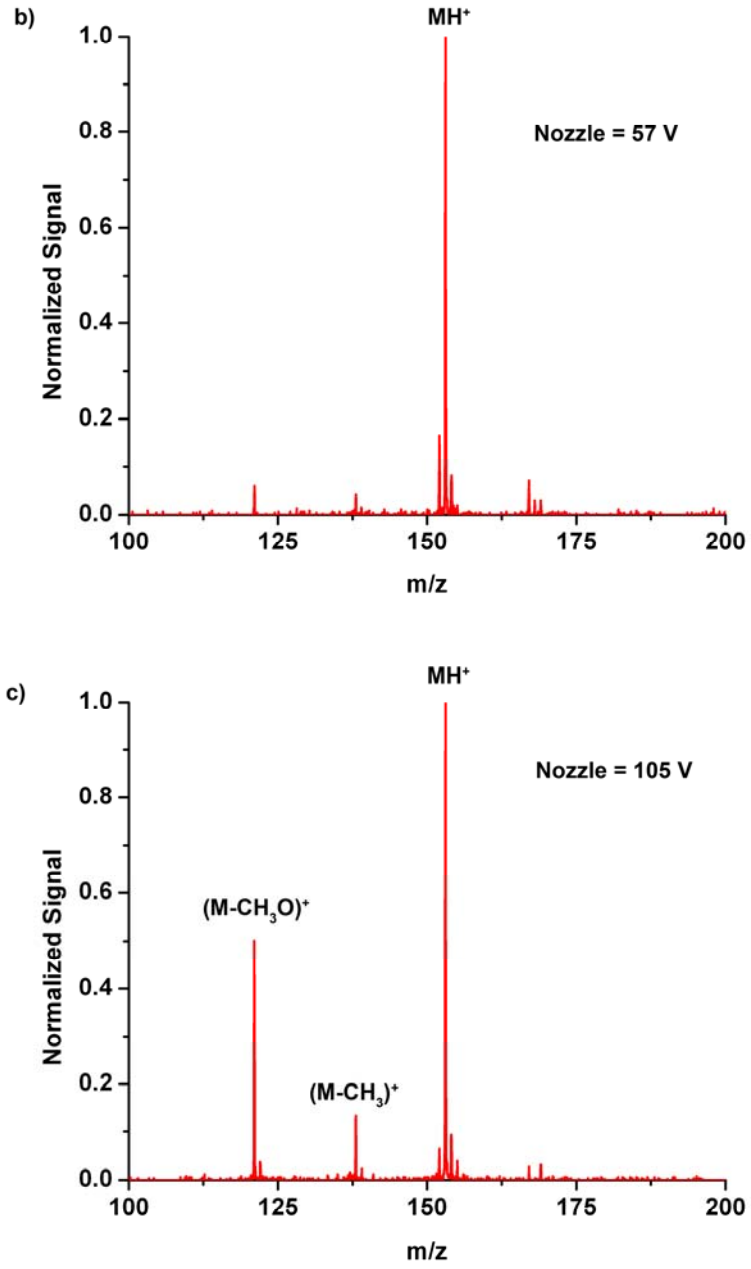

Figure 3.6bc Mass spectra corresponding to the points indicated in Figure 3.6a. By modulating the nozzle voltage at a fixed frequency, both molecular and fragmentation mass spectra could be obtained across a chromatographic peak.

Accordingly, future work will focus on other methods to overcome matrix effects and improve analyte identification.

References

1. Van Berkel, G. J.; Pasilis, S. P.; Ovchinnikova, O. *J. Mass Spectrom.* **2008**, *43*, 1161-1180.
2. Venter, A.; Nefliu, M.; Cooks, R. G. *TrAC, Trends Anal. Chem.* **2008**, *27*, 284-290.
3. Soparawalla, S.; Salazar, G. A.; Perry, R. H.; Nicholas, M.; Cooks, R. G. *Rapid Commun. Mass Spectrom.* **2009**, *23*, 131-137.
4. Steiner, R. R.; Larson, R. L. *Journal of Forensic Sciences* **2009**, *54*, 617-622.
5. Takats, Z.; Wiseman, J. M.; Cooks, R. G. *J. Mass Spectrom.* **2005**, *40*, 1261-1275.
6. Petucci, C.; Diffendal, J.; Kaufman, D.; Mekonnen, B.; Terefenko, G.; Musselman, B. *Anal. Chem.* **2007**, *79*, 5064-5070.
7. Leuthold, L. A.; Mandscheff, J. F.; Fathi, M.; Giroud, C.; Augsburger, M.; Varesio, E.; Hopfgartner, G. 2006, pp 190-194.
8. Zhao, Y. P.; Lam, M.; Wu, D. L.; Mak, R. *Rapid Commun. Mass Spectrom.* **2008**, *22*, 3217-3224.
9. Harris, G. A.; Fernandez, F. M. *Anal. Chem.* **2008**, *81*, 322-329.
10. Shelley, J. T.; Wiley, J. S.; Chan, G. C. Y.; Schilling, G. D.; Ray, S. J.; Hieftje, G. M. *J. Am. Soc. Mass. Spectrom.* **2009**, *20*, 837-844.
11. Shelley, J. T.; Hieftje, G. M. *J. Anal. At. Spectrom.* **2010**, DOI: 10.1039/B923564G.
12. Chen, H. W.; Venter, A.; Cooks, R. G. *Chem. Commun.* **2006**, 2042-2044.
13. Chen, H. W.; Wortmann, A.; Zenobi, R. *J. Mass Spectrom.* **2007**, *42*, 1123-1135.
14. Nemes, P.; Vertes, A. *Anal. Chem.* **2007**, *79*, 8098-8106.

15. Shelley, J. T.; Ray, S. J.; Hieftje, G. M. *Anal. Chem.* **2008**, *80*, 8308-8313.

16. Harper, J. D.; Charipar, N. A.; Mulligan, C. C.; Zhang, X. R.; Cooks, R. G.; Ouyang, Z. *Anal. Chem.* **2008**, *80*, 9097-9104.

17. Huang, G. M.; Zheng, O. Y.; Cooks, R. G. *Chem. Commun.* **2009**, 556-558.

18. Jonscher, K. R.; Yates, J. R. *Anal. Biochem.* **1997**, *244*, 1-15.

19. Brancia, F. L. *Expert Rev. Proteomics* **2006**, *3*, 143-151.

20. Cleven, C. D.; Cox, K. A.; Cooks, R. G.; Bier, M. E. *Rapid Commun. Mass Spectrom.* **1994**, *8*, 451-454.

21. Schneider, B. B.; Chen, D. D. Y. *Anal. Chem.* **2000**, *72*, 791-799.

22. Schneider, B. B.; Douglas, D. J.; Chen, D. D. Y. *Rapid Commun. Mass Spectrom.* **2001**, *15*, 249-257.

23. Smith, R. D.; Loo, J. A.; Barinaga, C. J.; Edmonds, C. G.; Udseth, H. R. *J. Am. Soc. Mass. Spectrom.* **1990**, *1*, 53-65.

24. Weinmann, W.; Wiedemann, A.; Eppinger, B.; Renz, M.; Svoboda, M. *J. Am. Soc. Mass. Spectrom.* **1999**, *10*, 1028-1037.

25. Tian, Q. G.; Duncan, C. J. G.; Schwartz, S. J. *J. Mass Spectrom.* **2003**, *38*, 990-995.

26. Letzel, T.; Poschl, U.; Rosenberg, E.; Grasserbauer, M.; Niessner, R. *Rapid Commun. Mass Spectrom.* **1999**, *13*, 2456-2468.

27. Plumb, R.; Castro-Perez, J.; Granger, J.; Beattie, I.; Joncour, K.; Wright, A. *Rapid Commun. Mass Spectrom.* **2004**, *18*, 2331-2337.

28. de Villiers, A.; Lestremau, F.; Szucs, R.; Gelebart, S.; David, F.; Sandra, P. *J. Chromatogr. A* **2006**, *1127*, 60-69.

29. Dzidic, I.; Carroll, D. I.; Stillwell, R. N.; Horning, E. C. *Anal. Chem.* **1976**, *48*, 1763-8.

30. Horning, E. C.; Horning, M. G.; Carroll, D. I.; Dzidic, I.; Stillwell, R. N. *Anal. Chem.* **1973**, *45*, 936-943.

31. Lee, C. Y.; Shiea, J. *Anal. Chem.* **1998**, *70*, 2757-2761.

32. McEwen, C. N.; McKay, R. G. *J. Am. Soc. Mass. Spectrom.* **2005**, *16*, 1730-1738.

33. Cody, R. B. *Anal. Chem.* **2009**, *81*, 1101-1107.

34. Andrade, F. J.; Shelley, J. T.; Wetzel, W. C.; Webb, M. R.; Gamez, G.; Ray, S. J.; Hieftje, G. M. *Anal. Chem.* **2008**, *80*, 2646-2653.

35. Kim, H. J.; Jang, Y. P. *Phytochem. Anal* **2009**, *20*, 372-377.

36. Van Berkel, G. J.; Ford, M. J.; Deibel, M. A. *Anal. Chem.* **2005**, *77*, 1207-1215.

37. Andrade, F. J.; Shelley, J. T.; Wetzel, W. C.; Webb, M. R.; Gamez, G.; Ray, S. J.; Hieftje, G. M. *Anal. Chem.* **2008**, *80*, 2654-2663.

38. Schilling, G. D.; Shelley, J. T.; Barnes Iv, J. H.; Sperline, R. P.; Denton, M. B.; Barinaga, C. J.; Koppenaal, D. W.; Hieftje, G. M. *J. Am. Soc. Mass. Spectrom.* **2009**, *In Press, Corrected Proof*.

39. Cody, R. B.; Laramee, J. A.; Durst, H. D. *Anal. Chem.* **2005**, *77*, 2297-2302.

Chapter 4

Characterization of Direct-Current Atmospheric-Pressure Discharges Useful for Ambient Desorption/Ionization Mass Spectrometry

4.1 Introduction

Direct-current (DC) discharges have been widely used for elemental analyses since they were first introduced for alloy characterization.[1] When DC discharges were coupled with mass spectrometry, the result was a very sensitive and powerful tool for elemental[1] and molecular analysis.[2-3] Of the many electrical regimes of DC discharges, three forms have been found to have particular analytical merit: the arc, the glow, and the corona. Among these three types of discharges, the fundamental distinction is the operating current and voltage. The arc occurs at very high currents (hundreds of

amperes) with a low voltage drop between electrodes (tens of volts). It also exhibits negative resistance; that is, the sustaining voltage drops as the current rises. The glow discharge (GD), which has conventionally been operated between 0.1 to 10 Torr, exists at much lower currents (tens of milliamperes) and a higher voltage drop (hundreds of volts). Lastly, the corona discharge operates with very low currents (a few microamperes) and a much higher voltage drop (several kilovolts).

Corona discharges find their most common analytical application in atmospheric pressure chemical ionization (APCI).[4-5] In conventional APCI, a corona discharge is formed by applying ~4 kV to a needle electrode in a selected atmosphere, to yield currents of ~5 μA. After a series of reactions,[5] reagent ions are produced that can then ionize a sample. Protonated water clusters are typically observed because of the presence of water vapor in the air. Such protonated clusters promote proton transfer ionization, resulting in mass spectra containing mainly the protonated molecular ion (MH^+). However, a limitation of APCI sources is the relatively low flux of reagent ions they produce because of the low discharge current. This low flux often results in ion suppression caused by competitive ionization reactions when multiple analytes are present. To overcome this problem, APCI is usually coupled with a separation technique.

Conventional glow discharge ionization sources operate at reduced pressure, which often results in fragmentation of the analyte by impact from energetic electrons, and leads to more complicated mass spectra. In addition, special sample introduction systems must be devised in order to place the sample under vacuum conveniently. One way to overcome these obstacles is to operate the discharge at atmospheric pressure.

However, when a DC discharge is operated at atmospheric pressure, some of its characteristics change dramatically, among them the current-voltage behavior.[6]

Lubman et al.[7-8] showed that an atmospheric-pressure glow discharge (APGD) can be used as an ionization source for molecular mass spectrometry. Lubman's source employed helium as the discharge gas and typically yielded a mass spectrum containing only a molecular ion peak (similar to APCI), making the spectra easy to interpret. However, his configuration required introduction of the sample into the discharge chamber, leading to memory effects, instabilities in the discharge, and sample-induced changes in the characteristics of the GD. Clearly, a source not requiring introduction of the sample into the discharge chamber would be desirable.

Recently, several ionization sources have been developed that separate the discharge from the sampling region.[9-11] By introducing the sample beyond the discharge chamber, the problems of discharge instability and memory effects have been overcome. These sources are commonly employed in the new field of ambient desorption/ionization mass spectrometry (ADI-MS),[12] which refers to an open-air ionization source that permits the direct ionization (and often desorption) of samples for mass spectrometry. One such ADI-MS source is Direct Analysis in Real Time (DART).[10] Unfortunately, little has been reported about the fundamental characteristics of the discharge used in DART, but both a corona and a glow discharge have been claimed. Developed by JEOL USA Inc. (Peabody, MA), DART is often operated near 3 kV with currents up to 5 mA.[10] The discharge is formed in helium between a pin cathode and a grounded, disk anode. Two filter electrodes are placed beyond the discharge chamber to remove any charged species, resulting in predominantly helium metastables (He*) exiting the source. Additionally,

the gas temperature is raised to approximately 300 °C by an auxiliary heater. Samples are introduced into the open-air sampling region, after the second filter electrode, for direct desorption/ionization. The interaction between He* and open air results in the production of reagent ions similar to those in APCI.[5] Thus, when an analyte is desorbed/ionized, the resulting mass spectrum consists mainly of the molecular ion.

Another ADI-MS source based on a DC discharge in helium has recently been developed and described by our laboratory.[13-15] This source, termed the flowing atmospheric pressure afterglow (FAPA) ionization source, operates by the formation of a true glow discharge in helium between a pin cathode and plate anode, with voltages between 400 and 500 V and operating currents of roughly 25 mA.[13] Although FAPA and DART might seem to be similar, a fundamental characterization of the two discharges is essential to understand them fully.

In the present study, the discharges used by DART and FAPA, a corona-to-glow (C-G) and a glow-to-arc (G-A) transitional discharge, respectively, were characterized on the basis of several criteria. Electrical characteristics of both the DART and FAPA discharge were initially used to classify each. The reagent ions produced, along with the mass spectra for ferrocene generated by both discharges were also compared. Thermal maps of the gas escaping the discharge cell of both sources were examined as well. Lastly, spatially resolved emission maps for O I and N_2^+ generated by both discharges were measured. Overall, it was found that the two kinds of discharge are fundamentally different, and might be best applied in dissimilar areas.

4.2 Experimental

4.2.1 Reagents

All reagents were analytical grade. High purity He (99.999% ultra-high purity helium, Airgas, Radnor, PA) was used as the discharge gas in all experiments. Ferrocene was purchased from Sigma-Aldrich (St. Louis, MO) and used as a model compound because of its high vapor pressure, which simplified sample introduction.

4.2.2 Instrumentation

An atmospheric pressure discharge in helium was formed in an airtight cell with a quartz body (cf. Figure 4.1). The discharge was established between a stainless steel pin (cathode) and a brass plate (anode) with a discharge gap of ~7 mm. A small hole (~1 mm dia.) in the center of the brass plate allowed species generated in the discharge to flow into the open atmosphere. To compensate for the inherent negative dynamic resistance of atmospheric pressure discharges, a ballast resistance was placed in series with the cathode. Ultimately, this ballast resistance limits the obtainable discharge current. A negative voltage was applied to the cathode with a high-voltage, DC power supply (Model BRC-5-400R, Universal Voltronics Corp, Mt. Kisco, NY), with helium being supplied to the cell by a mass flow controller (MKS Instruments, Andover, MA).

The C-G and G-A discharges (see section on discharge classification below) were formed in the same discharge chamber, but under different operating conditions. For this chamber, the current-voltage behavior is illustrated in Figure 4.2. The C-G (DART-like) discharge, with current-voltage conditions labeled with a red arrow in Figure 4.2, was sustained by using a ballast resistance of 1 MΩ and applying a voltage of -3 kV to the

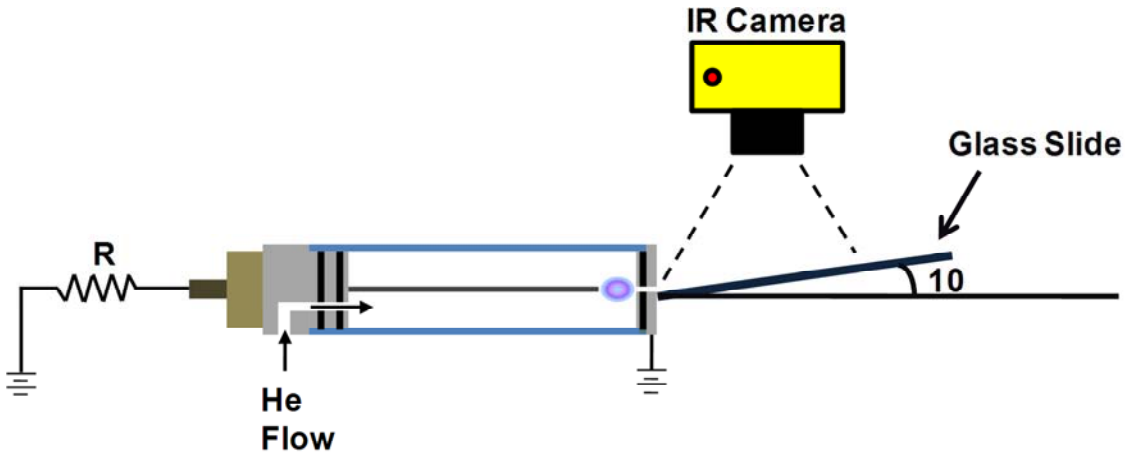

Figure 4.1 Diagram of the quartz cell used for forming the different discharges in helium in the configuration used for obtaining thermographic images of the gas exiting the cell. The slide was placed nearly parallel to the gas flow to measure the greybody emission from the glass slide.

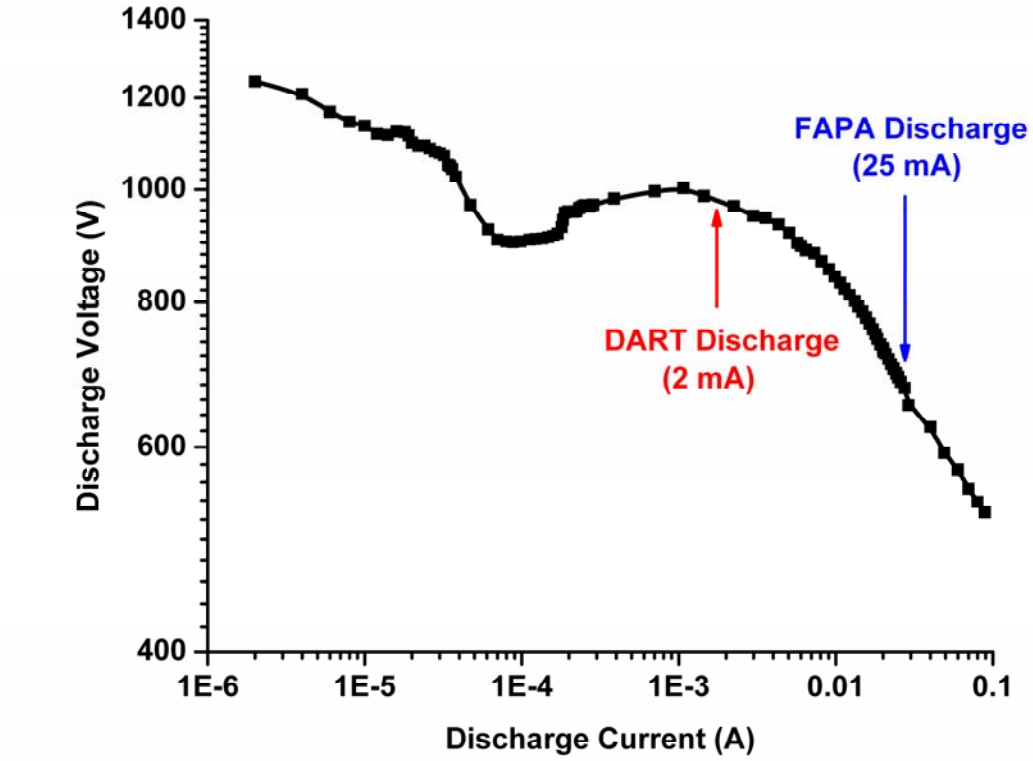

Figure 4.2 Characteristic current-voltage curve for atmospheric-pressure, DC discharges formed in helium. Cell configuration was a pin-to-plate geometry with a gap of ~7 mm (cf. Figure 4.1).

pin, resulting in currents of less than 3 mA. It is important to note that the additional electrodes and heater, which are used in the commercial DART, were excluded in order to investigate fundamental properties of the discharge. The G-A (FAPA-like) discharge, labeled with a blue arrow in Figure 4.2, was operated with a ballast resistance of 1.5 kΩ and operated at 25 mA and ~450 V. Helium metastables, along with other discharge products, exit the cell through the small hole in the anode, and ionize N_2 and H_2O in open air, resulting in the production of reagent ions.[4, 16-17] The voltage of the anode was adjusted with a low-voltage DC power supply (Model 6299A, Hewlett Packard, Palo Alto, CA) to maintain a field-free sampling region between the discharge cell and the mass spectrometer interface when mass spectrometry was performed. The cell was mounted on a locally built three-dimensional translation stage for alignment with the sampling orifice of the mass spectrometer.

4.2.3 Mass Spectrometer

Ions were detected by a modified LECO Renaissance® (LECO Corp. St. Joseph, MI) inductively coupled plasma (ICP) time-of-flight mass spectrometer (TOFMS), with the ICP source disabled and replaced with the discharge cell. Modifications to the MS have already been described,[13] but a brief overview is given here. The original sampling cone was machined flat to yield a stainless-steel sampling plate. In addition, a 3-mm diameter copper ring electrode, serving as an ion lens, was added between the skimmer and the front plate to better focus and guide the incoming ion beam. The voltage of the ion lens was independently controlled with a low voltage power supply (Model 6207B, Hewlett Packard-Harrison Division, Berkeley Heights, NJ). To overcome a higher first-

stage pressure caused by the introduction of helium, an additional roughing pump was added to the first stage. An integration time of 0.5 s was used in all MS experiments.

4.2.4 IR Thermography

Thermal spatial patterns of the gas exiting the discharge cell were taken for the C-G and G-A discharges by means of a Fluke Ti40 IR FlexCam (Everett, WA). A glass microscope slide was placed nearly parallel (~10°) to the gas flow, but slightly angled so the slide was in the path of the gas stream issuing from the cell (cf. Figure 4.1). The reason for this arrangement is that the gas leaving the discharge chamber does not behave as either a blackbody or greybody. In this experiment, the gas transfers its heat to the glass slide, the greybody emission of which can be detected with the camera. The poor thermal conductivity of glass (1.1 W/m·K) along with its high emissivity (0.92) made it a good choice for spatially resolved, greybody emission measurements. The emissivity of the glass was taken into consideration to obtain accurate temperatures.

4.2.5 Optical Spectroscopic Measurements

Longitudinally resolved (side-on) spectroscopic measurements of both discharges were obtained by mounting the quartz discharge cell in place of the ICP ordinarily used in a commercial emission spectrometer (ACTIVA, Horiba–Jobin Yvon, Longjumeau, France). The discharge cell was mounted on a movable platform for proper alignment of the discharge with the entrance slit. The spectral resolution of this instrument is between 8 and 16 pm, depending on the wavelength region being employed. The ACTIVA spectrometer has the advantage of simultaneously providing wavelength and spatial

information with a spatial resolution of ~200 μm. To achieve this spatial resolution, a cylindrical lens was placed in the entrance optics between the front mirror and the entrance slit. With this modification, the spectrometer also has the ability to image lengths greater than 20 mm, which allowed full spectral imaging of the electrodes and the discharge. Species of interest included N_2^+ and O I at emission wavelengths of 309.40 and 777.19 nm, respectively. Although ultra-high purity helium was used, these impurities apparent from the emission spectrum arise from the gas transfer lines. As previously noted,[13] the impurities could be removed by thorough baking of the transfer lines and gas purification immediately prior to the discharge chamber. However, this extensive procedure was deemed unnecessary in this initial study.

4.3 Results and Discussion

4.3.1 Discharge Classification

Figure 4.2 demonstrates the current-voltage (i-V) plot for an atmospheric-pressure DC discharge operated in a pin-to-plate geometry, with helium as the discharge gas. This i-V curve differs greatly from that for a reduced-pressure discharge. The transitions between the different discharge regimes become less pronounced, making discharge classification difficult. In addition, the pin-to-plate geometry introduces a corona realm. The red arrow in Figure 4.2 identifies where the discharge used by DART operates,[18-20] in a C-G transitional zone. The FAPA discharge, found in the G-A transitional regime, is labeled on the current-voltage curve of Figure 4.2 with the blue arrow.

Photographs of the C-G and G-A discharges are shown in Figure 4.3a and 4.3b, respectively. The exposure time for the photograph in Figure 4.3b is four times shorter than that required for Figure 4.3a, indicating that the G-A discharge is much brighter. In addition, only the tip of the cathode glows (negative glow region) in the C-G discharge, whereas the negative glow extends further down the cathode with the G-A discharge. This behavior is expected; in a "normal" glow discharge, the area of the negative glow is proportional to the supplied current. Another feature is the extended and brighter positive column found with the G-A discharge (Figure 4.3b), compared with the very dim positive column for the C-G discharge (Figure 4.3a). Atmospheric pressure glow discharges typically have a fairly bright positive column that fills most of the gap between the anode and cathode, as was observed with the G-A discharge. Corona discharges, in contrast, usually do not have a visible positive column; thus, the presence of a weak positive column with the C-G discharge suggests that it operates between the corona and the glow discharge regimes.

Interesting also are the standing striations in the positive column of the G-A discharge. Although these striations have been observed only with certain cell configurations and do not seem to affect the performance of the source, they are useful in characterizing the discharge. Such standing striations represent local maxima of current density. Because nearly all of the current density in a corona discharge resides at or near the tip of the electrode, corona discharges cannot exhibit such striations. For this reason, the striations do not appear in the C-G discharge.

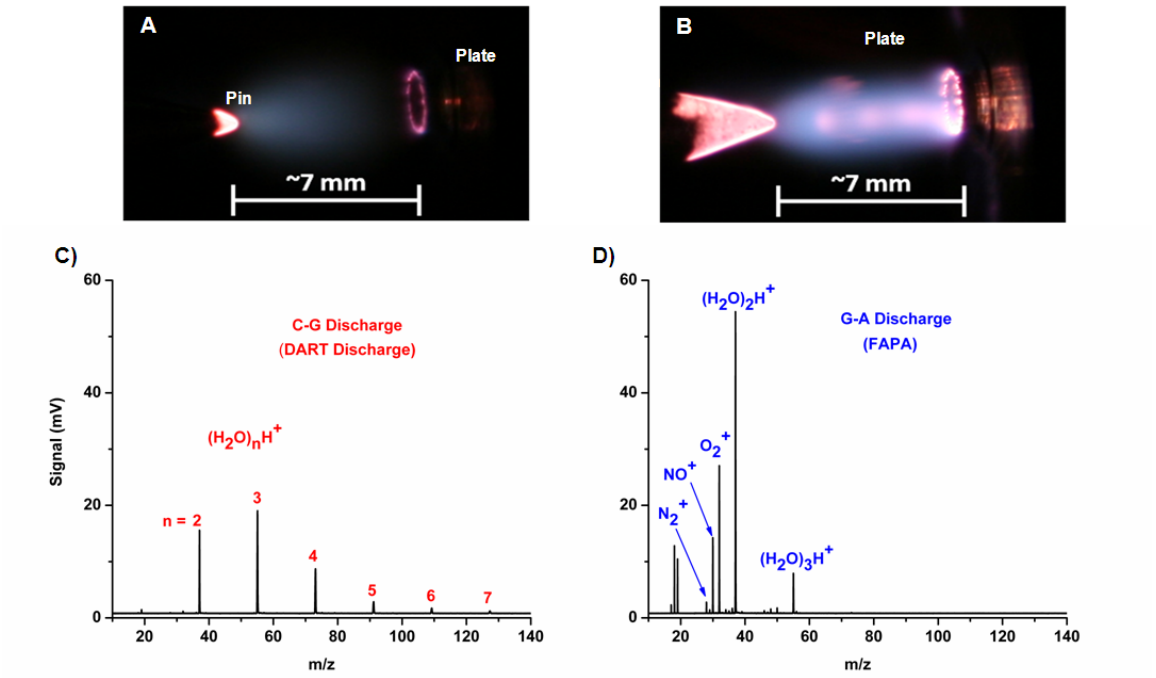

Figure 4.3 a) C-G discharge operated at a current of 2 mA and photographed with a 1/15 s exposure time. The strongest emission occurs at the tip of the pin cathode (left), with a very faint, diffuse positive column, similar to the pattern expected from a corona discharge. b) G-A discharge operated at a current of 25 mA and photographed with a 1/60 s exposure time. The negative glow extends farther down the cathode tip and there is a better confined, brighter positive column, just as in a conventional glow discharge. The standing striations in the positive column were present only in certain cell configurations and have not been found to affect the performance of the source. c) and d) Background mass spectra from the C-G and G-A discharges, respectively. The main features with the C-G discharge are protonated water clusters, whereas the G-A discharge contains additional charge-transfer reagent ions such as O_2^+, and fewer higher-order water clusters.

4.3.2 Reagent Ions

All discharge and MS parameters were tuned to maximize the signal from $(H_2O)_2H^+$ for both discharges. The strong signal for $(H_2O)_2H^+$ made it an effective reagent ion for optimization because of its high abundance in the mass spectrum of both discharges (Figure 4.3c and 4.3d) and its extremely high gas-phase acidity. This trait promotes efficient proton-transfer ionization even for analytes with a low gas-phase basicity, yielding an MH^+ molecular ion. The parameters that affected the reagent-ion signal included the voltage on the front plate of the mass spectrometer, the anode voltage, and the He flow. The resulting optimal operating conditions are given in Table 4.1.

To better understand the C-G and G-A discharges, it is useful to determine the relative abundance and type of reagent ions that are produced by each. The presence of protonated species, particularly protonated water clusters, suggests the likelihood of a proton-transfer ionization mechanism, in which the proton is transferred from the reagent ion to the sample species. Another type of ionization that might take place is charge transfer, in which a positively charged reagent ion steals an electron from the sample species, to become neutral while the sample species assumes a positive charge. For either mechanism, the greater the abundance of ions available to transfer their charge, the higher the ionization probability and the less likely that competitive ionization will distort observed spectra.

The reagent-ion spectrum from the C-G discharge, shown in Figure 4.3c, contains mainly protonated water clusters, which foster a proton-transfer ionization mechanism. Virtually no ions for charge-transfer ionization, such as N_2^+, NO^+, or O_2^+, were detected

Table 4.1. Operating conditions for the C-G and G-A discharges optimized for generating the strongest $(H_2O)_2H^+$ signal.

	C-G Discharge	**G-A Discharge**
Cathode Voltage, Current	-3000 V, ~2 mA	-500 V, 25 mA
Anode Voltage	110 V	70 V
MS Front-Plate Voltage	80 V	50 V
He Flow	~1.5 L/min	~1 L/min
Ballast Resistance	1 MΩ	1.5 kΩ

with the C-G discharge. The likely reason for this observation is that the lower power C-G discharge generates a lower abundance of He* and other species necessary for producing the charge-transfer reagent ions. The reagent ion spectrum from the G-A discharge was substantially different (Figure 4.3d). In addition to protonated water clusters, the G-A discharge produced a significant amount of NO^+, O_2^+, and N_2^+. These three ions have been shown to play a role in charge-transfer ionization,[21] which would result in the formation of molecular ions, $M^{+\cdot}$. Additionally, the mass spectrum from the G-A discharge exhibits a stronger reagent ion signal than does the C-G discharge. Moreover, the C-G discharge produces a greater abundance of higher-order water clusters, which have a lower gas-phase acidity and yield less efficient ionization than lower-order protonated clusters. Therefore, the G-A discharge would be expected to offer a wider range of ionization capabilities, in addition to being less affected by competitive ionization of multiple analytes.

4.3.3 Ferrocene Determination

Ferrocene was introduced into the sampling region of each discharge by passing helium, at ~120 mL/min, across a few crystals of ferrocene placed in a gas-tight flask and through a narrow glass tube (~300 μm i.d.). The tube was held in the sampling region by means of a micropositioner to optimize the ferrocene signal. The G-A discharge was first ignited, thereby ionizing the vapor-phase ferrocene, which was then detected with the TOFMS. The signal trace for the $M^{+\cdot}$ of ferrocene (m/z = 186) was recorded for three minutes. The discharge was then extinguished, and the current-voltage conditions were changed to those of the optimized C-G discharge. The C-G discharge was then ignited

and the signal for the M^+ from ferrocene again monitored for several more minutes. This time-trace for m/z 186 is given in Figure 4.4a. It is important to note that, while these sources typically ionize through proton transfer, ferrocene has a much lower ionization energy than gas-phase basicity, resulting in mainly the molecular ion.[22]

While the G-A discharge was running, there was a strong signal (~70,000 counts) for the M^+ of ferrocene. When the discharge was turned off, the signal went to zero, and then returned initially to ~70,000 counts when the C-G discharge was ignited. However, the subsequent signal decayed gradually to roughly 2% of its original strength. To verify that the signal decay was not due to a loss of ferrocene, the G-A discharge was later reignited and the signal returned to approximately its original level (~70,000 counts; data not shown). The gradual decay in signal during the initial C-G "on" period is believed to be related to discharge stabilization and slow cooling of the discharge cell. Although the cell temperature would not affect the ferrocene desorption process, because the analyte is in the vapor phase before reaching the sampling region, it can alter the concentration and type of reagent ions that are produced. It was found that switching to the C-G discharge resulted in ion signal decay for low-order water clusters and charge transfer ions, resulting in a drop in ionization efficiency. Additionally, the signal for higher-order clusters (n = 3 or 4) gradually rose over time (data not shown), which implies that the lower gas temperature resulted in condensation of water clusters. However, the exact reason for the decay in charge-transfer ion signal is not yet known.

Spectra of ferrocene obtained with the C-G and the G-A discharges are given in Figure 4.4b. The G-A discharge produced, in addition to the molecular ion, an adduct

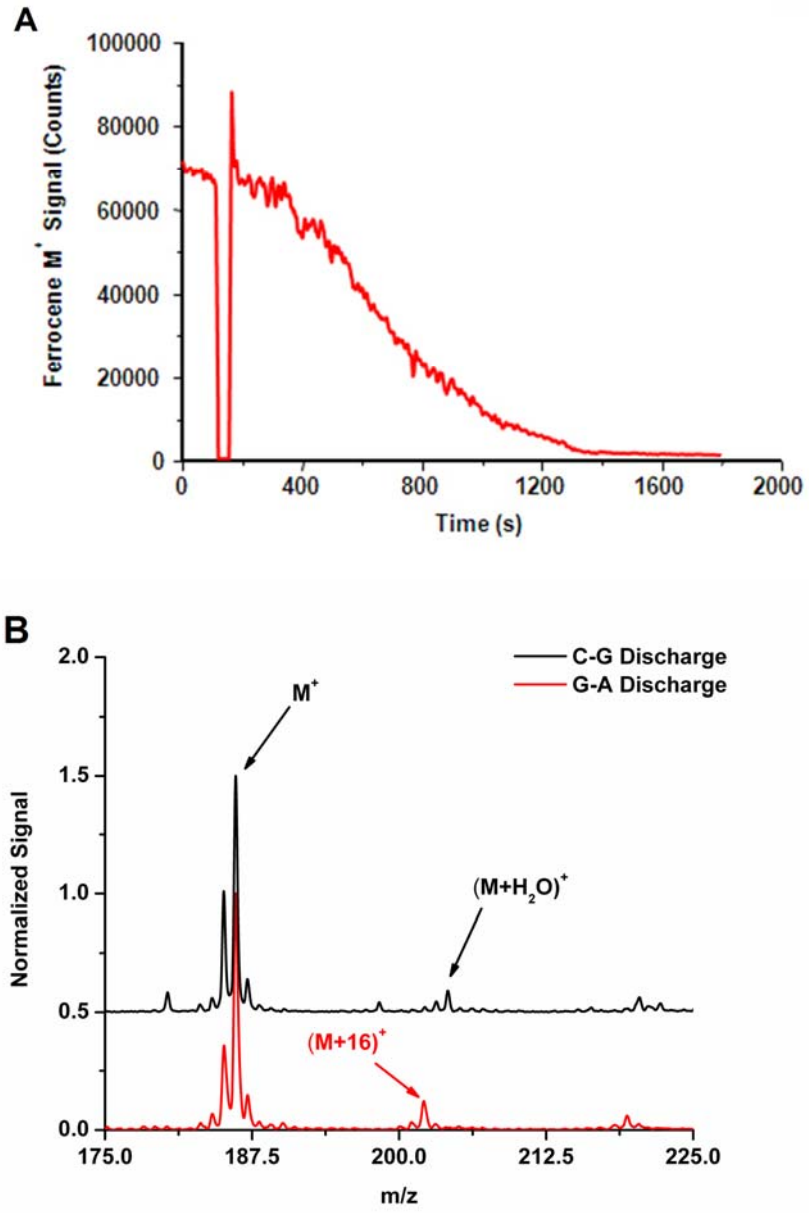

Figure 4.4 a) Time trace for the molecular ion (M^+) of ferrocene (m/z = 186) with the G-A discharge as the initial ionization source. After two minutes, the source was turned off and switched to a C-G discharge. The signal then decayed over time to ~2% of the original level. See text for discussion. b) Normalized mass spectra of ferrocene obtained with a G-A discharge (black), and a C-G discharge (red) as ionization sources. The spectra are vertically offset from each other for visualization.

with a mass shifted higher by 16 u, thought to be an addition of oxygen by the reaction of radical, atomic oxygen with the aromatic ring of ferrocene.[23] The only adduct observed with the C-G discharge was an addition of 18 u, attributed to water. Both of these spectra match well with those published for typical APCI sources[22] and the commercial DART source.[24]

4.3.4 IR Thermography

For a source to be attractive practically for ADI-MS, it must not only efficiently ionize, but also desorb analytes. Because it is believed that the major mechanism of desorption in APGD-based ADI-MS sources is thermal,[9] it is useful to measure the temperature of the gas exiting the discharge cell. Furthermore, a full thermographic map of the gas could yield important information about optimal sample positioning for desorption/ionization.

IR thermography of the C-G and G-A discharges was performed by measuring the blackbody emission from a glass microscope slide that was in contact with the gas stream. Temperature profiles for the C-G and G-A discharges under optimal conditions are given in Figures 4.5a and b, respectively. These images reveal that the gas issuing from the G-A discharge was much hotter (maximum temperature ~235 °C) than that from the C-G discharge (maximum temperature ~55 °C). This difference in temperature is due to a higher current density in the G-A discharge, stemming from larger operating currents, than in the C-G discharge. The higher temperature of the G-A discharge should yield more efficient desorption, and thus more sensitive detection, of molecules with lower vapor pressures. This fact also likely explains why an auxiliary heater is employed

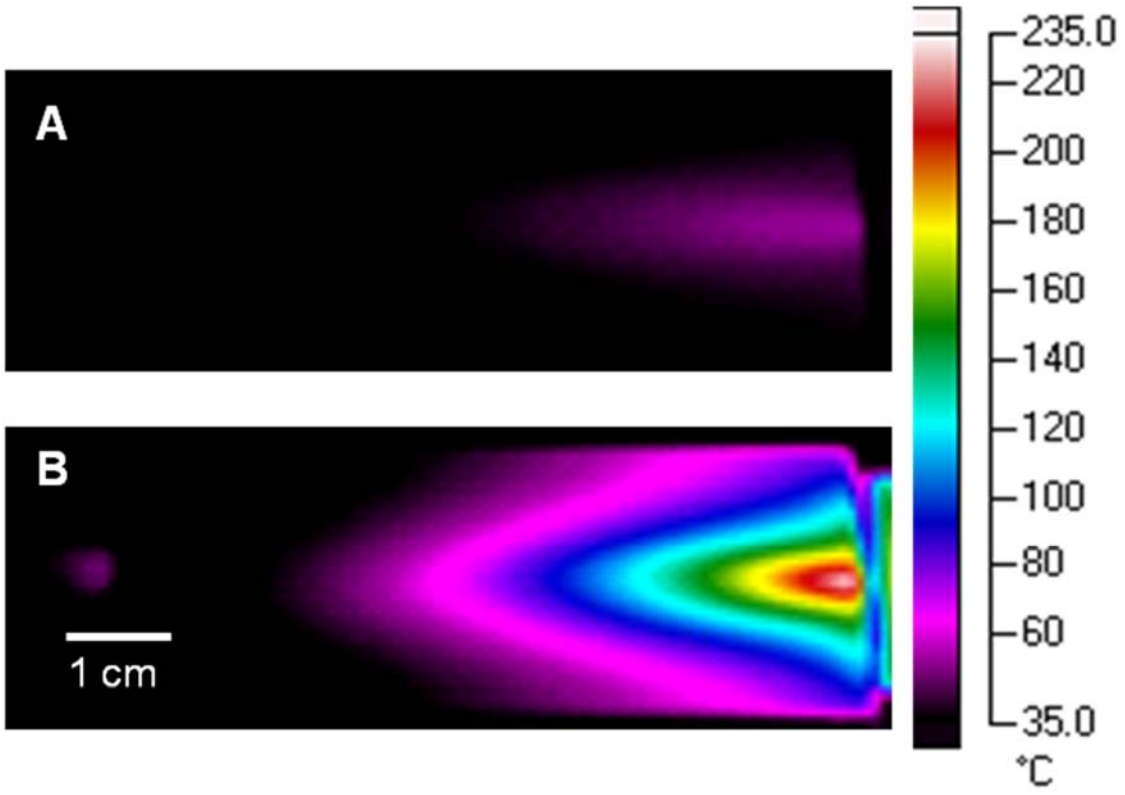

Figure 4.5 Thermographic map of the gas stream issuing from the C-G discharge (a) and the G-A discharge (b) under optimal conditions and on the same false-color temperature scale (right). The C-G discharge attains a maximum temperature of only ~55 °C, whereas the G-A discharge reaches ~235 °C.

with the DART source, which utilizes a C-G discharge. Otherwise, many solid samples would not be efficiently desorbed, resulting in low detection efficiency and sensitivity.

4.3.5 Optical Emission

To better understand the two discharges, the spatial distribution of selected emission features, known to exist in the spectrum,[13] was obtained. Spatially resolved emission maps for N_2^+ (at 391.4 nm) and O I (at 777.19 nm) are shown in Figures 4.6a and b, respectively. It should be emphasized that both features arise from contaminants in the He supply, so would be expected to be weak. For both spectral features, and both discharges, there are distinct emission maxima at the pin (cathode) and plate (anode). The peak at the cathode is due to the strong emission from the negative glow. Nearly all of the emission (~95% in the case of O I), and consequently current density, of the C-G discharge is restricted to the very tip of the pin. In contrast, the emission from the G-A discharge was distributed along the length of the pin (~2 mm) and the throughout the positive column. At atmospheric pressure, the positive column occupies much of the discharge region in glow discharges,[13] whereas corona discharges do not exhibit a strong positive column. In the maps of the two discharges, emission from N_2^+ and O can clearly be seen in the positive column of the G-A discharge, but not with the C-G discharge even at long exposure times (60 s). These emission patterns indicate that the G-A discharge is a true glow and should be capable of generating a large flux of excited species.

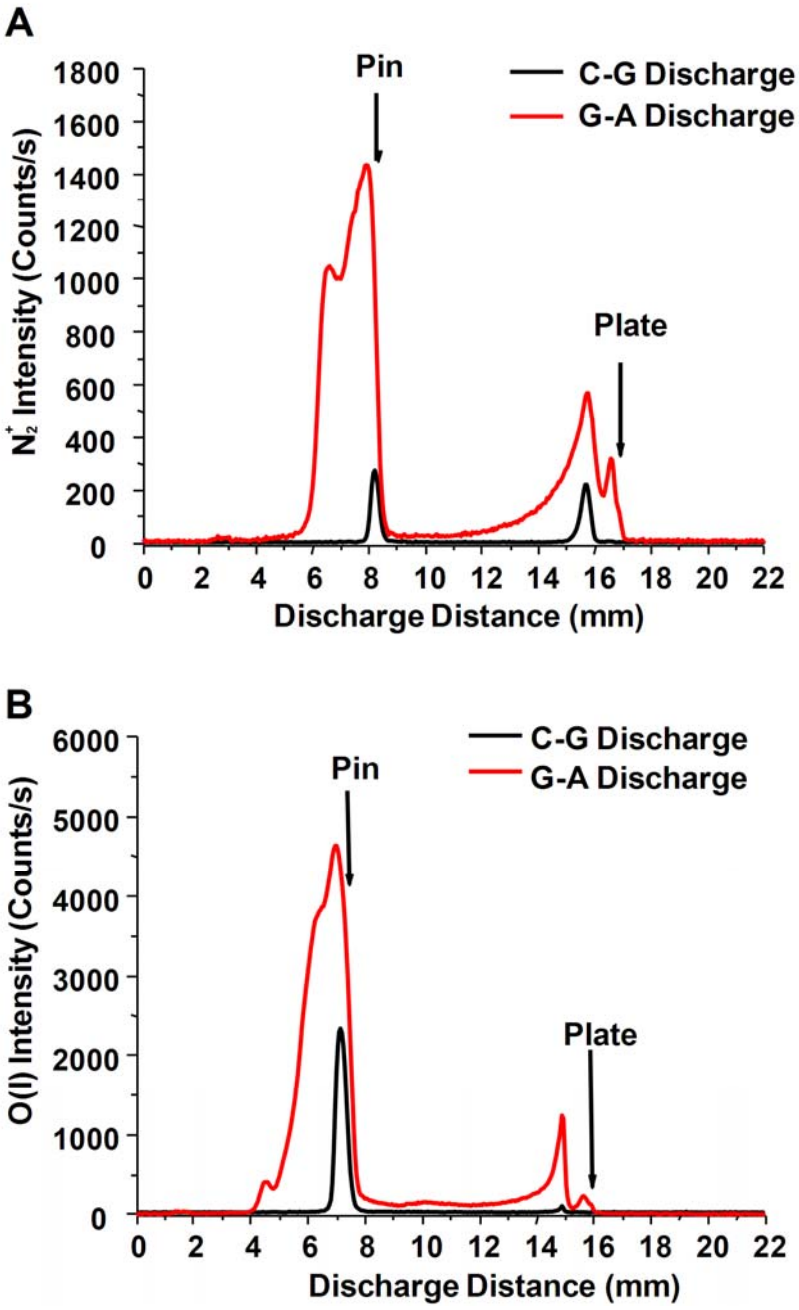

Figure 4.6 a) Spatially resolved optical emission from N_2^+ for C-G and G-A discharges. b) Optical emission from O(I) for the C-G and G-A discharges. These emission lines come from trace gas impurities in the transfer lines. The spatial emission plots demonstrate that the C-G discharge is confined to the tip of the pin with little or no positive column, which is indicative of a corona discharge.

4.4 Conclusions

The C-G and G-A discharges, used by DART and FAPA respectively, have been examined in some detail. They have been shown to produce different types and amounts of reagent ions. Additionally, the C-G discharge produces a water adduct with the M^+ of ferrocene, whereas an oxygen adduct was seen with the G-A discharge. Infrared thermography of the gas exiting the discharge cell revealed that the plume from the G-A discharge is much hotter than from the C-G discharge. This temperature difference suggests why an external heater is needed for direct analyses with the DART source. The relative peak heights at the anode and cathode for emission from atomic oxygen and N_2^+ suggests that the C-G discharge is closer to a corona discharge and the G-A closer to a GD. This study demonstrates that the two discharges are fundamentally different and should offer individual advantages. However, a direct comparison of the desorption/ionization capabilities of these sources is essential and will be the basis of a subsequent study. Additionally, a fundamental examination and comparison of all ADI-MS sources, including desorption electrospray ionization (DESI), FAPA, and DART, is needed. Parameters of interest include sensitivity, range of detectable analytes, stability, and matrix-effect ion suppression. Not only would this study provide users with information for choosing the proper source for a given application, but it is essential to the progression and widespread adoption of the method.

References

1. Kay, E.; Coburn, J. *Electronica y Fisica Aplicada* **1974**, *17*, 246-246.
2. Carazzato, D.; Bertrand, M. J. *J. Am. Soc. Mass. Spectrom.* **1994**, *5*, 305-15.
3. Mason, R.; Milton, D. *Int. J. Mass Spectrom. Ion Processes* **1989**, *91*, 209-25.
4. Horning, E. C.; Carroll, D. I.; Dzidic, I.; Haegele, K. D.; Horning, M. G.; Stillwell, R. N. *Journal of Chromatographic Science* **1974**, *12*, 725-9.
5. Horning, E. C.; Horning, M. G.; Carroll, D. I.; Dzidic, I.; Stillwell, R. N. *Analytical Chemistry* **1973**, *45*, 936-43.
6. Staack, D.; Farouk, B.; Gutsol, A.; Fridman, A. *Plasma Sources Science & Technology* **2005**, *14*, 700-711.
7. Sofer, I.; Zhu, J.; Lee, H. S.; Antos, W.; Lubman, D. M. *Appl. Spectrosc.* **1990**, *44*, 1391-8.
8. Zhao, J.; Zhu, J.; Lubman, D. M. *Anal. Chem.* **1992**, *64*, 1426-33.
9. Venter, A.; Nefliu, M.; Cooks, R. G. *Trac-Trends Anal. Chem.* **2008**, *27*, 284-290.
10. Cody, R. B.; Laramee, J. A.; Durst, H. D. *Anal. Chem.* **2005**, *77*, 2297-2302.
11. McEwen, C. N.; McKay, R. G.; Larsen, B. S. *Anal. Chem.* **2005**, *77*, 7826-7831.
12. Takats, Z.; Wiseman, J. M.; Gologan, B.; Cooks, R. G. *Science* **2004**, *306*, 471-473.
13. Andrade, F. J.; Wetzel, W. C.; Chan, G. C. Y.; Webb, M. R.; Gamez, G.; Ray, S. J.; Hieftje, G. M. *J. Anal. At. Spectrom.* **2006**, *21*, 1175-1184.
14. Andrade, F. J.; Shelley, J. T.; Wetzel, W. C.; Webb, M. R.; Gamez, G.; Ray, S. J.; Hieftje, G. M. *Anal. Chem.* **2008**, *80*, 2646-2653.

15. Andrade, F. J.; Shelley, J. T.; Wetzel, W. C.; Webb, M. R.; Gamez, G.; Ray, S. J.; Hieftje, G. M. *Anal. Chem.* **2008**, *80*, 2654-2663.

16. Dzidic, I.; Carroll, D. I.; Stillwell, R. N.; Horning, E. C. *Anal. Chem.* **1976**, *48*, 1763-1768.

17. Kambara, H.; Mitsui, Y.; Kanomata, I. *Anal. Chem.* **1979**, *51*, 1447-1452.

18. U.S. Pat. 7,112,785 B2, 2006.

19. Laramee, J. A.; Durst, H. D.; Cody, R. B.; Nilles, J. M. Amer Chemical Soc, 2005, pp 287-ANYL.

20. Kpegba, K.; Spadaro, T.; Cody, R. B.; Nesnas, N.; Olson, J. A. *Anal. Chem.* **2007**, *79*, 5479-5483.

21. Einolf, N.; Munson, B. *International Journal of Mass Spectrometry and Ion Physics* **1972**, *9*, 141-160.

22. Macha, S. F.; McCarley, T. D.; Limbach, P. A. *Anal. Chim. Acta* **1999**, *397*, 235-245.

23. Ascenzi, D.; Franceschi, P.; Guella, G.; Tosi, P. *J. Phys. Chem. A* **2006**, *110*, 7841-7847.

24. in *DART Applications Notebook*. JEOL Inc., 4th Edition edn., 2008, p 11.

Chapter 5

Ionization Matrix Effects in Plasma-based Ambient Mass Spectrometry Sources

5.1 Introduction

Over the past five years, there has been a resurgence in the area of ionization source development owing to the introduction of a new field termed Ambient Desorption/Ionization Mass Spectrometry (ADI-MS).[1-2] The goal of this emerging field is to lessen sample analysis times in mass spectrometry by reducing or eliminating sample pre-treatment, while maintaining the low limits of detection (LODs) and high chemical specificity of detection inherent to mass spectrometry. ADI-MS often relies on the ion source not only for ionization but also for the desorption or extraction of analytes from the sample surface.

The excitement in this field has led to the development of more than 25 different atmospheric-pressure desorption/ionization sources.[3] The most common ones found in the literature are desorption electrospray ionization (DESI)[4] and direct analysis in real

time (DART).[5] Although a large number of ADI-MS sources has been described, the majority rely on either electrospray-based or atmospheric-pressure chemical ionization mechanisms.[2] Furthermore, many of the described sources rely on an electrical discharge for the desorption and/or ionization processes.[5-10] These plasma-based sources include DART,[5] the flowing atmospheric-pressure afterglow (FAPA),[9, 11] the low-temperature plasma (LTP) probe,[8] and desorption atmospheric-pressure chemical ionization (DAPCI).[4] While these ionization sources have been shown to desorb/ionize many small, organic molecules from a wide variety of matrices[12-14] and offer low LODs (<10 fmol for many small, organic analytes),[8, 15] surprisingly little research has been performed to characterize the desorption mechanism they employ or their susceptibility to matrix effects. In this context, a matrix effect is defined as a physical or chemical process that inhibits or enhances detection or proper quantification of an analyte, A, in the presence of one or more matrix species, M.

Matrix effects, usually in the form of ion suppression, have long been known to exist for other atmospheric-pressure mass spectrometric analyses, such as liquid chromatography-electrospray ionization-mass spectrometry (LC-ESI-MS).[16-17] The most troublesome complications of ion suppression in LC-ESI-MS stem from co-eluting analytes or the need for extreme solvent gradients in the chromatographic separation. The observed matrix effect in this case is caused by a competitive desolvation/ionization process.[17] While ESI is known to suffer greatly from ion suppression, only recently has it been shown that matrix effects exist also for atmospheric-pressure chemical ionization-mass spectrometry (APCI-MS).[18] The ion suppression observed in APCI-MS is often not

as severe as in ESI-MS because the volatilization and ionization processes are separated in time.

Because the ADI-MS sources are often responsible for both desorption and ionization, matrix effects should be investigated correspondingly. In desorption, for example, one matrix effect that can occur is through preferential phase change of a solid or liquid matrix, M(s,l), to the gas phase, M(g), while the phase of the analyte, A(s,l), remains unchanged. An illustration of this mechanism is given below,

$$A(s,l) + M(s,l) \rightarrow A(s,l) + M(g) \quad (1)$$
$$if\ \Delta E_{des,A} \gg \Delta E_{des,M}$$

where $\Delta E_{des,A}$ is the energy required for desorption of analyte A and $\Delta E_{des,M}$ is the desorption energy of matrix M. Additionally, the internal energy of the desorption/ionization source, ΔE_{source}, must be less than $\Delta E_{des,A} + \Delta E_{des,A}$. The resulting discrepancy between the relative concentrations in the bulk and the gas phase can also cause or enhance ionization suppression, leading to desorption-induced matrix effects.

Because many of the plasma-based ADI-MS sources employ chemical ionization, through the generation of reagent ions, it is probable that the ion suppression mechanisms are similar to those for APCI-MS.[18] For proton-transfer reactions, the most common ion-molecule reaction involved in APCI-MS, the suppression mechanism operates through competitive ionization caused by differing proton affinities (PAs). Gaseous analytes, A(g), are often ionized through interactions with gas-phase, protonated water clusters $[(H_2O)_nH^+]$:[19]

$$A(g) + (H_2O)_nH^+ \rightarrow AH^+(g) + (H_2O)_n \quad (2)$$
$$if\ PA_A > PA_{(H_2O)_nH^+}$$

where PA_A and $PA_{(H2O)nH+}$ are the proton affinities of the analyte and the protonated water cluster, respectively. If a matrix molecule M is also present in the gas phase, the system can suffer competitive ionization:

$$AH^+ + M^\circ \rightarrow A^\circ + MH^+ \quad (3)$$
$$if\ PA_M > PA_A$$

where PA_M is the proton affinity of the matrix molecule.

Because there is often little separation in space or time between the desorption and ionization processes in plasma-based ADI-MS, it is likely that matrix effects play an important role in the analysis of complex samples. However to date, matrix effects have been discussed only for extractive electrospray ionization (EESI)-MS.[20-21] In those studies, it was determined that ion suppression effects in EESI were minimal because the desorption and ionization processes were separated in time and space.

In the present study, proton-transfer ionization matrix effects were quantified for three of the most popular plasma-based ADI-MS ionization sources, DART, FAPA, and LTP. Varying the proton affinity and concentration of the gas-phase matrix species enabled the presence and degree of ion suppression to be determined. Additionally, because the analyses were performed on the same instrument, direct comparisons of the ionization sensitivity of the sources could be made. This manuscript will serve as an

introduction to future investigations of desorption/ionization matrix effects and desorption mechanisms of these plasma-based ADI-MS sources.

5.2 Experimental

5.2.1 Reagents

All reagents were analytical grade. High-purity helium (99.999% ultra-high purity helium, Airgas, Radnor, PA) was used as the discharge gas in all experiments. Acetophenone, methyl salicylate, naphthalene, and triethyl phosphate were purchased from Sigma Aldrich (St. Louis, MO) and used as model analytes/matrices because of their high vapor pressure and varying proton affinities.

5.2.2 ADI-MS Ionization Sources

All three ionization sources (DART, FAPA, and LTP) were fabricated in-house based on descriptions in the literature. In all cases, the helium flow was supplied to the ionization source by a mass flow controller (MKS Instruments, Andover, MA).

The FAPA cell has already been described in detail,[22] but a brief description will be given here. An atmospheric-pressure glow discharge in helium was formed in an airtight cell with a quartz body between a 1 mm diameter tapered steel pin and a brass plate with a discharge gap of 7 mm (cf. Figure 5.1). The tip of the pin was sanded to a sharp point of ~50 μm. A negative DC potential of ~500 V and 25 mA was applied to the pin in a current-controlled mode through a 2.5 kΩ ballast resistor by means of a high-voltage power supply (Model DRC-5-400R, Universal Voltronics, Mount Kisco, NY). A small hole (~1 mm dia.) in the center of the brass plate allowed species generated in the

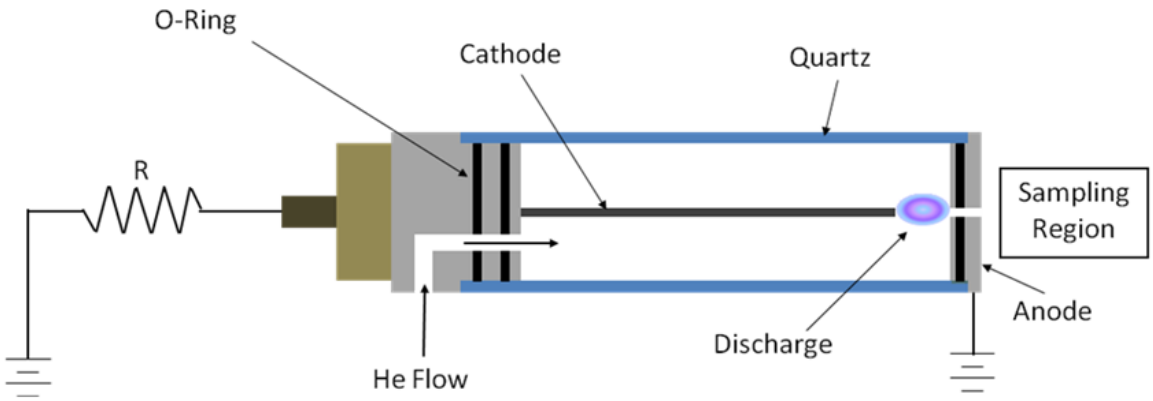

Figure 5.1 Diagram of the FAPA source used in this study.

discharge to flow into the open atmosphere and interact directly with the samples. The helium flow rate for the FAPA source was optimized and maintained at 1 L/min.

The locally built DART source was based on the limited information found in the literature.[5, 23-24] For details about this source, refer to Figure 5.2. A corona-to-glow discharge was formed between a tungsten pin cathode and an aluminum grounded anode. The body of the cell was constructed from Teflon® with the exception of the heated section from electrode 1, E1, to electrode 2, E2, which was made from alumina. E1 and E2, the filter electrodes responsible for removing charged species, were an aluminum disk and a 95% transmissive nickel grid, respectively. A band heater (Watlow Electric Manufacturing Co., St. Louis, MO) was placed around the alumina tube to heat the gas leaving the source chamber. This heater was controlled and monitored with a temperature controller (Omega Engineering Inc, Stamford, CT). A -3000 V potential was applied to the pin through a 1 MΩ current-limiting resistor with a high-voltage DC power supply (Model BRC-5-400R, Universal Voltronics Corp, Mt. Kisco, NY). The resulting discharge current was ~2 mA. In all cases the DART helium flow was fixed at 2.5 L/min with a heater temperature of 300 °C.

For the LTP probe, a 1 mm diameter, grounded steel pin was placed inside a glass tube (1 cm i.d.) with a copper counter electrode placed on the outside of the tube. For details about this source, refer to Figure 5.3. The straight pin was positioned 3 mm from the front edge of the copper electrode. A dielectric barrier discharge was formed by flowing 700 mL/min of helium through the glass tube and applying a high voltage AC voltage to the copper electrode. The AC potential was supplied with a commercial ozone

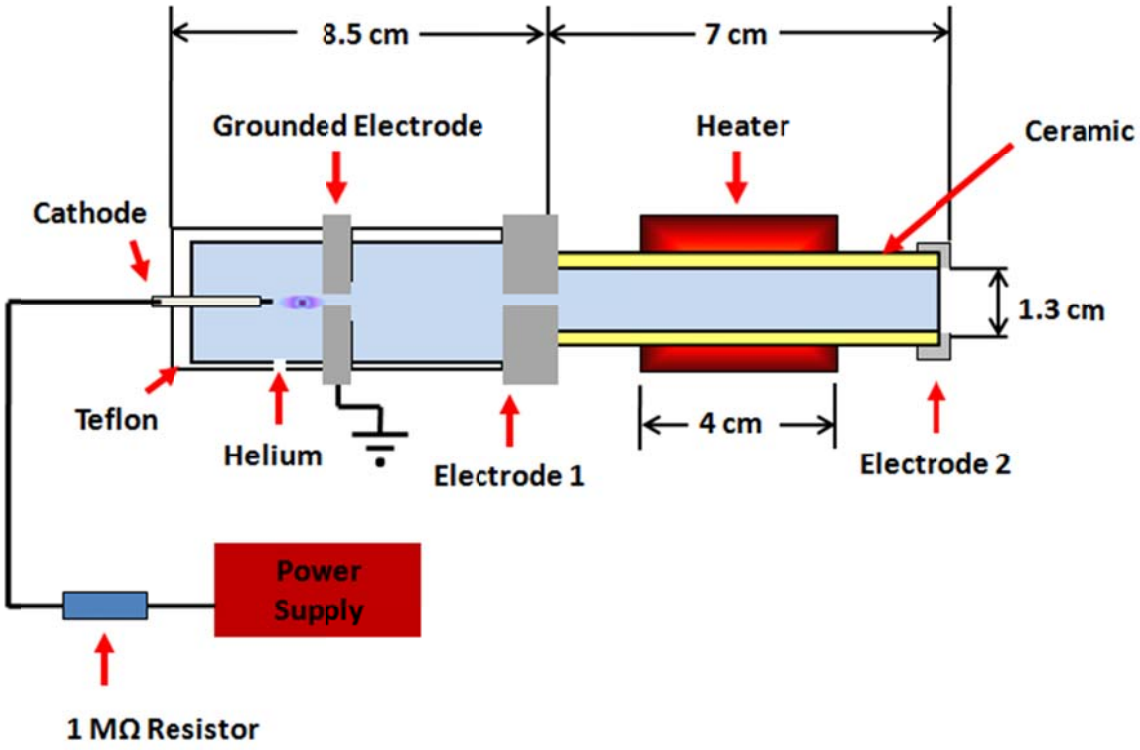

Figure 5.2 Diagram of the home-built DART source used in this study.

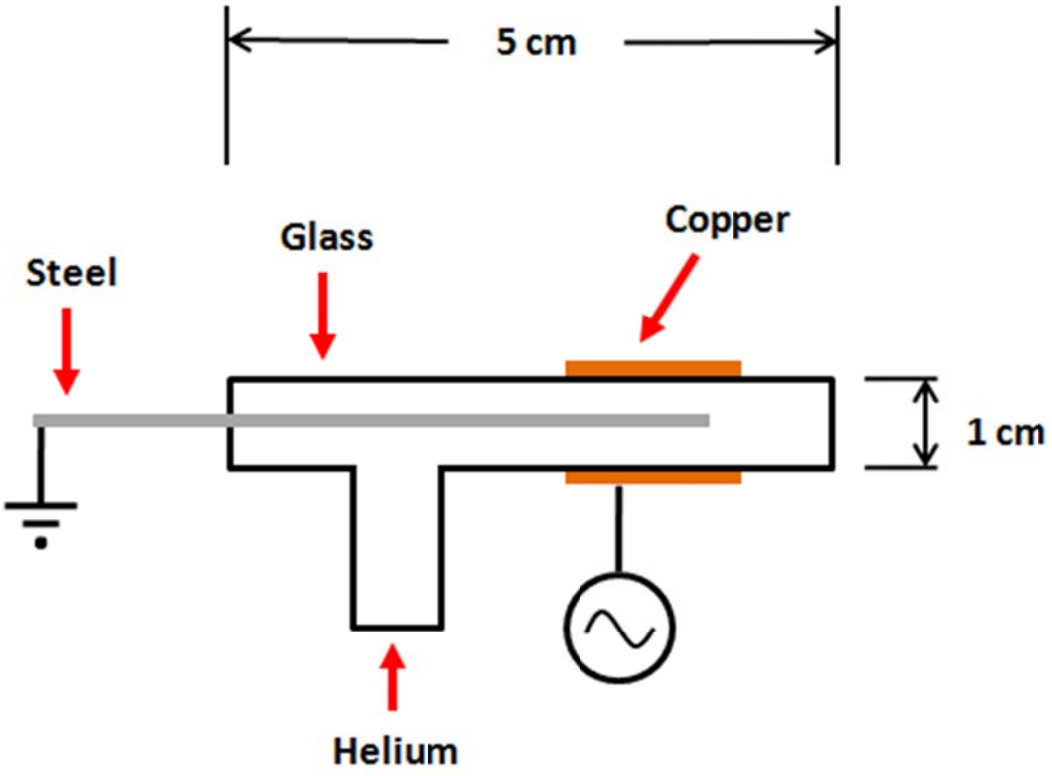

Figure 5.3 Diagram of the home-built LTP source used in this study.

generator power supply (Beijing Guoke Ozone Application Technology Co., Ltd., Beijing, China) with a peak-to-peak voltage of ~6 kV at a frequency of ~30 kHz.

5.2.3 Instrumentation

A schematic diagram of the system used to investigate ionization matrix effects is given in Figure 5.4. The ionization source of interest, DART, FAPA, or LTP, was positioned directly in front the inlet to the mass spectrometer. A continuous stream of gaseous analyte was introduced into a mixing tee, by means of a gas-tight syringe and syringe pump, after which the analyte was transferred by a 200 mL/min carrier stream of helium to the reaction zone between the ionization source and inlet to the mass spectrometer. A small plug of concentrated matrix vapor was then injected with a gas-tight syringe into a stirred round-bottom flask, so the matrix vapor concentration declined exponentially with time. The helium sweep gas enabled the matrix and analyte vapor to mix before being introduced into the ionization source. The flask, syringes, and transfer lines we all heated to ~40 °C to minimize adsorption.

Ions generated in the reaction zone were detected with a LECO HT Unique® (LECO Corp. St. Joseph, MI) time-of-flight (TOF) mass spectrometer. This instrument was designed for conventional APCI and ESI sources, so its vacuum system could not cope with the helium flow. Accordingly, an additional turbomolecular pump (V71, Varian, Inc., Lexington, MA) was added to the second stage of the vacuum system.

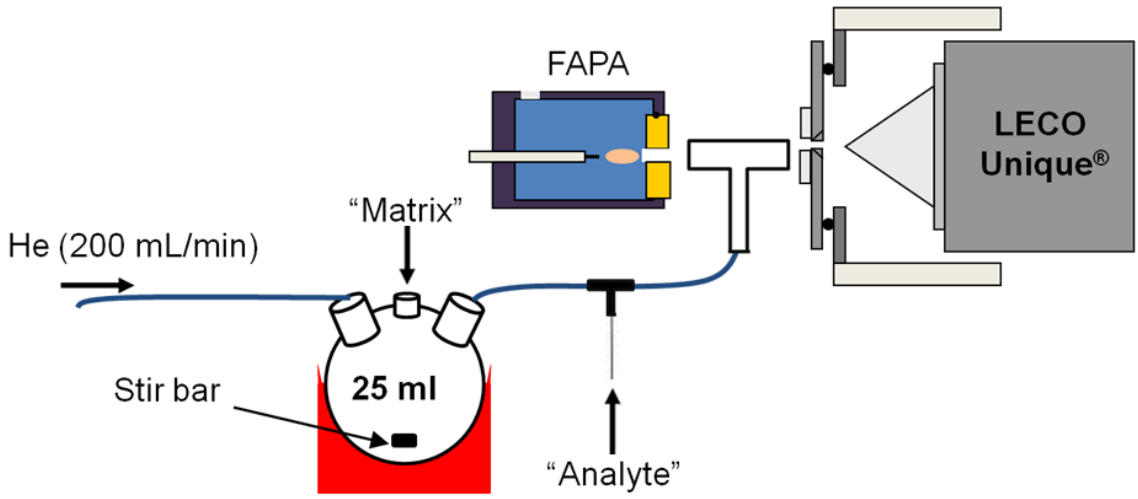

Figure 5.4 Arrangement to measure ion suppression with the FAPA, DART, and LTP sources. A constant stream of gaseous analyte is introduced into the ionization region, while a plug of matrix vapor is injected into the stirred round-bottom flask.

5.3 Results and Discussion

5.3.1 Direct Source Comparison

Because the three plasma-based ADI-MS ionization sources were coupled to the same sample-introduction system and mass spectrometer, their analytical performance could be directly compared. Headspace aliquots from four volatile substances, acetophenone, naphthalene, methyl salicylate, and triethyl phosphate, were introduced into each ion source at the same mass flow. The summed mass spectra corresponding to the introduction of 45 pmol of methyl salicylate into the FAPA, DART, and LTP sources are shown in Figures 5.5a, b, and c, respectively. The FAPA source yielded higher signal levels for all four gas-phase analytes. In particular, the vertical scales on the plots of Figure 5.5 show that FAPA produced signal levels five times greater than that from the other two sources. Interestingly, for the other three analytes, FAPA and LTP responses were more closely similar, with the differences in sensitivity being less than 80%.

It is apparent in the spectra of Figure 5.5 that there was a high degree of fragmentation of the analytes, which is not typically observed in ADI-MS. The detected fragments were identical to those obtained from performing collision-induced dissociation (CID) of the same molecules in an ion trap mass analyzer.[25] This type of fragmentation was also observed previously with this same modified TOF mass analyzer and was attributed to the mass spectrometer rather than to the ion source.[15]

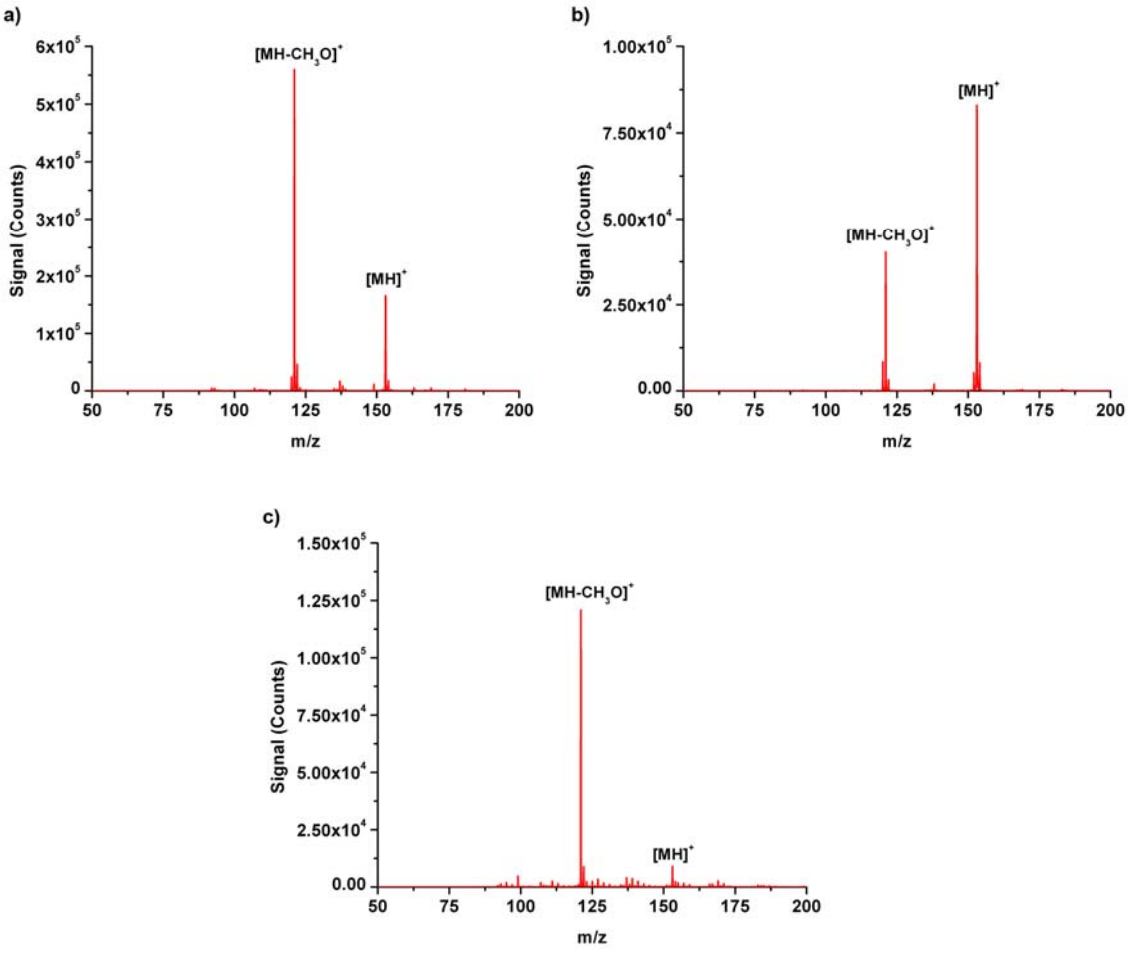

Figure 5.5 Mass spectra of methyl salicylate (MH^+ = 153) obtained with (a) FAPA, (b) DART, and (c) LTP ionization sources.

However, the relative signals from the parent and daughter ions were not equivalent for the three sources. This finding indicates that the source contributed to the fragmentation process, most likely from the internal energy imparted to the molecule by the ionization source. Furthermore, it is possible to compare the approximate, relative internal energies produced by FAPA, DART, and LTP because all other parameters were identical.

The energy deposited into a molecule by an ionization source, which dictates the softness or hardness of the ionization process, is directly related to the survival yield (SY).[26] The SY is calculated in the following manner,

$$SY = \frac{S(parent\ ion)}{S(parent\ ion) + \sum S(fragment\ ion)} \quad (4)$$

where s(parent ion) and s(fragment ion) are the mass spectral signals for the parent molecular ion and any fragment ions, respectively.

The energy distribution of the ions can be found if multiple fragments of known fragmentation energy exist. Because only a single fragment was observed here, a comparison of the SYs can provide information about only the relative softness of each source.

For methyl salicylate, the SYs for FAPA, DART, and LTP were calculated to be 22.8%, 67.3%, and 6.9%, respectively. These numbers suggest that there is a large variance in the energy imparted by these ionization sources, with DART being the softest

and LTP being the hardest. Furthermore, the same trend in SYs was observed for acetophenone and triethyl phosphate. The large difference in fragmentation energy could be related to the degree of direct plasma interaction with the analyte. In the home-built DART, the discharge was physically and electrically isolated from the sample introduction region, with only helium metastables purportedly interacting with the sample species. In the case of FAPA, the afterglow, which partially extends into the ionization region, has been shown to be an active plasma.[27] Lastly, the LTP has a direct plasma-analyte interaction, which would be capable of depositing not only thermal but also electrical energy into the ions. Additional experiments are being performed not only to validate this finding, but also to obtain the distribution of ion energies produced by each source.

5.3.2 Detection and Quantification of Ion Suppression

Although matrix effects can occur in both the desorption and ionization processes during plasma-based ADI-MS analyses (cf. Eqs. 1 and 3), this initial study was limited to the examination of signal suppression resulting from the ionization step. This goal was achieved by introducing gas-phase analytes and matrices into the ionization source separately. Substances were chosen based on their volatility as well as proton affinity. A list of the compounds along with their corresponding vapor densities and proton affinities is given in Table 5.1. As a point of reference, the proton affinity of the commonly detected reagent ion, hydronium ion (H_3O^+), is also cited.

The most likely cause of signal suppression for analytes ionized by proton transfer is competitive ionization with another substance of higher proton affinity (cf. Eq. 3).

Table 5.1. Substances used for studies on ion suppression, with corresponding vapor densities and proton affinities.

	Reagent, analyte, or matrix	Vapor density ($nmol/cm^3$)[a]	Proton affinity (kJ/mol)[b]
Hydronium ion	Reagent	-	691
Naphthalene	Matrix	11.1	802.9
Methyl salicylate	Matrix	3.49	855
Acetophenone	Analyte	19.4	861.1
Triethyl phosphate	Matrix	17.8	909.3

[a] Values calculated at 22 °C.

[b] Values measured at 25 °C.

To assess the importance of this kind of error, a continuous stream of a selected analyte, acetophenone in this case, was introduced into each ionization source. At a certain time, a plug of matrix vapor, methyl salicylate, naphthalene or triethyl phosphate, was introduced into a stirred round-bottom flask inserted in the same transfer line that carried the analyte vapor. Ion suppression was determined by monitoring the molecular ion signals for both the analyte and matrix. A drop in analyte signal upon introduction of a matrix vapor into the ionization source implies that ion suppression has taken place. Assuming that the competitive ionization process cited above is the predominant matrix-effect mechanism, a drop in analyte signal should be observed when the matrix has a higher proton affinity than the analyte.

An example of ion suppression observed for FAPA and DART is shown in Figure 5.6. In this case, the analyte, acetophenone, was introduced at a molar flow rate of 258 pmol/s with the total amount of matrix, triethyl phosphate, integrated over time being 17 nmol. It should be noted that the intial increase in analyte observed with the DART source was due to an instantaneous change in carrier gas flow rate with the introduction of the matrix vapor. Because the matrix had a much higher proton affinity than the analyte, a matrix effect would be expected because of competitive ionization. Indeed, a large decrease in analyte signal was clearly observed in this case for FAPA, DART, and LTP (not shown). It should also be noted that the LTP source suffered from complete analyte signal suppression upon introduction of the matrix. Also, the home-made DART source was more greatly affected (>70% suppression) by the triethyl phosphate matrix than was the FAPA (~50% suppression). The vertical scales on Figure 5.6 illustrate the difference in sensitivity between FAPA and DART.

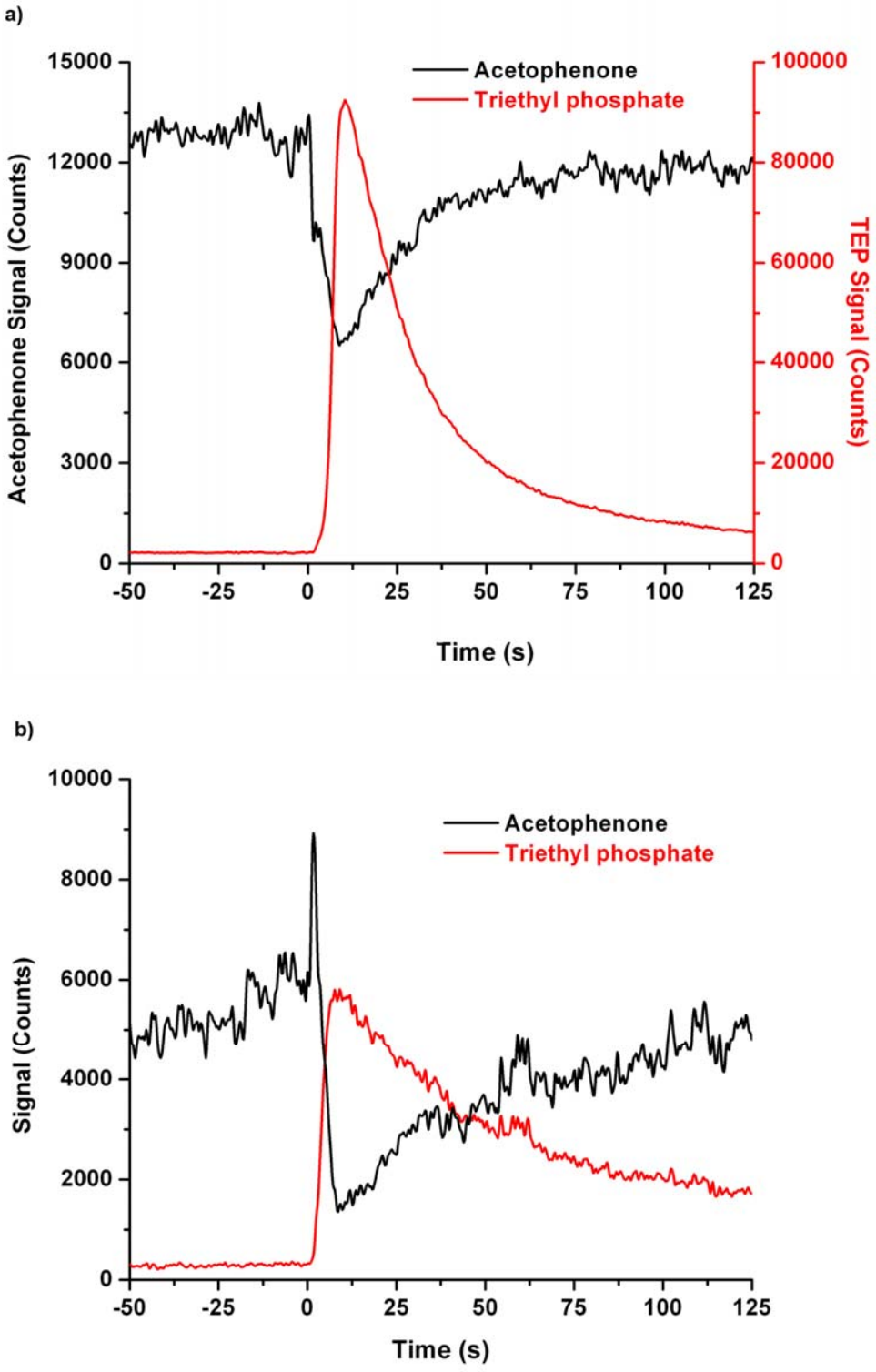

Figure 5.6 Suppression of acetophenone signal by a triethyl phosphate matrix for (a) FAPA and (b) DART.

Once a matrix effect was observed, the concentration of matrix vapor introduced into the system was determined by treating the introduction system as an exponential-dilution chamber. The concentration of matrix exiting the round-bottom flask, C(t), was determined from the well-stirred tank equation (Eq. 5),

$$C(t) = C_o \times \exp(-\frac{F}{V} \times t) \tag{5}$$

where C_o is the initial concentration of matrix vapor after its injection into the chamber, F is the carrier gas flow rate, V is the chamber volume, and t is the time after injection. The analyte signal suppression was then plotted as a function of varying matrix-to-analyte mole ratio to quantify the ion suppression.

Figure 5.7 shows the suppression of acetophenone signal by TEP for various matrix-to-analyte mole ratios. Because TEP has a higher proton affinity than acetophenone, it would be predicted by Eq. 3 that competitive ionization should take place for all three ionization sources. Indeed, analyte signal suppression was detected for all three. Remarkably, even at equimolar amounts of matrix and analyte, signal suppression of greater than 60% was observed for DART and LTP. In the analysis of a real-world sample, it is realistic to imagine that a substance with a higher proton affinity than the analyte would be present at levels similar to those investigated in this study. For all matrix-to-analyte ratios, the FAPA source was the least affected by the TEP matrix, which could be due to its higher operating power and consequently greater reagent-ion yields. Additionally, the FAPA source tolerated higher relative matrix amounts, indicating that it was overall the most robust in this situation.

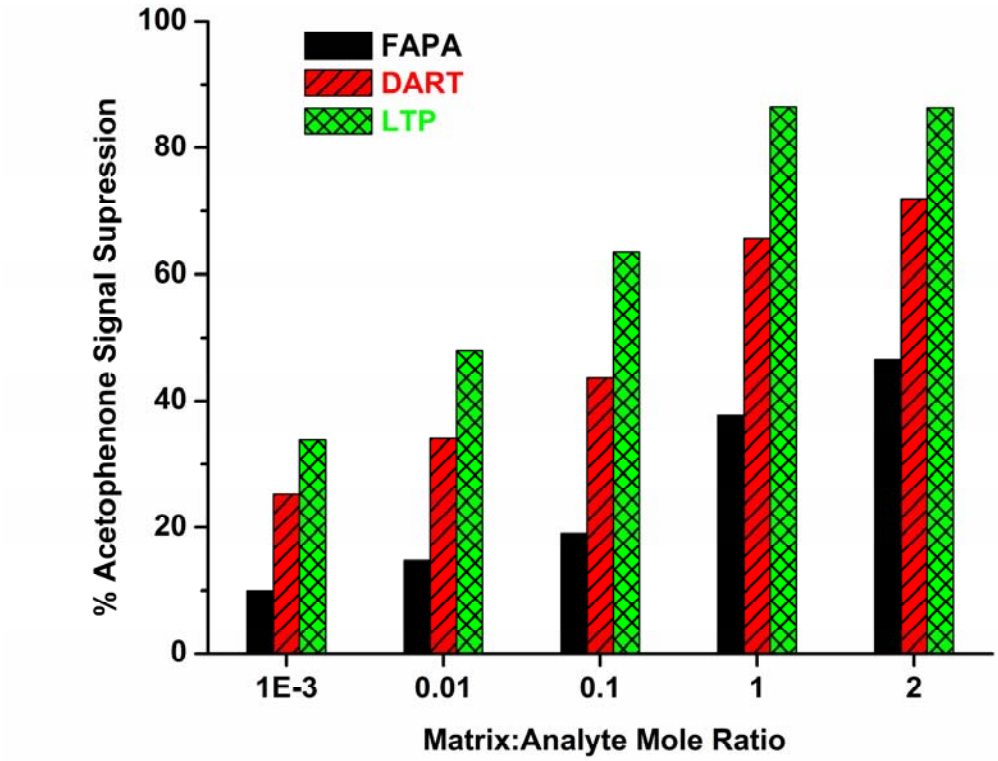

Figure 5.7 Quantification of acetophenone signal suppression during the introduction of a triethyl phosphate matrix for FAPA, DART, and LTP. A taller bar signifies a greater signal suppression.

In another example (cf. Figure 5.8), the acetophenone signal was monitored during the introduction of naphthalene, a matrix with a lower proton affinity,. In naphthalene, the proton affinity is low enough that the most commonly observed ion in its spectrum is probably formed through charge transfer with alternative reagent species such as NO^+ or N_2^+ rather than by proton transfer. Therefore, it would be predicted that no matrix effect should take place. Yet, naphthalene induced a suppression of the acetophenone ion for both FAPA and LTP. As in the previous example, less competitive ionization was observed for the FAPA source than the LTP. In contrast, the home-built DART source did not suffer any analyte signal suppression.

Because naphthalene does not likely ionize by proton transfer, the observed matrix effect could be due to a reduced formation of protonated water clusters needed to ionize the analyte (acetophenone). The formation of water clusters in these plasma-based ADI-MS is believed to be the same as in APCI, which is as follows,[5, 8-9]

$$N_2^+ + 2N_2 \rightarrow N_4^+ + N_2 \quad (6)$$

$$N_4^+ + H_2O \rightarrow H_2O^+ + 2N_2 \quad (7)$$

$$H_2O^+ + H_2O \rightarrow H_3O^+ + OH\cdot \quad (8)$$

$$H_3O^+ + H_2O + N_2 \rightarrow (H_2O)_2H^+ + N_2 \quad (9)$$

The naphthalene could ionize via charge transfer from either N_2^+ or H_2O^+, which would result in a decrease in protonated water clusters and, ultimately, in protonated acetophenone. In the case of LTP and FAPA, an active plasma region interacts with the sample and analytes, whereas the DART discharge is physically separated from the

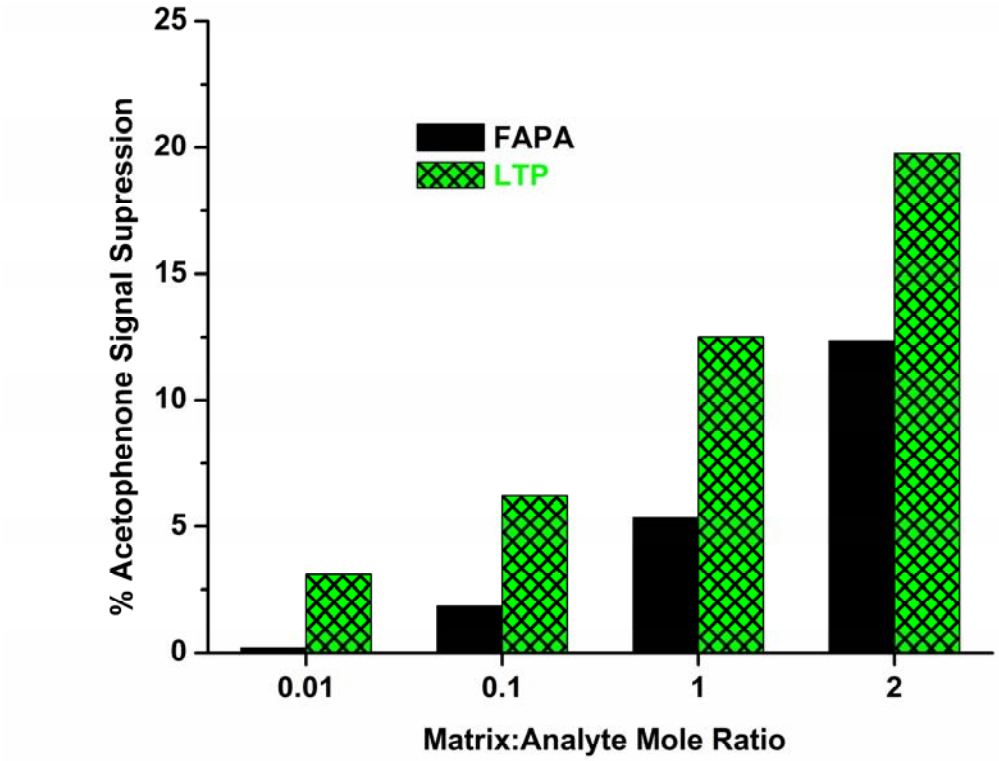

Figure 5.8 Quantification of acetophenone signal suppression by a naphthalene matrix for FAPA and LTP. A taller bar signifies a greater signal suppression. No matrix effect was detected for DART for this matrix/analyte combination.

ionization region, preventing efficient quenching of this reaction from occurring. This hypothesis is currently being tested and will be the focus of future publications.

By utilizing matrices of varying proton affinity with respect to the analyte, the plasma-based ionization sources can be compared. In an ideal proton source, a matrix effect would be observed only if the matrix had a higher proton affinity than the analyte (Eq. 3). Table 5.2 summarizes the cases in which analyte signal suppression was observed for FAPA, DART, and LTP. The sources are ranked based on their susceptibility to ion suppression, with 1 being the most affected and 3 the least.

Interestingly, the only case in which no matrix effect was observed with the DART was when the proton affinity of the analyte was greater than that of the matrix. This finding implies that, under the chosen operating conditions, the home-built DART source behaves as an ideal proton source. Ultimately, these findings suggest that DART would be the preferred ionization source for the quantitative analysis of basic analytes as it does not suffer from ionization matrix effects.

However, in the cases in which the matrix had a similar or higher proton affinity than the analyte, the FAPA source exhibited the least amount of signal suppression. These findings suggest that the FAPA source is more resistant to competitive ionization and would be the best option for quantitative analyses from complex samples where matrix constituents and/or their corresponding proton affinities are unknown.

Table 5.2. Order of susceptibility of ionization sources to matrix effects under different combinations of matrix-analyte proton affinity. A ranking of 1 indicates the source that was most prone, 3 the least, and X represents no detected matrix effect.

	$PA_A > PA_M$	$PA_A \approx PA_M$	$PA_A < PA_M$
FAPA	2	3	3
DART	X	2	2[a]
LTP	1	1[a]	1[a]

[a] No analyte signal detected with matrix-to-analyte mole ratio of 10.

5.4 Conclusions

Ionization matrix effects were investigated for three plasma-based ADI-MS sources: FAPA, DART, and LTP. All sources exhibited analyte ion suppression when the matrix had a higher proton affinity than the analyte, even at equal molar quantities of matrix and analyte. In most cases, the FAPA was more resistant to competitive ionization, likely owing to its higher power and ion current. It was also observed that analyte signals could be entirely suppressed at matrix-to-analyte mole ratios of less than 10 with the LTP and DART.

These findings demonstrate the severity that matrix effects unknowingly have in ambient mass spectrometric analyses. Furthermore, because only the ionization process was considered in this study, matrix effects in desorption/ionization analyses of solids is almost certainly more severe and will be the focus of future studies. It will be essential for the ambient mass spectrometry community to recognize the influence that matrix effects have not only on quantification but also detection of analytes from complex systems. Future studies should and will be focused on understanding ion suppression phenomena and methods to overcome these matrix effects with minimal impact on sensitivity and analysis time.

References

1. Cooks, R. G.; Ouyang, Z.; Takats, Z.; Wiseman, J. M. *Science* **2006**, *311*, 1566-1570.
2. Venter, A.; Nefliu, M.; Cooks, R. G. *Trends Anal. Chem.* **2008**, *27*, 284-290.
3. Van Berkel, G. J.; Pasilis, S. P.; Ovchinnikova, O. *J. Mass Spectrom.* **2008**, *43*, 1161-1180.
4. Takats, Z.; Wiseman, J. M.; Gologan, B.; Cooks, R. G. *Science* **2004**, *306*, 471-473.
5. Cody, R. B.; Laramee, J. A.; Durst, H. D. *Anal. Chem.* **2005**, *77*, 2297-2302.
6. Ratcliffe, L. V.; Rutten, F. J. M.; Barrett, D. A.; Whitmore, T.; Seymour, D.; Greenwood, C.; Aranda-Gonzalvo, Y.; Robinson, S.; McCoustra, M. *Anal. Chem.* **2007**, *79*, 6094-6101.
7. Na, N.; Zhao, M.; Zhang, S.; Yang, C.; Zhang, X. *J. Am. Soc. Mass. Spectrom.* **2007**, *18*, 1859-1862.
8. Harper, J. D.; Charipar, N. A.; Mulligan, C. C.; Zhang, X. R.; Cooks, R. G.; Ouyang, Z. *Anal. Chem.* **2008**, *80*, 9097-9104.
9. Andrade, F. J.; Shelley, J. T.; Wetzel, W. C.; Webb, M. R.; Gamez, G.; Ray, S. J.; Hieftje, G. M. *Anal. Chem.* **2008**, *80*, 2646-2653.
10. Nyadong, L.; Galhena, A. S.; Fernandez, F. M. *Anal. Chem.* **2009**, *81*, 7788-7794.
11. Andrade, F. J.; Shelley, J. T.; Wetzel, W. C.; Webb, M. R.; Gamez, G.; Ray, S. J.; Hieftje, G. M. *Anal. Chem.* **2008**, *80*, 2654-2663.
12. Yu, S.; Crawford, E.; Tice, J.; Musselman, B.; Wu, J.-T. *Anal. Chem.* **2008**, *81*, 193-202.

13. Yang, S.; Ding, J.; Zheng, J.; Hu, B.; Li, J.; Chen, H.; Zhou, Z.; Qiao, X. *Anal. Chem.* **2009**, *81*, 2426-2436.

14. Huang, G. M.; Zheng, O. Y.; Cooks, R. G. *Chem. Commun.* **2009**, 556-558.

15. Shelley, J. T.; Ray, S. J.; Hieftje, G. M. *Anal. Chem.* **2008**, *80*, 8308-8313.

16. Jessome, L. L.; Volmer, D. A. *Lc Gc N. Am.* **2006**, *24*, 498-+.

17. King, R.; Bonfiglio, R.; Fernandez-Metzler, C.; Miller-Stein, C.; Olah, T. *J. Am. Soc. Mass. Spectrom.* **2000**, *11*, 942-950.

18. Sangster, T.; Spence, M.; Sinclair, P.; Payne, R.; Smith, C. *Rapid Commun. Mass Spectrom.* **2004**, *18*, 1361-1364.

19. Nicol, G.; Sunner, J.; Kebarle, P. *Int. J. Mass Spectrom. Ion Processes* **1988**, *84*, 135-155.

20. Chen, H. W.; Wortmann, A.; Zenobi, R. *J. Mass Spectrom.* **2007**, *42*, 1123-1135.

21. Chen, H. W.; Zenobi, R. *Nat. Protoc.* **2008**, *3*, 1467-1475.

22. Shelley, J. T.; Wiley, J. S.; Chan, G. C. Y.; Schilling, G. D.; Ray, S. J.; Hieftje, G. M. *J. Am. Soc. Mass. Spectrom.* **2009**, *20*, 837-844.

23. Harris, G. A.; Fernandez, F. M. *Anal. Chem.* **2008**, *81*, 322-329.

24. U.S. Pat. 7,112,785 B2, 2006.

25. Shelley, J. T.; Hieftje, G. M.

26. Nefliu, M.; Smith, J. N.; Venter, A.; Cooks, R. G. *J. Am. Soc. Mass. Spectrom.* **2008**, *19*, 420-427.

27. Schilling, G. D.; Shelley, J. T.; Broekaert, J. A. C.; Sperline, R. P.; Denton, M. B.; Barinaga, C. J.; Koppenaal, D. W.; Hieftje, G. M. *J. Anal. At. Spectrom.* **2009**, *24*, 34-40.

Chapter 6

Spectroscopic Plasma Diagnostics on a Low-Temperature Plasma Probe for Ambient Mass Spectrometry

6.1 Introduction

Ambient desorption/ionization mass spectrometry is a relatively new field that combines the selectivity and sensitivity of mass spectrometry with direct, ambient analysis of samples with little or no pretreatment.[1] This goal is often achieved with a single ionization source, which is capable of desorbing or extracting analytes from the solid or liquid phase prior to the ionization step. For example, sources such as Desorption ElectroSpray Ionization (DESI)[2] and the Liquid Micro-Junction Surface-Sampling Probe (LMJ-SSP)[3] utilize a micro- or macro- liquid-extraction event, respectively, to probe the sample followed by ionization, typically through electrospray-based processes. Interestingly, over half of the published ambient desorption/ionization

sources incorporate an electrical discharge to generate excited species that are then used for desorbing and/or ionizing molecules from a sample. The first such source presented in the literature was Direct Analysis in Real Time (DART)[4], which incorporates a direct-current (DC) corona-like discharge most often sustained in helium.[5] Other DC discharges that have been used for ambient mass spectrometry include a helium atmospheric-pressure glow discharge, in the form of the Flowing Atmospheric-Pressure Afterglow (FAPA)[6-7], and a true corona discharge in nitrogen, as illustrated by the Atmospheric-pressure Solids Analysis Probe (ASAP)[8] and Desorption Atmospheric-Pressure Chemical Ionization (DAPCI).[9]

Various forms of alternating-current (AC) discharges have also been exploited as ambient desorption/ionization sources. Plasma-Assisted Desorption/Ionization (PADI)[10] utilizes a radio-frequency glow discharge, often in helium, between a pin electrode and the sample or the mass spectrometer (MS) inlet, which serves as the counter electrode. Dielectric-Barrier Discharge Ionization (DBDI)[11] employs a capacitively coupled discharge between a pin and a plate, with the sample positioned on a dielectric substrate placed between the electrodes. Although the DBDI operates at low gas flow rates, less than 100 mL/min, it results in a higher degree of analyte fragmentation than has been observed with other plasma-based sources. Furthermore, placing the sample directly within the discharge likely alters the characteristics of the plasma, which could ultimately lead to limited reproducibility, matrix effects, and degraded sensitivity.

For these reasons, another dielectric-barrier discharge was configured in which the main discharge was physically isolated from the sampling region. The

Low-Temperature Plasma (LTP) probe[12], as it has been termed, uses a concentric electrode arrangement with a glass tube serving as the dielectric. In this design, the sample is placed within the plasma plume, termed the afterglow, emanating from the tube. Advantages of this geometry include the ability to analyze any surface regardless of its shape or size, low power consumption (less than 2 W), and high sensitivity.

Although numerous publications have focused on basic descriptions and applications of these plasma-based ambient desorption/ionization sources, few fundamental examinations have appeared on either the desorption/ionization processes they employ or even the nature of the discharges. Two papers have suggested possible mechanisms for negative-ion formation by DART, by comparing spectra of a large suite of compounds with those produced by Atmospheric-Pressure Chemical Ionization (APCI) and Atmospheric-Pressure PhotoIonization (APPI).[13-14] Similarly, Cody[15] explored methods to alter the gas-phase ion chemistry of DART, which enabled detection of saturated hydrocarbons that do not ionize readily under customary operating conditions. In another fundamental mass spectrometric study, Shelley et al.[16] examined the level of ionization matrix effects for FAPA, LTP, and DART based on differences in analyte proton affinity. Andrade et al.[17] outlined the current-voltage behavior and performed a thorough optical spectroscopic investigation of the He-APGD, which ultimately led to the development of the FAPA. Shelley et al.[5] compared discharges similar to those employed by DART and FAPA through optical and mass spectrometric methods.

Optical characterization of the discharges employed in plasma-based ambient-ionization sources can yield insight into the plasma reactions taking place, which can then directly be used to determine factors affecting desorption and mechanisms involved in analyte ionization. This information is essential not only for a better understanding of the mechanisms by which plasma-based ambient desorption/ionization sources operate, but also for optimization of their performance for mass spectrometric analyses.

In the present study, the dielectric-barrier discharge and afterglow of the LTP probe were characterized by means of optical spectroscopy. Plasma parameters that were measured include the electron number density (n_e) and rotational temperature (T_{rot}). The spatial dependence of reactive species present in the plasma was also determined, which aided in deducing the origin of background ions commonly observed in mass spectrometric analyses. These findings were then used to explain the behavior and processes that were previously reported for mass spectral analyses with the LTP probe.

6.2 Experimental

6.2.1 Construction and Operation of the LTP Probe

A schematic diagram of the experimental setup is given in Figure 6.1. The LTP probe (cf. Figure 6.1) utilized a Pyrex® glass tube (o.d. 6.4 mm and i.d. 3.8 mm) as the dielectric barrier between two electrodes. A central, coaxial, stainless-steel pin electrode (o.d. 1.6 mm) was grounded while a high-voltage, AC waveform was applied to a 2.5-cm long copper, ring electrode. The AC waveform was generated by gating a DC potential through the primary winding of an automobile ignition coil (Model 8140C, Accel,

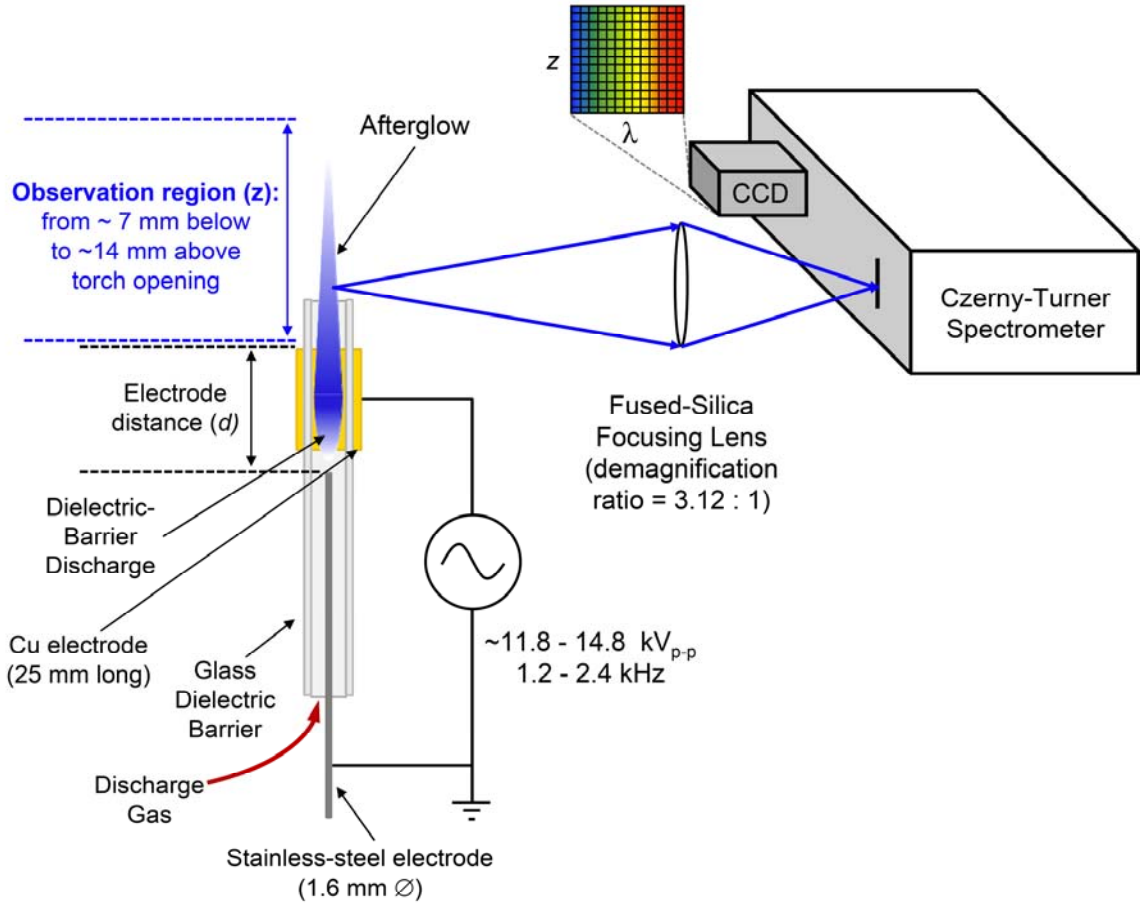

Figure 6.1 Schematic diagram of the experimental setup. Listed electrode gaps of the LTP probe are taken as the lateral distance between the edge of the 2.5-cm long copper electrode near the torch opening and the tip of the pin counter electrode. Smaller gaps result in larger capacitances. The discharge tube was made of Pyrex® with o.d. 6.4 mm and i.d. 3.8 mm; the stainless-steel center electrode had a diameter of 1.6 mm.

Cleveland, OH) by means of a MOSFET. The resulting power supply can produce 11.8-14.8 kV_{p-p} at an adjustable frequency of 1.2-2.4 kHz, without a capacitive load. The total power consumption of the ionization source was typically less than 2 W. Either helium (99.999% ultra-high purity, Airgas, Radnor, PA) or argon (boil-off from cryogenic liquid container, Airgas, Radnor, PA) was used as the discharge gas at flow rates between 0.40 and 1.60 L/min. A perfluoroalkoxy (PFA) Swagelok® tee was used to couple the stainless-steel grounded electrode, glass tube, and gas-transfer tubing for the discharge gas. The distance between the grounded and AC electrodes (labeled *d* in Figure 6.1), which was varied in one study, corresponds to the distance between the tip of the pin and the edge of the copper ring electrode nearest the exit of the probe (i.e., a distance of zero corresponds to the greatest capacitance between the electrodes).

6.2.2 Spectroscopic Measurements

Spectroscopic measurements were performed on a commercial spectrometer ordinarily used for inductively coupled plasma (ICP) atomic emission spectroscopy (ACTIVA, Horiba–Jobin Yvon, Longjumeau, France), but with two in-house modifications. First, the original ICP torch housing was removed from the instrument and the LTP probe was mounted vertically on a 3D translation stage for fine positional adjustment of the source. Second, the original entrance optics of the ACTIVA spectrometer were replaced by a single, fused-silica converging lens (100 mm focal length) attached to a 1D translation stage. An adjustable iris was mounted on the front of the lens to match the f/no. (f/8.5) of the spectrometer. The advantage of the ACTIVA spectrometer in this application is that it combines a Czerny-Turner grating configuration

and a two-dimensional charge-coupled device (CCD) detector, enabling simultaneous measurement of the entire vertical emission profile of the plasma over a defined spectral range (i.e., the *x*-axis of the CCD detector corresponds to wavelength and the *y*-axis to vertical location in the plasma). In addition, the spectrometer is equipped with two long-pass wavelength filters with cutoffs at 310 nm and 510 nm. The appropriate filter was automatically inserted into the optical path to reject emission from second and higher grating orders.

The image of the LTP was demagnified by a ratio of 3.12:1, enabling a maximum simultaneously observable height of 21.5 mm. Because emission from the LTP discharge was weak, long exposure times (e.g., 1 minute) were typically needed. To further improve light throughput and enhance the signal-to-noise ratio, the entrance slit was widened to 20 μm, resulting in a spectral resolution of 13.7 pm full-width at half maximum (FWHM), which was adequate for all species examined. Furthermore, CCD data corresponding to the vertical axis of the plasma were either software-binned in groups of 4 when spatial resolution was required or fully binned by the hardware when such information was not needed. Processing of raw CCD data was carried out with in-house written software. Emission intensities were obtained by integrating the area under each spectral peak with background subtraction taken from nearby pixels.

Because of the relatively small size of the LTP probe (3.8 mm i.d.), alignment of the LTP torch with the entrance optics was particularly critical and performed daily or whenever the source was physically touched (e.g., when the pin-electrode distance was adjusted). Alignment was achieved by setting the spectrometer to zero order and moving

the torch housing laterally for maximum emission intensity. For spatial calibration, the location of the upper edge of the LTP torch on the CCD was determined by monitoring light from a laser diode that was scattered from the tip of the plasma torch. Under typical operating conditions, the plasma extended less than 15 mm beyond the exit of the LTP torch. The tip of the plasma torch was set at a vertical position such that ~ 7 mm of the plasma within the torch was imaged onto the CCD, in addition to the full plasma extending beyond the torch opening (i.e. the afterglow). Once the LTP probe was aligned with the spectrometer and under fixed conditions, the stability of the discharge and emission was quite good over time, with relative standard deviations below 5%. However, altering source parameters, such as electrode distance, changed the efficiency of power coupling to the plasma, which altered overall emission intensities.

6.3 Results and Discussion

6.3.1 Spectroscopic Characteristics and Identification of Plasma Species in the He-LTP

Identification of plasma species helps to shortlist the candidates that are likely involved in the ionization of analyte species; in addition, it provides information on which thermometric species are readily available for further plasma diagnostics (e.g., measurement of various temperatures and electron number density). Figure 6.2 shows a UV-visible emission spectrum, integrated along the entire vertical axis of the He-LTP probe. The helium flow rate was 1.60 L/min with a gap between the inner and the outer electrodes of 9.0 mm. Strong emission from molecular species, such as OH, N_2, N_2^+, as well as from atomic species, like He I, H I and O I, was readily observable. Plasma

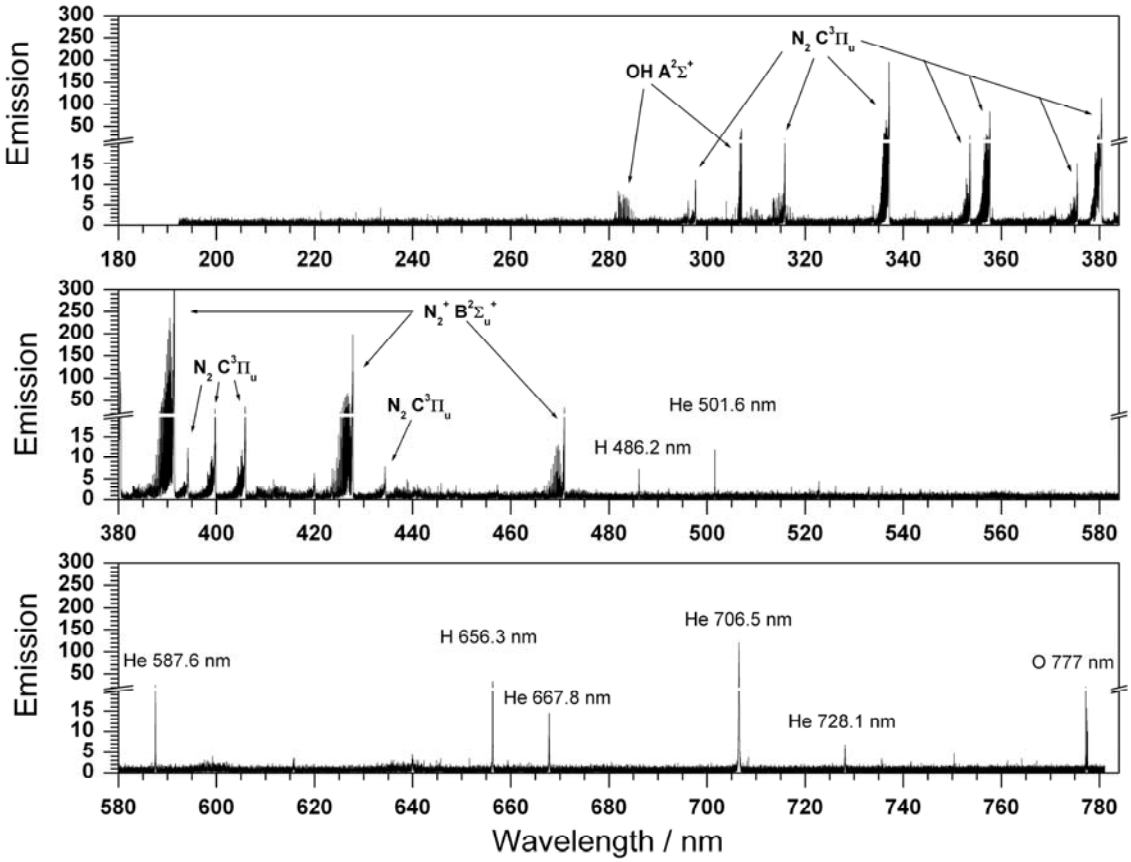

Figure 6.2 UV-visible emission spectrum obtained from the He-LTP probe with a helium flow rate of 1.60 L min^{-1}. Major atomic lines and molecular bands have been labeled for easy identification. Note the break in the vertical axis.

species found in the LTP probe were quite similar to those seen with other types of helium-DBDs operated at atmospheric pressure (AP).[18-19] Interestingly, emission from the molecular species NO was not detected, whereas it has occasionally been observed in other AP helium DBDs.[20] From this survey of emitting plasma species, it is clearly possible to determine rotational temperatures from the structure of OH emission features, and electron number densities from the Stark broadening of H_β and He emission lines; these measurements will be presented in later sections.

6.3.2 Spatial Distribution of Emission from He-LTP

Figure 6.3 shows normalized emission maps of selected atomic and molecular species in the LTP. In these figures, the zero position refers to the edge of the plasma torch, with positive positions extending outside the torch into the open atmosphere. Signals for atomic hydrogen and oxygen appear noisy due to their weak emission and, presumably, low abundance in the plasma. There are a few interesting observations: First, the maximum emission for He (the plasma gas), H, O, and molecular OH occurred inside the torch, whereas the maximum emission for both N_2 and N_2^+ appeared in the open atmosphere. Second, the shape of the emission profiles for N_2 and N_2^+ were similar but were spatially shifted, with the maximum in N_2 occurring farther downstream from the powered electrodes than N_2^+. Additionally, little N_2 emission was detected within the plasma torch, except near the edge open to atmosphere, whereas significant N_2^+ was observed for all measured regions inside the plasma torch., Because the emission of both nitrogen molecular species decayed from the torch edge inwards, we believe that nitrogen species observed in these emission studies, as well as those previously recorded in

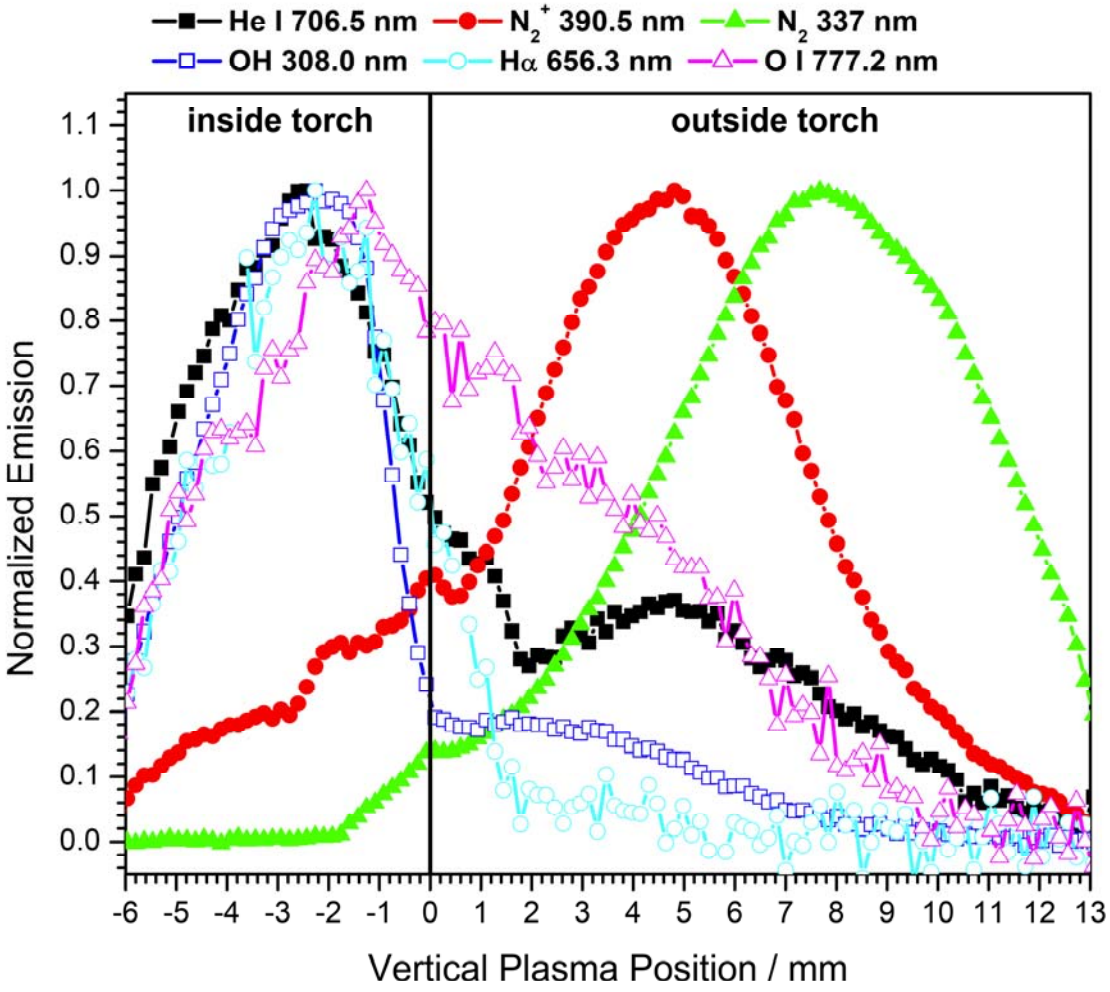

Figure 6.3 Normalized vertical emission profile of He I, N_2^+ ($B\ ^2\Sigma_u^+ - X\ ^2\Sigma_g^+$, the first negative system), O I, OH ($A\ ^2\Sigma^+ - X\ ^2\Pi$), H_α, and N_2 ($C\ ^3\Pi_u - B\ ^3\Pi_g$, the second positive system) in the He-LTP with a gas flow rate of 1.60 L/min.

mass-spectral investigations of similar ionization sources[5, 15], result from atmospheric nitrogen diffusing into the ionization source rather than from impurities in the gas supply. Third, approximately 4 mm outside the plasma torch, a local maximum existed for He I emission that directly coincides with the peak emission of N_2^+. Fourth, the majority of atomic hydrogen emission was confined within the plasma torch whereas emission from atomic oxygen extended to about 8 mm beyond the torch.

Because both N_2^+ and N_2 emission signals attained their maxima 5 mm and 8 mm, respectively, outside the plasma torch, it is logical to deduce that the dominant mechanism of excitation for both species is *not* through electron impact. There are two reasons for this deduction. First, electron-impact energy transfer, resulting in either excitation or ionization, is generally non-selective. Emission from N_2^+ was detected even -6 mm inside the edge of the torch, whereas there was no significant emission from N_2 from -6 mm to -2 mm, where the electron density and energy are expected to be highest. It has been shown that electron-impact excitation of nitrogen results in at least ten times stronger emission from N_2 ($C\ ^3\Pi_u$, the second positive system) than from N_2^+ ($B\ ^2\Sigma_u^+$, the first negative system).[21-22] This finding alone suggests that little or no nitrogen excitation occurs through electron-impact. Second, the spatial shift of N_2 emission relative to that of N_2^+ implies that the excited N_2 molecules might be formed via recombination of N_2^+ with an electron. This spatial shift between N_2 and N_2^+ emission was observed for all LTP gas flow rates examined.

In contrast, a plausible mechanism for the formation of N_2^+ is through Penning ionization from excited-state helium, as suggested in previous studies on similar

plasmas.[12, 19] The coincidence of the peak emission maxima for N_2^+ and He located 5 mm outside the torch further suggests a correlation between these two species. As will be discussed in detail in another paper[23], charge transfer from He_2^+ ion is a significant mechanism for the production of N_2^+ outside the LTP torch, while at the same time, the dissociative recombination of He_2^+ with an electron gives rise to excited helium species.

6.3.3 Influence of Plasma-Gas Flow on Spatially Resolved Emission Features in the He-LTP

Figure 6.4a shows spatially resolved emission profiles of the He I 706.52 nm line at helium flows from 0.40 to 1.60 L/min. The intensities in Figure 6.4 are not normalized, and therefore are directly comparable to each other for all flow rates. Helium atomic emission intensities, for all studied flow rates, were very similar within the LTP torch whereas a second emission maximum was observed outside the torch for flow rates between 1.20 and 1.60 L/min. In addition, the intensity, as well as the length of detectable helium emission, which corresponds to the length of the afterglow plume, increased with plasma-gas flow rate. At a helium flow of 1.60 L/min, He I emission was still measurable 11 mm beyond the torch, whereas at 0.40 L/min, helium emission did not extend past 3 mm. Similar observations were noted for other He I emission lines. These findings imply that a greater concentration of high-energy helium species, which are ultimately responsible for reagent-ion formation, can be produced outside of the torch simply by increasing the helium flow rate. It has been postulated that these helium species could be responsible for analyte desorption through chemical sputtering at the sample surface.[4, 10] Accordingly, the optimal position for sample introduction can be tuned by adjusting the flow rate.

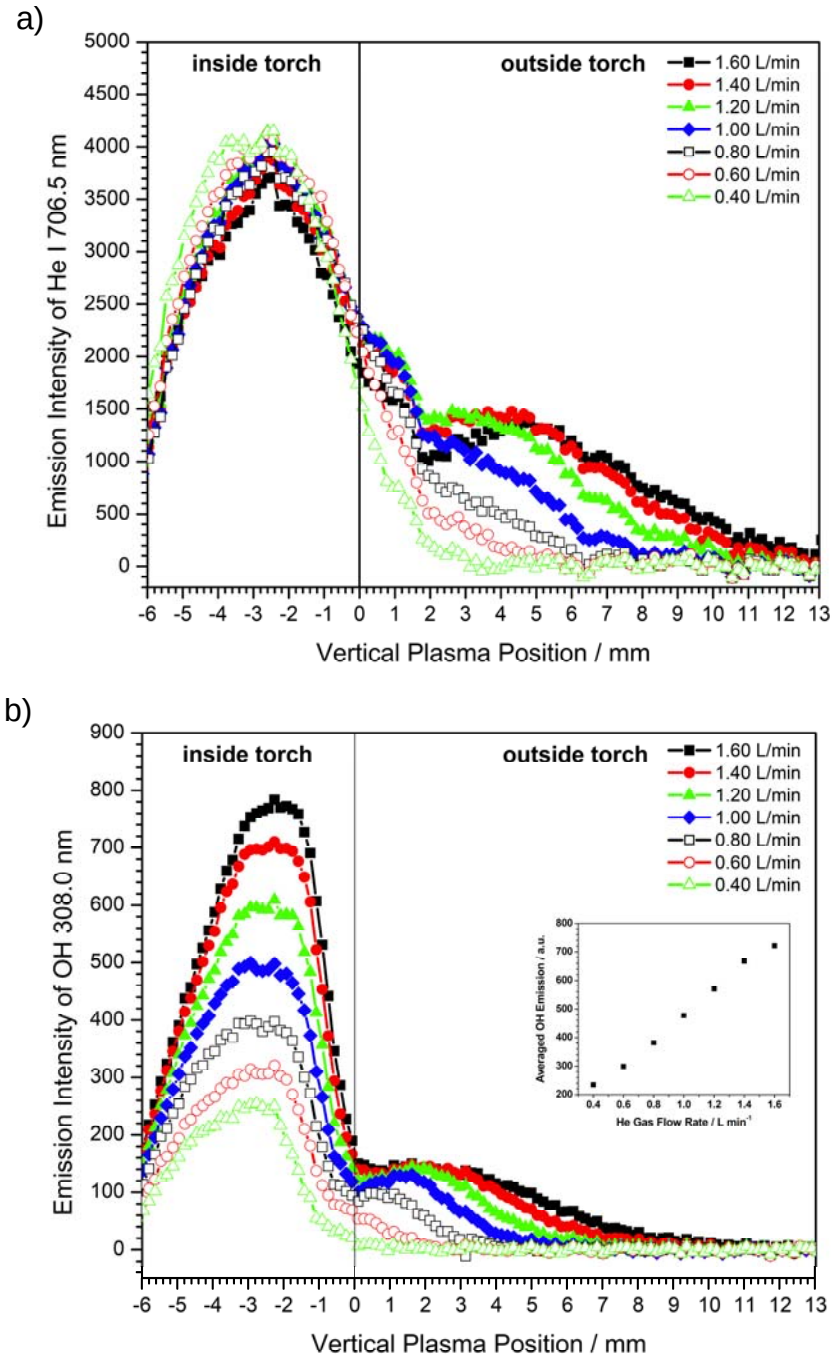

Figure 6.4ab Vertical emission profiles of (a) He I 706.5 nm and (b) OH 308.0 nm in the He-LTP for a variety of plasma gas (He) flow rates. Inset in (b) shows the spatially averaged OH 308.8 nm emission from -4 to -2 mm from the exit of the LTP torch.

c)

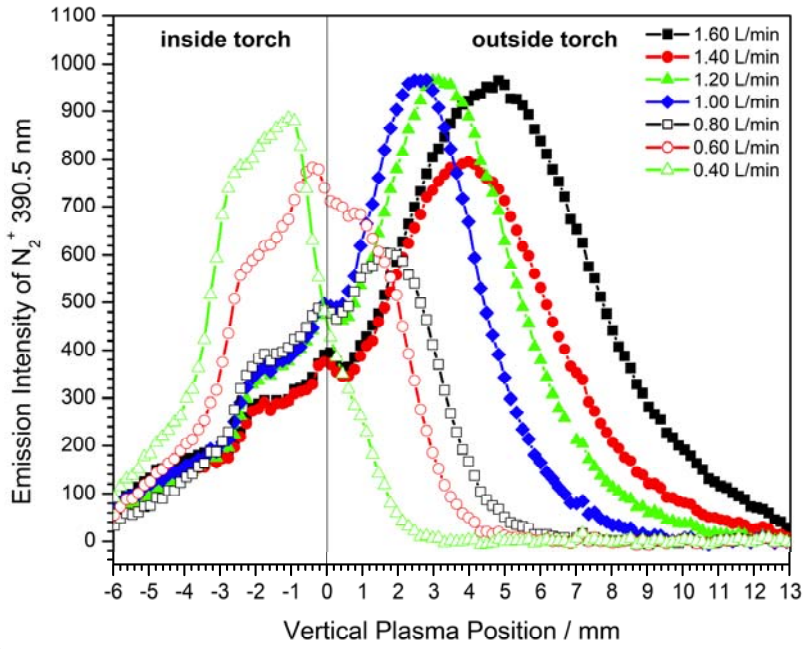

d)

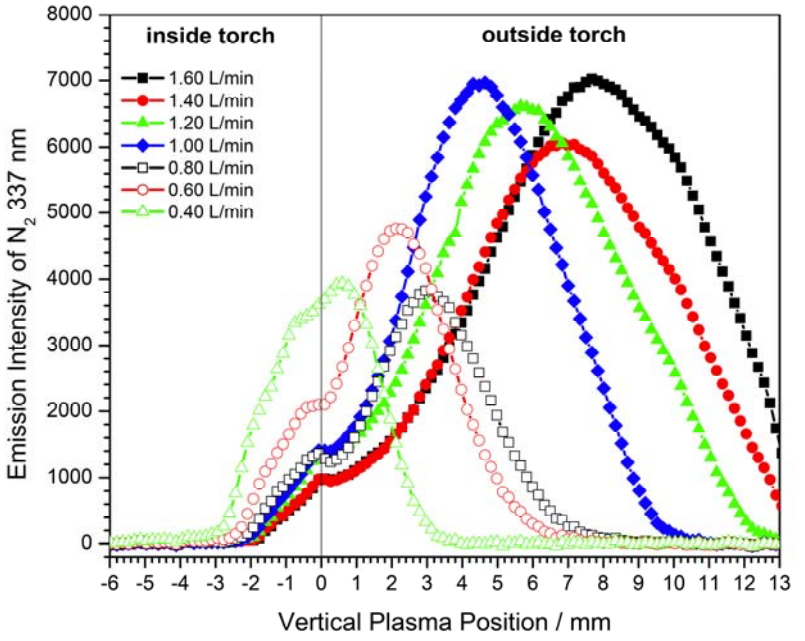

Figure 6.4cd Vertical emission profiles of (c) N_2^+ 390.5 nm and (d) N_2 337 nm in the He-LTP for a variety of plasma gas (He) flow rates.

e)

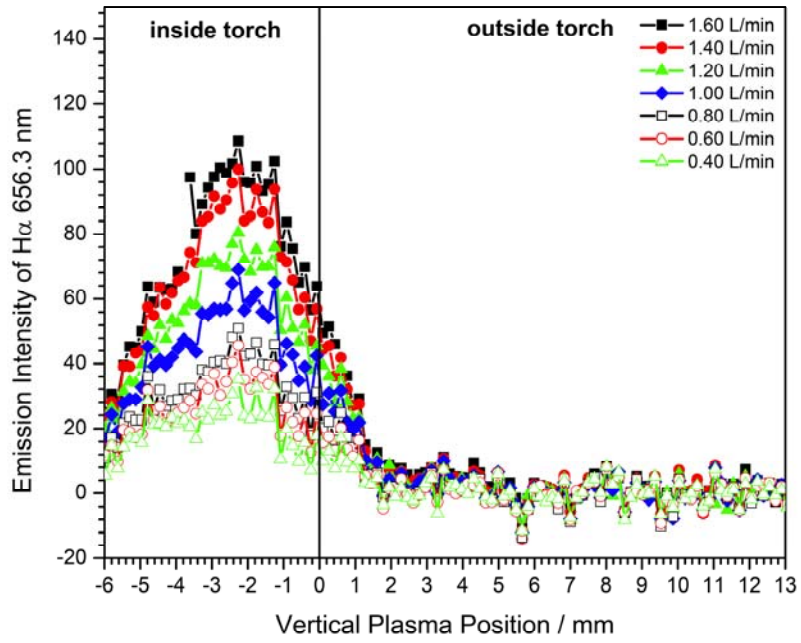

f)

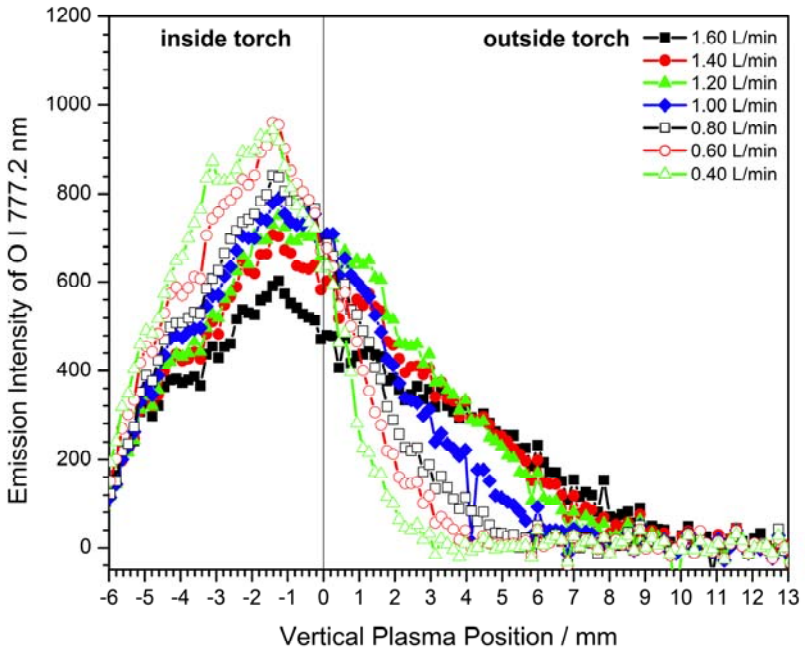

Figure 6.4ef Vertical emission profiles of (e) H_α 656.3 nm and (f) O I 777.2 nm in the He-LTP for a variety of plasma gas (He) flow rates.

Figure 6.4b shows the spatial emission pattern of the OH molecular emission band head at 308.0 nm. In contrast to He I emission, OH emission inside the LTP torch was strongly dependent on, and monotonically increased with, the helium flow rate. This observation is seemingly counter-intuitive because the helium emission profiles (cf. Figure 6.4a) suggest that the energetics of the plasma inside the torch were nearly independent of plasma-gas flow rate; additionally, diffusional penetration of atmospheric water vapor, the most likely candidate for the source of OH emission, should be lowest at the highest helium flow. Conversely, emission from N_2 and N_2^+ inside the plasma torch exhibited the opposite behavior (cf. Figures 6.4c and 6.4d), which suggests that atmospheric diffusion was the major source of N_2 in the discharge. From these data, the trend in OH emission intensity is likely due to water contamination in the gas supply. Given the high purity of helium used for the plasma gas, the water is likely adsorbed onto the walls of the polyethylene gas-transfer tubing. It is noteworthy that OH emission inside the torch climbed almost linearly with gas flow rate (see inset in Figure 6.4b). Additionally, when the emission profiles were normalized, the spatial distributions inside the torch effectively overlap each other, arguing that diffusion of air into the plasma torch was not the dominant source for these OH species; if it were, the spatial dependence would be expected to differ with changing plasma-gas velocity.

Water, in the form of protonated water clusters [$(H_2O)_nH^+$], has been shown to be an essential species for analyte ionization in plasma-based ambient-ionization analyses.[4, 7, 12] Because of their low proton affinity, these clusters are good reagent ions for proton transfer, which is the most common ionization pathway observed with these types of sources. Interestingly, the source of water vapor in these ionization sources has

often been attributed to atmospheric diffusion. Here we have shown that a substantial portion comes from the gas supply as well.

Outside the plasma torch, the OH emission profiles of Figure 6.4b share some similarities with those of He I emission (cf. Figure 6.4a). For both species, the relative intensities and the extended distances beyond the torch follow the order of studied flow rates. However, the distances where OH emission decays to baseline-noise levels are closer to the torch exit than those for He I. For example, He I emission extended to about 3 mm and 11 mm outside the torch for He flows of 0.40 and 1.60 L/min, respectively, whereas the OH emission decayed to baseline level at roughly 0 mm and 8 mm, respectively, for the same flow rates.

Figures 6.4c and 6.4d show the spatial emission profiles of the R(6) line of the N_2^+ band at 390.48 nm and the entire N_2 band at 337 nm, respectively. The whole N_2 band was integrated because individual emission lines from the band were relatively weak and hence noisy; as a result, the intensity axes of Figures 6.4c and 6.4d cannot be directly compared. With the exception of the two lowest studied gas flows, emission maxima for both N_2^+ and N_2 occur outside the plasma torch; emission maxima for the two lowest studied gas flows (0.40 and 0.60 L/min) were within 1 mm of the torch opening. For all examined flow rates, N_2^+ and N_2 exhibited similar spatial patterns, but with a spatial shift in which N_2 emission peaks occurred 2 to 3 mm beyond those in N_2^+ emission. This shift is likely caused by the recombination of N_2^+ with an electron. Interestingly, emission from N_2^+ was detected deep within the LTP torch, greater than 6 mm from the LTP outlet, whereas no such signal was observed for N_2. It is also

significant that there is a close correlation between the flow-dependent spatial locations of the N_2^+ emission maxima (Figure 6.4c) and the second maxima for atomic He emission (Figure 6.4a) outside the torch. This close correlation is believed to be due to a common formation/excitation mechanism involving He_2^+, which is discussed in detail in another paper.[23].

The slightly lower N_2^+ (Figure 6.4c) and N_2 (Figure 6.4d) emission intensities at 1.40 and 0.80 L/min, compared to those at neighboring flow rates, is believed to be caused by a slight change in plasma shape at the different gas flow rates. The shape of the afterglow, in particular the flicker and turbulence in its tail, was found to depend slightly on the gas flow rate. Because the physical width of the plasma that was imaged onto the slit of the spectrometer was narrow (approximately 70 μm), the exact physical location of the afterglow that was imaged was affected by plasma-gas flow rate. However, because all spectral windows were taken from the same plasma image, emission intensities of different species obtained at the same gas flow rate can still be validly compared.

Figures 6.4e and 6.4f show spatial emission profiles of the H I 656.28 nm (the hydrogen alpha, H_α) line and the O I 777.19 nm line. Emission from both species was weak and comparatively noisy and their spatial patterns appear to be nearly independent of plasma gas flow rate. Additionally, the strongest emission from atomic hydrogen and oxygen occurred inside the plasma torch. Interestingly, the effect of flow rate on emission was opposite for the two species; H_α monotonically increased whereas O I declined with gas flow. The spatial pattern for H_α was similar to that of OH molecular

emission (cf. Figure 6.4b) inside the plasma torch, but differed greatly outside of the tube. Specifically, OH emission extended well beyond the torch opening at moderate and high gas flows (e.g., from 0.80 to 1.60 L/min) and exhibited an additional emission maximum or inflection point, which was not observed for H_α emission. These findings suggest that atomic hydrogen and molecular OH are formed through the same mechanism, likely dissociation of water impurities within the LTP torch, but that an additional excitation mechanism exists for OH in the ambient atmosphere.

Atomic emission of O I at 777.19 nm (Figure 6.4f) does not resemble any of the other spatial patterns discussed thus far. The O I emission intensity inside the plasma torch declined with increasing gas flow rate; outside the torch, these excited species survived longer at higher gas flow rates, but did not exhibit any additional inflection points or maxima. This trend implies that the majority of atomic oxygen was produced from a species diffusing into the plasma torch, similar to N_2, and that this parent species is different from that of H_α and OH. Thus, it is believed that most of the atomic oxygen arises from atmospheric O_2 diffusing into the LTP torch. In addition, these excited states of atomic oxygen survive quite a distance beyond the opening of the LTP torch. The presence of radical, atomic oxygen is particularly problematic in molecular mass spectrometry as it can complicate otherwise simple mass spectra.[24] For instance, it has been noted that atomic oxygen radicals created in plasma-based ambient desorption/ionization sources can oxidize aromatic species, yielding a series of oxygen-adduct peaks in addition to that of the protonated molecular ion.[5] The source of atomic oxygen was previously attributed to impurities in the supply gas. The present data

suggest that a controlled atmosphere surrounding the ionization source would be helpful to reduce these species and, in turn, to simplify mass spectra of aromatic species.

6.3.4 Spatially Resolved Rotational Temperature in the He-LTP

The rotational temperature is an important plasma diagnostic, in part because it approximates the gas-kinetic temperature due to the rapid equilibrium that ordinarily exists between rotational and translational energies of a molecule. Various thermometric species for rotational-temperature measurement have been employed; examples include CN, NO, OH, N_2 and N_2^+.[25-26] Only the OH rotational temperature will be discussed in the present paper.

Rotational temperatures are derived from the Boltzmann population distribution among rotational energy levels. For the OH rotational temperature, four emission lines (cf. Table 6.1) from the Q_1 branch[27-28] were selected based on their emission intensities (I) and freedom from spectral interferences. The rotational temperature (T) is obtained from a plot of $\ln(I\lambda/gA)$ versus E_{exc}, where λ is the emission wavelength, A is the transition probability, g is the degeneracy of the excited energy level, and E_{exc} is the energy of the upper excited state (cf. Table 6.1); the slope of such a plot is equal to $(-11605/T)$ when E_{exc} is plotted in eV.[29]

A prerequisite for using a Boltzmann plot for temperature measurement is that the excited states of the thermometric species must be populated in accordance with the Boltzmann distribution. It is possible for Boltzmann plots to deviate from a straight line (e.g., when a particular group of levels is over- or under-populated compared to other

levels[30-31]). Accordingly, representative Boltzmann plots are presented here and their linearity examined. Figure 6.5a shows Boltzmann plots of OH for a He-LTP operated at 1.60 L/min helium flow at observation heights of -4, 0, +4, and +8 mm with respect to the opening of the plasma torch. All four plots yield straight lines with correlation coefficients > 0.997. Although the linear fits are vertically shifted, they are parallel to each other, indicating that they have similar slopes and, hence, correspond to similar OH rotational temperatures. The parallel shift is related only to the number densities of emitting species and not to temperature values. The OH rotational temperatures determined from the slopes of the linear regressions, in ascending order of observation height, are 286 K, 297 K, 281 K, and 311 K at the four positions. Uncertainties in the temperature measurements are assumed to be from the error of the linear-regression slope, which was ≤ 5%, corresponding to an uncertainty of ±15 K. Measured OH rotational temperatures were not statistically different from the ambient temperature, which agrees well with the results from gas-temperature measurements obtained through other means (e.g., IR thermometry and physical contact of the plasma with a human finger during ambient-MS sampling).[12]

Figure 6.5b displays the rotational-temperature spatial profile when the LTP was operated with 1.60 L/min helium. Error bars indicate uncertainties of the slope from the linear regressions. This uncertainty is related to the emission strength of the species and is therefore spatially dependent. Rotational temperatures of the OH molecules were very similar to room temperature throughout the whole plasma (i.e. both inside and outside the torch).

Table 6.1. Spectroscopic constants of the Q_1 branch of the OH (0,0) band ($A\ ^2\Sigma^+ - X\ ^2\Pi$) used for rotational-temperature measurement.

Branch, (N', J')	Wavelength, λ / nm	Excitation energy, E_{exc} / eV	Relative A-factor, A	Degeneracy, g
Q_1 – 2, (2, 2.5)	307.99	4.03484	599	6
Q_1 – 4, (4, 4.5)	308.32	4.0641	701	10
Q_1 – 5, (5, 5.5)	308.52	4.08505	724	12
Q_1 – 6, (6, 6.5)	308.73	4.1104	736	14

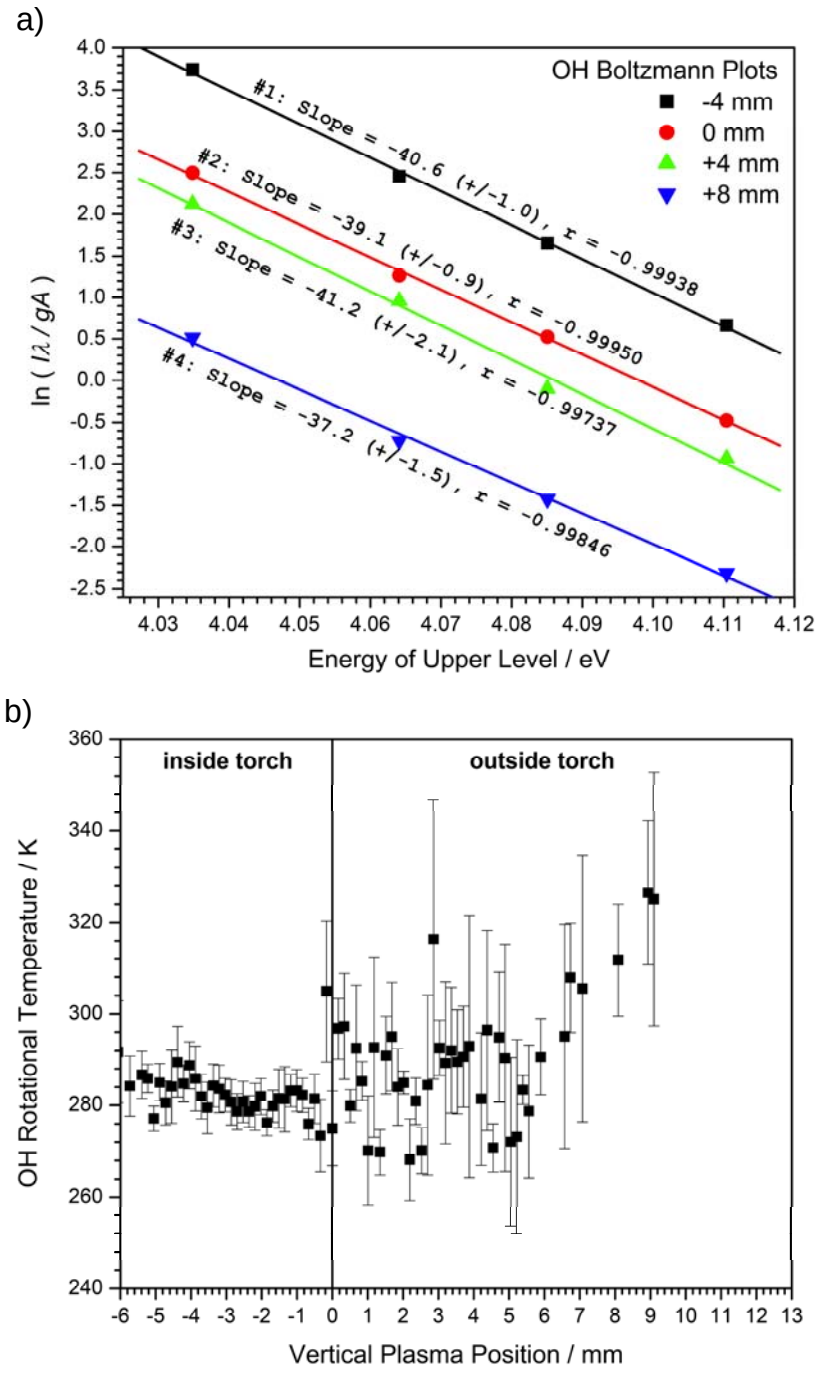

Figure 6.5 a) Boltzmann plots of OH rotational temperature at −4, 0, +4, and +8 mm from the exit of the LTP torch. b) Vertical profile of measured OH rotational temperatures of the He-LTP. The error bars represent only the error of the slope in the linear regression. The helium gas flow was 1.60 L min^{-1}.

Although gas-kinetic temperatures theoretically could be determined from N_2^+ emission, we found that these apparent temperatures were significantly (a maximum of ~550 K was obtained for the N_2^+ rotational temperature) higher than those measured from OH emission or IR thermometry. The reason for the discrepancy in N_2^+ temperature was that additional rotational energy is imparted to the molecule during the ionization process. This N_2^+ rotational-energy distribution was essential in deducing that a significant fraction of N_2 is ionized via charge transfer with He_2^+;[23] this finding is contrary to most published ionization mechanisms for plasma-based ambient desorption/ionization sources, which solely assumed a Penning ionization process.[4, 10, 12]

6.3.5 Measurement of Electron Number Density in the He-LTP

The electron number density in the He-LTP was measured by means of Stark broadening of the hydrogen beta line from the Balmer series. This line has well-characterized Stark-broadening parameters, its width can be readily related to electron number densities, and it is relatively insensitive to the electron temperature of the plasma.[32-33] Unfortunately, emission from the H_β line was weak in the He-LTP, so its spectral shape could be measured only in a spatially integrated mode (i.e., all CCD vertical pixels were binned to enhance the signal-to-noise ratio). During these measurements no hydrogen or water vapor was added to the plasma; rather, the hydrogen emission was due to dissociation of water originating from the gas supply (cf. Section 3.3).

The H_β emission line was fitted with a Voigt profile including a Gaussian width of 13.7 pm (FWHM) to correct for instrumental broadening of the spectrometer. This slit

function was determined from the 576.961 nm and 690.752 nm lines from a low-pressure Hg lamp; the two lines exhibited Gaussian shapes with spectral widths of 13.9 pm and 13.5 pm, respectively. After correction for the Gaussian component, the Lorentzian portion (FWHM) of the H_β line was found to be 53.6 pm. The Stark width could then be obtained by subtracting other Lorentzian-linewidth contributions. In the present study, only van der Waals broadening was taken into account; resonance and Doppler broadening were negligible because the number density of ground-state atomic hydrogen atoms and the gas-kinetic temperature of the plasma were both very low.

Because the strongest H I emission was found inside the LTP torch (cf. Figure 6.3), where the dominant perturber for van der Waals broadening would be atomic helium, van der Waals broadening for H was assumed to be due solely to He as a perturber. From the classical Lindholm-Foley impact theory[34-35], the mean van der Waals broadening for the H_β line in 1 atm of helium at 300 K was estimated to be 44.6 pm. Accordingly, Stark broadening of the H_β line was then estimated as the difference between the measured Lorentzian linewidth (53.6 pm) and the estimated van der Waals broadening. The resulting Stark width for H_β of the He-LTP was found to be 9.0 pm. The electron number density for the He-LTP was then estimated from the numerical formula given by Gigosos et al.[36] to be 9.9×10^{12} cm^{-3}. A recent model of a He-DBD such as is typically employed in analytical chemistry predicted a stimulated electron number density on the order of 10^{11} cm^{-3}.[37]

Although many discharges have been incorporated into ambient desorption/ionization sources, their electron number densities were seldom

experimentally determined or compared. Such values could yield a number of important fundamental and analytical insights. First, because the bulk plasma maintains electrical neutrality, the number density of positive ions (e.g., He^+, He_2^+, and N_2^+) in the LTP is also on the order of 10^{12} cm^{-3}. Second, number densities of electrons and positive ions are important for modeling these analytically useful plasmas. Third, even though most ambient desorption/ionization mass spectrometry applications have focused on analyte detection in the positive-ionization mode, operation of these sources in the negative ion mode is also attractive.[12, 38] For example, the LTP has been operated in both positive- and negative- ion modes.[12] Proposed mechanisms for negative ion formation in these ambient desorption/ionization sources include direct electron capture and dissociative electron capture.[38] The electron density would then be an important factor to consider when comparing the effectiveness of these ambient desorption/ionization sources for the generation of negative analyte ions.

6.3.6 Effect of Electrode Separation on Spectral Characteristics of the He-LTP

It was previously shown with the LTP probe that analyte fragmentation could be induced by increasing the distance between the high-voltage ring electrode and the grounded pin electrode.[12] This enhanced fragmentation could be the result of a more energetic plasma, leading to increased energy deposition from reagent species to analyte molecules during desorption or ionization.[12] Alternatively, the fragmentation could be due to a change in reactive gas species formed in the plasma, thereby altering the gas-phase ion chemistry. To distinguish between these two possibilities, the LTP probe was spectroscopically characterized at varying electrode distances. Interestingly, it was found

that there was no change in the identity of the emitting species; however, emission strengths for all species were enhanced at greater electrode spacings (i.e., at lower electrode capacitances).

Figure 6.6 shows spectra of molecular OH A $^2\Sigma^+$, N_2 C $^3\Pi_u$, N_2^+ B $^2\Sigma_u^+$ and atomic He I and O I emission when the inner electrode was positioned 15.2, 22.0, and 31.5 mm from the edge of the outer ring electrode (cf. Figure 6.1). In this case, the helium flow rate was 0.60 L/min, which is typical for mass spectrometric analyses with the LTP probe. With the exception of OH, all molecular and atomic emission declined by about 50% when the electrode distance was reduced from 32.5 mm to 22.0 mm; a drop of 70% was observed for OH emission. When the electrode distance was further decreased to 15.2 mm, emission levels from OH, N_2, He I and O I were approximately 20% to 30% of the original whereas N_2^+ emission declined to about 10%. Because emission from most plasma species changed by similar degrees as the electrode gap was varied, it can be concluded that a more energetic plasma was created; yet, the generated chemical species and associated gas-phase chemistry are largely the same. Overall, analyte fragmentation observed at greater electrode gaps is likely due to an increase in internal energy deposition from reactive plasma species.

6.3.7 He-LTP with Trace Water Vapor and the Ar-LTP

The effect of trace amounts of water vapor in the helium plasma gas and of complete replacement of helium with argon for LTP operation were also explored. Through mixing with a supplemental flow saturated with water vapor, helium doped with approximately 98 ppm v/v water vapor was used as the plasma gas.

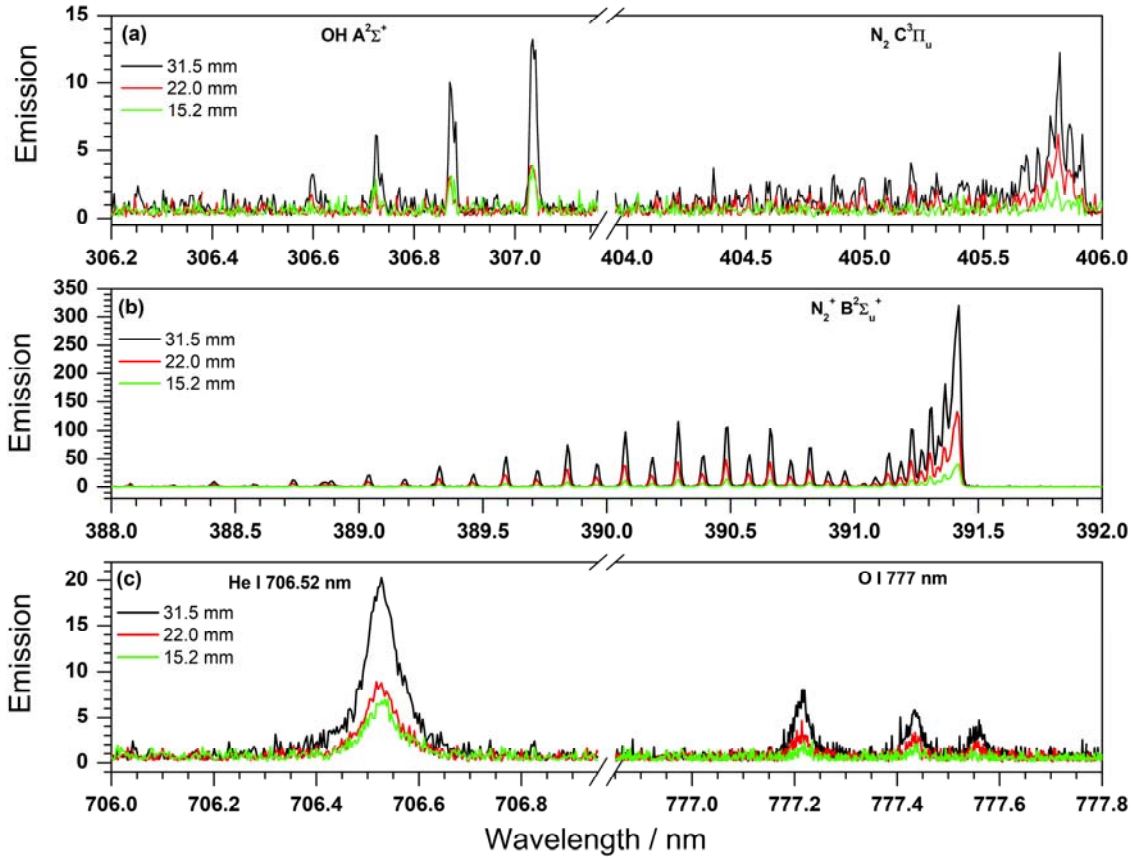

Figure 6.6 Emission spectra of (a) OH ($A\ ^2\Sigma^+ - X\ ^2\Pi$) and N_2 ($C\ ^3\Pi_u - B\ ^3\Pi_g$), (b) N_2^+ ($B\ ^2\Sigma_u^+ - X\ ^2\Sigma_g^+$), and (c) He I and O I in the He-LTP at various electrode distances at a helium flow rate of 0.60 L/min. A distance of zero would result in the greatest electrode-area overlap, and yield the largest capacitance.

Representative spatially integrated emission spectra of the LTP supplied with humid helium are presented in Figure 6.7. The identities of emitting species in water-vapor-doped helium were identical to those without the doping. However, weaker emission signals, of up to 90% depression, were observed for all species in the presence of trace (< 100 ppm) amounts of water vapor. The most strongly affected emission in the presence of trace water vapor was from OH and H, despite the fact that these species originated from water dissociation. The signals for OH and H emission were only about 10% and 15%, respectively, of their strengths in the absence of water vapor.

Clearly, the He-LTP is very sensitive to the presence of water vapor in the plasma gas, an observation that is in agreement with previous mass-spectrometric results obtained when dopants were added to the discharge gas to alter the gas-phase ion-chemistry of the LTP.[39] This so-called reactive LTP, which is loosely based on the principle of reactive DESI, takes advantage of specific gas-phase or plasma reactions that foster selective desorption and/or ionization of particular analytes that are not detected under usual operating conditions. For example, it was reported[39] that addition of hydrogen peroxide and water vapor to the LTP probe enabled mass spectrometric detection of highly non-polar hydrocarbons, such as squalene. Yet, the overall MS signal dropped by more than one order of magnitude, which further confirms that dopants introduced into the discharge effectively quench the plasma, limiting production of reagent/background ions. Although it might initially seem that reduced reagent-ion production would be counterproductive, it is beneficial if it promotes the desorption/ionization of an otherwise undetectable analyte or lowers background ions. The success of a specific reactive LTP system will depend on finding the optimal to

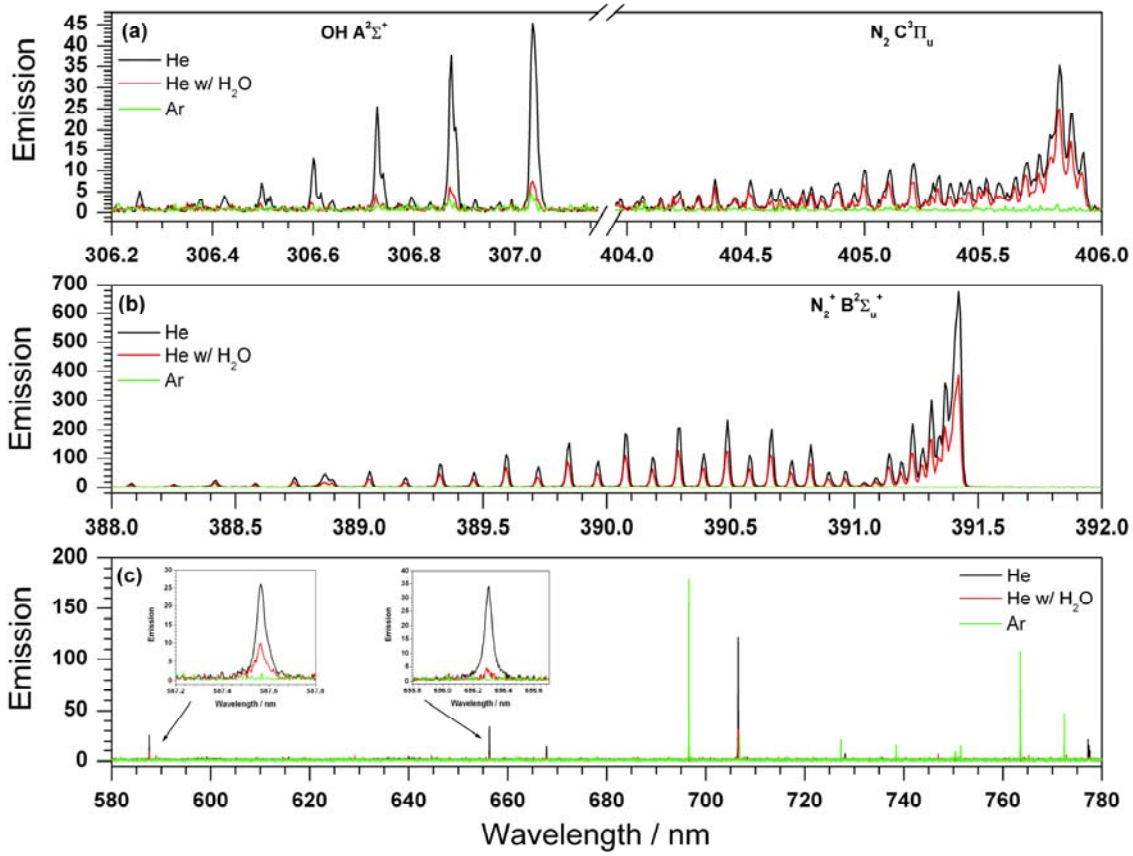

Figure 6.7 Emission spectra of (a) OH ($A\ ^2\Sigma^+ - X\ ^2\Pi$) and N_2 ($C\ ^3\Pi_u - B\ ^3\Pi_g$), (b) N_2^+ ($B\ ^2\Sigma_u^+ - X\ ^2\Sigma_g^+$), and (c) over the wavelength range from 580 nm to 780 nm (the insets show the expanded-scale spectra of He I 587.56 nm and H_α 656.28 nm) in the LTP operated with high-purity helium, helium with trace (< 100 ppm v/v) water vapor, and high-purity argon. Plasma gas flow rates were 1.60 L/min in all cases.

concentrations of discharge-gas dopants so the plasma is only minimally affected, while determination of the compounds of interest is facilitated. The only way to accomplish both of these feats is to correlate optical measurements of the discharge with mass spectrometric analysis of samples.

The effect of complete replacement of helium with argon as the plasma gas is also presented in Figure 6.7. Not surprisingly, the Ar-LTP produces an almost entirely different spectrum than the He-LTP (cf. Figure 6.2), indicating the distinct gas-phase chemistry of the two plasmas. The only common feature in He-LTP and Ar-LTP emission spectra is OH molecular emission, although OH emission intensities in the Ar-LTP were only about 10% of those found in the He-LTP. Emission from N_2 C $^3\Pi_u$ or N_2^+ B $^2\Sigma_u^+$, could not be detected from the Ar discharge. Similarly, atomic emission from H and O are not distinguishable from the background. However, strong emission from atomic argon (e.g., Ar I at 696.5, 706.7, 727.3, 738.4, 763.5, and 772.4 nm) is readily observable.

The intense emission lines from the plasma gas, but a lack of N_2 and N_2^+ emission in the Ar-LTP further argue that the excited-state chemistry of helium is crucial for the formation of reactive nitrogen species for ambient mass spectrometry. This phenomenon correlates well with mass spectral data acquired with an Ar-LTP, which often yields 10-100 times weaker ion signals for an analyte of interest. The lower MS sensitivity with an Ar-LTP is likely due to reduced formation of reactive nitrogen species, resulting in less efficient production of water clusters that are often considered to be responsible for the proton transfer that is typically observed in LTP-MS.[12]

6.4 Conclusions

A low-temperature plasma probe, based on a helium dielectric barrier discharge, was characterized by means of optical spectroscopy. The spatial emission profiles of N_2 and N_2^+, the latter of which is essential for reagent-ion formation, were found to resemble each other but with a downstream spatial offset in the N_2 signal. In addition, peak emission for both species was found to lie beyond the plasma torch, in the open atmosphere. It is clear from these findings that the dominant mechanism of excitation for both the N_2 and N_2^+ species is not through electron impact; rather, it is suggested that excited N_2 molecules are formed via recombination of N_2^+ with an electron.

It was also concluded that the dominant source of OH emission is water from the gas supply, likely adsorbed on the walls of the gas transfer lines, rather than diffusional penetration of atmospheric water vapor into the plasma. In contrast, it is believed that most of the N_2, N_2^+ and atomic oxygen emission was from ambient N_2 and O_2 diffusing into the LTP torch. This last finding is particularly important as N_2^+ and atomic-oxygen radicals play important roles in mass spectrometric analyses. In future studies, it will be important to examine the effects of controlling the atmosphere surrounding the ionization source as well as the composition of the gas entering the plasma torch.

Reduced emission signals, up to 90% weaker, were observed for all species in the presence of trace (< 100 ppm) water vapor added to the He discharge gas. Such high sensitivity of the plasma characteristics to dopants or contaminants in the plasma gas indicates that optimization of operating conditions for reactive LTP could be challenging; the dopants must be present at concentrations that affect the plasma minimally, while at

the same time promote selective and efficient desorption/ionization of the compound of interest.

Lastly, depressions in emission were observed when the inter-electrode distances were reduced. Dropping the electrode spacing from 32.5 mm to 15.2 mm lowered all molecular and atomic emission features by at least 70%. Interestingly, the chemical species that were generated, and the associated gas-phase chemistry, remained similar regardless of electrode separation. This observation suggests that analyte fragmentation at greater electrode gaps, which had previously been reported, is likely the result of an increase in internal energy deposition from reactive plasma species. In contrast, completely different gas-phase chemistry was observed when the plasma gas was changed from helium to argon. The only common feature in the He-LTP and Ar-LTP spectra is OH molecular emission; emission from N_2, N_2^+, H and O were not distinguishable from baseline level, if present, in the Ar-LTP. Despite the fact that strong emission from the plasma gas (atomic argon) was readily observed for the Ar-LTP, the lack of N_2 and N_2^+ emission in Ar-LTP indicates that the excited-state chemistry of helium is crucial for the formation of reactive nitrogen species for ambient mass spectrometry, which further correlates with mass spectral data acquired with an Ar-LTP probe that often yields 10 – 100 times weaker ion signal for an analyte of interest.

References

1. Cooks, R. G.; Ouyang, Z.; Takats, Z.; Wiseman, J. M. *Science* **2006**, *311*, 1566-1570.
2. Takats, Z.; Wiseman, J. M.; Gologan, B.; Cooks, R. G. *Science* **2004**, *306*, 471-473.
3. Kertesz, V.; Ford, M. J.; Van Berkel, G. J. *Anal. Chem.* **2005**, *77*, 7183-7189.
4. Cody, R. B.; Laramee, J. A.; Durst, H. D. *Anal. Chem.* **2005**, *77*, 2297-2302.
5. Shelley, J. T.; Wiley, J. S.; Chan, G. C. Y.; Schilling, G. D.; Ray, S. J.; Hieftje, G. M. *J. Am. Soc. Mass Spectrom.* **2009**, *20*, 837-844.
6. Andrade, F. J.; Shelley, J. T.; Wetzel, W. C.; Webb, M. R.; Gamez, G.; Ray, S. J.; Hieftje, G. M. *Anal. Chem.* **2008**, *80*, 2646-2653.
7. Andrade, F. J.; Shelley, J. T.; Wetzel, W. C.; Webb, M. R.; Gamez, G.; Ray, S. J.; Hieftje, G. M. *Anal. Chem.* **2008**, *80*, 2654-2663.
8. McEwen, C. N.; McKay, R. G.; Larsen, B. S. *Anal. Chem.* **2005**, *77*, 7826-7831.
9. Takats, Z.; Cotte-Rodriguez, I.; Talaty, N.; Chen, H. W.; Cooks, R. G. *Chemical Communications* **2005**, 1950-1952.
10. Ratcliffe, L. V.; Rutten, F. J. M.; Barrett, D. A.; Whitmore, T.; Seymour, D.; Greenwood, C.; Aranda-Gonzalvo, Y.; Robinson, S.; McCoustra, M. *Anal. Chem.* **2007**, *79*, 6094-6101.
11. Na, N.; Zhao, M. X.; Zhang, S. C.; Yang, C. D.; Zhang, X. R. *J. Am. Soc. Mass Spectrom.* **2007**, *18*, 1859-1862.
12. Harper, J. D.; Charipar, N. A.; Mulligan, C. C.; Zhang, X. R.; Cooks, R. G.; Ouyang, Z. *Anal. Chem.* **2008**, *80*, 9097-9104.

13. Song, L. G.; Dykstra, A. B.; Yao, H. F.; Bartmess, J. E. *J. Am. Soc. Mass Spectrom.* **2009**, *20*, 42-50.

14. McEwen, C. N.; Larsen, B. S. *J. Am. Soc. Mass Spectrom.* **2009**, *20*, 1518-1521.

15. Cody, R. B. *Anal. Chem.* **2009**, *81*, 1101-1107.

16. Shelley, J. T.; Hieftje, G. M. *J. Anal. At. Spectrom.* **2010**, *25*, 345-350.

17. Andrade, F. J.; Wetzel, W. C.; Chan, G. C. Y.; Webb, M. R.; Gamez, G.; Ray, S. J.; Hieftje, G. M. *J. Anal. At. Spectrom.* **2006**, *21*, 1175-1184.

18. Michels, A.; Tombrink, S.; Vautz, W.; Miclea, M.; Franzke, J. *Spectrochim. Acta Part B* **2007**, *62*, 1208-1215.

19. Olenici-Craciunescu, S. B.; Michels, A.; Meyer, C.; Heming, R.; Tombrink, S.; Vautz, W.; Franzke, J. *Spectrochim. Acta Part B* **2009**, *64*, 1253-1258.

20. Zhu, Z. L.; Chan, G. C. Y.; Ray, S. J.; Zhang, X. R.; Hieftje, G. M. *Anal. Chem.* **2008**, *80*, 8622-8627.

21. Paris, P.; Aints, M.; Valk, F.; Plank, T.; Haljaste, A.; Kozlov, K. V.; Wagner, H. E. *J. Phys. D.* **2005**, *38*, 3894-3899.

22. Paris, P.; Aints, M.; Laan, M.; Valk, F. *J. Phys. D.* **2004**, *37*, 1179-1184.

23. Chan, G. C. Y.; Shelley, J. T.; Wiley, J. S.; Engelhard, C.; Jackson, A. U.; Cooks, R. G.; Hieftje, G. M. *Anal. Chem.* **2010**, submitted.

24. Ascenzi, D.; Franceschi, P.; Guella, G.; Tosi, P. *The Journal of Physical Chemistry A* **2006**, *110*, 7841-7847.

25. Moon, S. Y.; Choe, W. *Spectrochim. Acta Part B* **2003**, *58*, 249-257.

26. Ishii, I.; Montaser, A. *Spectrochim. Acta Part B* **1991**, *46*, 1197-1206.

27. Dieke, G. H.; Crosswhite, H. M. *J. Quant. Spectrosc. Radiat. Transf.* **1962**, *2*, 97-&.

28. Chidsey, I. L.; Crosley, D. R. *J. Quant. Spectrosc. Radiat. Transf.* **1980**, *23*, 187-199.

29. Mermet, J. M., in *Inductively Coupled Plasma Emission Spectroscopy-Part 2*, ed. P. W. J. M. Boumans. Wiley-Interscience: New York, 1987, vol. 90, pp 353-386.

30. Bruggeman, P.; Schram, D. C.; Kong, M. G.; Leys, C. *Plasma Processes and Polymers* **2009**, *6*, 751-762.

31. Linss, V.; Kupfer, H.; Peter, S.; Richter, F. *J. Phys. D.* **2004**, *37*, 1935-1944.

32. Kelleher, D. E.; Wiese, W. L.; Helbig, V.; Greene, R. L.; Oza, D. H. *Phys. Scr.* **1993**, *T47*, 75-79.

33. Torres, J.; van de Sande, M. J.; van der Mullen, J.; Gamero, A.; Sola, A. *Spectrochim. Acta Part B* **2006**, *61*, 58-68.

34. Lindholm, E. *Ark. Mat. Astron. Fys.* **1946**, *32A*, No. 17.

35. Foley, H. M. *Phys. Rev.* **1946**, *69*, 616.

36. Gigosos, M. A.; Gonzalez, M. A.; Cardenoso, V. *Spectrochim. Acta Part B* **2003**, *58*, 1489-1504.

37. Martens, T.; Bogaerts, A.; Brok, W. J. M.; van der Mullen, J. *J. Anal. At. Spectrom.* **2007**, *22*, 1033-1042.

38. Chen, H.; Gamez, G.; Zenobi, R. *J. Am. Soc. Mass Spectrom.* **2009**, *20*, 1947-1963.

39. Jackson, A. U. Method Development, Novel Applications and Fundamental Studies of Ambient Ionization Methods: Desorption Electrospray Ionization

(Desi) and Low Temperature Plasma (Ltp) Ionization. Ph.D. Thesis, Purdue University, West Lafayette, 2010.

Chapter 7

Elucidation of Reaction Mechanisms Responsible for Afterglow and Reagent-Ion Formation in the Low-Temperature Plasma Probe Ambient Ionization Source

---

7.1 Introduction

There has been considerable recent interest within the mass spectrometry community in the direct analysis of complex samples in the open, ambient atmosphere. Much of the research in this new field, termed ambient desorption/ionization mass spectrometry[1], has focused on the development of ionization sources that are also capable of desorbing or extracting analytes directly from sample surfaces. The ultimate goal is a portable ionization source and mass spectrometer combination that can directly analyze a

wide variety of sample surfaces with little or no pretreatment. The first ambient desorption/ionization sources introduced as such in the literature were Desorption ElectroSpray Ionization (DESI)[2] and Direct Analysis in Real Time (DART)[3], which rely on electrospray droplets and plasma species, respectively, for the desorption and ionization processes. Both sources are now available commercially.

Since the initial introduction of these devices, over 25 ambient desorption/ionization sources have been described in the literature.[4] Nearly all of these sources can be classified as being either electrospray, laser or plasma-based, with the plasma-based sources accounting for a large number of all ambient desorption/ionization sources. The systems that utilize an electrical discharge can be further classified by either an indirect or a direct plasma-sample interaction. Sources that physically isolate the discharge from the sample, such as DART, the Atmospheric-pressure Solids Analysis Probe (ASAP)[5], and Desorption Atmospheric-Pressure Chemical Ionization (DAPCI)[6], use the excited species generated in the discharge for ionization and rely on an external means (e.g., heating of the discharge gas) to desorb analytes from a surface. In contrast, sources in which the discharge comes into direct contact with the sample surface, including the Flowing Atmospheric-Pressure Afterglow (FAPA)[7, 8], Plasma-Assisted Desorption/Ionization (PADI)[9], and the Low-Temperature Plasma (LTP) probe[10], can achieve both desorption and ionization simultaneously, which often makes them simpler and less expensive to construct.

All of the plasma-based ambient desorption/ionization sources are thought to rely mainly on thermal processes to liberate analytes from a surface into the gas phase. After

this volatilization process, subsequent ionization has been thought to occur directly or indirectly from species created in the discharge; evidence has been derived from background and analyte ions observed in mass spectra. Although a variety of discharge gases have been used with these sources, DART[3], FAPA[7, 8], and the LTP probe[10] yield the highest sensitivity for a wider range of analyte ions with helium as a discharge gas, rather than argon, nitrogen, or air. This finding is often attributed to long-lived, high-energy helium metastables (He^m), which can ionize most analytes (M) directly through Penning ionization (cf. Reaction 1).[3]

$$He^m\ (19.8 \text{ or } 20.9 \text{ eV}) + M \rightarrow He + M^{+\cdot} + e^- \quad (1)$$

It has also been proposed[7] that He^m could ionize atmospheric gases, such as water vapor or nitrogen to produce reagent ions,

$$He^m\ (19.8 \text{ or } 20.9 \text{ eV}) + N_2 \rightarrow He + N_2^+ + e^- \quad (2)$$

$$He^m\ (19.8 \text{ or } 20.9 \text{ eV}) + H_2O \rightarrow He + H_2O^+ + e^- \quad (3)$$

Though N_2^+ and H_2O^+ have been reported in the background mass spectra of the FAPA source[11], the most abundant background ions from plasma-based ambient desorption/ionization sources are protonated water clusters, $(H_2O)_nH^+$, which are well known to be formed in atmospheric-pressure chemical ionization sources such as a corona discharge or ionization by electron-impact from the β-emitter ^{63}Ni foil in air. The following sequence of reactions is reported to be responsible for water-cluster formation.[12-14]

$$N_2^+ + 2\ N_2 \rightarrow N_4^+ + N_2 \quad (4)$$

$$N_4^+ + H_2O \rightarrow H_2O^+ + 2\ N_2 \quad (5)$$

$$H_2O^+ + H_2O \rightarrow H_3O^+ + OH \quad (6)$$

$$H_3O^+ + (n\text{-}1)\ H_2O + N_2 \rightarrow (H_2O)_nH^+ + N_2 \quad (7)$$

Gas-phase analytes that have a higher proton affinity than the water cluster can then be ionized via proton transfer.

$$(H_2O)_nH^+ + M \rightarrow n\ H_2O + MH^+ \quad (8)$$

Surprisingly, neither the presence of He^m in the desorption/ionization region nor the direct involvement of He^m in the analyte-ionization pathway has been experimentally verified for any plasma-based ambient desorption/ionization source. This information is essential not only for better understanding of the mechanisms by which plasma-based ambient ionization sources operate, but also for optimization of their performance for mass spectrometric analyses. Examples of improved performance would be reduced matrix effects and more efficient desorption.

We recently performed a spatially resolved optical characterization of the dielectric-barrier discharge (DBD) and afterglow of the LTP probe to identify atomic and diatomic species created within the discharge, as well as in the open atmosphere, under a variety of operating conditions.[15] In the present study, similar spatially resolved measurements along with known spectrochemistry of gaseous discharges are used to reveal reaction mechanisms ultimately responsible for analyte ionization. The LTP probe

is well suited for these studies because the emitting species within the discharge and the sample introduction region (i.e., the afterglow) can be monitored simultaneously. In addition, the inherently transient nature of the DBD, and of the gas-phase reactions that occur in it, enables unambiguous identification of the various reactions with spatial information.

7.2 Experimental

7.2.1 LTP Probe

A schematic diagram and detailed description of the experimental setup have been given elsewhere[15]; as a result, the setup will be described only briefly in the present paper. The LTP probe was formed from a dielectric-barrier discharge which was sustained between a stainless-steel pin (1.5 mm diameter) electrode and a 25-mm wide, copper ring electrode; a Pyrex® glass tube (o.d. 6.4 mm and i.d. 3.8 mm) between the two electrodes served as the dielectric barrier. A high-voltage AC waveform was applied to the copper ring with the centered pin electrode grounded. A power supply was locally built by modulating a DC potential through the primary winding of an automobile ignition coil (Model 8140C, Accel, Cleveland, OH) with a MOSFET. The output voltage and frequency from the secondary winding of the coil were both adjustable by changing the input DC potential and the frequency of the TTL waveform into the gate of the MOSFET, respectively. Without a capacitive load, the power supply produced a waveform of 11.8 to 14.8 kV_{p-p} over frequencies ranging from 1.2 to 2.4 kHz; the ionization source had a total power consumption of less than 2 W. In all studies helium (99.999% ultra-high purity helium, Airgas, Radnor, PA) was used as the discharge gas at

flow rates between 0.40 and 1.60 L/min. The stainless-steel grounded pin electrode, glass tubing, and gas transfer tubing for the discharge gas were all held in place with a non-conductive perfluoroalkoxy (PFA) Swagelok® tee. The distance between the grounded and AC electrodes, taken as the distance between the tip of the pin and the edge of the copper electrode nearest the exit of the probe, was fixed at 9 mm, which is the optimal value for mass spectrometric analyses.

7.2.2 Spectroscopic Measurements

The setup for spectroscopic measurements of the LTP probe has previously been detailed[15], but will be briefly described here. Spectroscopic measurements were performed on a commercial spectrometer ordinarily used for inductively coupled plasma (ICP) atomic emission spectroscopy (ACTIVA, Horiba–Jobin Yvon, Longjumeau, France). The focal length of the spectrometer is 0.64 m and a grating with groove density of 2400 lines/mm was used throughout the experiments. The LTP probe was mounted vertically on a translation stage and positioned in the torch box in place of the ICP torch. Alignment of the LTP probe with respect to the spectrometer was performed daily by adjusting the torch for maximum zero-order (white light) intensity. The ACTIVA spectrometer combines a Czerny-Turner-configured grating and a two-dimensional CCD detector, which together enable simultaneous measurement of the entire vertical emission profile of the plasma over a wide spectral range. This instrument design is useful for determining the location of emitting species, as well as for point-by-point fundamental measurements, such as rotational temperature.

The incoming image to the spectrometer was demagnified by 3.12 times, which resulted in a 21.5 mm vertical observation window in the plasma. This vertical observation window was placed so that 7 mm of the plasma within the LTP torch could be imaged, as well as the entire plasma plume (afterglow) emanating from the torch. Exposure times of 60 s and a rather wide entrance slit (20 μm) were needed to detect the weak emission from the LTP afterglow. After these changes, the spectral resolution of the spectrometer was 13.7 pm FWHM. Additionally, pixels in the spatial dimension were binned in groups of four for all spatial profiles. Raw CCD data were processed with software written in-house. Emission intensities were obtained by integrating the area under each spectral peak, with background subtraction taken from nearby pixels.

7.2.3 N_2^+ Rotation Temperature Measurement

The principle for rotational temperature measurements performed here is based on the Boltzmann population distribution of N_2^+ rotational energy levels. Twelve emission lines (cf. Table 7.1) from the R branch[16] of N_2^+ were used for spatially resolved, rotational temperature measurements. A greater number of emission lines could be employed for N_2^+ than for the previously reported[15] OH measurements because N_2^+ emission was much stronger, yielding more emission lines with adequate signal-to-background ratios. A plot of $\log[I/2(K''+1)]$ versus $(K''+1)\times(K''+2)$ was constructed, where K'' is the rotational number for the lower level. The rotational temperature was obtained from the slope of this linear plot, which is equal to $-1.296 / T$.[16] Line intensities with odd K'' values must be multiplied by a factor of 2 because of the statistical weight from the nuclear spin of the N_2^+ molecule.[16, 17]

Table 7.1. Spectroscopic constants of the R branch of the N_2^+ (0,0) band ($B\ ^2\Sigma_u^+ - X\ ^2\Sigma_g^+$) for rotational temperature measurement.

K"	Wavelength, λ / nm	Intensity Correction Factor	*(K"+1)×(K"+2)*
6	390.49	1	56
7	390.40	2	72
8	390.29	1	90
9	390.19	2	110
10	390.08	1	132
11	389.97	2	156
12	389.85	1	182
13	389.73	2	210
16	389.33	1	306
18	389.04	1	380
20	388.74	1	462
21	388.58	2	506

7.3 Results and Discussion

7.3.1 Overview of Spectroscopically Identified Plasma Species in the He-LTP

Table 7.2 lists the assignments of ***all*** species observed in the emission spectrum of the He-LTP probe used in this study.[18, 19] The helium gas flow rate was 1.60 L/min and the gap between the inner and the outer electrodes was 9.0 mm. The emission spectrum was relatively simple and consisted of emission from simple diatomic molecules, such as OH, N_2, N_2^+, as well as atomic species, like He I, H I and O I. In addition to this survey of emitting plasma species, the rotational temperature (from OH) and the electron number density (by Stark broadening from H_β and He) have already been determined;[15] however, the spatial distribution of emitting species in the open atmosphere and their spatially dependent relative energies offer additional information about the LTP afterglow structure and the reactions that occur in it. Here as before, the *afterglow* of the LTP refers to the portion of the LTP that extends beyond the plasma torch.

7.3.2 Spatial Correlation of Atomic He I and N_2^+ Emission in the He-LTP

Spatial emission profiles from the six identified emitting species (cf. Table 7.2) as a function of helium flow rates between 0.60 and 1.60 L/min have previously been presented.[15] Particularly relevant to the present discussion of reaction mechanisms in the afterglow region is the fact that there was a close correlation between the spatial location of greatest N_2^+ emission and a maximum for atomic He emission located outside the torch. Figure 7.1 presents the normalized emission profiles of He I and N_2^+ ($B\ ^2\Sigma_u^+ - X\ ^2\Sigma_g^+$, the first negative system) in the afterglow region at selected helium flow rates in

Table 7.2. Identification of ***all*** atomic[18] and molecular[19] emission features in the He-LTP over the wavelength range from 185 nm to 780 nm.

Emitting Species	Transition	Wavelength / nm
OH	$A\ ^2\Sigma^+ - X\ ^2\Pi$	281 – 285 (ν'=1, ν"=0)
		306 – 309 (ν'=0, ν"=0)
N_2	$C\ ^3\Pi_u - B\ ^3\Pi_g$	295 – 298 (ν'=2, ν"=0)
		313 – 317 (ν'=1, ν"=0)
		335 – 337 (ν'=0, ν"=0)
		350 – 353 (ν'=1, ν"=2)
		355 – 357 (ν'=0, ν"=1)
		373 – 375 (ν'=1, ν"=3)
		378 – 381 (ν'=0, ν"=2)
		392 – 394 (ν'=2, ν"=5)
		398 – 400 (ν'=1, ν"=4)
		404 – 406 (ν'=0, ν"=3)
		432 – 434.5 (ν'=0, ν"=4)
N_2^+	$B\ ^2\Sigma_u^+ - X\ ^2\Sigma_g^+$	387 – 391 (ν'=0, ν"=0)
		425 – 428 (ν'=0, ν"=1)
		468 – 471 (ν'=0, ν"=2)
H I	H_β	486.13
	H_α	656.28
He I	$3p\ ^1P_1° - 2s\ ^1S_0$	501.57
	$3d\ ^3D_{1,2,3} - 2p\ ^3P_{0,1,2}°$	587.56
	$3d\ ^1D_2 - 2p\ ^1P_1°$	667.82
	$3s\ ^3S_1 - 2p\ ^3P_{0,1,2}°$	706.52
	$3s\ ^1S_0 - 2p\ ^1P_1°$	728.14
O I	$(^4S°)3p\ ^5P_3 - (^4S°)3p\ ^5S_2°$	777.194
	$(^4S°)3p\ ^5P_2 - (^4S°)3p\ ^5S_2°$	777.417
	$(^4S°)3p\ ^5P_1 - (^4S°)3p\ ^5S_2°$	777.539

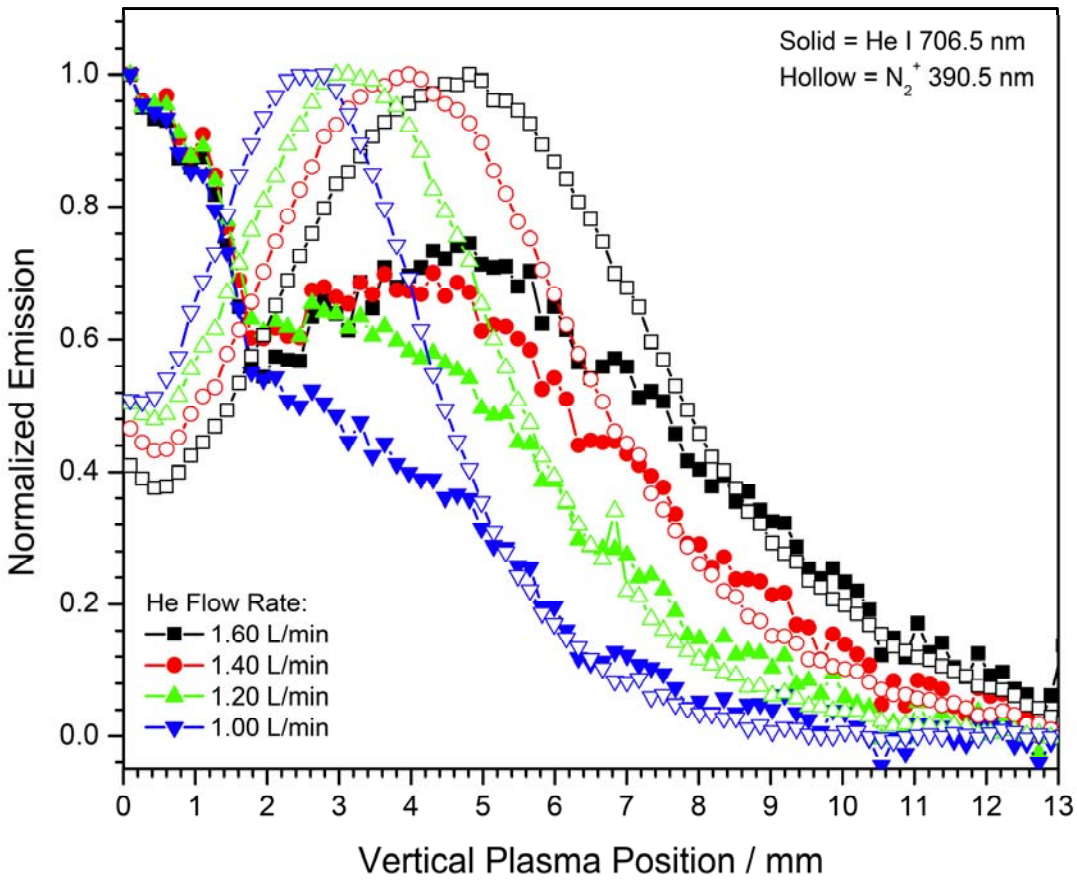

Figure 7.1 Normalized vertical emission profiles of He I 706.5 nm (solid symbols) and N_2^+ 390.5 nm (hollow symbols) in the He-LTP as a function of helium flow. Position zero is the edge of the glass torch with positive values extending into the ambient atmosphere.

the LTP. Position zero in Figure 7.1 refers to the edge of the plasma torch, with positive vertical distances extending into the open atmosphere (i.e. the typical sample introduction region). From Figure 7.1, the emission maxima for N_2^+ for gas flow rates of 1.00, 1.20, 1.40 and 1.60 L/min were found to be at 2.6, 3.0, 4.0 and 4.8 mm, respectively, whereas the second maxima for He I occur at 2.0, 2.6, 4.0 and 4.8 mm, respectively. The close correlation of spatial maxima for these species is likely due to a common formation/excitation mechanism, which is the subject of the present study. One plausible candidate for the formation of the N_2^+ ion is through Penning ionization from excited-state helium, as suggested in previous studies with similar plasmas.[10, 20]

7.3.3 Spatially Resolved Rotational Temperatures in the He-LTP

The rotational temperature is an important parameter for plasma diagnostics. One reason is that it is commonly assumed that the rotational temperature resembles the gas-kinetic temperature because of the rapid equilibrium between rotational levels and translational energies of a molecule. It was previously shown[15] that rotational temperatures in the LTP calculated from OH molecular emission bands agreed well with values from infrared thermometry obtained using gray-body emission from a glass substrate. However, in the present study, when N_2^+ was employed as the thermometric species, it was found that the above assumption was violated.

A prerequisite for using a Boltzmann plot for temperature measurement is that the excited states of the thermometric species must be populated according to the Boltzmann distribution. However, in some situations, Boltzmann plots deviate from a straight line; for example, when a particular group of levels is over- or under-populated compared to

other levels.[21, 22] Accordingly, representative Boltzmann plots are presented here and their linearity examined.

Figure 7.2a shows Boltzmann plots for N_2^+ from the He-LTP probe operated with a 1.60 L/min helium flow at observation heights of -4, 0, +4, and +8 mm with respect to the exit of the plasma torch. These Boltzmann plots are all satisfyingly linear with correlation coefficients > 0.997. However, unlike with the earlier OH emission measurements, there are clear differences in the slopes of the Boltzmann plots obtained at different observation heights. The corresponding N_2^+ rotational temperatures, in ascending order of observation height, were 358, 365, 400, and 436 K, with an estimated uncertainty of less than $\pm$ 10 K.

The spatial change in measured N_2^+ rotational temperatures is shown in Figure 7.2b. For comparison, OH rotational temperatures from the same experiment are also displayed in Figure 7.2b. Error bars indicate uncertainties in the slope of the linear regression, which in turn represent the uncertainty in the temperature measurements. This uncertainty is dictated by the emission strength of the species and is therefore spatially and species- dependent. Rotational temperatures for N_2^+ inside the plasma torch were relatively steady at about 350 K, but gradually increased after the exit of the LTP torch to a maximum of approximately 550 K in the tail of the plasma afterglow. In contrast, measured OH rotational temperatures were lower, in the range of 280 to 300 K, and were not statistically different from the temperature of the surrounding bath gas.

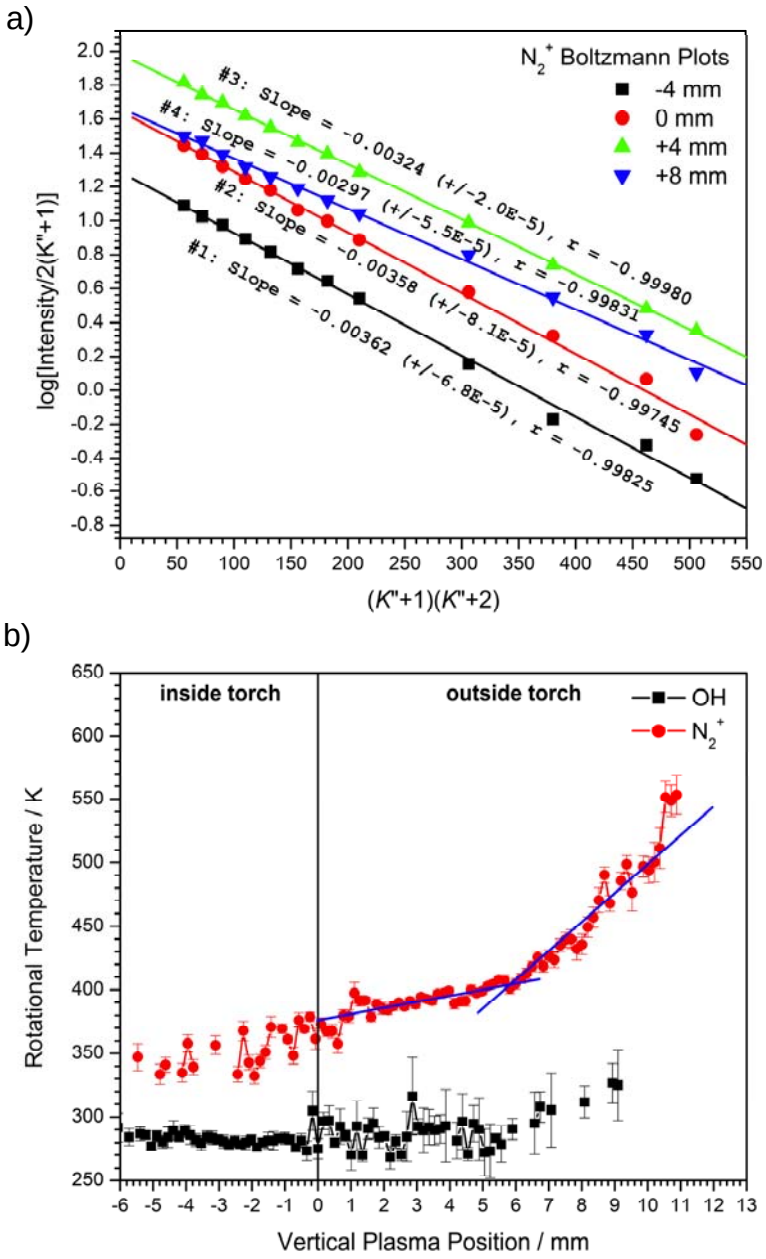

Figure 7.2 a) Boltzmann plots of N_2^+ rotational temperature at -4, 0, +4, and +8 mm from the exit of the LTP torch. b) Vertical profile of measured OH and N_2^+ rotational temperatures of He-LTP. Note the monotonically increasing trend for the N_2^+ rotational temperature. The two straight lines for the N_2^+ rotational temperature are included for visualization purposes. The error bars represent only the error of the slope in the linear regression. Helium flow rate was 1.60 L/min.

Inside the plasma torch, where the rotational temperatures of the two species were relatively steady, rotational temperatures from N_2^+ were still about 60 K higher than those from OH. Since the estimated uncertainties were only 10 K and 15 K for the rotational temperature measurements of N_2^+ and OH, respectively, this 60 K difference between these two species inside the plasma torch was statistically significant. Clearly, the common assumption that a rapid equilibrium exists between rotational levels and translational energies of a molecule in an atmospheric-pressure plasma is violated in the present case; otherwise, the temperatures from the two thermometric species would agree. Also, a monotonic increase in the N_2^+ rotational temperature is initially counter-intuitive, with the highest temperature being found in the decaying tail of the plasma. Because all the Boltzmann plots in Figure 7.2a are linear with correlation coefficients > 0.990 for OH and > 0.995 for N_2^+, the upward trend in the N_2^+ rotational temperature is not due to experimental artifacts. It is hypothesized that the high N_2^+ rotational temperature in the tail of the LTP is related to the ionization-excitation mechanism of the N_2^+ species, which will be discussed in the next section.

To a first approximation, the increase in N_2^+ rotational temperature outside the plasma torch can be divided into two sub-regions. First, the temperature exhibited a slow ramp until ~ 6 mm from the torch opening, beyond which it rose more rapidly in the tail of the plasma. The two regions are denoted in Figure 7.2b with straight lines only for identification purposes. The transition temperature between these two regions was approximately 400 K, and was located 5.8 mm outside the LTP torch. As will be shown below, the spatial location of this transition is flow-rate dependent and correlated with the spatial maximum of N_2^+ emission.

The effect of helium flow on the spatial pattern of the N_2^+ rotational temperature is displayed in Figure 7.3. For all helium flow rates from 0.40 to 1.60 L/min, the temperature profiles follow similar behavior – relatively steady and spatially independent values of 350 K inside the plasma torch, followed by a rapid increase outside the torch. In contrast, OH rotational temperatures (not shown) exhibited no spatial dependence and were statistically similar to the ambient temperature for helium flow rates between 0.40 and 1.60 L/min. Although the onset position for the rising N_2^+ rotational temperature changed with He flow rate, the maximum attainable temperature was found to be independent of gas velocity; maximum rotational temperatures of ~ 550 K were always observed in the tail of the afterglow (i.e., where N_2^+ emission decays and approaches baseline level, cf. Figure 7.1). Also, for all studied gas flow rates, the N_2^+ rotational temperature profiles exhibited two distinct regions outside the LTP torch – a slow temperature-ramp region and a rapidly rising zone toward the tail of afterglow. The transition between the two regions occurred at a temperature of about 400 K in every case, which corresponded to spatial locations of -0.6, 0.0, 0.7, 2.0, 2.5, 4.0, and 5.8 mm with respect to the torch opening for all ascending gas flows presented in Figure 7.3. Table 7.3 compares the spatial locations of the He I second emission maximum, the N_2^+ emission maximum, the N_2^+-rotation temperature transition, and the N_2 emission maximum for different gas flow rates. Generally, the spatial location of this transition aligned well with the spatial maximum of N_2^+ emission, which, in turn, correlated with the second maximum of helium atomic emission (cf. Figure 7.1 and Table 7.3), but is different from the position of maximum N_2 emission.

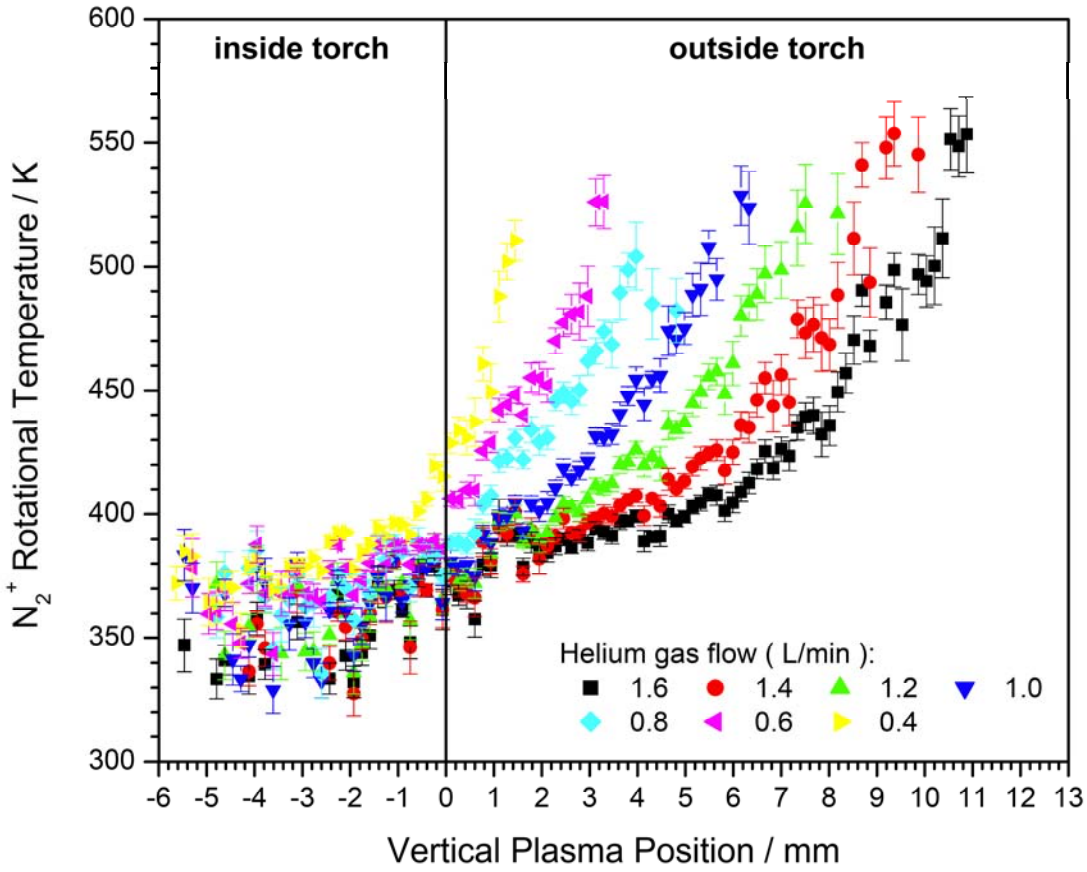

Figure 7.3 Vertically resolved N_2^+ rotational temperature of He-LTP at helium flows from 0.40 to 1.60 L/min. The error bars represent only the error of the slope in the linear regression.

Table 7.3. Spatial locations, relative to the exit of the LTP torch, of the second maximum of He I emission at 706.5 nm, peak emission of molecular N_2^+ at 390.5 nm and N_2 at 337 nm, and the transition point where the rotational temperature of N_2^+ starts to rise rapidly in the afterglow region.

Flow Rate (L/min)	He I Second Maximum (mm)	N_2^+ Emission Maximum (mm)	N_2^+ Rotational Temperature Transition (mm)	N_2 Emission Maximum (mm)
1.00	2.0	2.6	2.0	4.6
1.20	2.6	3.0	2.5	5.6
1.40	4.0	4.0	4.0	6.8
1.60	4.8	4.8	5.8	7.7

7.3.4 Proposed Mechanisms in the He-LTP Afterglow

7.3.4.1 Proposed Mechanism for N_2^+ Formation

The nitrogen dimer ion, N_2^+, has been widely reported to be a key intermediate species for analyte ionization with the He-LTP probe, as well as with other plasma-based ambient ionization sources.[3, 7, 10, 11] It has often been stated that Penning ionization of ambient nitrogen by metastable helium is the major or even the only mechanism for the generation of N_2^+, which subsequently leads to the formation of other reagent ions such as protonated water clusters.[10, 20] However, from the experimental results presented above, it appears that another important mechanism exists. Specifically, the two-region behavior of the rotational temperature of N_2^+ and the fact that rotational temperatures rapidly increase toward the tail of the plasma afterglow (where energy is almost completely dissipated) clearly suggest that another important mechanism exists. While it is not necessary to limit the explanation of these processes to only a single additional mechanism, the close correlation between the N_2^+ spatial profiles (both emission and rotational temperature) and He I emission profiles imply that the processes governing ionization/excitation of these two species might be linked. In addition, because N_2^+ is regarded as the ion primarily responsible for the generation of protonated water clusters (Reactions 5 to 8), which are ultimately the dominant species for analyte ionization in plasma-based ambient desorption/ionization sources, the close correlation between the spatial emission profiles of N_2^+ and He I suggests that it might be possible to optimize sample placement in ambient mass spectrometry by means of optical emission from helium and nitrogen species.

The second maximum in He I emission (cf. Figure 7.1), for intermediate to high helium flow rates, clearly indicates that some excited states of helium are formed outside the plasma torch. Furthermore, the chemical species that carry the energy from the DBD inside the torch to the afterglow region must be of high energy – higher than the upper energy level of the studied He I lines, 23.07 eV for the line at 587.56 nm. In a helium discharge, commonly identified high-energy chemical species are He^* ($n \geq 2$, including He^m), He_2^*, He^+ and He_2^+. In the present paper, He^m refers to excited helium specifically in the metastable states whereas He^*, unless given with specified principal quantum number(s), refers to any general excited states of helium including the metastable levels. For reasons that will become clear in the discussion that follows, the He_2^+ ion is likely the energy carrier for both the second emission maxima for He I lines and the N_2^+ maximum in the afterglow region of the He-LTP probe.

The helium dimer ion, He_2^+, was the subject of several very early studies on helium discharges and plasma afterglows.[23, 24] This dimer ion is a comparatively stable molecule with a bond order of ½ and bond dissociation energy about 2.5 eV.[25, 26] Unfortunately, the first and only documented electronic excited state for He_2^+ (the $A\ ^2\Sigma_g^+$ state) with the same dissociation product (He ($1\ ^1S$) + He^+ ($1\ ^2S$)) as the ground state of He_2^+ ion ($X\ ^2\Sigma_g^+$) is a dissociative repulsive state[34]; therefore, measurements of He_2^+ optical emission is practically not feasible. There are at least three main routes for He_2^+ formation in a helium plasma[27, 28] :

1) Ion conversion (three-body association reaction):

$$He^+ + 2\ He \rightarrow He_2^+ + He \qquad (k = 1.1 \text{ to } 1.4 \times 10^{-31}\ cm^6\ s^{-1})^{27, 28} \qquad (9)$$

2) Associative ionization (Hornbeck-Molnar[29] process):

$$He^{*}\ (n\geq 3) + He \rightarrow He_2^{+} + e^{-} \qquad (10)$$
($k = 0.13$ to 8.2×10^{-10} $cm^3\ s^{-1}$, He^{*}-level dependent[28])

3) Associative ionization (metastable conversion):

$$He^{m} + He^{m} \rightarrow He_2^{+} + e^{-} \qquad (k = 1.5 \text{ to } 2.0 \times 10^{-9}\ cm^3\ s^{-1})^{27, 28} \qquad (11)$$

It is generally agreed that He_2^{+} is dominant and of greater population density than the He^{+} ion in plasmas operated at pressures higher than 5 torr.[30, 31] At room temperature and atmospheric pressure, the He^{+}-ion conversion process (Reaction 9) is so efficient that typical times for conversion of the He^{+} population to He_2^{+} range between 12 ns and 27 ns.[32] Recently, a modeling study on a dielectric-barrier discharge showed that He_2^{+} completely dominates the positive-charge density at pressures higher than 105 torr. Even in lower-pressure regimes, from 38 to 105 torr, He^{+} is only 30% of the total positive-charge density in the discharge whereas the rest of positive-charge density exists in the form of He_2^{+} ion.[33]

In the afterglow region of the He-LTP, N_2^{+} could be formed by several ionization pathways that involve the aforementioned high-energy helium species (i.e., He^{*}, He_2^{*}, He^{+} and He_2^{+}). Figure 7.4 shows the energy levels of He_2^{+},[34, 35] He^{*} and He^{+},[18] selected He_2^{*},[34, 36] and the lowest four electronic states of the N_2^{+} ion.[34, 37, 38] Only vibrational levels are shown while rotational levels are omitted for clarity. For all these high-energy helium species, there exist energy levels of the N_2^{+} ion with a close energy match, so

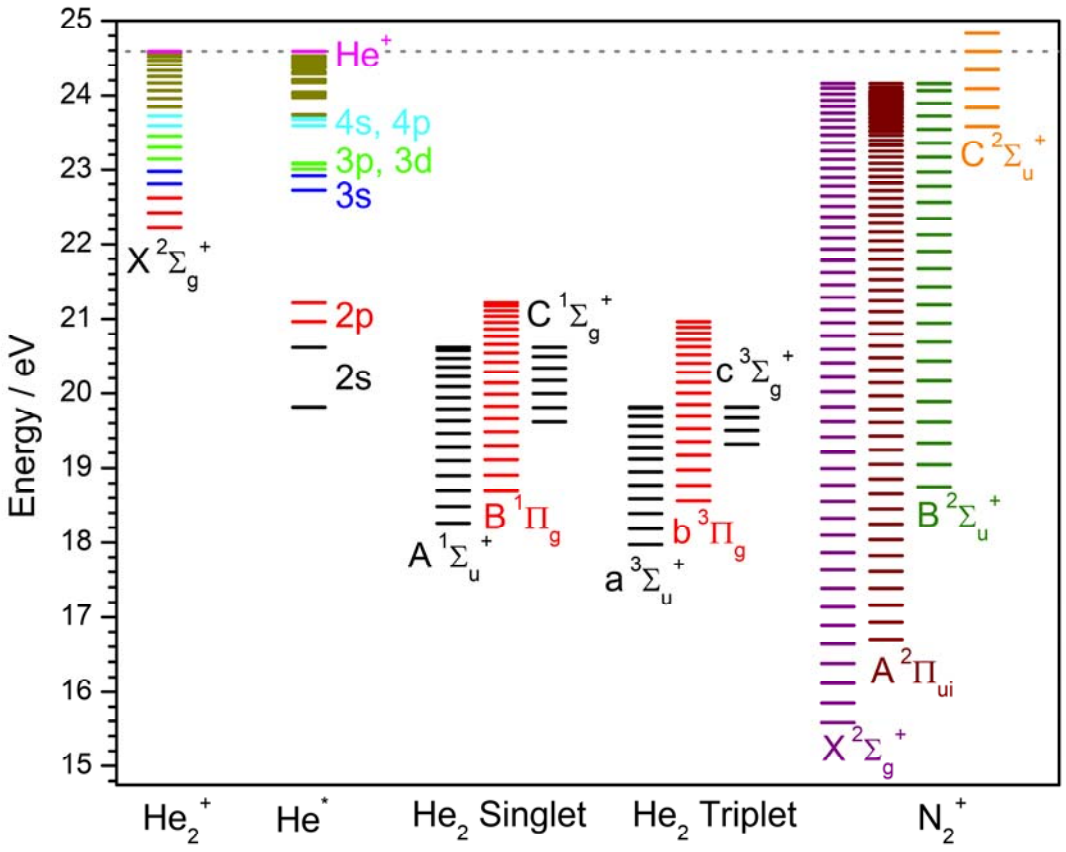

Figure 7.4 Energy level diagram of He_2^+, He^*, and He^+, selected He_2 excimer levels, and the four lowest electronic states of N_2^+. Zero energy refers to the constituent elements in their standard states (i.e., ground-state He atom for He^*, He^+, He_2^+ and He_2^* and ground-state N_2 molecule for N_2^+). The horizontal dotted line at 24.6 eV shows the ionization potential of helium. The vibrational energy levels of He_2^+ are color-coded to indicate the maximum energy levels of He^* that direct ion-electron dissociative recombination could produce. The He_2^* levels are color coded to reflect their limit of dissociation into the atomic helium energy levels. Energy levels of He_2^* are shown for the dissociation limit of the 2*s* and 2*p* levels of helium only; similarly, He_2^* electronic states will be formed from other excited states of He^* and they are omitted for clarity. For N_2^+, only the four lowest electronic states are shown, X $^2\Sigma_g^+$, A $^2\Pi_{ui}$ and B $^2\Sigma_u^+$ which all converge to the same dissociation limit.[37, 38]

near-resonance charge transfer is possible. For example, charge transfer (CT) from He_2^+ can ionize atmospheric nitrogen according to the reaction

CT from He_2^+: $He_2^+ + N_2 \rightarrow 2\ He + N_2^+$ (12)

Of course this CT reaction is a special case and a close match in energy levels is not required[39] because the dissociation of He_2^+ into two helium atoms can effectively carry away the excess energy of the reaction. Although there are other potential mechanisms for the ionization of N_2, CT from He_2^+ corresponds particularly well with the spatial profiles of the N_2^+ rotational temperature obtained here; as will be explained below, CT from He_2^+ is responsible for the "abnormal" rotational-temperature profile of N_2^+.

Two other known mechanisms for ionization of N_2 in helium plasmas are CT from He^+ and Penning ionization (PI) from metastable helium:

CT from He^+: $He^+ + N_2 \rightarrow He + N_2^+$ (13)

PI from He^m: $He^m + N_2 \rightarrow He + N_2^+ + e^-$ (14)

Reaction 14, it will be recalled, is the one currently favored in most recent publications involving plasma-based ambient desorption/ionization sources. It would seem that another PI mechanism could occur with the helium excimer, a $^3\Sigma_u^+$ He_2^*, which has an energy of around 18.1 eV[40] (vibrational ground state) – higher than the ionization potential of N_2 (15.6 eV). However, the sum of the ionization and excitation energies of the N_2^+ B $^2\Sigma_u^+$ electronic state (which emits from the first negative system with a

bandhead at 391 nm and was experimentally observed in the present study) is 18.9 eV, appreciably higher than that of the vibrational ground state of the helium excimer (cf. Figure 7.4). Moreover, unlike He_2^+ and He^+ ions, number densities of He_2^* are lower than those of He^m in both atmospheric- and reduced-pressure discharges.[33, 41] Therefore, mechanisms involving He_2^* need not be considered further.

Although Reactions 12, 13, and 14 above are all capable of producing N_2^+ in the $B\ ^2\Sigma_u^+$ electronic state (i.e., the first negative system with emission at 391 nm), the rotational energy distribution of the product ion, N_2^+ ($B\ ^2\Sigma_u^+$), is heavily dependent on the ionization pathway. Endoh[42] and co-workers studied Penning ionization of N_2 by He^m (Reaction 14) and charge transfer from He_2^+ (Reaction 12) at thermal energies. Emission from different rotational levels of the product ion, N_2^+ ($B\ ^2\Sigma_u^+ - X\ ^2\Sigma_g^+$), was reported for both reactions. The resulting Boltzmann plots for N_2^+ rotational levels were linear for both Reactions 12 and 14.[42] However, the rotational temperatures from these plots were quite different, with Reactions 12 and 14 yielding temperatures of 900±60 K and 360±30 K, respectively.[42] Richardson and Setser[43] also reported linear Boltzmann plots from the $N_2^+(B)$ rotational system for the $He(2\ ^3S)$–N_2 PI pathway (Reaction 14), but the derived rotational temperatures were consistently 30 to 50 K higher than the bath-gas temperature at either 175 K or 300 K. In the current work, rotational temperatures of approximately 350 K were measured inside the plasma torch (cf. Figure 7.3), which is in good agreement with the hypothesis that PI with He^m (i.e., Reaction 14) is one important pathway for the generation of N_2^+ ions within the He-LTP probe.

Concerning Reaction 13, it has been reported that the Boltzmann plot for the rotational levels of the $N_2^+(B)$ system formed by the $He^+–N_2$ charge-transfer reaction demonstrated a clear bimodal (i.e., non-linear) behavior[44]; the higher rotational levels of the $N_2^+(B)$ ion were reported to be overpopulated and exhibited a rotational temperature of 900±60 K. Because the $N_2^+(B)$ rotational temperatures of the He-LTP probe measured here were often higher than 400 K (cf. Figure 7.3) and because it is known, through the measurement of OH rotational temperatures and infrared thermometry, that the temperature of the LTP is similar to room temperature, the much higher $N_2^+(B)$ rotational temperature in the afterglow region seems likely to be caused by contributions from charge transfer reactions.

While charge transfer from either He^+ or He_2^+ could produce a rotationally heated $N_2^+(B)$ ion, Reaction 12 is more likely than Reaction 13 for several reasons: First, the population density of He_2^+ generated by a discharge at atmospheric pressure is orders of magnitude higher than that of He^+.[30, 31, 33] Second, the observed distribution of $N_2^+(B)$ vibrational states more closely resembles those previously reported for Reaction 12 than for Reaction 13.[39] In $He_2^+–N_2$ collisions, the dominant product is the $N_2^+(B)$ ion in vibrational level $\nu' = 0$, with a small fraction in $\nu' = 1$ and an even smaller fraction in $\nu' = 2$.[39] As a result, the $N_2^+(B)$ resulting emission spectrum is comparatively simple, with four discrete bands corresponding to $\Delta\nu = -1, 0, +1$, and $+2$[39], similar to the $N_2^+(B)$ bands observed in the present study (cf. Table 7.2). In contrast, $He^+–N_2$ collisions were reported to produce a much wider vibrational-state distribution, extending beyond $\nu' = 10$, and the resultant $N_2^+(B)$ spectrum to be dominated by unresolved features with tail bands.[39] Third, the Boltzmann plots of the $N_2^+(B)$ system for our He-LTP probe were

quite linear ($r \geq 0.995$) and lacked the characteristic bimodal feature of the He^+–N_2 charge transfer process.[44] Fourth, the lack of N_2^+ emission from the C $^2\Sigma_u^+$ state, which is a characteristic consequence of Reaction 13, strongly argues against such a reaction in the He-LTP probe. Emission characteristics from both N_2^+(B) and N_2^+(C) excited states after a near-thermal (≤ 0.1 eV) CT reaction between He^+ and N_2 were reported by Govers et al.[45] For He^+–N_2 charge transfer, the dominant product is not the N_2^+(B) state, but rather the N_2^+(C) state with $\nu' = 3$ and $\nu' = 4$, because of the near resonance in energy (energy difference from He^+ of 0.0037 eV and 0.0014 eV for N_2^+(C) at $\nu' = 3$, $K' = 36$ and $\nu' = 4$, $K' = 4$, respectively).[45] With our He-LTP probe, there was no measurable emission from N_2^+ (C $^2\Sigma_u^+$–X $^2\Sigma_g^+$, i.e., the second negative system located from 191.3 nm to 205.9 nm[19]).[15]

The highest N_2^+ rotational temperature measured for the He-LTP probe was only 550 K (cf. Figure 7.3), substantially lower than the 900 K given by Endoh *et al.*[42] in their He_2^+–N_2 charge-transfer study. However, this mismatch in rotational temperatures cannot be regarded as experimental evidence to refute the He_2^+–N_2 hypothesis. If Reactions 12 and 14 are both important pathways with comparable weighting, then a rotational temperature between the limits of 360 K and 900 K is expected.

Moreover, when emission intensities from two Boltzmann distributions having different temperatures are integrated, the resultant Boltzmann plot would ***not*** show bimodal behavior. Rather, the resulting Boltzmann plot would still be linear, as long as the individual components obey a proper Boltzmann distribution. Figure 7.5 shows simulated Boltzmann plots for N_2^+(B) bands consisting of different fractions of two

rotational populations, representative of 350 K and of 900 K as reported for Reactions 14 and 12, respectively. The plots are linear for all simulated cases and correlation coefficients are greater than 0.997. Boltzmann plots for integrated intensities with thermal gradients of 1 eV (i.e., ~ 11600 K) in the shape of a Gaussian distribution and another with a dip in the center have also been found to be linear.[46] Figure 7.5 indicates that contributions of only 10% or 30% from a high-temperature population (900 K) lead to apparent rotational temperatures of 400 K or 550 K, respectively.

Due to rotational relaxation, the exact contribution of Reaction 12 to N_2^+ formation in the afterglow cannot be determined. Collisions would relax the rotational populations toward thermal equilibrium. However, when the collisional time is of the same order as or longer than the lifetime of the rotational level, the rotational temperature would not be determined by the temperature of the surrounding bath gas; rather, it would be indicative of the excitation process because the rotational levels have not had sufficient time to equilibrate before undergoing radiative decay.[21] In contrast, if the collision time is significantly shorter than the lifetime of the rotational level, rotational relaxation would lead to a rotational temperature approaching the kinetic temperature of the ambient gas. The radiative lifetime of $N_2^+(B)$ rotational levels is about 66 ns.[47] However, quenching shortens the effective lifetime and it is known that electronic quenching is a major factor that prohibits thermalization of rotational levels, in particular at atmospheric pressure.[21, 48] Bibinov[47] and co-workers calculated that the rotational levels of $N_2^+(B)$, in 760 torr of helium, would thermalize and approach the distribution of

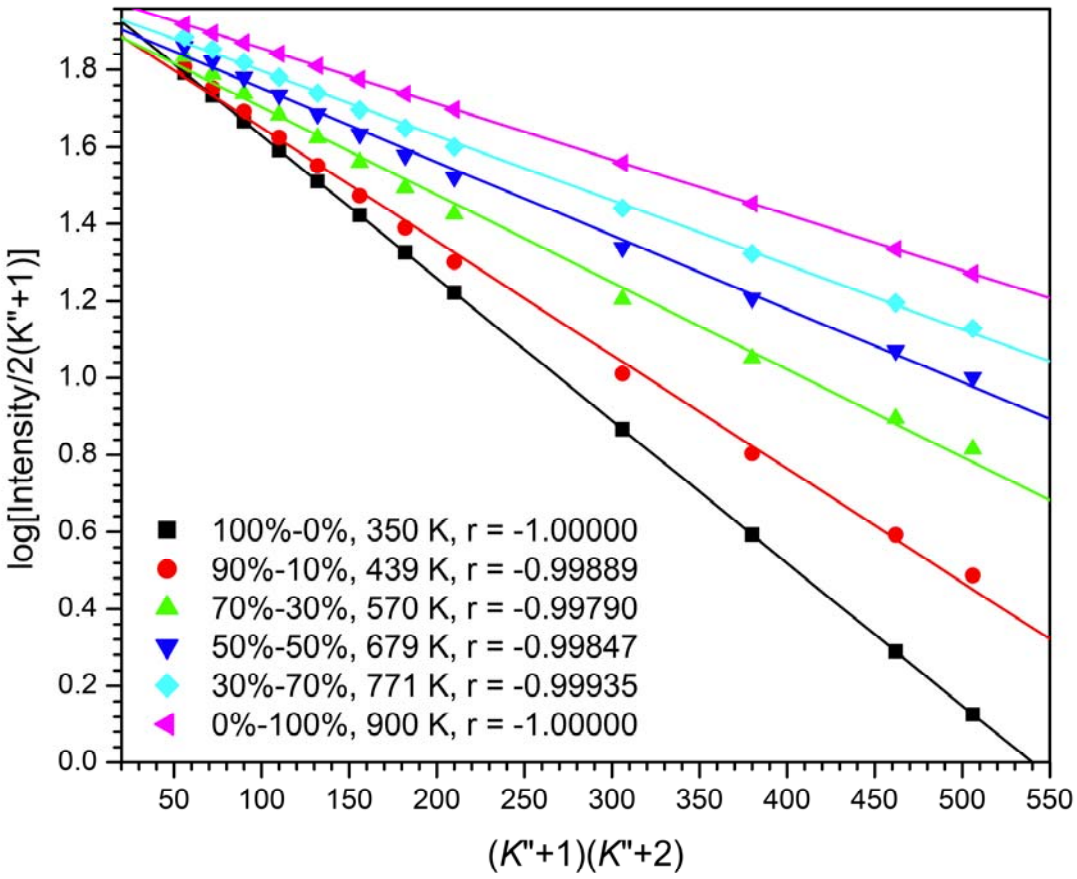

Figure 7.5 Simulated N_2^+ Boltzmann plots for different number-density combinations from two N_2^+ populations with hypothetical rotational temperatures of 350 K and 900 K. The number density combination is expressed as *a*%-*b*%, where *a*% and *b*% represent the weighing factors from the low- (350 K) and high- (900 K) temperature populations, respectively. The apparent temperature and the correlation coefficient of linear regression are also given.

the ambient temperature after a relaxation time of 5 ns. The rate of quenching of $N_2^+(B)$ states is a function of the partial pressure of nitrogen. It was reported that the effective lifetime of $N_2^+(B)$ is 5 ns when the partial pressure of nitrogen is 15 torr and the effective lifetime declines to 2 ns at a partial pressure of 48.7 torr.[47] As a result, thermalization of $N_2^+(B)$ rotational levels is not expected in the afterglow of the He-LTP, where the partial pressure of nitrogen is anticipated to be higher than 49 torr (i.e., ~ 7%).

Based on the above argument involving effective lifetime and rotational relaxation, the 350 K rotational temperature observed inside the LTP torch, where a low N_2 partial pressure exists, does not indicate an exclusive PI mechanism. Reaction 12 could have a significant contribution within the torch, but, due to rotational relaxation, the rotational temperature is partially relaxed and might not show characteristically overpopulated, high rotational levels. More realistically, the 10% and 30% contributions presented in Figure 7.5 define the *lower* limits on the contributions from Reaction 12 in the afterglow region for spatial locations that show apparent temperatures of around 400 K and 550 K, respectively. It should be stressed that the theme of the this paper is not to exclude the importance of Penning ionization in either the dielectric-barrier discharge itself or the afterglow region; instead, the main theme is to present experimental findings that demonstrate the significant and important contribution of charge transfer from He_2^+ ion.

7.3.4.2 Proposed Mechanism for Second Maximum in He I Emission

The presence of a second maximum in some He I emission profiles indicates that a channel for He^* (n = 3) generation exists in the afterglow. There are two reasons why it

is unlikely that this second peak is a direct consequence of radiative cascade from high-energy He^* states (e.g., He^* with $n \geq 4$). First, spontaneous emission is a very fast process with typical lifetimes on the order of 10 ns. The fact that the measured He I profiles demonstrate an initial valley followed by second peak suggests that the He I emission is generated from a long-lived species by a comparatively slow process. Second, atomic emission from higher levels ($n \geq 4$) (e.g., 396.47 nm, 447.15 nm, 492.19 nm and 504.77 nm)[18] was not detected.[15]

In contradistinction, dielectronic recombination of He_2^+ ion is a plausible candidate for producing the second maximum of He I emission in the afterglow. There are two routes for recombination of He_2^+ ion with electrons. In the indirect route, He_2^+ interacts with two electrons through a three-body collision to form a highly excited Rydberg dimer, He_2^{**}[49]:

$$He_2^+ + 2\ e^- \rightarrow He_2^{**} + e^- \tag{15}$$

This excited dimer can either revert back to He_2^+ through autoionization (typically back to a vibrational energy level that is lower than the original, due to energy loss) or dissociate through a three-body process:

$$He_2^{**} + He \rightarrow He^* + 2\ He \tag{16}$$

The second route, direct ion-electron dissociative recombination, can occur according to the following reaction[50, 51]:

$$He_2^+ + e^- \rightarrow He^* + He + K.E. \tag{17}$$

There are abundant literature reports on dissociative recombination of He_2^+.[50-53] It has been well documented that in order to generate an excited He^* with n = 3, the He_2^+ ion needs to be in a vibrationally excited state with $\nu \geq 3$ (i.e., the reverse of Reaction 10, the Hornbeck-Molnar process). Similarly, vibrationally excited states with $\nu \geq 8$ are needed to generate excited He^* with n = 4 (cf. Figure 7.4). For example, helium emission in plasma afterglows, with n = 3 and 4, has previously been traced back to dissociative recombination of vibrationally excited He_2^+.[54-57] Roger and Biondi[57] showed that broadening of the He I emission line at 587.6 nm (3d ^{3}D–2p ^{3}P transition) was caused by a gain in kinetic energy of the excited helium atom after dissociative recombination with He_2^+.

In contrast, He_2^+ in lower vibrational states, ν = 0, 1 or 2, can generate only metastable helium or other excited helium levels with n = 2, through direct dissociative recombination (cf. Figure 7.4); the branching ratio of the final excited state of He* after the direct dissociative recombination from He_2^+ ν = 0 was reported to be 4% for 2s ^{3}S, 37% for 2s ^{1}S, 59% for 2p ^{3}P and 3% for 2p ^{1}P (i.e., all with n = 2).[52] It is known that dissociative recombination of electrons with He_2^+ in its lowest vibrational states yields a significant portion of helium in one of its two metastable levels. These metastables could then serve as reactants for Penning ionization of ambient nitrogen (i.e., Penning ionization via a two-step process). However, this two-step process is rather inefficient compared to direct charge transfer from He_2^+ because direct dissociative recombination is particularly slow for ν = 0 and ν = 1[50, 58]. Effective dissociative recombination requires a crossing between the potential-energy curves of a repulsive (i.e., dissociative) excited He_2^* neutral molecule (which acts as a transition state) and the stable He_2^+ ion.[53, 58] The

early classic work by Mulliken[58], through theoretical considerations on the forms of the potential-energy curves, indicated that only vibrating He_2^+ ions are capable of undergoing dissociative recombination with electrons. The calculated potential-energy curves by Cohen[35] confirmed that there is no favorable curve crossing between the ground vibrational state of the ion and the repulsive state of the neutral dimer. The first vibrational level of He_2^+ that has a favorable curve crossing with the repulsive excited He_2^* dimer is $\nu = 3$;[35, 50, 59] the calculated cross section for dissociative recombination of He_2^+ indicates that the reaction rate would climb by four orders of magnitude when the initial vibrational levels are raised from $\nu = 0$ to $\nu = 3$.[59] Orders of magnitude increase in the experimentally determined rate of dissociative recombination for $\nu = 0$ and 1 versus $\nu \geq 2$ has recently been reported.[52, 60] Although the published reaction rate at room temperature for radiative recombination of He_2^+ with an electron ($\sim 1.7 \times 10^{-9}$ cm^3 s^{-1} for $\nu = 0$ or 1)[60] and charge transfer between He_2^+ and N_2 ($\sim 1.1 \times 10^{-9}$ cm^3 s^{-1})[61] are very similar, a consideration of the number densities of electrons and nitrogen in the afterglow region (ambient atmosphere) argues that charge transfer between He_2^+ and N_2 is the more favorable reaction (nitrogen is orders of magnitude more abundant than electrons in the afterglow). This further suggests that the two-step, coupled reaction – radiative recombination followed by Penning ionization – is competitively unlikely, even when He_2^+ becomes vibrationally relaxed. Of course, a fraction of He_2^+ might eventually become helium metastables, for example, through radiative recombination of those higher vibrational levels followed by radiative cascade of excited helium atoms, and the possibility of Penning ionization should not be completely excluded.

Our hypothesis for the origin of the second maximum in the He I emission profile within the LTP afterglow (cf. Figure 7.1) is dissociative recombination of vibrationally excited He_2^+, where $\nu \geq 3$. This hypothesis has two prerequisites – the presence of vibrationally excited He_2^+ and that the lifetimes of these vibrationally excited states are comparatively long. As mentioned above, there are three major mechanisms for the generation of He_2^+ in a plasma. For ion conversion (cf. Reaction 9), it was reported that the He_2^+ molecular ion is formed in excited vibrational states with $\nu \sim 15$.[30] For the Hornbeck-Molnar process (Reaction 10), both theoretical and experimental investigations indicate that the process is near-resonant and result in a vibrationally excited molecular ion of energy similar to that of He^* (e.g., $\nu = 4$ for 3d ^{1}D).[30] For metastable conversions (Reaction 11), it has been shown that for a collision energy of 0.03 eV (i.e., thermal energy), the He_2^+ product ions appear in a broad range of rotational states, with $j = 0$ to 38, and are concentrated in high vibrational states, with ν from 10 to 20.[62] Clearly, in any of the three mechanisms potentially responsible for He_2^+ formation in the LTP afterglow, the helium dimer ion would always be formed in highly excited vibrational and rotational states.[30]

With regard to the lifetime of these excited dimer ions, radiative decay of the vibrational levels is forbidden because $^4He_2^+$ possesses no permanent dipole moment; radiative lifetimes for various rovibrational states ($\nu = 2$ to 10) of the isotopomer $^3He^4He^+$ are reported to range from 0.2 to 1.0 s.[63] Additionally, the populations of vibrationally excited He_2^+ exceed the equilibrium value by several orders of magnitude, even at lower gas pressures of tens of torr.[64] Experimentally determined vibrational relaxation rates of

He_2^+ in helium have been reported to be $\leq 10^{-14}$ cm^3/s (for $k_{v,v-1}$)[54] and 0.8×10^{-16} cm^3/s[55], which correspond to characteristic times of ≥ 4 μs and 500 μs, respectively, at room temperature and atmospheric pressure. If one assumes that the gas-flow pattern exiting the LTP torch is laminar and flat-topped, the estimated travel times from the exit of the torch to the second emission maximum of He I (cf. Table 7.3) range from 1.4 to 2.0 ms. This travel time should be shorter for the central part of the afterglow because the velocity profile inside the LTP torch is expected to be in a parabolic shape. Considering this reduced transport time due to the parabolic velocity profile and the uncertainty typically encountered in measured reaction rates, it is reasonable to expect a non-negligible portion of vibrationally hot He_2^+ to survive well into the afterglow. Based on these results from the literature, the two prerequisites for the hypothesis of the He I emission mechanism in the afterglow of He-LTP are satisfied.

7.3.4.3 Proposed Mechanism for Formation of Excited Neutral N_2

Spatial emission profiles of N_2^+ and N_2 share some similarities and at the same time exhibit some distinct differences. In general, emission maxima for both N_2^+ and N_2 occurred outside the plasma torch. For all examined flow rates, N_2^+ and N_2 exhibited similar spatial profiles, but with a spatial shift in which N_2 emission occurred 2 to 3 mm beyond N_2^+ emission (cf. Table 7.3). It was concluded that the dominant mechanism of excitation for both N_2^+ and N_2 is not through electron impact because the experimentally observed emission intensity from $N_2^+(B)$ was much higher than that of $N_2(C)$, whereas electron-impact excitation of N_2 results in at least ten times more emission from N_2 than from N_2^+.[65, 66] Instead, for all the studied gas flow rates, the fixed spatial shift of N_2

emission relative to that of N_2^+ implies that excited N_2 molecules are likely formed via a recombination mechanism involving an electron and N_2^+, which is, in turn, created through charge transfer from helium dimer ion in the afterglow region, as discussed above. This recombination mechanism for N_2^+ can be either through direct recombination with any remaining electrons in the decaying tail of the afterglow or via electron transfer with an ambient molecule. The ionization potential (IP) of N_2 is high enough (15.58 eV) to capture an electron from (i.e., to ionize) other ambient molecules (e.g., O_2 and H_2O) in the open atmosphere that have lower ionization potentials (IP = 12.1 and 12.6 eV for O_2 and H_2O, respectively).

7.4 Conclusions

In this study, it was found that Penning ionization from metastable helium is not the sole ionization pathway for the production of N_2^+ ion in the LTP probe. A set of reaction mechanisms responsible for afterglow formation in the LTP probe ambient ionization source is then proposed (cf. Figure 7.6). Within the DBD plasma that powers the LTP probe, He_2^+ is formed and is the dominant positive ion in the plasma. The majority of He_2^+ is formed in highly excited vibrational and rotational states. Most importantly, this dimer ion acts as the carrier to transfer energy from the plasma to the afterglow region in the open atmosphere. Charge transfer between the He_2^+ ion and atmospheric nitrogen were identified to occur in the afterglow region to form the N_2^+ molecular ion, which is frequently reported to be an important reagent ion as well as the key reaction intermediate for the formation of other reagent ions, such as protonated water clusters, in ambient mass spectrometry. This He_2^+–N_2 charge-transfer reaction is

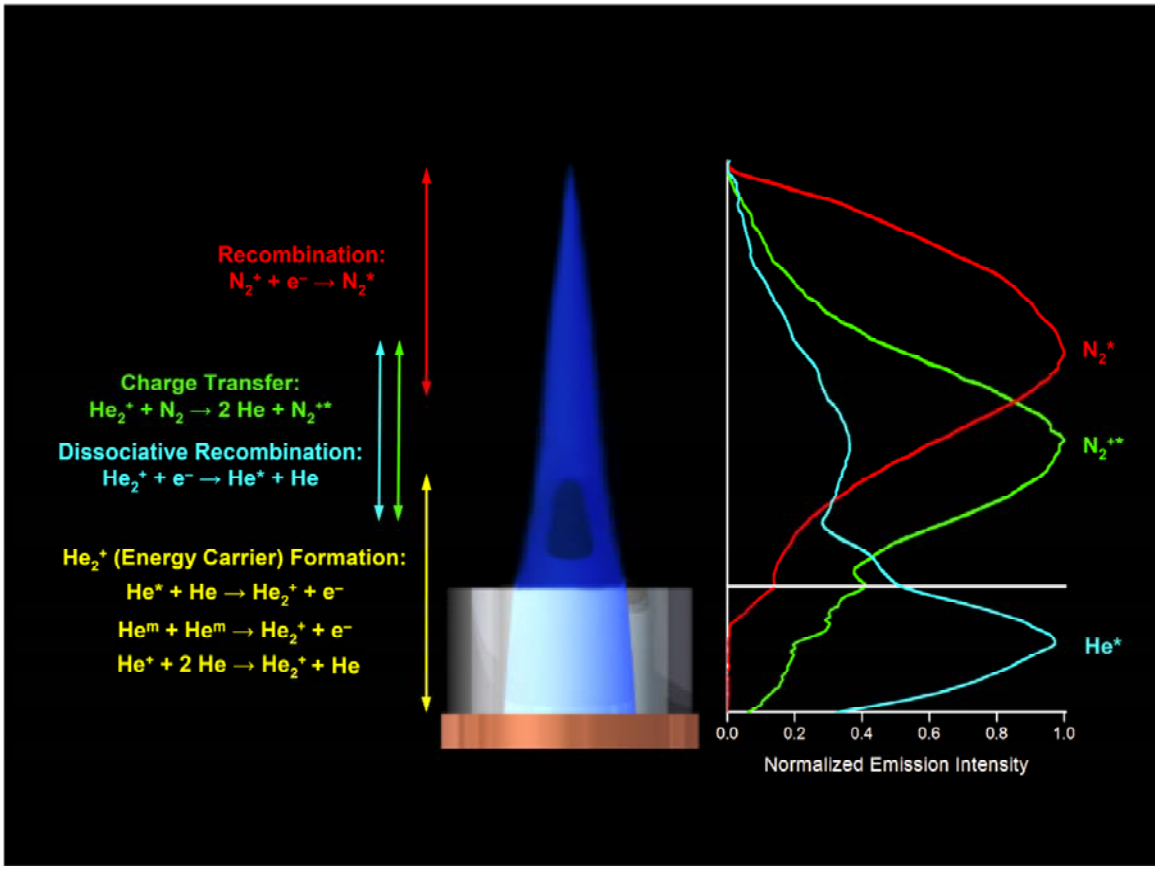

Figure 7.6 Schematic diagram showing the identified spatially dependent reactions for the afterglow and reagent-ion formation in the LTP probe ambient ionization source.

strongly supported by the fact that the N_2^+ rotational temperature in the afterglow region is significant higher than the ambient temperature measured by either OH rotational levels or IR thermometry. From the present study, it is not possible to determine the relative contributions of Penning ionization from helium metastable and charge transfer from helium dimer ion in the formation of N_2^+; however, it was determined that the ***minimum*** contribution of charge transfer from He_2^+ at the tail of the afterglow is 30%. At the same time, recombination of vibrationally excited He_2^+ with electrons leads to excited states of neutral atomic helium with $n \geq 3$, which then undergo radiative decay at characteristic emission wavelengths (e.g., 587.56 nm, 706.52 nm and 728.14 nm). As a result, the emission profiles of N_2^+ and atomic He are correlated in the afterglow. A portion of these N_2^+ molecules leads to the formation of reagent ions in ambient mass spectrometry as discussed above, whereas another portion undergoes a recombination process to form excited N_2 molecules, either directly with any remaining electron in the decaying tail of the afterglow or through ionizing an ambient molecule. Finally, it should be stressed again that the theme of this paper is not to refute the importance of Penning ionization in either the dielectric barrier discharge itself or the afterglow region. Instead, it should be realized that Penning ionization is not the lone or even dominant reaction for the generation of reagent ions in ambient desorption/ionization sources, and the possible important contribution and role of He_2^+ ion in helium-plasma-based ambient desorption/ionization sources should also be noted.

Although the current study has focused on only one type of discharge used as an ambient desorption/ionization source, it might be possible to apply these findings on fundamental reaction mechanisms to other plasma-based ambient desorption/ionization

sources. It has been reported in numerous plasma-physics publications that the helium dimer ion (He_2^+) is the dominant positive ion formed in many different kinds of discharges that operate in pure helium (despite their dissimilarities in physical characteristics), as long as the pressure is higher than approximately 5 torr. Because the reported plasma temperatures for all other types of helium discharges used in ambient mass spectrometry are comparatively low, and do not differ dramatically from the LTP, it is reasonable to expect that a significant portion of positive charges produced in other helium-plasma-based ambient desorption/ionization sources exists as He_2^+.

However, whether charge transfer from He_2^+ to N_2 is an important reaction for the generation of N_2^+ and, consequently, protonated water clusters, likely depends on the physical construction of the discharge chamber, which dictates the degree of plasma-sample interaction. For example, Direct Analysis in Real Time (DART) incorporates additional electrodes located outside of the plasma chamber, through which the plasma gas must pass prior to reaching the ambient air. In such a situation, the amount of He_2^+ that eventually enters the sample introduction region might be strongly reduced or completely eliminated.

Physical distance and transport time of the plasma effluent between the discharge cell and the sample location is another key parameter to consider because of the recombination process between He_2^+ and electrons. If the transport time is long with respect to the time scale of He_2^+ recombination, the population of He_2^+ might be too low for the charge-transfer reaction to be important. However, for sources in which the plasma directly extends into the open atmosphere and interacts with the sample (e.g.,

FAPA and PADI), it is reasonable to expect that charge transfer from He_2^+ is important for the formation of N_2^+. This charge transfer mechanism definitely should be considered in future studies of this kind and possibly be re-investigated in other established ambient desorption/ionization sources.

References

1. Cooks, R. G.; Ouyang, Z.; Takats, Z.; Wiseman, J. M. *Science* **2006**, *311*, 1566-1570.
2. Takats, Z.; Wiseman, J. M.; Gologan, B.; Cooks, R. G. *Science* **2004**, *306*, 471-473.
3. Kertesz, V.; Ford, M. J.; Van Berkel, G. J. *Anal. Chem.* **2005**, *77*, 7183-7189.
4. Cody, R. B.; Laramee, J. A.; Durst, H. D. *Anal. Chem.* **2005**, *77*, 2297-2302.
5. Shelley, J. T.; Wiley, J. S.; Chan, G. C. Y.; Schilling, G. D.; Ray, S. J.; Hieftje, G. M. *J. Am. Soc. Mass Spectrom.* **2009**, *20*, 837-844.
6. Andrade, F. J.; Shelley, J. T.; Wetzel, W. C.; Webb, M. R.; Gamez, G.; Ray, S. J.; Hieftje, G. M. *Anal. Chem.* **2008**, *80*, 2646-2653.
7. Andrade, F. J.; Shelley, J. T.; Wetzel, W. C.; Webb, M. R.; Gamez, G.; Ray, S. J.; Hieftje, G. M. *Anal. Chem.* **2008**, *80*, 2654-2663.
8. McEwen, C. N.; McKay, R. G.; Larsen, B. S. *Anal. Chem.* **2005**, *77*, 7826-7831.
9. Takats, Z.; Cotte-Rodriguez, I.; Talaty, N.; Chen, H. W.; Cooks, R. G. *Chemical Communications* **2005**, 1950-1952.
10. Ratcliffe, L. V.; Rutten, F. J. M.; Barrett, D. A.; Whitmore, T.; Seymour, D.; Greenwood, C.; Aranda-Gonzalvo, Y.; Robinson, S.; McCoustra, M. *Anal. Chem.* **2007**, *79*, 6094-6101.
11. Na, N.; Zhao, M. X.; Zhang, S. C.; Yang, C. D.; Zhang, X. R. *J. Am. Soc. Mass Spectrom.* **2007**, *18*, 1859-1862.
12. Harper, J. D.; Charipar, N. A.; Mulligan, C. C.; Zhang, X. R.; Cooks, R. G.; Ouyang, Z. *Anal. Chem.* **2008**, *80*, 9097-9104.

13. Song, L. G.; Dykstra, A. B.; Yao, H. F.; Bartmess, J. E. *J. Am. Soc. Mass Spectrom.* **2009**, *20*, 42-50.

14. McEwen, C. N.; Larsen, B. S. *J. Am. Soc. Mass Spectrom.* **2009**, *20*, 1518-1521.

15. Cody, R. B. *Anal. Chem.* **2009**, *81*, 1101-1107.

16. Shelley, J. T.; Hieftje, G. M. *J. Anal. At. Spectrom.* **2010**, *25*, 345-350.

17. Andrade, F. J.; Wetzel, W. C.; Chan, G. C. Y.; Webb, M. R.; Gamez, G.; Ray, S. J.; Hieftje, G. M. *J. Anal. At. Spectrom.* **2006**, *21*, 1175-1184.

18. Michels, A.; Tombrink, S.; Vautz, W.; Miclea, M.; Franzke, J. *Spectrochim. Acta Part B* **2007**, *62*, 1208-1215.

19. Olenici-Craciunescu, S. B.; Michels, A.; Meyer, C.; Heming, R.; Tombrink, S.; Vautz, W.; Franzke, J. *Spectrochim. Acta Part B* **2009**, *64*, 1253-1258.

20. Zhu, Z. L.; Chan, G. C. Y.; Ray, S. J.; Zhang, X. R.; Hieftje, G. M. *Anal. Chem.* **2008**, *80*, 8622-8627.

21. Paris, P.; Aints, M.; Valk, F.; Plank, T.; Haljaste, A.; Kozlov, K. V.; Wagner, H. E. *J. Phys. D.* **2005**, *38*, 3894-3899.

22. Paris, P.; Aints, M.; Laan, M.; Valk, F. *J. Phys. D.* **2004**, *37*, 1179-1184.

23. Chan, G. C. Y.; Shelley, J. T.; Wiley, J. S.; Engelhard, C.; Jackson, A. U.; Cooks, R. G.; Hieftje, G. M. *Anal. Chem.* **2010**, submitted.

24. Ascenzi, D.; Franceschi, P.; Guella, G.; Tosi, P. *The Journal of Physical Chemistry A* **2006**, *110*, 7841-7847.

25. Moon, S. Y.; Choe, W. *Spectrochim. Acta Part B* **2003**, *58*, 249-257.

26. Ishii, I.; Montaser, A. *Spectrochim. Acta Part B* **1991**, *46*, 1197-1206.

27. Dieke, G. H.; Crosswhite, H. M. *J. Quant. Spectrosc. Radiat. Transf.* **1962**, *2*, 97-&.

28. Chidsey, I. L.; Crosley, D. R. *J. Quant. Spectrosc. Radiat. Transf.* **1980**, *23*, 187-199.

29. Mermet, J. M., in *Inductively Coupled Plasma Emission Spectroscopy-Part 2*, ed. P. W. J. M. Boumans. Wiley-Interscience: New York, 1987, vol. 90, pp 353-386.

30. Bruggeman, P.; Schram, D. C.; Kong, M. G.; Leys, C. *Plasma Processes and Polymers* **2009**, *6*, 751-762.

31. Linss, V.; Kupfer, H.; Peter, S.; Richter, F. *J. Phys. D.* **2004**, *37*, 1935-1944.

32. Kelleher, D. E.; Wiese, W. L.; Helbig, V.; Greene, R. L.; Oza, D. H. *Phys. Scr.* **1993**, *T47*, 75-79.

33. Torres, J.; van de Sande, M. J.; van der Mullen, J.; Gamero, A.; Sola, A. *Spectrochim. Acta Part B* **2006**, *61*, 58-68.

34. Lindholm, E. *Ark. Mat. Astron. Fys.* **1946**, *32A*, No. 17.

35. Foley, H. M. *Phys. Rev.* **1946**, *69*, 616.

36. Gigosos, M. A.; Gonzalez, M. A.; Cardenoso, V. *Spectrochim. Acta Part B* **2003**, *58*, 1489-1504.

37. Martens, T.; Bogaerts, A.; Brok, W. J. M.; van der Mullen, J. *J. Anal. At. Spectrom.* **2007**, *22*, 1033-1042.

38. Chen, H.; Gamez, G.; Zenobi, R. *J. Am. Soc. Mass Spectrom.* **2009**, *20*, 1947-1963.

39. Jackson, A. U. Method Development, Novel Applications and Fundamental Studies of Ambient Ionization Methods: Desorption Electrospray Ionization

(Desi) and Low Temperature Plasma (Ltp) Ionization. Ph.D. Thesis, Purdue University, West Lafayette, 2010.

Chapter 8

Understanding the Flowing Atmospheric-Pressure Afterglow Ambient Ionization Source Through Optical Means

---

8.1 Introduction

Recently, a large number of atmospheric-pressure ionization sources has been introduced that enable direct analysis of samples for detection by mass spectrometry. This emerging technology has resulted in a new field termed ambient desorption/ionization mass spectrometry (ADI-MS). Since the introduction of the field in 2004,[1-2] over 30 ambient desorption/ionization sources have been described in the literature.[3-4] While the designs of these sources differ substantially, they can be categorized by the physical principles that ultimately lead to extraction and ionization of analytes from a sample surface. The three main categories are spray-based, laser-based, and plasma-based methods.

Spray-based sources include desorption electrospray ionization (DESI),[1] extractive electrospray ionization (EESI),[5] and easy ambient sonic spray ionization (EASI).[6] The mass spectra obtained with these sources are often similar to those of electrospray ionization (ESI) mass spectrometry (MS). The desorption process, however, was not as well studied. Thus, considerable attention has been focused on understanding the fundamental processes governing analyte extraction/desorption, particularly in the case of DESI.[7-9]

Laser-based sources include matrix-assisted laser desorption electrospray ionization (MALDESI),[10] laser diode thermal desorption (LDTD),[11] and laser ablation electrospray ionization (LAESI).[12] Such sources employ a laser to volatilize analytes and rely on an established secondary process for ionization, such as ESI or atmospheric-pressure chemical ionization (APCI). Because the ionization pathways are fairly well known, much of the fundamental examination of these sources has focused on establishing parameters that lead to optimal analyte sampling and transport, such as laser wavelength and ablation-plume formation.[13-14]

Plasma-based devices are probably the most diverse group of ADI-MS sources because of the many types of discharges that have been used. Examples include direct-current plasmas,[15-17] dielectric-barrier discharges (DBDs),[18-19] radiofrequency glow discharges,[20] and microhollow cathode discharges.[21] It is commonly believed that most of the plasma-based ADI-MS sources thermally desorb analytes and ionize them with reagent ions, similarly to APCI, that are generated from the interaction of plasma species with atmospheric constituents. While many of these plasmas have been fundamentally

characterized, it is often in the context of their use in atomic spectroscopy. In such studies, these discharges have been found to differ drastically in electron number density (n_e), excitation temperature (T_{exc}), gas-kinetic temperature, and other conventional plasma parameters. Although these factors are known to dictate the performance of a plasma in atomic analyses, their role in ionization of molecules for mass spectrometry is not necessarily the same.

A few publications have addressed fundamental characteristics of discharges utilized for molecular mass spectrometry. A transient microenvironment mechanism was used to explain analyte ionization and matrix effects observed with direct analysis in real time (DART), a DC-discharge-based source.[22] Similarly, ionization matrix effects for three plasma-based sources, DART, the flowing atmospheric-pressure afterglow (FAPA), and the low-temperature plasma (LTP) probe, were compared based on analyte and matrix proton affinity.[23] Ionization mechanisms for DART in the negative-ionization mode were compared with those for APCI and atmospheric-pressure photoionization (APPI) by analyzing a large suite of molecules.[24-25] Franzke et al.[26] compared emission spectra from a DBD, using different discharge gases, with protonated analyte signals from an ion-mobility spectrometer.

Our research group has examined in some detail three plasma-based ADI-MS sources. Direct-current, helium discharges used by DART and FAPA were examined by optical and mass spectrometry to characterize discharge structures.[27] Spatially resolved emission from the DBD-based LTP probe was used to determine the origin of species such as water and oxygen that are important in the ionization process, and also conditions

that affect formation of plasma species relevant to ADI-MS.[28] In a subsequent publication, these spatial profiles in conjunction with a detailed literature survey revealed that He_2^+ contributes significantly to the reagent-ion formation process.[29] Fundamental characterization of plasma-based ambient-ionization sources through optical and mass spectrometric means can yield insight into reactions taking place in the discharge and conditions affecting analyte desorption/ionization

In the present study, the atmospheric-pressure glow discharge (APGD) and the corresponding afterglow of the FAPA source were studied via optical spectroscopy under a variety of plasma operating conditions. Spatially resolved emission spectra from the discharge provide information about the species created in the plasma, as well as values for gas temperature and electron number density. These findings will be discussed in the context of ADI-MS analyses with the FAPA.

8.2 Experimental

8.2.1 FAPA Source

To enable emission from the discharge and afterglow of the FAPA to be detected, a special FAPA cell with a quartz body was constructed.[27] The helium APGD was established between a stainless-steel pin (3.1-mm diameter with ~39° taper angle) and a brass plate that were sealed to a quartz tube (13.2-mm o.d., 12-mm i.d.) with Viton® o-rings (cf. Figure 8.1). The distance between the electrodes was fixed at 7.5 mm. A 1.6-mm diameter hole in the center of the brass plate allowed species generated in the discharge to flow into the open atmosphere, resulting in the afterglow. A small raised

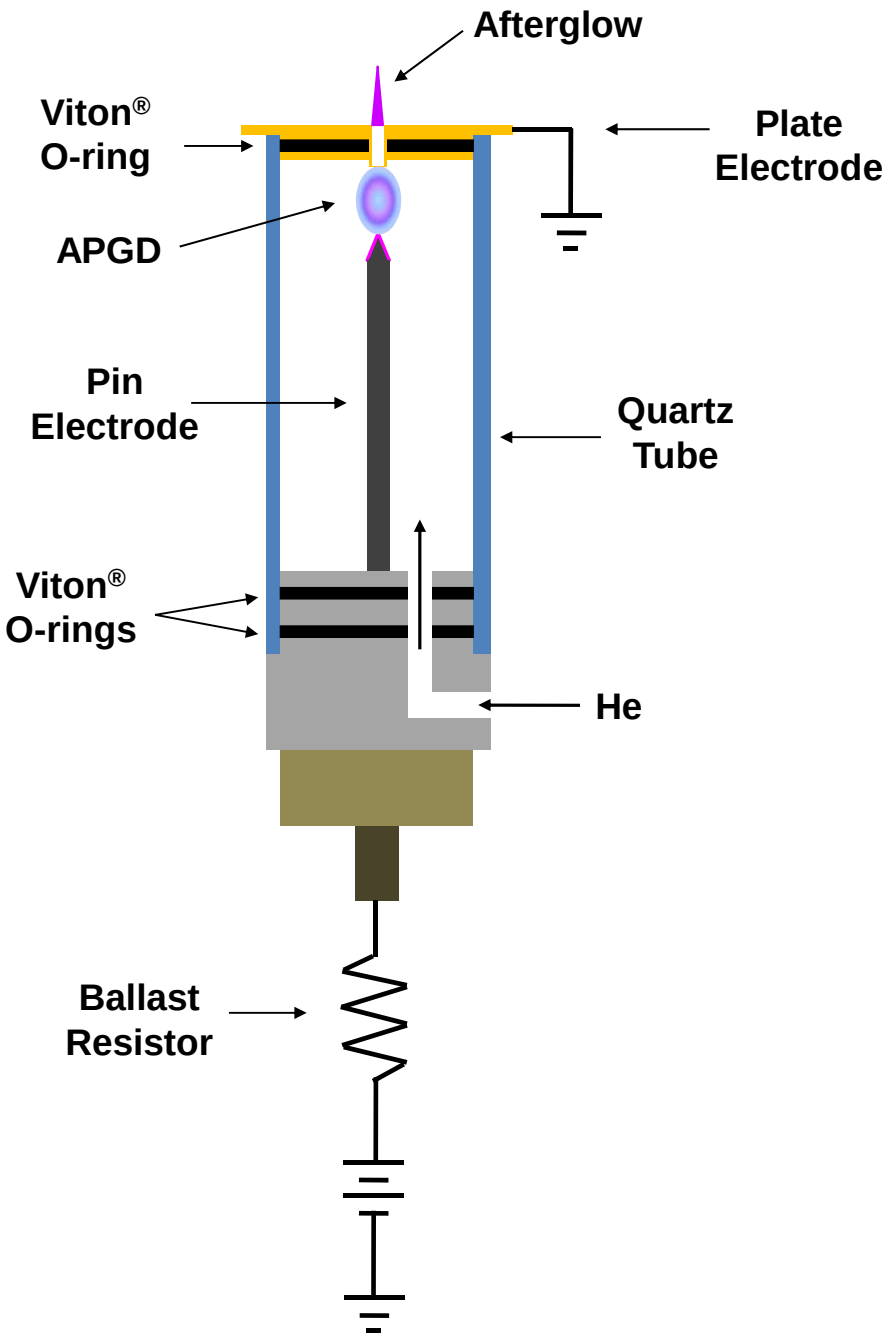

Figure 8.1 Diagram of the quartz-bodied FAPA cell used for the present optical studies. A positive or negative DC potential was applied to the pin electrode, while the brass plate was grounded. The inter-electrode distance was fixed at 7.5 mm for all experiments.

edge around the hole in the plate inside the discharge chamber ensured that the discharge reproducibly formed from the pin to the raised edge on the hole. The discharge was always operated in a current-controlled mode with either a positive or negative potential applied to the pin electrode with a high-voltage, DC power supply (Model BRC-5-400R, Universal Voltronics Corp, Mt. Kisco, NY), while the plate electrode was always maintained at ground potential. A 5 kΩ ballast resistor was placed in series with the pin to compensate for the inherent negative dynamic resistance of glow discharges at atmospheric pressure. Ultrahigh purity helium (99.999% purity, Airgas, Radnor, PA) was supplied to the discharge chamber with a mass flow controller (MKS Instruments, Andover, MA).

8.2.2 Optical Emission Measurements

Spatially resolved spectroscopic measurements were made with a commercial emission spectrometer (ACTIVA, Horiba–Jobin Yvon, Longjumeau, France) ordinarily used for inductively coupled plasma (ICP) atomic emission spectroscopy with a few optical modifications.[30] The quartz FAPA cell was positioned in place of the ICP torch on a translational stage for alignment with the slit of the spectrometer. The ACTIVA spectrometer utilizes a Czerny-Turner configuration, which preserves the spatial image focused onto the entrance slit. With the aid of a two-dimensional charge-coupled device (CCD) detector, spatial and spectral information were simultaneously obtained.

The image of the FAPA was demagnified by a ratio of 3.7:1, which resulted in a maximum observable distance of 25.6 mm. This large viewing range enabled imaging of the APGD and the afterglow of the FAPA without changing the position of the source.

However, the intensity of those two discharge regions was drastically different. Accordingly, to prevent detector saturation and blooming, the APGD region was covered with black paper when it was desired to measure emission from the weak afterglow. Integration times for the APGD and the afterglow were 1 to 10 s and 65 s, respectively.

The entrance slit of the spectrometer was set to 10 μm, which led to a spectral resolution between 8 and 16 pm for UV and visible wavelengths, respectively. This resolution was satisfactory even for distinguishing between different rotational features of molecules. The physical size of the APGD and the afterglow are narrow, less than 1.5 mm in diameter, so alignment of the source with respect to the spectrometer was crucial. This alignment was achieved with the spectrometer set to zero order; the source position was then adjusted for maximum signal. This maximum signal was checked every few hours and at the beginning of each day. Conveniently, the discharge was so stable that zero-order emission never deviated more than 10% from the optimal signal, so the FAPA never needed to be realigned.

8.3 Results and Discussion

8.3.1 Plasma Species Present in the APGD and Afterglow of the FAPA

UV-visible emission spectra can help identify species present in a plasma that might be useful for plasma diagnostics and for characterizing ionization pathways. Andrade et al.[31] presented an emission spectrum from a He APGD in a sealed discharge chamber. In addition to the expected emission lines from He, atomic emission from oxygen and nitrogen as well as emission bands of various diatomic species (NO, OH, N_2,

and N_2^+) were observed. For a DC He APGD similar to that employed in FAPA, Gielniak et al.[32] also discovered the presence of CN and NH. In both cases, the presence of non-helium species was attributed to impurities in the gas supply or transfer lines.

Table 8.1 lists the most abundant atomic and molecular species detected in the APGD of the FAPA used in the present study with a pin-negative configuration at 25 mA and a He flow rate of 1.5 L/min, which are the normal operating conditions of this source in ADI-MS analyses. Compared to the previously mentioned studies, only a few different species were detected in our APGD. Both atomic and molecular carbon, in the form of CO^+, were readily observed in the low-wavelength region of the spectrum. The source of carbon in the discharge is believed to be the Viton® o-ring used to seal the plate electrode to the inside of the glass chamber. As the plate electrode is heated by the discharge, the o-ring will outgas or, under extreme operating conditions, even melt, leading to the presence of hydrocarbons in the discharge.

Another species that was detected in the present APGD was the helium excimer, He_2^*, with multiple bands between 460 and 650 nm (cf. Table 8.1). The He_2^* molecule is particularly interesting because it has a ground vibrational state of ~18 eV[33] and the upper energy levels of the observed transitions are greater than 20 eV;[34] these energies are sufficient to cause Penning ionization of atmospheric constituents. Of particular interest are N_2 and H_2O, with ionization energies of 15.6 and 12.6 eV, respectively, because the ionic forms of these molecules are well known reagent species in APCI; these reagent ions can undergo charge-transfer or proton-transfer ionization with gas-phase analyte molecules, leading to simple mass spectra and a wide-range of ionizable analytes.

Table 8.1. Major atomic and molecular species observed in the emission spectrum of the helium APGD from the FAPA operated at 25 mA with a helium flow rate of 1.5 L/min.

Emitting Species	Transition	Wavelength / nm
NO	$A\ ^2\Sigma^+ - X\ ^2\Pi$	202 – 273 (ν'=0, 1)
CO^+	$B\ ^2\Sigma - X\ ^2\Sigma$	203 – 277 (ν'=0, 1, 2, 3, 4, 5)
OH	$A\ ^2\Sigma^+ - X\ ^2\Pi$	281 – 309 (ν'=0, 1)
N_2	$C\ ^3\Pi_u - B\ ^3\Pi_g$	295 – 434.5 (ν'=0, 1, 2)
N_2^+	$B\ ^2\Sigma_u^+ - X\ ^2\Sigma_g^+$	387 – 471 (ν'=0)
He_2	$e\ ^3\Pi_g - a\ ^3\Sigma_u^+$	460 – 475 (ν'=0)
	$f\ ^3\Delta_u - b\ ^3\Pi_g$	568 – 605 (ν'=0)
	$F\ ^1\Delta_u - B\ ^1\Pi_g$	605 – 630 (ν'=0)
	$d\ ^3\Sigma_u^+ - b\ ^3\Pi_g$	630 – 650 (ν'=0)
H I	H_β	486.13
	H_α	656.28
He I	$3p\ ^3P_2^\circ - 2s\ ^3S_1$	388.86
	$3p\ ^1P_1^\circ - 2s\ ^1S_0$	501.57
	$3d\ ^3D_{1,2,3} - 2p\ ^3P_{0,1,2}^\circ$	587.56
	$3d\ ^1D_2 - 2p\ ^1P_1^\circ$	667.82
	$3s\ ^3S_1 - 2p\ ^3P_{0,1,2}^\circ$	706.52
	$3s\ ^1S_0 - 2p\ ^1P_1^\circ$	728.14
O I	$(^4S^\circ)3p\ ^5P_3 - (^4S^\circ)3p\ ^5S_2^\circ$	777.194
	$(^4S^\circ)3p\ ^5P_2 - (^4S^\circ)3p\ ^5S_2^\circ$	777.417
	$(^4S^\circ)3p\ ^5P_1 - (^4S^\circ)3p\ ^5S_2^\circ$	777.539

It was earlier theorized that reagent ions in helium-plasma ambient ionization sources were produced by Penning ionization of N_2 and H_2O with helium metastable atoms, He^m.[16, 18, 20] However, it was recently demonstrated with the LTP probe that at least 30% of N_2^+ is formed through charge transfer with He_2^+.[29] Furthermore, a theoretical characterization of a helium APGD[35] found that the number densities of He^m and He_2^* in the bulk of the plasma were approximately the same. Therefore, it is reasonable to hypothesize that He_2^* serves as an additional energy carrier from the discharge to the atmosphere and would thus be an additional mechanism of reagent-ion formation. This mechanism might be particularly relevant for DART, in which grids are placed after the discharge region such that only neutral species enter the open atmosphere.

In contrast to the APGD itself, the UV-visible emission spectrum of the afterglow was much weaker and simpler (cf. Figure 8.2). Because emission from the afterglow is very weak under usual FAPA operating conditions, 1.5 L/min helium and 25 mA discharge current, the gas flow rate and discharge current were increased to 3.25 L/min and 50 mA, respectively, to produce the spectrum in Figure 8.2. Additionally, the integration time of the detector was set to the maximum, 65 s. The only detected atomic species were hydrogen and oxygen, likely from the dissociation of H_2O and O_2, respectively,[28] with the rest of the spectrum consisting of vibrational bands of molecules. The strongest emitting species were OH ($A_2\Sigma^+$) and N_2^+ ($B^2\Sigma_u^+$), which were significantly more intense than any other species in the afterglow. Both OH and N_2^+ are thought to be important in the formation of protonated water clusters, $(H_2O)_nH^+$, which are the most abundant positive reagent ions produced by the FAPA.[15] Other molecular species found

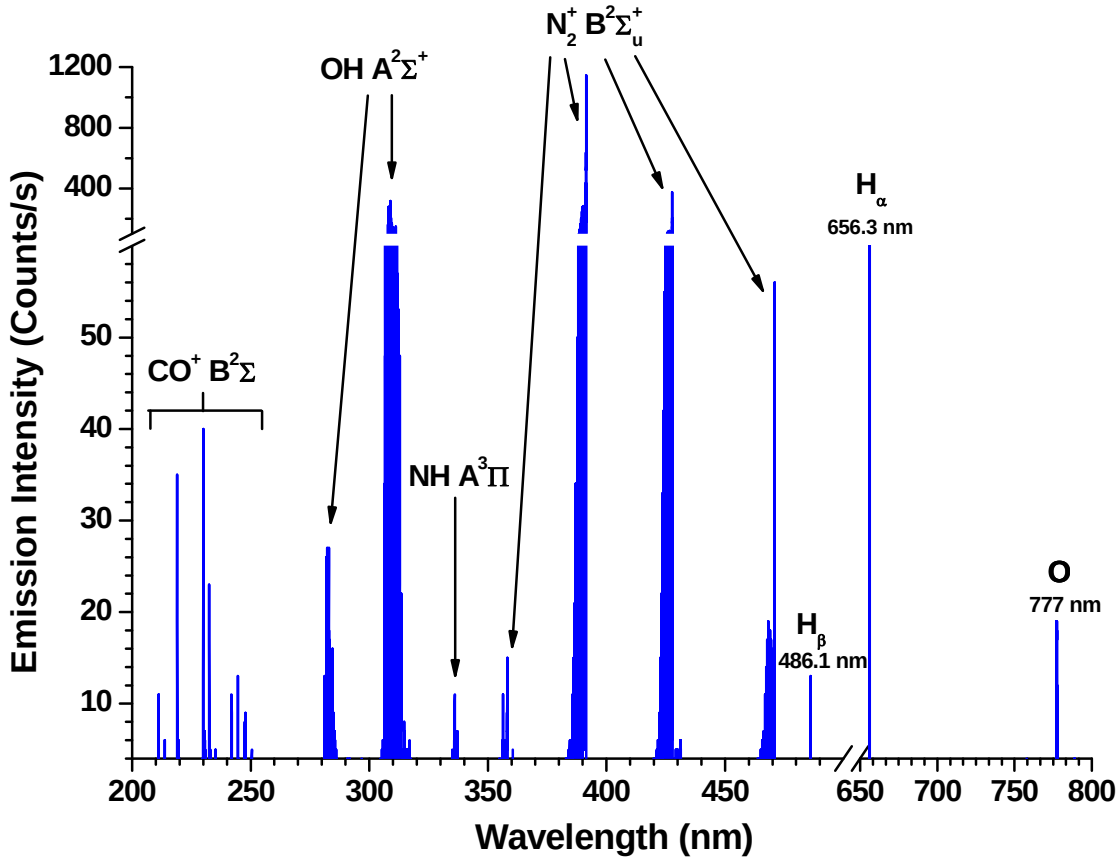

Figure 8.2 UV-visible emission spectrum from the afterglow of the pin-negative FAPA source. Due to the weak intensity of the afterglow, the source was operated at 50 mA with 3.25 L/min of helium. Note that no helium emission was observed.

in the afterglow spectrum include CO^+ ($B^2\Sigma$) and NH ($A^3\Pi$). Surprisingly, no emission was detected from any helium species, indicating that the majority of excited helium species in the afterglow have either decayed to a state that emits outside of the accessible spectral window (e.g. He^* with n = 2 or He^m), or exist in a form that does not decay radiatively (e.g. He_2^+).

8.3.2 Effect of He Flow Rate and Discharge Polarity on Emitting Species in the He APGD

Spatially resolved profiles of emitting species in atmospheric-pressure discharges have already provided information on the source of impurities in the discharge, the relative distribution of ions and excited species needed for analyte excitation/ionization, and even mechanisms of ion formation.[28-29] Here, the polarity, operating current, and gas flow rate of the FAPA were varied to determine the discharge structure and conditions that favor production of species essential for APCI ionization pathways. Figures 8.3a and 8.3b show the spatial profile of the He I line at 706.5 nm for two He APGDs in a pin-negative and a pin-positive configuration, respectively. For all APGD profiles, a discharge distance (x-axis) of zero corresponds to the tip of the pin electrode, with positive distances approaching the plate electrode. Optimal mass spectrometric performance of the FAPA typically arises at 25 mA in the pin-negative polarity.[36] As a comparison, the 2 mA discharge is more similar to the one used in the DART source.[27, 37]

Both polarities and current levels exhibited distinct emission maxima at both the cathode and the anode. For the 25-mA discharge in the pin-negative configuration (cf. Figure 8.3a, blue trace), the He I maximum resides on the cathode pin and is due to

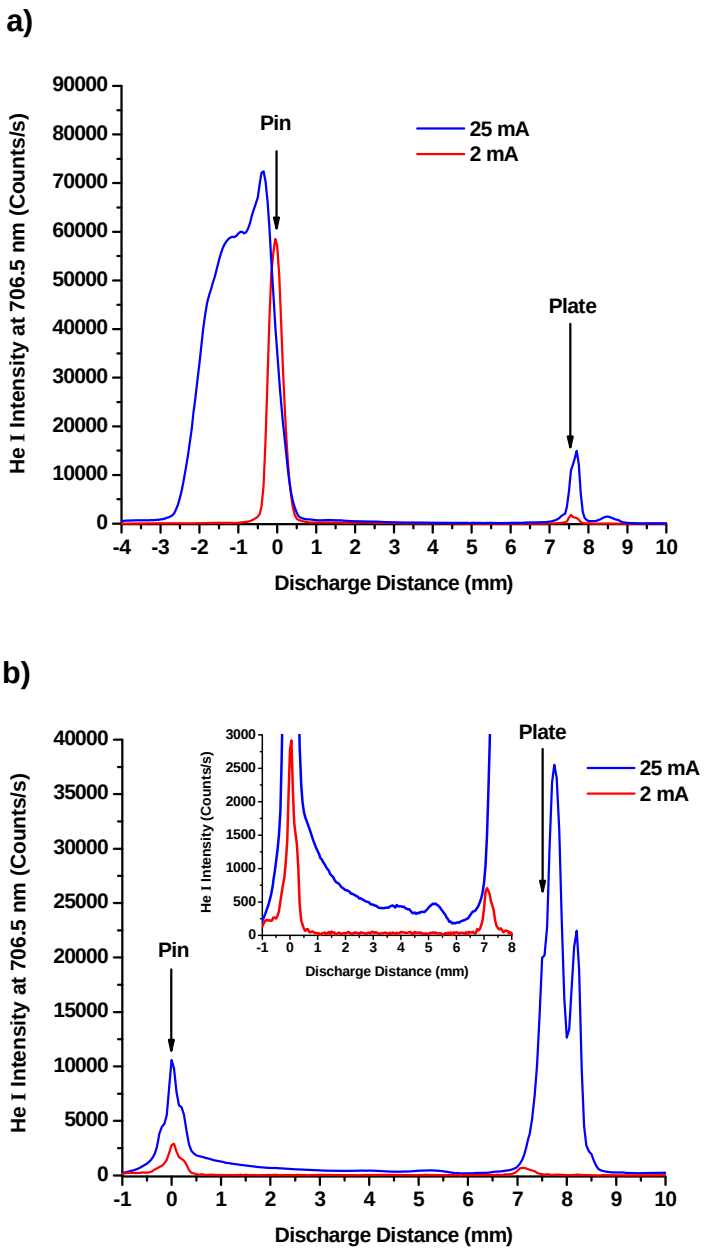

Figure 8.3 Spatially resolved emission profiles of the 706.5-nm He I line in the APGD at discharge currents of 25 mA (blue trace) and 2 mA (red trace) with a helium flow rate of 1.5 L/min. The discharge was operated in both the pin-negative (a) and pin-positive (b) polarity. The inset in (b) is on an expanded vertical axis to demonstrate helium emission in the positive column of the 25-mA APGD. In all APGD plots, a discharge distance of zero refers to the tip of the pin electrode.

the strong emission from the negative glow, which is where the majority of helium ions and excited species are produced. In addition, the emission intensity for He I was distributed along the length of the pin (~2 mm) and throughout the positive column. For the pin-negative, 2-mA discharge (cf. Figure 8.3a, red trace), the He-emission maximum was located at the very tip of the pin and was shifted 300 μm from that of the 25-mA discharge. Even though the operating current differs by only one order of magnitude, the locations of the emission maxima indicate an altered plasma structure; specifically, the 2-mA discharge exhibits corona-to-glow discharge behavior.

Although the maximum emission from the two current levels was similar, the He I intensity for the 25-mA discharge integrated along the entire plasma was more than five times that of the 2-mA discharge. The greater abundance of excited He created in the 25-mA APGD should lead to more efficient production of N_2^+ and a greater density of reagent ions. In fact, the N_2^+ produced has been mass spectrometrically and optically shown to be much higher, at least 17 times more abundant, with the FAPA plasma than with the 2-mA discharge.[27] Both current levels exhibited a second maximum in emission intensity at the anode, where electric field and electron energies should be low. Models of a helium APGD similarly showed a second maximum in number density at the anode for nearly all species included in the model.[35] Unlike in reduced-pressure GDs, a positive potential gradient in the positive column towards the anode causes an excess of low-energy electrons at the anode, which are capable of ionizing/exciting plasma species;[35] the high electron densities at the anode are likely the origin of the second emission maximum.

When the polarity of the 25-mA discharge was reversed to the pin-positive mode (cf. Figure 8.3b, blue trace), maximum He I emission occurred at the plate cathode where the negative glow resides. The relative amount of excited helium in the positive column was higher with this polarity. In pin-positive mode, the area of the negative glow is restricted to the surface of the raised edge on the exit plate, which causes a larger portion of the current density to exist in the positive column. It would at first seem that this polarity would be favored for ambient MS analyses because the negative glow, and thus the greatest source of He*, would be closer to the sample. However, the integrated He emission for the pin-negative polarity was more than four times greater than that for the pin-positive configuration with an operating current of 25 mA. While the cause for the differences in emission intensities is not yet known, this result supports the finding that the FAPA performs better as an ionization source with a pin cathode.[15, 36]

When the pin-positive discharge was operated at 2 mA, the strongest helium emission still existed at the tip of the pin (cf. Figure 8.3b, red trace). As the inset in Figure 8.3b shows, excited helium was observed between the two electrodes at 25 mA, whereas no such emission could be detected with the discharge operated at 2 mA. Similar behavior at these two operating currents was observed for N_2^* (337 nm) and O I (777 nm) emission. These data provide further evidence that the discharge operated at 2 mA behaves like a corona rather than a true glow such as the FAPA maintained at 25 mA.[27, 31]

Several species from impurities were also detected in the APGD of the FAPA at various plasma-gas flow rates and for both polarities. Emission profiles of atomic

oxygen at 777 nm in a pin-negative and a pin-positive APGD are shown in Figures 8.4a and 8.4b, respectively. The presence and location of atomic oxygen is particularly important for mass spectrometric analyses. It has been noted in APCI reactions that the neutral atomic oxygen radical can react with aromatic bonds to form alcohols.[38-39] This reaction often results in complicated mass spectra for aromatic molecules, which feature not only molecular ion peaks but also a series of oxygen-adduct peaks.[27] As a result, determining the source of oxygen and factors that limit atomic oxygen production is of importance for these sources. For both discharge polarities, O I emission near the plate region (i.e. closest to the open atmosphere) declines with increasing He flow rate. This finding suggests that an appreciable amount of atmospheric oxygen is diffusing into the discharge region through the hole in the plate electrode. Higher helium flows oppose diffusion into the discharge and thereby reduce the amount of oxygen reaching the negative glow region. This finding is congruous with spectroscopic studies on a similar atmospheric-pressure, helium discharge, the LTP probe, which showed that the majority of oxygen in the discharge region was due to diffusion from the atmosphere.[28]

This trend does not necessarily hold for other regions of the APGD, particularly for the positive column. We attribute these differences to the concentration gradient of impurities near the plate electrode. As atmospheric constituents diffuse through the hole into the discharge chamber, their volume expands as the linear velocity of the plasma gas drops. This effect results in a lower impurity concentration in the discharge chamber than in the narrow channel separating the discharge from the atmosphere. As a result, diffusion and plasma-gas flow rate would contribute minimally to variances in impurity

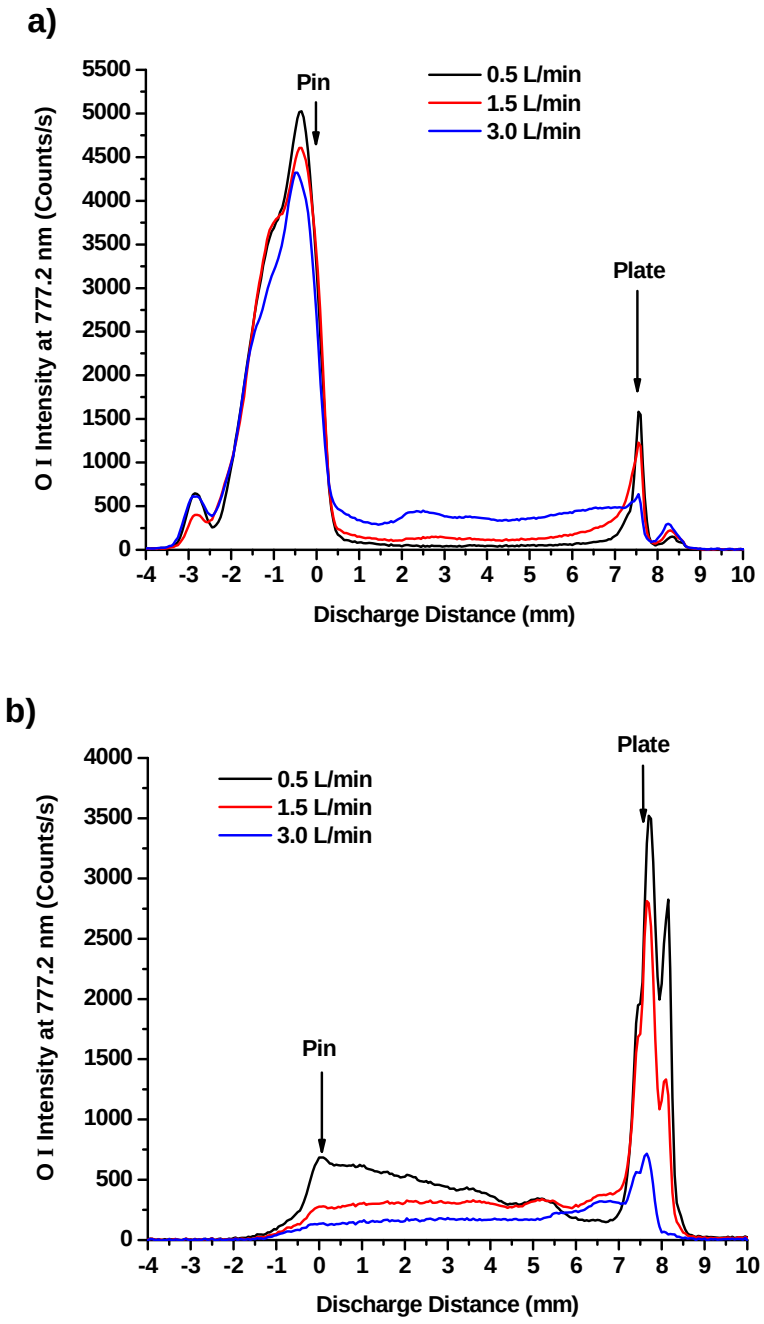

Figure 8.4 Atomic oxygen emission profiles (777 nm) for the APGD operated in the pin-negative (a) and pin-positive (b) configuration for a variety of He plasma-gas flow rates.

concentration within the larger volume of the discharge chamber. Changes in flow rate would alter only the amount of reactive species formed in these regions.

In fact, the oxygen emission monotonically increased with flow rate for the pin-negative configuration, while it had the opposite effect for the pin-positive configuration. This difference is likely due to the different reaction pathways occurring at the cathode and the anode. Theoretical modeling has suggested that, at the cathode, the majority of He^+ is produced from electron impact with ground state helium.[35] Because the greatest potential drop is in the cathode dark space, the electrons in this region have sufficient energy to ionize ground-state helium directly. In contrast, and as was mentioned earlier, low-energy electrons accumulate at the anode because of the slight potential gradient in the positive column. Because electron energies are so low in this region, He^+ is almost exclusively produced from electron impact with previously formed He^*.[35] From these factors, more He_2^+, and other species important in the dissociation/excitation process, exist at the anode than other places in the APGD, which likely contributes to the enhanced sensitivity of the FAPA in the pin-negative configuration.

The spatial distribution of two other species important in the ionization pathways of the FAPA source, OH (306.0 nm) and N_2^+ (391.4 nm), are shown in Figures 8.5a and 8.5b, respectively. These profiles were collected under different gas flow rates for a pin-positive APGD. The OH emission dropped monotonically with helium flow rate across the entire APGD, suggesting that the majority of OH was produced from a species that diffused into the discharge from the atmosphere. This trend was observed for the opposite discharge polarity, as well (data not shown). For N_2^+ (Figure 8.5b), emission

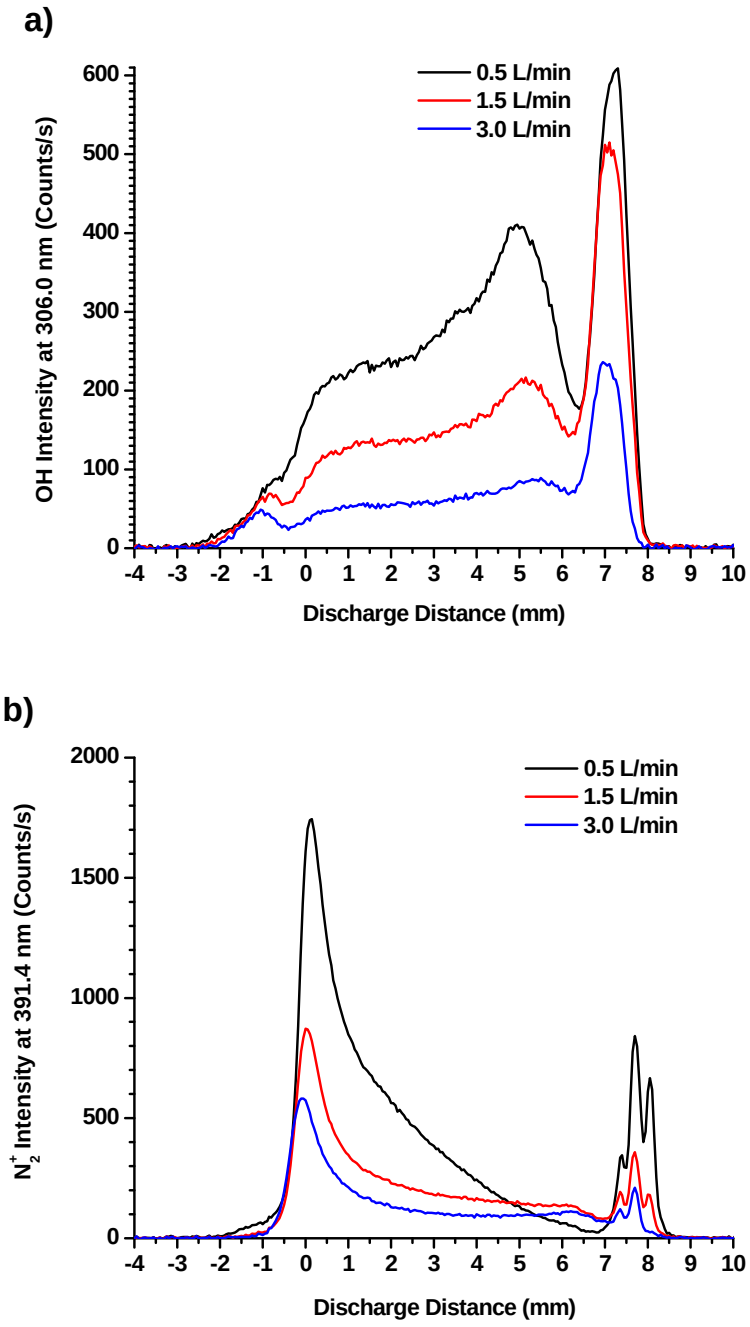

Figure 8.5 Spatial emission from a) OH at 306.0 nm and b) N_2^+ at 391.4 nm in a pin-positive APGD for selected helium flow rates.

similarly declined with increasing He flow at both electrodes, further suggesting that most of the nitrogen in the discharge chamber was not from the gas supply or transfer lines. Interestingly, N_2^+ emission near the plate electrode was stronger in the pin-negative configuration providing further explanation why better mass spectrometric performance is seen with the FAPA in this polarity. Regardless of discharge polarity, N_2^+ had a strong emission maximum at the anode, which decayed deep into the positive column. In a helium APGD, the majority of N_2^+ is formed from a charge-transfer reaction involving He_2^+.[35] Further, the He_2^+ density is known to be the greatest at the anode and to slowly decay into the positive column, mirroring the N_2^+ emission profile. Therefore, we believe this feature is indicative of the presence of He_2^+.

8.3.3 N_2^+ Emission Profiles in the Afterglow

Because emission from the afterglow of the FAPA was very weak, spatially resolved spectral information could be collected for only two emitting species, N_2^+ and OH. Additionally, the spatial emission behavior of both molecules was nearly identical, so only N_2^+ will be discussed here. Afterglow emission profiles for the N_2^+ bandhead at 391.4 nm for various discharge currents and helium flow rates are shown in Figures 8.6a and 8.6b, respectively. An afterglow distance of zero in these profiles corresponds to the edge of the plate electrode, with positive values extending into the open atmosphere. In Figure 8.6a the APGD current was incremented from 30 mA to 70 mA at a fixed He flow rate of 2.9 L/min. Emission of N_2^+ in the afterglow became stronger at higher operating currents, because of the greater production of reactive species within the discharge that are capable of ionizing and exciting N_2. The N_2^+ emission decayed to baseline

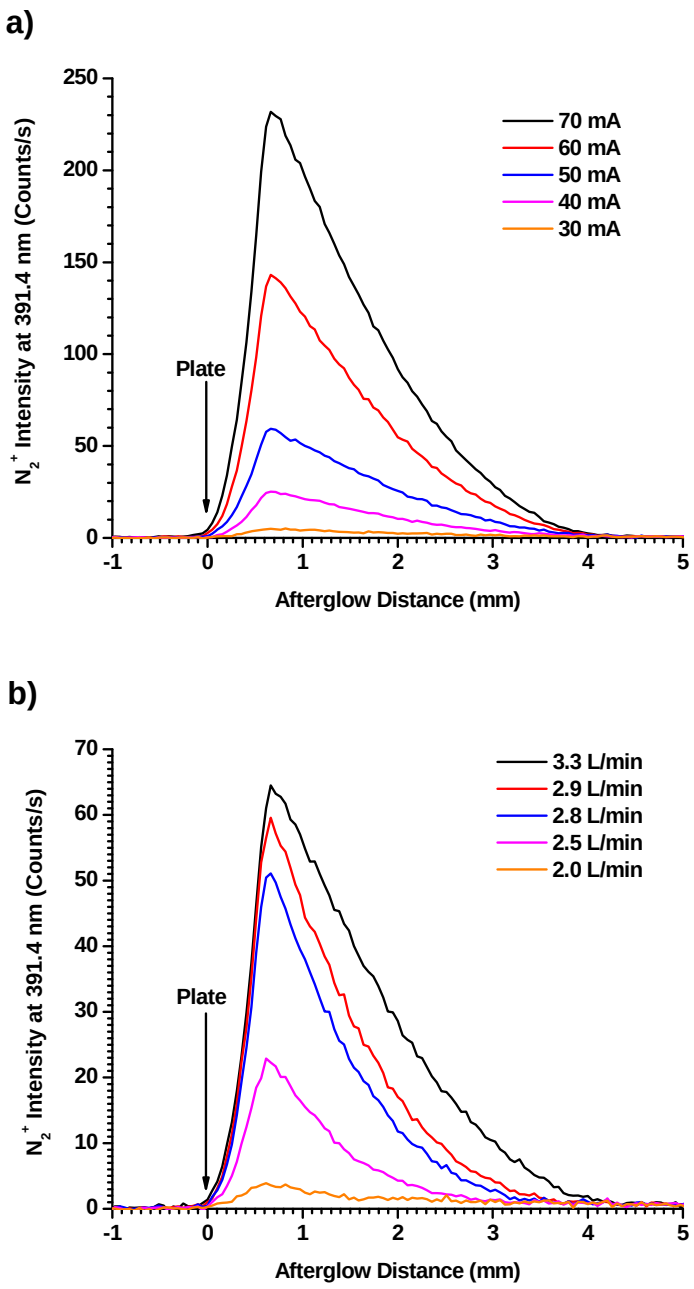

Figure 8.6 Afterglow emission of the N_2^+ bandhead at 391.4 nm for a pin-negative FAPA. The traces in (a) are for different discharge currents at a He flow rate of 2.9 L/min whereas (b) demonstrates the effect of He flow rate on N_2^+ emission at a discharge current of 50 mA. In both a) and b), an afterglow distance of zero refers to the edge of the plate electrode, with positive values extending into the open atmosphere.

approximately 4 mm from the plate electrode, regardless of discharge current. The presence of N_2^+ emission in the afterglow is therefore likely dependent on diffusion of an atmospheric quenching agent, which then undergoes charge transfer.

This hypothesis is supported by the behavior of afterglow emission profiles at changing He flow rates (cf. Figure 8.6b). Both the amount of N_2^+ generated and the location where emission decayed to baseline increased monotonically with He flow rate. At higher flows, more excited/ionized helium species are generated per unit time and, at the same time, the outward gas velocity opposes the inward diffusion of quenchers into the beam. This behavior in the afterglow is the opposite of what was observed in the APGD, where N_2^+ emission decreased with plasma-gas flow rate. We attribute this disparity to the relative concentrations of reactants leading to N_2^+ formation. In the APGD, N_2 is limiting as it must diffuse from the atmosphere into the discharge chamber through the hole in the plate electrode, through which a high opposing velocity of plasma gas issues; in the afterglow, the velocity of the discharge gas is lower than in the hole of the plate electrode, resulting in a greater concentration of diffused N_2 in the afterglow and making excited helium species the limiting reactants.

Another interesting feature of the afterglow emission profiles is that the maximum occurred consistently about 0.5 mm downstream from the anode plate, suggesting that some species are acting as a carrier to transfer energy from the discharge into the open atmosphere.

8.3.4 OH Rotational Temperatures and Electron Number Densities of the APGD

The rotational temperature (T_{rot}) is an important diagnostic for plasma-based ambient desorption/ionization sources because it approximates the gas-kinetic temperature, which correlates with desorption of molecules from surfaces for many plasma-based ADI-MS sources.[2, 40] Rotational temperatures are derived from the Boltzmann population distribution among rotational energy levels of a well characterized thermometric molecule. Though numerous diatomics have been successfully used to measure T_{rot}, only OH and N_2^+ offered sufficient intensity in the APGD and afterglow of the FAPA to be useful in the present study (cf. Figure 8.2). Because of non-thermal excitation from excited helium species, N_2^+ does not yield reliable gas-kinetic temperature values;[29] this fact will be demonstrated below for the afterglow region. In the case of the FAPA, only OH temperatures should be viewed as being valid.

Four emission lines in the Q_1 branch[41-42] were used for determining OH rotational temperatures as they had sufficient intensity. These lines were the same as those used by Chan et al.[28] Plotting $\ln(I\lambda/gA)$ versus E_{exc}, where I is intensity of the line, λ is the emission wavelength, A is the transition probability, g is the degeneracy of the excited energy level, and E_{exc} is the energy of the upper excited state in eV, yields a linear plot with a slope equal to $(-11605/T)$.[43] Only temperature values where the correlation coefficient (r^2) of the fit was greater than 0.99 were used. The relative standard deviation of the measured temperature was taken as the relative error of the slope from the linear fit, which was less than 10% in the APGD.

The spatial profiles of OH rotational temperatures of the APGD for pin-negative and pin-positive modes are given in Figures 8.7a and 8.7b, respectively. The maximum T_{rot} of 1170 K for the pin-negative configuration was located at the tip of the pin within the negative glow. The temperature throughout the positive column was lower and remained roughly constant at ~770 K. These temperatures are more than 600 K and 200 K lower, than those measured for He APGDs with a restricted cathode and positive column[32] and sealed from air with a restricted cathode area,[31] respectively. The reason for the drastic temperature differences could be due to the confined cathode area utilized in those APGDs, but this effect will be explored in the future.

When the polarity of the APGD was reversed (cf. Figure 8.7b), the temperature of the positive column was approximately the same as in the pin-negative discharge; however, the maximum T_{rot} was much lower, 780 K, and was located in the positive column. Raising the plasma-gas flow rate for either polarity resulted in a drop in temperature, likely due to convective heat transfer. Ultimately, the lower maximum temperature in the pin-positive mode would result in less efficient desorption and could be one of the reasons the FAPA offers less sensitivity in the pin-positive polarity.

Spatially resolved electron number densities, n_e, in the pin-negative APGD were measured from the Stark broadening of the hydrogen beta line, H_β, at 486.1 nm. This spectral line is preferred because its broadening parameters are well known and are less affected by perturbers other than electrons.[44-45]

In addition to Stark broadening, the measured H_β line for this type of system is known to experience appreciable contributions from instrumental and van der Waals

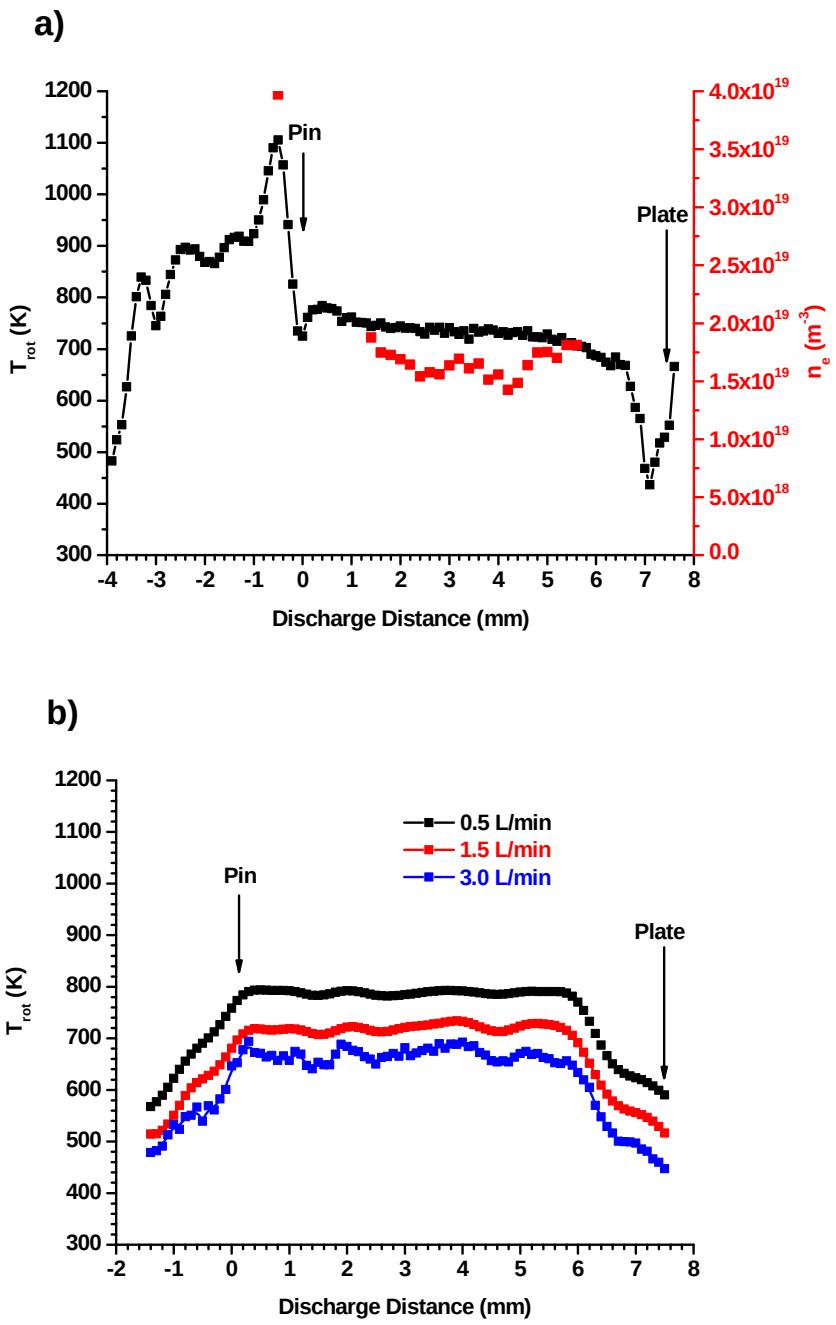

Figure 8.7 a) OH rotational temperatures, T_{rot}, and electron number densities, n_e, for a 25-mA, pin-negative APGD with a helium flow of 1.5 L/min. b) OH rotational temperatures for a 25-mA, pin-positive APGD for selected gas flow rates. The relative error of all measurements was less than 10% and was assumed to be the same as those of the fits.

broadening. The H_β line in the positive column was fit with a Voigt profile containing a fixed Gaussian component of 13.7 pm, which was previously found to be the instrumental broadening of this particular spectrometer.[28] The Lorentzian contribution from van der Waals broadening was determined from the Lindholm-Foley impact theory[46-47] to account for changes in local temperature with the spatially resolved T_{rot} shown in Figure 8.7a. The van der Waals width was subtracted from the Lorentzian component of the Voigt fit to yield an estimated Stark width. Electron number density was calculated from the formula provided by Gigosos et al.[48] The relative error of n_e was taken as the relative error of the Lorentzian width from the fit and was less than 15%.

Estimating electron number density in the negative-glow region near the pin was similar to the process described above but required an additional step. It is known that broadening of hydrogen emission lines can also be caused by strong external electric fields.[49-50] Glow discharges at atmospheric pressure have a very thin cathode dark space, due to the very short mean free path, where the majority of the potential drop occurs. The result is a very high electric field (>10 kV/cm) at the tip of the pin electrode, which introduces an additional broadening component. Thus, the H_β profiles near the pin cathode exhibited two distinct Lorentzian profiles; an intense, narrow component indicative of the true electron number density and a less intense, broad component due to the strong electric field. To deconvolute these two broadening contributions, the center narrow portion of the profile was removed, leaving the broad wings due solely to the electric field. The wings were fit with a Lorentzian, which was then subtracted from the original emission line. The remaining profile was then treated like those in the positive column.

The estimated n_e values in the pin-negative APGD with 1.5 L/min helium flow rate are shown in Figure 8.7a. The relative error of n_e was taken as the relative error of the Lorentzian width from the fit and was less than 15%. Because of the involved data processing needed to determine n_e in the negative glow, only one data point is shown. The electron density reaches a maximum of $\sim 4\times10^{19}$ m^{-3} at the same location as the highest emission intensity and rotational temperature. The n_e drops in the positive column to $\sim 1.5\times10^{19}$ m^{-3}.

Compared to values derived from a numerical simulation of a helium APGD,[35] the n_e figures in this study are almost exactly one order of magnitude higher. The relative spatial distribution of n_e in the APGD was nearly identical between the two studies. Unfortunately, H_β was too weak at the anode plate to measure electron number densities. Assuming the number of ions and electrons are equal at each location in the discharge, the degree of ionization within the APGD is on the order of 10^{-6}, based on the ideal gas law. This value is fairly low, considering that reduced-pressure GDs have ionization efficiencies between 10^{-5} and 10^{-3}.[51-52] However, because the FAPA is at atmospheric pressure, the number of collisions per second is about three orders of magnitude higher than in a reduced-pressure GD, so ionization reaction rates should be comparable.

8.3.5 Rotational Temperatures in the Afterglow

The gas temperature in the afterglow region of the FAPA is particularly important because samples are introduced directly into the afterglow and thermal processes are believed to play a major role in the desorption of molecules from their surfaces. Infrared thermography has already been used to approximate the temperature of the FAPA gas

stream impinging on a glass surface,[27, 53] but it is unknown how much the surface affects the measured temperature. Therefore, OH rotational temperatures were spectroscopically determined here for the afterglow of a pin-negative FAPA operated at 70 mA with a He flow rate of 3.25 L/min (cf. Figure 8.8). Within the error of the measurement, the OH T_{rot} was constant at ~500 K across the 3-mm range where temperature could be reliably measured. Although thermographic measurements of the FAPA afterglow temperature were not obtained with the present combination of relatively high operating currents and gas flow rates, the maximum temperature increases linearly with current, but falls with flow rates above 1.5 L/min. Extrapolating from the thermographic data in Ref. 51, the maximum temperature under the present conditions would be 500 K, in excellent agreement with the spectroscopic values.

In addition to the OH rotational temperature, the N_2^+ emission profile and N_2^+ rotational temperature are shown in Figure 8.8. The T_{rot} for N_2^+ was determined in the same way as described by Chan et al.[29] with all Boltzmann plots exhibiting good linearity ($r^2 > 0.99$). The N_2^+ temperature reaches a maximum of 860 K and then drops to nearly a constant value of ~670 K throughout the rest of the afterglow. Clearly, a discrepancy of ~150 K exists between the temperature measurements from OH and N_2^+ for this discharge. Because the measured OH temperature is similar to the thermographic temperatures, it is likely that the N_2^+ population distribution violates the assumption that a rapid equilibrium exists between the rotational and translational energies of the molecule. We have previously demonstrated that the N_2^+ temperature is a good indicator of the dominant ionization mechanism of nitrogen.[29] In particular, charge transfer between He_2^+ and N_2 yields a N_2^+ rotational temperature of ~900 K,[54] whereas charge

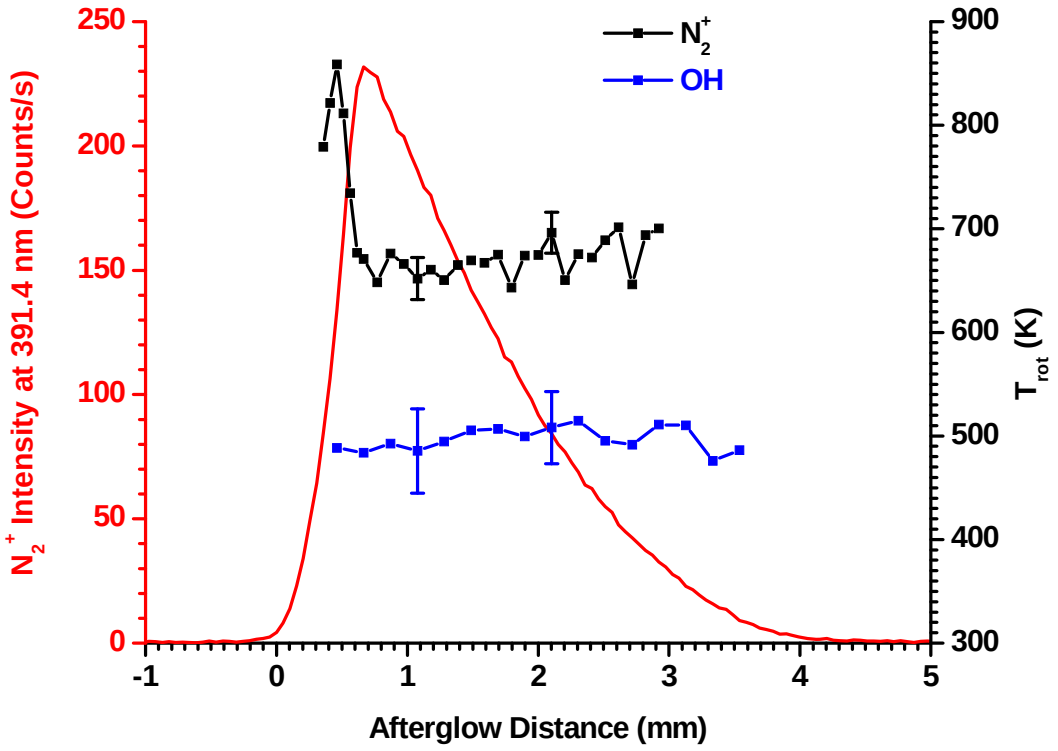

Figure 8.8 Rotational temperatures for OH (blue trace) and N_2^+ (black trace) in the afterglow of the pin-negative FAPA at 3.25 L/min and 70 mA. The red trace shows the N_2^+ emission profile as a frame of reference.

transfer with He^+ and Penning ionization with He^m produce nonlinear Boltzmann plots[55] and temperatures 30 to 50 K higher than expected,[54, 56] respectively. Accordingly, we believe that the elevated N_2^+ temperatures (~850 K) near the plate electrode, but before the maximum N_2^+ emission, are due to charge-transfer ionization of atmospheric nitrogen with He_2^+. As was suggested above, the maximum N_2^+ emission probably represents the point at which atmospheric nitrogen is no longer the limiting reagent. This behavior is seen also in the rotational temperature, when it reaches a constant value of ~660 K, as the point where much of the He_2^+ is depleted.

8.4 Conclusions

The afterglow and APGD from the He-based FAPA desorption/ionization source were characterized through optical spectroscopy under a variety operating conditions to better understand factors that affect desorption and ionization for mass spectrometric analyses. The background emission spectrum of the APGD contained numerous high-energy atomic helium lines, as well as molecular and atomic emission from contaminant species such as N_2, N_2^+, OH, O, and CO^+. Helium excimer, He_2^*, emission was also observed, which was not previously reported in spectroscopic studies of similar He-APGDs. Although not commonly mentioned in the ambient mass spectrometry literature, He_2^* and other similar species, such as He_2^+, could contribute significantly to analyte ionization or reagent-ion formation. The spectrum of the afterglow in the open atmosphere did not contain emission features from any helium species, indicating that the majority of energetic helium moieties have either decayed to a state that emits outside of

the measured spectral window (e.g. He^* with n = 2 or He^m) or exist in a form that does not radiatively decay (e.g. He_2^+).

Spatially resolved emission profiles of species in the APGD were employed to understand the role of operating parameters (discharge current, He flow rate, and discharge polarity) on production of excited atoms and molecules as well as to deduce the origin of impurities within the discharge region. Reducing the operating current from 25 mA to 2 mA transitioned the discharge from a true glow to more of a corona discharge, in which much of the emission and the majority of plasma species were created at the pin electrode, regardless of polarity. Emission from impurities, O, OH, and N_2^+, all decreased monotonically with He flow rate near the plate electrode. It is suggested that a substantial amount of H_2O vapor, O_2, and N_2 enters the discharge chamber through diffusion from the atmosphere, rather than originating from the gas supply.

The emission profiles also revealed that the polarity of the electrodes affects the formation of species that control the sensitivity of the FAPA in mass spectrometric analyses. Specifically, the pin-positive configuration consistently yielded less intense emission, and thus a lower number density, for all examined species throughout the discharge compared to the pin-negative polarity. The gas-kinetic temperature, determined from the OH rotational temperature, was higher with a pin-negative polarity. Also, for both polarities, N_2^+ emission exhibited a maximum at the anode that slowly decayed into the positive column of the discharge, despite the fact that the gas flow moved from the pin electrode to the plate. This behavior implies that different

chemistries and excitation conditions exist at the cathode and the anode. We believe an abundance of low-energy electrons is present at the anode, which promotes the ionization of He^* and the formation of He_2^+, leading to the ionization of atmospheric constituents in an environment less energetic or harsh than in the negative glow at the cathode. Collectively the findings explain why FAPA exhibits better sensitivity in a pin-negative configuration.

References

1. Takats, Z.; Wiseman, J. M.; Gologan, B.; Cooks, R. G. *Science* **2004**, *306*, 471-473.
2. Venter, A.; Nefliu, M.; Cooks, R. G. *Trac-Trends Anal. Chem.* **2008**, *27*, 284-290.
3. Van Berkel, G. J.; Pasilis, S. P.; Ovchinnikova, O. *J. Mass Spectrom.* **2008**, *43*, 1161-1180.
4. Weston, D. J. *Analyst* **2010**, *135*, 661-668.
5. Chen, H. W.; Venter, A.; Cooks, R. G. *Chem. Commun.* **2006**, 2042-2044.
6. Haddad, R.; Sparrapan, R.; Kotiaho, T.; Eberlin, M. N. *Anal. Chem.* **2008**, *80*, 898-903.
7. Costa, A. B.; Cooks, R. G. *Chem. Phys. Lett.* **2008**, *464*, 1-8.
8. Bereman, M. S.; Muddiman, D. C. *J. Am. Soc. Mass. Spectrom.* **2007**, *18*, 1093-1096.
9. Wood, M. C.; Busby, D. K.; Farnsworth, P. B. *Anal. Chem.* **2009**, *81*, 6407-6415.
10. Sampson, J. S.; Hawkridge, A. M.; Muddiman, D. C. *J. Am. Soc. Mass. Spectrom.* **2006**, *17*, 1712-1716.
11. Wu, J.; Hughes, C. S.; Picard, P.; Letarte, S.; Gaudreault, M.; Levesque, J. F.; Nicoll-Griffith, D. A.; Bateman, K. P. *Anal. Chem.* **2007**, *79*, 4657-4665.
12. Nemes, P.; Vertes, A. *Anal. Chem.* **2007**, *79*, 8098-8106.
13. Chen, Z. Y.; Vertes, A. *Phys. Rev. E* **2008**, *77*.
14. Nemes, P.; Marginean, I.; Vertes, A. *Anal. Chem.* **2007**, *79*, 3105-3116.
15. Andrade, F. J.; Shelley, J. T.; Wetzel, W. C.; Webb, M. R.; Gamez, G.; Ray, S. J.; Hieftje, G. M. *Anal. Chem.* **2008**, *80*, 2646-2653.

16. Cody, R. B.; Laramee, J. A.; Durst, H. D. *Anal. Chem.* **2005**, *77*, 2297-2302.

17. Chen, H. W.; Zheng, J.; Zhang, X.; Luo, M. B.; Wang, Z. C.; Qiao, X. L. *J. Mass Spectrom.* **2007**, *42*, 1045-1056.

18. Harper, J. D.; Charipar, N. A.; Mulligan, C. C.; Zhang, X. R.; Cooks, R. G.; Ouyang, Z. *Anal. Chem.* **2008**, *80*, 9097-9104.

19. Na, N.; Zhao, M. X.; Zhang, S. C.; Yang, C. D.; Zhang, X. R. *J. Am. Soc. Mass. Spectrom.* **2007**, *18*, 1859-1862.

20. Ratcliffe, L. V.; Rutten, F. J. M.; Barrett, D. A.; Whitmore, T.; Seymour, D.; Greenwood, C.; Aranda-Gonzalvo, Y.; Robinson, S.; McCoustra, M. *Anal. Chem.* **2007**, *79*, 6094-6101.

21. Symonds, J. M.; Galhena, A. S.; Fernandez, F. M.; Orlando, T. M. *Anal. Chem.* **2009**.

22. Song, L.; Gibson, S. C.; Bhandari, D.; Cook, K. D.; Bartmess, J. E. *Anal. Chem.* **2009**, *81*, 10080-10088.

23. Shelley, J. T.; Hieftje, G. M. *J. Anal. At. Spectrom.* **2010**, *25*, 345-350.

24. McEwen, C. N.; Larsen, B. S. *J. Am. Soc. Mass. Spectrom.* **2009**, *20*, 1518-1521.

25. Song, L. G.; Dykstra, A. B.; Yao, H. F.; Bartmess, J. E. *J. Am. Soc. Mass. Spectrom.* **2009**, *20*, 42-50.

26. Olenici-Craciunescu, S. B.; Michels, A.; Meyer, C.; Heming, R.; Tombrink, S.; Vautz, W.; Franzke, J. *Spectroc. Acta Pt. B-Atom. Spectr.* **2009**, *64*, 1253-1258.

27. Shelley, J. T.; Wiley, J. S.; Chan, G. C. Y.; Schilling, G. D.; Ray, S. J.; Hieftje, G. M. *J. Am. Soc. Mass. Spectrom.* **2009**, *20*, 837-844.

28. Chan, G. C. Y.; Shelley, J. T.; Jackson, A. U.; Wiley, J. S.; Engelhard, C.; Cooks, R. G.; Hieftje, G. M. *J. Anal. At. Spectrom.* **2011**, In Press.

29. Chan, G. C. Y.; Shelley, J. T.; Wiley, J. S.; Jackson, A. U.; Engelhard, C.; Cooks, R. G.; Hieftje, G. M. *Anal. Chem.* **2011**, In Press.

30. Chan, G. C. Y.; Hieftje, G. M. *J. Anal. At. Spectrom.* **2008**, *23*, 181-192.

31. Andrade, F. J.; Wetzel, W. C.; Chan, G. C. Y.; Webb, M. R.; Gamez, G.; Ray, S. J.; Hieftje, G. M. *J. Anal. At. Spectrom.* **2006**, *21*, 1175-1184.

32. Gielniak, B.; Fiedler, T.; Broekaert, J. A. C. *Spectroc. Acta Pt. B-Atom. Spectr.* **2011**, *66*, 21-27.

33. Golubovskii, Y. B.; Maiorov, V. A.; Behnke, J.; Behnke, J. F. *J. Phys. D-Appl. Phys.* **2003**, *36*, 39-49.

34. Tsuji, M.; Oda, E.; Tanaka, M.; Nakamura, M.; Nishimura, Y. *Chem. Lett.* **1997**, 465-466.

35. Martens, T.; Mihailova, D.; van Dijk, J.; Bogaerts, A. *Anal. Chem.* **2009**, *81*, 9096-9108.

36. Andrade, F. J.; Shelley, J. T.; Wetzel, W. C.; Webb, M. R.; Gamez, G.; Ray, S. J.; Hieftje, G. M. *Anal. Chem.* **2008**, *80*, 2654-2663.

37. U.S. Pat. 7,112,785 B2, 2006.

38. Ascenzi, D.; Franceschi, P.; Guella, G.; Tosi, P. *J. Phys. Chem. A* **2006**, *110*, 7841-7847.

39. Tosi, P.; Ascenzi, D.; Franceschi, P.; Guella, G. *Plasma Sources Science & Technology* **2009**, *18*.

40. Nilles, J. M.; Connell, T. R.; Durst, H. D. *Analyst* **2010**, *135*, 883-886.

41. Dieke, G. H.; Crosswhite, H. M. *J. Quant. Spectrosc. Radiat. Transf.* **1962**, *2*, 97-&.

42. Chidsey, I. L.; Crosley, D. R. *J. Quant. Spectrosc. Radiat. Transf.* **1980**, *23*, 187-199.

43. Mermet, J. M., in *Inductively Coupled Plasma Emission Spectroscopy-Part 2*, ed. P. W. J. M. Boumans. Wiley-Interscience: New York, 1987, vol. 90, pp 353-386.

44. Kelleher, D. E.; Wiese, W. L.; Helbig, V.; Greene, R. L.; Oza, D. H. *Phys. Scr.* **1993**, *T47*, 75-79.

45. Torres, J.; van de Sande, M. J.; van der Mullen, J.; Gamero, A.; Sola, A. *Spectroc. Acta Pt. B-Atom. Spectr.* **2006**, *61*, 58-68.

46. Lindholm, E. *Ark. Mat. Astron. Fys.* **1946**, *32A*, No. 17.

47. Foley, H. M. *Physical Review* **1946**, *69*, 616.

48. Gigosos, M. A.; Gonzalez, M. A.; Cardenoso, V. *Spectroc. Acta Pt. B-Atom. Spectr.* **2003**, *58*, 1489-1504.

49. Kuraica, M. M.; Konjevic, N. *Appl. Phys. Lett.* **1997**, *70*, 1521-1523.

50. Videnovic, I. R.; Konjevic, N.; Kuraica, M. M. *Spectroc. Acta Pt. B-Atom. Spectr.* **1996**, *51*, 1707-1731.

51. Bogaerts, A.; Gijbels, R. *Spectroc. Acta Pt. B-Atom. Spectr.* **1998**, *53*, 437-462.

52. Bogaerts, A.; Gijbels, R. *Anal. Chem.* **1996**, *68*, 2676-2685.

53. Shelley, J. T.; Wiley, J. S.; Hieftje, G. M. *Anal. Chem.* **2011**, Submitted.

54. Endoh, M.; Tsuji, M.; Nishimura, Y. *J. Chem. Phys.* **1983**, *79*, 5368-5375.

55. Belikov, A. E. *Chem. Phys.* **1997**, *215*, 97-109.

56. Richardson, W. C.; Setser, D. W. *J. Chem. Phys.* **1973**, *58*, 1809-1825.

Chapter 9

Ultrasensitive Ambient Mass Spectrometric Analysis with a Pin-to-Capillary Flowing Atmospheric-Pressure Afterglow Source

9.1 Introduction

Plasma sources for mass spectrometry have traditionally been viewed as tools for elemental analysis. However, plasmas operated at atmospheric pressure, such as corona and glow discharges, have been used for over 30 years for molecular analyses through soft, chemical-ionization pathways. Horning et al.[1] first described a corona discharge sustained at atmospheric pressure for the analysis of small, organic molecules; the method is commonly referred to as atmospheric-pressure chemical ionization (APCI).

In APCI, just as in reduced-pressure chemical ionization, reagent ions that are generated through electron impact undergo chemical reactions to induce analyte ionization. However, because the ionization process occurs at atmospheric pressure, collisional cooling greatly reduces molecular fragmentation. Moreover, the reaction chemistry can be tuned by introducing selected solvent vapors into the plasma region. Because of these features, APCI is typically viewed as a softer and more versatile ionization method than electron impact or reduced-pressure chemical ionization.

Because of its simplicity, the corona discharge is currently the most widely used plasma-based source for molecular mass spectrometry. However, the low operating current of the corona discharge, usually a few microamperes, leads to a relatively low density of reagent ions, which compromises detection limits and makes the ionization process more prone to matrix effects than with other plasma-based ionization sources.[2-3]

It was later found that APCI could be performed with increased reagent-ion densities through the use of a helium, atmospheric-pressure glow discharge (APGD).[4-5] The higher operating currents (50 – 250 μA) and highly energetic states of helium formed in the APGD (>19 eV) produce a greater flux and a wider variety of reagent ions. In the original APGD configuration, samples are passed directly through the discharge, just as in corona-discharge APCI. However, the well-defined structure of a glow discharge occupies a significant volume, so this sample-introduction method leads to plasma instabilities and memory effects, which are less severe with point-source corona discharges.

To further improve on the APGD source design, Andrade et al.[6] developed a helium-APGD geometry that physically and electrically isolates the discharge from the sampling region. In the new geometry, the sample is introduced into the flowing afterglow, which extends into the open atmosphere; accordingly, the new ionization source was termed the Flowing Atmospheric-Pressure Afterglow (FAPA). Because the sample does not enter the active plasma region, discharge currents between 10 mA and 50 mA could be used without substantial analyte fragmentation or degradation. In fact, the base peak in the mass spectra for most analytes corresponds to either the molecular ion ($M^{+\cdot}$) or the protonated parent molecule (MH^+). The FAPA source was first used for the detection of gas-phase analytes and as a detector for gas chromatography, with detection limits in the femtomole regime, even for molecules that exhibit poor sensitivity with corona-discharge APCI.[6-7]

The FAPA can also be used as a source for ambient desorption/ionization mass spectrometry[8], in which species are directly desorbed and ionized from sample surfaces, and with minimal sample preparation.[9-10] The desorption feature is presumably due to the temperature of the gas (>200 °C) and to the excited species present in the afterglow region.[11] Desorption/ionization with the FAPA source has been employed for the detection of pesticides on fruit,[12] polymer characterization,[13] and determination of active pharmaceutical ingredients.[14] The source can also be used to generate positive or negative ions and the desorption/ionization detection limits are comparable to those for gas-phase samples.[14-15] Furthermore, FAPA has been shown to be less affected by ionization matrix effects than other plasma-based ambient desorption/ionization sources.[3]

These features, in conjunction with the simple source design and operation, should make the FAPA an attractive source for ambient mass spectrometric analyses. Unfortunately, some issues with the initial source design have constrained widespread use of the FAPA source. Most notably, the original FAPA design produced substantial mass-spectral background and significant oxidation of some species. These limitations ultimately led to compromised analyte identification and quantification. In the present study, a significantly improved FAPA design is presented and compared with the original FAPA. The capabilities of the improved FAPA are demonstrated through the detection of a variety of compounds, including pesticides and explosives. Lastly, detection of analytes in bulk liquid samples is shown.

9.2 Experimental

9.2.1 Reagents

All reagents were analytical-grade. High-purity helium (99.995% purity helium, Indiana Oxygen, Indianapolis, IN) was used as the discharge gas in all cases. PETN, RDX, and TNT were purchased as 0.1 mg/mL standards in methanol/acetonitrile from AccuStandard Inc. (New Haven, CT). Pesticide standards were purchased from Dr. Ehrenstorfer GmbH (Augsburg, Germany) and from Riedel de Haën, Pestanal® (Seelze, Germany). The standard agrochemical solutions were the same as those used by Wiley et al.[16]

9.2.2 Ionization Source Design

Two FAPA designs and geometries were used in these studies. The first was similar to the original one described by Andrade et al.[6] Briefly, an APGD was sustained between a stainless-steel pin cathode and a brass-plate anode; hereafter this source will be referred to as the pin-to-plate FAPA (cf. Figure 9.1a). The electrodes were held in place within a Teflon® discharge chamber that also served to seal the discharge region from the ambient atmosphere. A 1.6-mm hole in the plate enabled excited species, ions, and electrons formed in the discharge to flow into the open atmosphere for desorption and ionization of analytes.

The second design maintained the discharge between a pin cathode and a conductive capillary anode (1.6-mm o.d., 1.3-mm i.d., 25 mm long, McMaster-Carr, Chicago, IL); this source design will be referred to as the pin-to-capillary FAPA (cf. Figure 9.1b). Both electrodes were made of stainless steel and fixed in place within a machineable-ceramic discharge cell (Mykroy®, McMaster-Carr, Chicago, IL). These electrodes were also sealed to the discharge cell to limit atmospheric gases from reaching the discharge. The plasma gas entered the chamber through a port in the side and flowed into the open atmosphere through the capillary anode.

Although the two source designs were different, many of the optimal operating conditions were found to be the same between the two geometries. A negative potential was applied to the cathode through a 5 kΩ ballast resistor, from a high-voltage, DC power supply (model NO1HA60, Acopian Technical Co., Easton, PA); the anode was connected to the ground terminal of the power supply. The APGD of the FAPA was

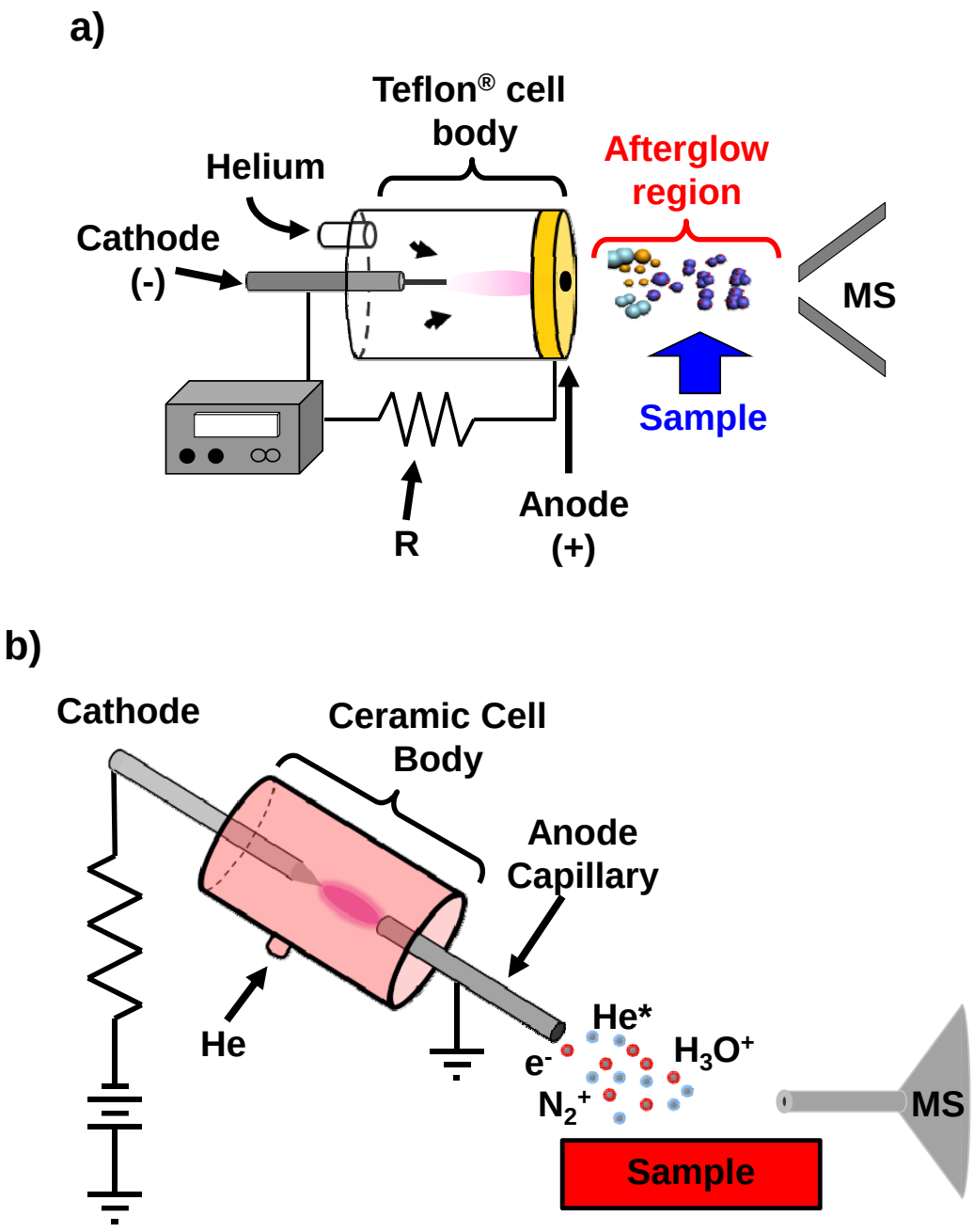

Figure 9.1 a) Diagram of the original, pin-to-plate FAPA configuration with the discharge chamber constructed from Teflon®. A hole in the plate anode allows discharge species to flow into the sample-introduction region. b) Depiction of the new pin-to-capillary geometry FAPA with a Mykroy® ceramic discharge cell. Discharge species flow into the sampling region through the anode capillary.

operated in a current-controlled mode at 25 mA, which resulted in a discharge voltage of ~400 V. While both versions of the FAPA could be operated with a helium discharge gas at flow rates from 0.1 to 1.5 L/min, it was found that 0.6 L/min was the optimal flow rate for detection of most analytes. This gas flow rate was adjusted with a rotameter (Key Instruments, Trevose, PA) and monitored with a mass flow meter (Fathom Technologies, Georgetown, TX). It was found that an inter-electrode gap of ~7 mm yielded the strongest mass spectrometric signals, so that spacing was used for both sources throughout. Both sources were mounted onto a home-built 3D translation stage for precise alignment of the exit aperture of the source with the mass spectrometer inlet.

9.2.3 Mass Spectrometric Analyses

Ions produced from each source were detected with a Thermo LTQ XL linear ion trap mass spectrometer (Thermo-Finnigan San José, CA, USA). Agrochemicals and most other compounds were detected in the positive-ion mode, while explosives were detected in negative-ion mode. To change between ionization modes, the polarity of the mass-spectrometer DC potentials was switched in the Xcalibur software. No changes to either configuration of the FAPA were needed to detect analytes in either ionization mode. Spectra were collected in automatic gain-control mode with a maximum ion trap injection time of 200 ms and 2 microscans per spectrum. The key experimental parameters for positive-ion detection were as follows: m/z range of 50–700; capillary temperature at 200 °C; capillary voltage at 15 V; tube lens at 65 V. Tandem mass spectrometry (MS/MS) was performed via collision-induced dissociation (CID) to improve signal-to-

noise ratios and to confirm the presence of the tested analytes. These MS/MS spectra were obtained with an isolation window of 1.5 Th and 25–35% relative collision energy.

9.2.4 Temperature Measurements of the Flowing Afterglow

Temperatures of the gas stream exiting the two FAPA designs were measured by infrared thermography with a thermal imaging camera (Fluke Ti40 IR FlexCam, Everett, WA). The method of temperature measurement was similar to that described previously.[11] Briefly, greybody emission from a glass microscope slide placed in the flowing helium stream was recorded with the IR camera. Temperature scales in the images were corrected for the emissivity of the glass slide, 0.92, and the ambient temperature, 22 °C, in the SmartView™ software.

9.3 Results and Discussion

9.3.1 Background Mass Spectra

The pin-to-plate FAPA has been shown to be capable of directly desorbing/ionizing samples in any phase (solid, liquid, or gas), and with impressive sensitivity (<100 fmol).[8, 15] Unfortunately, the original design also produces a complex background spectrum, with ions detected at nearly every m/z value. Typical pin-to-plate FAPA background mass spectra in positive- and negative-ionization modes are shown in Figures 9.2a and 9.3a, respectively. Given these background levels, detection of low-abundance or unknown species with the pin-to-plate FAPA is quite difficult without some means of removing the interfering ion signals, such as background subtraction or MS/MS. Proper background subtraction can be difficult with all ambient mass

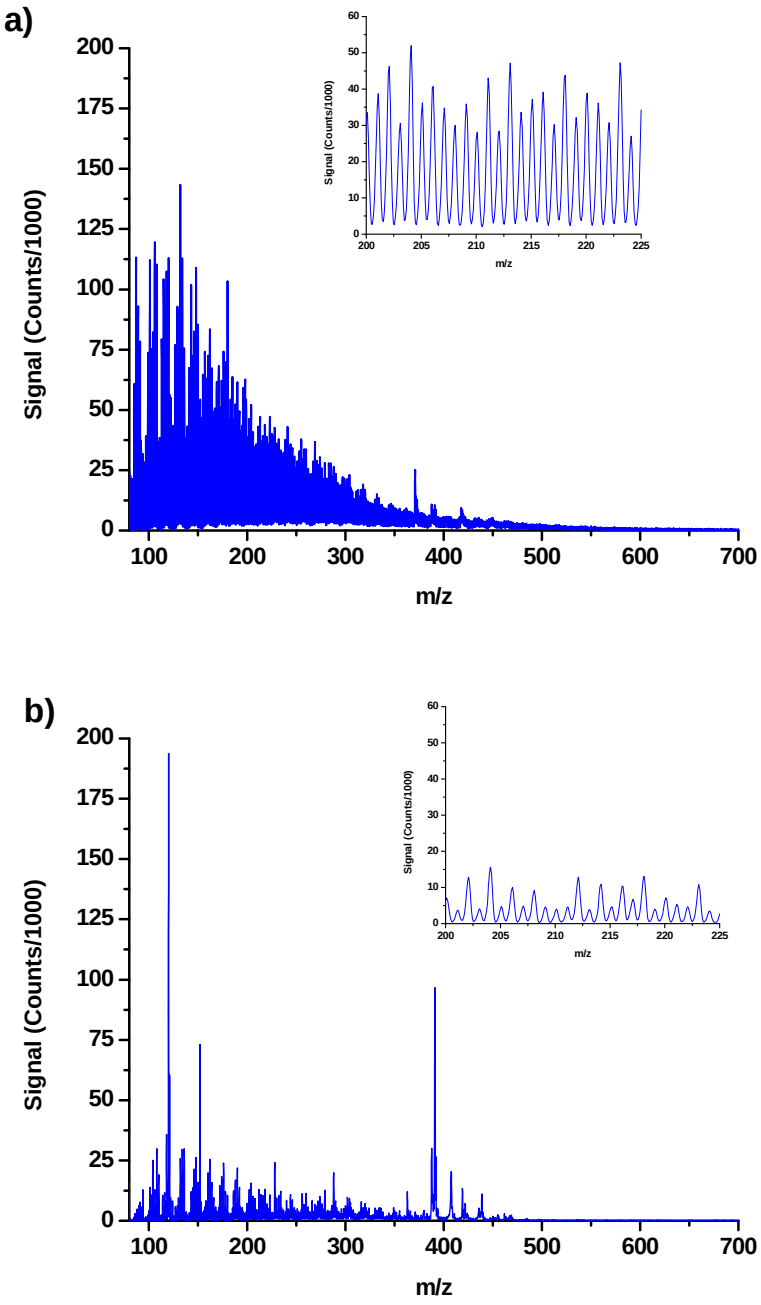

Figure 9.2 Positive-ion background mass spectra for the (a) pin-to-plate and (b) pin-to-capillary FAPA sources. The insets are of the mass range between 200 and 225 m/z to emphasize the difference in background signals.

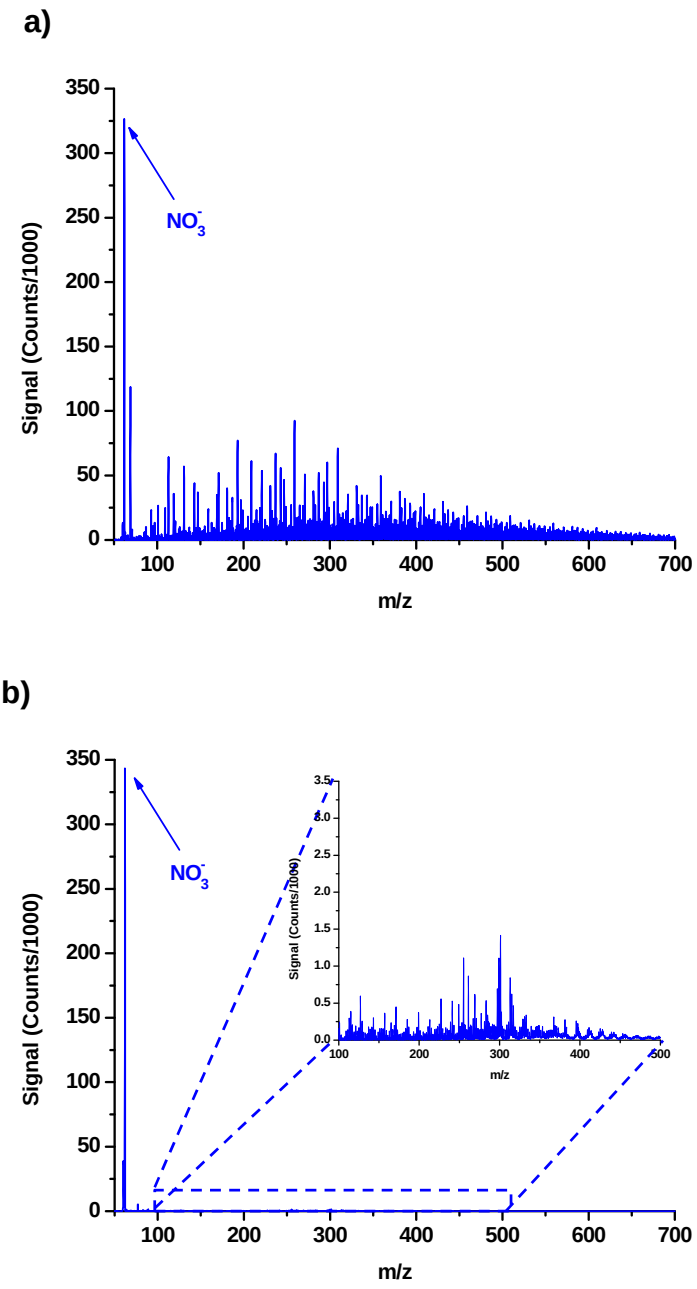

Figure 9.3 Negative-ion background mass spectra for (a) the Teflon®-bodied, pin-to-plate FAPA and (b) the Mykroy®-bodied, pin-to-capillary FAPA. With both sources the base peak corresponds to NO_3^- and exists at approximately the same signal strength. However, with the use of the ceramic cell body, the continuum background has been reduced by at least 99%.

spectrometry sources, because sample shape and position are known to greatly affect detection precision[14] and MS/MS requires *a priori* knowledge of expected ions from a sample.

Schilling et al.[14] noted a complex, discrete background in the low-mass range, 0 to 100 Th, for a Teflon®-bodied, pin-to-plate FAPA in negative-ionization mode. The majority of those features can be attributed to fluorinated hydrocarbons, presumably from degradation of the polymeric discharge cell. A glass discharge chamber resulted in a simpler low-mass spectrum. Schilling et al.[14] offered no comments regarding the effect of the glass chamber on the higher-mass, quasi-continuum background or even on the positive ion background.

From these earlier findings it was clear that the discharge cell should be fabricated from a more stable material than Teflon®. A glass-bodied, pin-to-plate FAPA was first explored to improve source performance. However, the background clutter was very similar and yielded a continuum background reduction of only ~50% for the positive-ionization mode over that shown in Figure 9.2a. The FAPA cell constructed from glass was also fragile and was not thermally insulating. One distinct advantage of the FAPA over other plasma-based ambient desorption/ionization sources is that the discharge directly heats the gas so no additional heat source is needed. Therefore, it is advantageous to use a source chamber that is thermally insulating to preserve the gas temperature, thus enhancing thermal desorption.

Of a variety of discharge-cell materials that were tested, the one that exhibited the best performance was Mykroy®, a machineable ceramic. Mykroy® is a glass-bonded

ceramic that exhibits low electrical and thermal conductivity, has a low thermal expansion coefficient, is stable up to 400 °C, and has high tensile strength. Also, it is not porous to oxygen or water, so outgassing or leaching of carbonaceous molecules from the chamber into the discharge, which could contribute to the background, will not occur. Lastly, Mykroy® can be easily machined or injection-molded, similar to organic thermoplastics, making it suitable for a FAPA source body.

In addition to the ceramic cell body, the discharge configuration was changed to a pin-to-capillary design (cf. Figure 9.1b). Positive- and negative-ion background spectra for the pin-to-capillary FAPA are shown in Figures 9.2b and 9.3b, respectively. For the positive-ion mode, the quasi-continuum background was reduced by 89% and 84% over the integrated mass ranges of 100-110 Th and 200-210 Th, respectively, compared to the pin-to-plate geometry. Although this improvement in background is quite significant, the effect is even more dramatic for the negative-ionization mode. In this case, the background was reduced by 99% or more, which ultimately improves detection limits by greater than two orders of magnitude. Importantly, the signal for NO_3^-, a common reagent ion in negative mode, was nearly the same between the two geometries. This point suggests that the reagent-ion flux, and thus the ionization efficiency, was unaffected by the change in design.

9.3.2 Oxidation of Aromatic Species

Another problem previously noted with the pin-to-plate FAPA is significant oxidation of aromatic systems, which can lead to complicated spectra.[11] An example of the severity of this oxidation is shown by the analysis of 1 ng of diphenylamine from a

glass probe with the pin-to-plate FAPA (cf. Figure 9.4a). The parent molecular ion (MH^+) of diphenylamine at m/z 170 was readily observed, but it was not the base peak in the spectrum. Rather, oxidized forms of the molecule dominated the spectrum, with the addition of up to six oxygen atoms being observed. Distributing the signal for an analyte across many m/z values, in conjunction with the quasi-continuum background, results in extremely poor signal-to-noise ratios and could make analyte identification in a complex sample difficult.

The addition of oxygen atoms is further complicated because it is not a simple, non-covalent adduct, which often occurs with water. Rather, it is a rearrangement reaction to form an alcohol. As a result, collision-induced dissociation in the first-stage of the mass spectrometer cannot be used to unravel these spectral features. While not as severe, oxidation of aromatic species is known to exist with corona-discharge APCI and has been shown to be induced by radical, atomic oxygen ($O^{\cdot}$) formed in the discharge.[17] In addition, spatially resolved, optical emission measurements of atomic oxygen in the discharge and afterglow of another helium plasma often used for ambient mass spectrometry, the low-temperature plasma (LTP) probe, demonstrate that the major source of the radical oxygen was from molecular oxygen diffusing from the atmosphere into the discharge region.[18]

When the pin-to-capillary FAPA was used to desorb/ionize 1 ng of diphenylamine, significantly less oxidation occurred (cf. Figure 9.4b). The result was a cleaner mass spectrum, consisting of an MH^+ base peak and a peak corresponding to the addition of one oxygen atom at only 9% relative abundance. Also, the MH^+ signal with

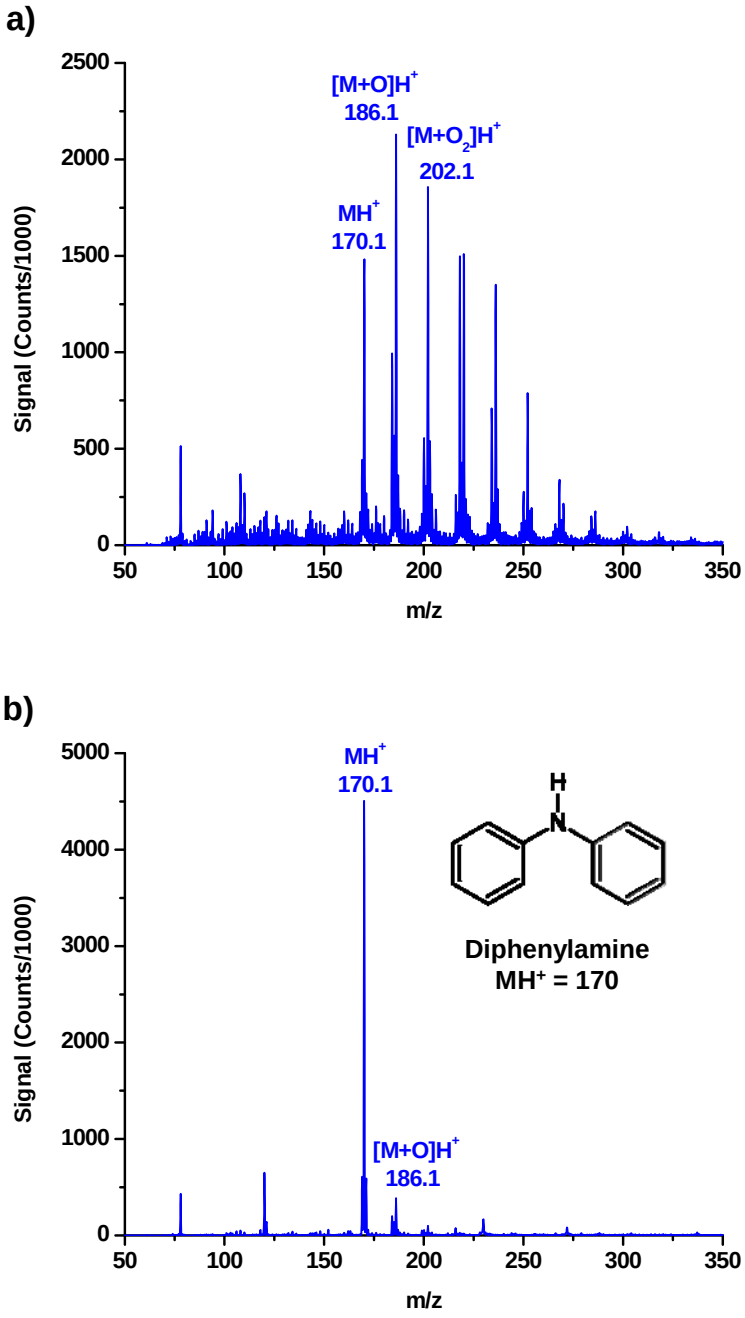

Figure 9.4 Mass spectra of 1 ng of diphenylamine obtained with the (a) pin-to-plate and (b) pin-to-capillary FAPA source. The oxidation of aromatic species is attributed to $O^{\cdot}$ produced in the APGD.

the pin-to-capillary FAPA was more than three times that obtained with the pin-to-plate FAPA. By extending the physical distance between the discharge of the FAPA and the ambient air, via the capillary anode, atmospheric oxygen is unable to diffuse into the discharge region. Similarly, if any atomic oxygen is formed in the discharge, potentially from the gas supply, much of it is likely lost to the capillary walls before the discharge effluent enters the sampling region.

9.3.3 Flowing Afterglow Temperature

While the spectral background and analyte oxidation were improved with the pin-to-capillary FAPA, it was not known how the modified source design would affect sample desorption. It has been shown that the temperature of the gas stream heavily influences analyte desorption for plasma-based ambient ionization sources.[16, 19-20] Accordingly, the maximum temperature of the flowing afterglow was measured for both FAPA designs.

Figure 9.5 shows the maximum temperature of the helium stream issuing from the pin-to-plate and pin-to-capillary FAPA geometries under a range of operating conditions. Maximum temperatures were found to be no farther than 5 mm from the anode. Regardless of discharge current and helium flow rate, the pin-to-plate FAPA produced higher temperatures. This finding is expected because the desorbing gas stream is located much closer to the discharge for the pin-to-plate design; for the pin-to-capillary FAPA, the anode capillary is exposed to the open air, which can act as a heat sink as the discharge-heated helium travels through the capillary. Interestingly, for both designs, the afterglow temperature increased linearly with discharge current (cf. Figure 9.5a). Thus,

modulating the discharge current could provide a way to selectively desorb analytes with different vapor pressures, similarly to what has been done with the DART source.[19] However, with the FAPA there is no need for an external gas heater and the temperature changes are more rapid, less than 5 seconds. Another interesting feature of the linear fits in Figure 9.5a is that the slopes were identical between the two source designs, 2.6 °C/mA, indicating that the structures of the APGDs are quite similar. This similarity further supports the suggestion that the differences in afterglow temperature are almost exclusively due to heat loss as the gas travels through the capillary.

The temperature in the afterglow also was affected by changing the plasma-gas flow rate (cf. Figure 9.5b). The pin-to-plate geometry reached a maximum temperature at a flow rate of ~1.5 L/min and then slowly decayed at higher gas flows. It is hypothesized that the gas flow at the exit of the source becomes turbulent at higher flow rates, resulting in more rapid cooling of the afterglow. In contrast, the gas temperature of the pin-to-capillary FAPA increased monotonically with helium flow until ~3 L/min, after which a more gradual decline in temperature occurred. The anode capillary allows the plasma gas to establish a laminar flow profile prior to entering the open atmosphere, which makes the desorbing helium stream stable over a greater range of flow rates than the pin-to-plate geometry. Although the afterglow temperature is lower for the newer FAPA design, it is still comparable to gas temperatures measured for DART;[21] furthermore, it can be easily and rapidly adjusted by changing discharge current and flow rate.

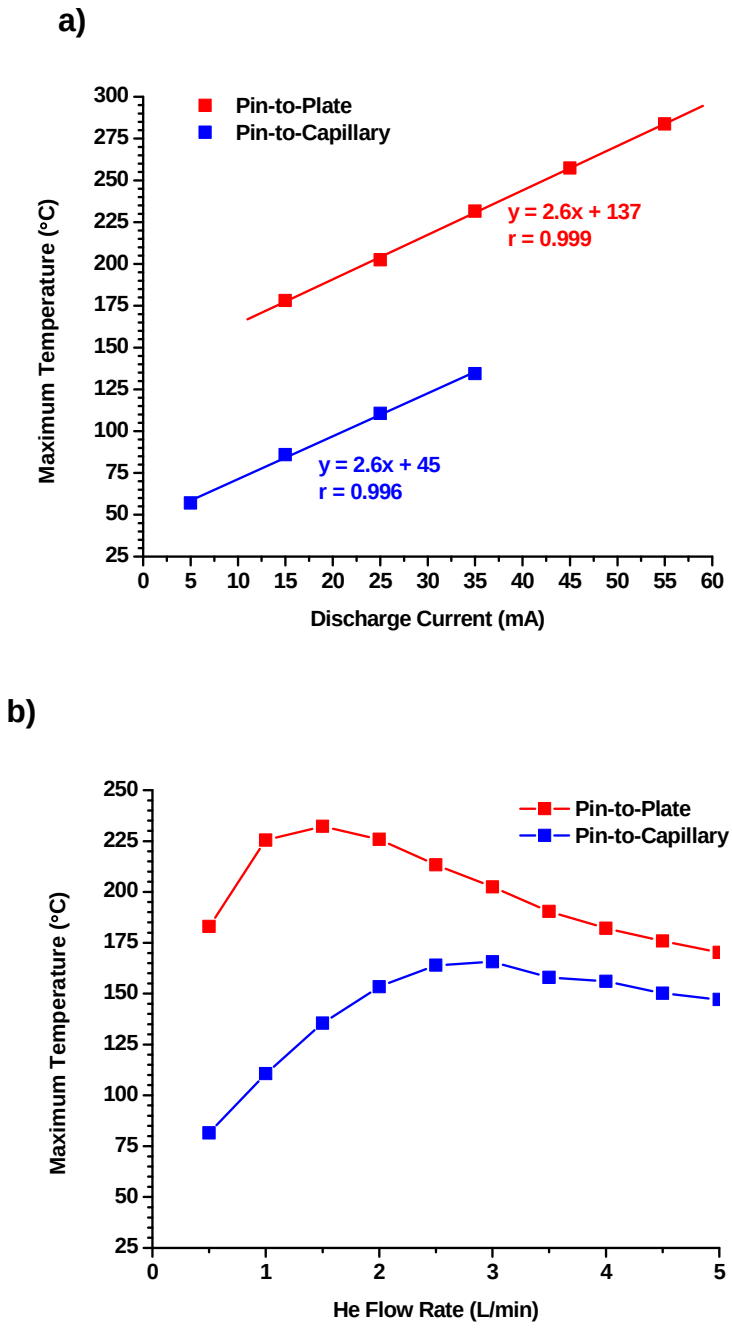

Figure 9.5 Maximum afterglow temperature for the pin-to-plate (red symbols) and pin-to-capillary (blue symbols) FAPA sources as a function of (a) APGD current and (b) helium flow rate. The flow rate in (a) was held at 1 L/min, while the discharge current in (b) was fixed at 25 mA. The decrease in temperature at higher He flow rates is caused by turbulent flow.

9.3.4 Analytical Performance of Pin-to-Capillary FAPA

To assess the sensitivity of the new pin-to-capillary FAPA, a variety of chemical substances was analyzed in positive- and negative-ionization mode. One set was commonly used agrochemicals, a list of LODs for which is compiled in Table 9.1. As a point of reference, the solutions and mass spectrometer were exactly the same as those used for an LTP-MS study.[16] Each sample was applied to a glass probe that was then reproducibly introduced (<7% RSD for analyte signals) into the FAPA source. MS/MS was used to improve analyte signal-to-noise ratios and thus LODs. As in a previous FAPA study,[7] detection limits were better than 10 fmol for all tested agrochemicals. However, the source was significantly more sensitive for some compounds. For instance, the LOD for the direct desorption/ionization of ametryn with the pin-to-capillary FAPA was approximately 4 amol, a value that appears to be instrument-limited. To the best of our knowledge, this is the best detection limit that has been reported for any plasma-based ambient mass spectrometry source. Furthermore, these LODs are more than one order of magnitude better than any previously achieved with similar helium discharge sources.[12, 16]

Operation of the FAPA source in the negative-ionization mode was not explored in detail in earlier investigations because of the complicated background spectra arising from the polymeric discharge cell. This limitation was unfortunate, because some functional groups preclude the formation of positive ions and are more readily observed in the negative-ionization mode; nitrate-based explosives are one such group of compounds. The dramatic improvement in negative-ion background with the

Table 9.1. Limits of detection (LOD) for selected pesticides and herbicides obtained with the pin-to-capillary FAPA ionization source

	m/z (MS/MS ions included)	LOD for FAPA (fmol)
Ametryn	228 → 186	0.004
Diphenylamine	170 → 92	1.2
Ethoxyquin	218 → 190 + 176	9.2
Isofenphos-methyl	332 → 290 + 271	0.9[a]
Isoproturon	207 → 165 + 72	0.24
Malathion	331 → 285 + 127	6
Parathion-ethyl	292 → 264	1.7
Terbuthylazine	230 → 174	0.043

[a] MS/MS not used for FAPA in this case.

pin-to-capillary FAPA expands the potential utility of the source for direct analyses of such compounds.

Although many plasma-based ambient desorption/ionization MS sources have been found useful for the detection of explosives, they experience several complications. Under customary operating conditions, DART requires the introduction of an electronegative species, such as trifluoroacetic acid or chlorine from methylene chloride, to generate negative reagent ions that can undergo ion attachment with the target molecules.[22-23] The LTP probe is capable of self-generating negative reagent ions, (e.g. NO_2^- and NO_3^-); however, the low gas temperature of that source (~30 °C) limits the types of explosives that can be detected to those with relatively high vapor pressure, such as TNT.[20]

In contrast, the FAPA can both generate negative reagent ions directly and produce high gas temperatures, enabling direct detection of explosives without modification to the operating parameters or ionization source. Figure 9.6a shows an example mass spectrum of the direct analysis of 66 fmol of the explosive pentraerythritol tetranitrate (PETN) from a glass surface. Both the electron and nitrate-attachment species, at m/z 316 and 378, respectively, were clearly detected, in addition to a denitration product (pentaerythritol dinitrate) at m/z 226 that occurs at temperatures greater than 100 °C.[24] These signals correspond to a limit of detection of approximately 500 amol. Figure 9.6b displays a mass spectrum of the explosive RDX detected from a latent fingerprint. Approximately 4.5 pmol of RDX was applied to a human finger. Two hours after the application, during which time the subject pursued normal activities, the

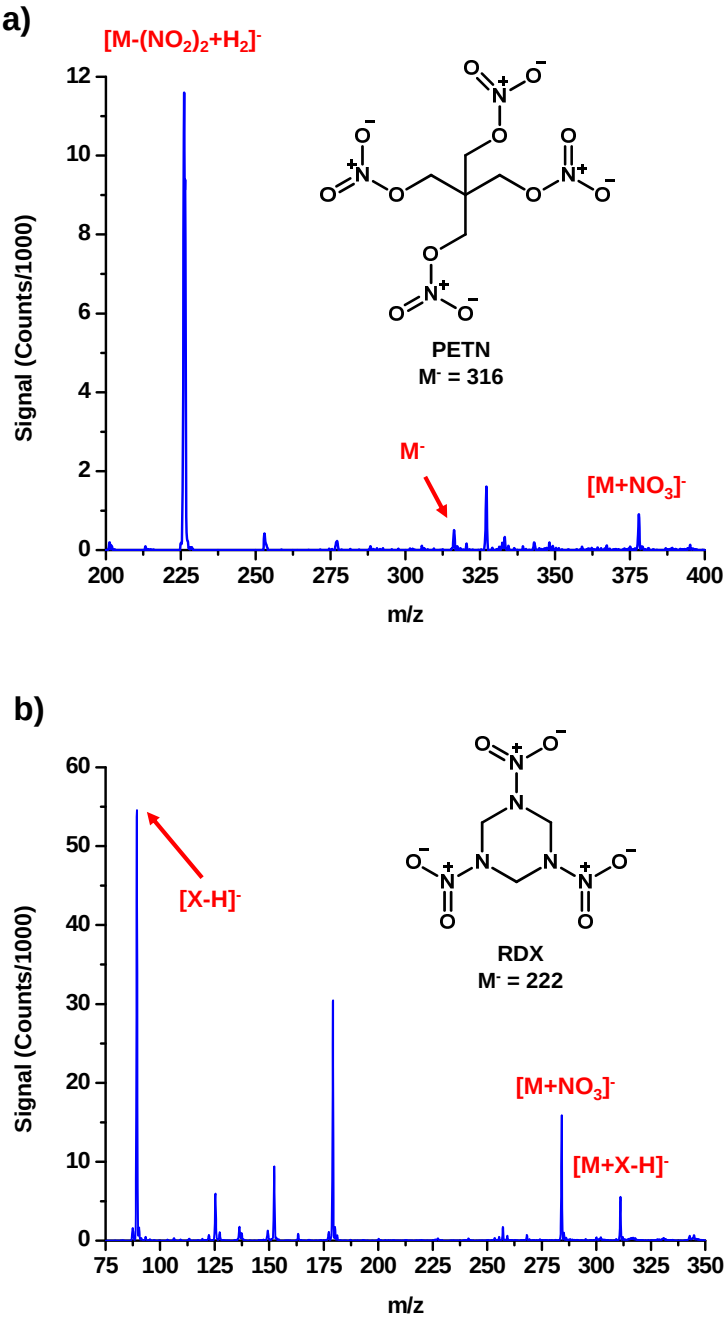

Figure 9.6 a) Mass spectrum of 66 fmol of PETN analyzed with the FAPA source. b) Mass spectrum of RDX detected from a latent fingerprint deposited on a glass slide 2 hours after exposure to the explosive. X corresponds to lactic acid present in the fingerprint.

fingerprint was deposited on a glass surface and analyzed with the FAPA source. In addition to the nitrated form of RDX, lactic acid (labeled X in the spectrum), at m/z 89, and the corresponding adduct with RDX could be detected. The simple design, impressive sensitivity to explosives, and simple mass spectra obtained by the pin-to-capillary FAPA make it an attractive source for homeland security applications.

9.3.5 Analysis of Bulk Liquid Samples

It was found that the new FAPA source was also capable of directly desorbing and ionizing analytes present in a solution. Of the numerous ambient desorption/ionization sources that have been described in the literature, only the LTP probe has been shown capable of directly analyzing bulk solutions (>100 μL).[25] This method of analysis could not be performed with the pin-to-plate FAPA due to spatial considerations that often limited the size and shape of a sample that could be analyzed. In contrast, the pin-to-capillary FAPA source can be angled with respect to the MS inlet, making analysis of large or oddly shaped objects more feasible. By positioning solution samples, 2 mL contained in microcentrifuge tubes, beneath the inlet of the mass spectrometer and directing the afterglow of the FAPA onto the liquid surface, analytes were desorbed and ionized.

Figure 9.7a shows a mass spectrum obtained from an 8-μg/mL solution of terbuthylazine (MH^+ = 230) dissolved in a 50:50 methanol-water mixture. While the protonated molecular ion can clearly be detected in the raw spectrum (cf. Figure 9.7a), a significant number of background species, presumably from the more volatile components in the solvent, were also observed. This spectral clutter could obviously

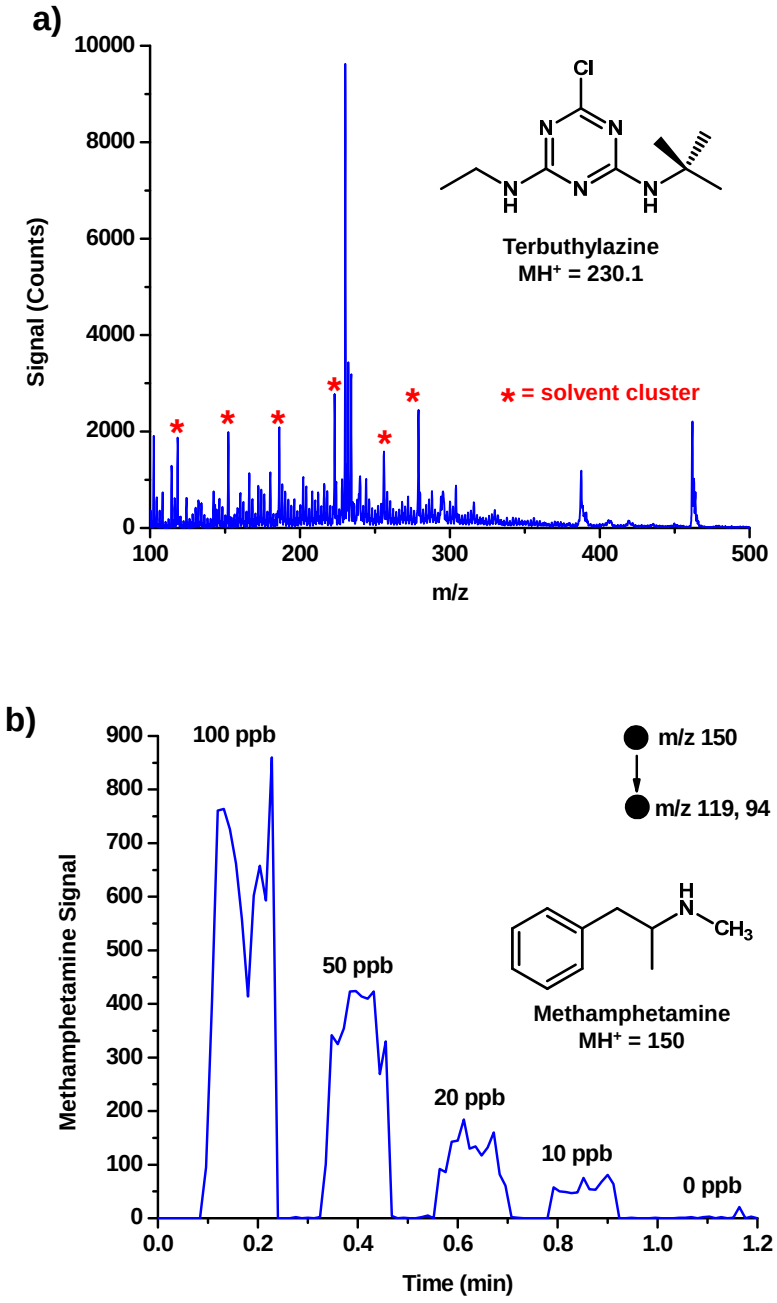

Figure 9.7 a) Direct analysis of a bulk solution of 8 µg/mL terbuthylazine in methanol:water. The asterisk (*) denotes a solvent cluster. b) Chronogram of methamphetamine MS/MS fragments for different concentrations in tap water. Resulting calibration curve has an r^2 of 0.999 and a LOD of 0.7 ppb.

compromise detection and identification. This problem was overcome by means of background subtraction with the blank solvent or by MS/MS of m/z 230. After background subtraction, the isotopic distribution of the chlorine-containing herbicide could be used to verify the presence of terbuthylazine; MS/MS provided structural information through the characteristic loss of the tert-butyl group.

Direct, bulk-solution analysis by FAPA-MS was found also to be quantitative by scanning solutions of varying analyte concentration underneath the FAPA source. This ability was demonstrated with the direct detection of methamphetamine in tap water. Methamphetamine was detected via MS/MS of the protonated molecular ion (m/z 150), which resulted in characteristic fragment ions at m/z 119 and 94. The chronogram of these two ions for several analyte concentrations is shown in Figure 9.7b. The calibration curve resulting from this analysis was found to be linear (r^2 = 0.999) and resulted in a detection limit of 0.7 ng/mL. This method of analysis was also applied to more complex solution matrices, such as untreated urine, with minimal loss of sensitivity. Although the mechanism of analyte desorption is not known, a correlation was found between sensitivity and vapor pressure of the analyte. For example, caffeine, which has a vapor pressure seven orders of magnitude lower than that of methamphetamine, could not be detected in the bulk solution. However, caffeine is readily detected and is a model analyte for FAPA analysis of solid samples. These findings demonstrate that bulk solution analysis with FAPA-MS could prove to be a rapid and convenient screening tool for explosives detection at airports or illicit drug detection in bodily fluids.

References

1. Horning, E. C.; Horning, M. G.; Carroll, D. I.; Dzidic, I.; Stillwel, R. N. *Anal. Chem.* **1973**, *45*, 936-943.
2. Sangster, T.; Spence, M.; Sinclair, P.; Payne, R.; Smith, C. *Rapid Commun. Mass Spectrom.* **2004**, *18*, 1361-1364.
3. Shelley, J. T.; Hieftje, G. M. *J. Anal. At. Spectrom.* **2010**, *25*, 345-350.
4. Sofer, I.; Zhu, J. Z.; Lee, H. S.; Antos, W.; Lubman, D. M. *Appl. Spectrosc.* **1990**, *44*, 1391-1398.
5. Zhao, J. G.; Zhu, J. Z.; Lubman, D. M. *Anal. Chem.* **1992**, *64*, 1426-1433.
6. Andrade, F. J.; Shelley, J. T.; Wetzel, W. C.; Webb, M. R.; Gamez, G.; Ray, S. J.; Hieftje, G. M. *Anal. Chem.* **2008**, *80*, 2646-2653.
7. Shelley, J. T.; Hieftje, G. M. *Analyst* **2010**, *135*, 682-687.
8. Andrade, F. J.; Shelley, J. T.; Wetzel, W. C.; Webb, M. R.; Gamez, G.; Ray, S. J.; Hieftje, G. M. *Anal. Chem.* **2008**, *80*, 2654-2663.
9. Venter, A.; Nefliu, M.; Cooks, R. G. *Trac-Trends in Analytical Chemistry* **2008**, *27*, 284-290.
10. Weston, D. J. *Analyst* **2010**, *135*, 661-668.
11. Shelley, J. T.; Wiley, J. S.; Chan, G. C. Y.; Schilling, G. D.; Ray, S. J.; Hieftje, G. M. *J. Am. Soc. Mass. Spectrom.* **2009**, *20*, 837-844.
12. Jecklin, M. C.; Gamez, G.; Touboul, D.; Zenobi, R. *Rapid Commun. Mass Spectrom.* **2008**, *22*, 2791-2798.
13. Jecklin, M. C.; Gamez, G.; Zenobi, R. *Analyst* **2009**, *134*, 1629-1636.

14. Schilling, G. D.; Shelley, J. T.; Barnes, J. H.; Sperline, R. P.; Denton, M. B.; Barinaga, C. J.; Koppenaal, D. W.; Hieftje, G. M. *J. Am. Soc. Mass. Spectrom.* **2010**, *21*, 97-103.

15. Shelley, J. T.; Ray, S. J.; Hieftje, G. M. *Anal. Chem.* **2008**, *80*, 8308-8313.

16. Wiley, J. S.; Garcia-Reyes, J. F.; Harper, J. D.; Charipar, N. A.; Ouyang, Z.; Cooks, R. G. *Analyst* **2010**, *135*, 971-979.

17. Ascenzi, D.; Franceschi, P.; Guella, G.; Tosi, P. *J. Phys. Chem. A* **2006**, *110*, 7841-7847.

18. Chan, G. C. Y.; Shelley, J. T.; Jackson, A. U.; Wiley, J. S.; Engelhard, C.; Cooks, R. G.; Hieftje, G. M. *J. Anal. At. Spectrom.* **2010**, In Press.

19. Nilles, J. M.; Connell, T. R.; Durst, H. D. *Analyst* **2010**, *135*, 883-886.

20. Garcia-Reyes, J. F.; Harper, J. D.; Salazar, G. A.; Charipar, N. A.; Ouyang, Z.; Cooks, R. G. *Anal. Chem.* **2011**, *83*, 1084-1092.

21. Harris, G. A.; Fernandez, F. M. *Anal. Chem.* **2009**, *81*, 322-329.

22. Cody, R. B.; Laramee, J. A.; Durst, H. D. *Anal. Chem.* **2005**, *77*, 2297-2302.

23. Nilles, J. M.; Connell, T. R.; Stokes, S. T.; Durst, H. D. *Propellants Explosives Pyrotechnics* **2010**, *35*, 446-451.

24. Basch, A.; Margalit, Y.; Abramovich-Bar, S.; Bamberger, Y.; Daphna, D.; Tamiri, T.; Zitrin, S. *J. Energ. Mater.* **1986**, *4*, 77-91.

25. Harper, J. D.; Charipar, N. A.; Mulligan, C. C.; Zhang, X. R.; Cooks, R. G.; Ouyang, Z. *Anal. Chem.* **2008**, *80*, 9097-9104.

Appendix

Distributed, Colorimetric Fiber-Optic Sensor Based on Fiber-Loop Ring-Down Spectroscopy

A.1 Introduction

Since its inception in the 1980s,[1] cavity ring-down spectroscopy (CRDS) has become a highly sensitive method for measuring the absorbance of gaseous species, but has also been used in the analysis of solids[2] and liquids[3-4] through evanescent-wave absorption. The most common implementation of CRDS involves forming a very high finesse optical cavity with two highly reflective mirrors ($\rho \geq 0.99$). When a pulse of laser light is injected into the cavity, through the back of one of the mirrors, it is reflected back and forth within the cavity. The light that is reflected within the cavity decays exponentially because of the transmittance losses of the cavity. Consequently, the time-dependent light intensity within an empty cavity can be described in the following fashion,

$$i(t) = i_o \exp\left[-(1-R)\frac{tc}{L}\right] \tag{1}$$

where *i(t)* is the light intensity at time *t* after the laser pulse enters the cavity, i_o is the initial light intensity, *R* is the reflectivity of the mirrors, *c* is the speed of light, and *L* is the distance between the mirrors. The time constant of this decay, referred to as the ring-down time τ, is the point at which Eq. (1) becomes

$$i(t) = i_o e^{-1} \tag{2}$$

Therefore, the ring-down time, τ_1, of an empty optical cavity can be expressed as,

$$\tau_1 = \frac{t_r}{2(1-R)} \tag{3}$$

where t_r is the round-trip time of the light within the cavity.

When an absorbing species is placed within the cavity, the ring-down time is shortened, and becomes a function of the absorbance, αl, the material within the cavity, where α and *l* are the absorption coefficient and path length of the absorbing medium, as is shown in Eq. (4).

$$\tau_2 = \frac{t_r}{[2(1-R)+\alpha l]} \tag{4}$$

The classical Beer's Law absorbance, *A*, can then be determined by combining Eqs. (3) and (4), as seen below.

$$\alpha l = A = \frac{L}{c}\left(\frac{1}{\tau_2} - \frac{1}{\tau_1}\right) \tag{5}$$

A representation of the time-dependent light intensity within the cavity is obtained by placing a photomultiplier tube (PMT) at the back of one mirror and measuring the small amount of light that is transmitted with each pass of the light pulse. The amount of light within the cavity is directly proportional to the fraction transmitted by the mirror and registered by the PMT.

CRDS offers several advantages over traditional absorption measurements. First, the absorption determination in CRDS is independent of the initial light intensity, because the rate of decay of light within the cavity (rather than the absolute radiant power) is measured. Therefore, it obviates the need to have a highly stable light source. Also, because the light passes though the sample numerous times, the pathlength is significantly increased, to effective distances of tens of kilometers. Finally, the very high signal-to-noise ratio results in extremely small detectable absorbance values (~10^{-8}).

Although CRDS offers many advantages over conventional absorption measurements, it introduces a new set of difficulties. The optical alignment of the mirrors that form the cavity can be tedious and, even when achieved, the typical cavity lengths of ~1 m can consume a significant amount of laboratory space. In addition, CRDS requires highly reflective mirrors and a coherent, intense light source, such as a laser, which can be very costly and difficult to maintain. Furthermore, the reflectivity of the mirrors changes with wavelength, which makes obtaining a full UV-visible

absorption spectrum with CRDS nearly impossible. These shortcomings led to the development of a similar technique: fiber-loop ring-down spectroscopy (FLRDS).

In FLRDS, an optical resonator is created by splicing the ends of a single optical fiber together, forming a loop. Light is injected from a pulsed light source through the cladding of the fiber and into the core.[5-7] A bend[7-8] in the fiber or a directional coupler[9-10] is used to scatter or leak light from the fiber core at a different point along the fiber. The intensity of the detected light is then directly proportional to the light held in the core, so the ring-down time can be measured. A typical FLRDS system can be found in Reference 5.

The initial description of FLRDS was for the detection of trace gases through direct absorption.[9] In this arrangement, a 5-cm gas cell was placed between two ends of an erbium-doped fiber. Complicated optics were needed to minimize light loss through the gas cell as well as to pump the Er-doped fiber, which is needed to generate the near-infrared (NIR) radiation. Additionally, any gas with overtone absorption bands between 1530 and 1580 nm could result in a shift in ring-down time, making the sensor useful only for simple, known gas mixtures.

FLRDS has also been used for absorption measurements of liquids in which a solution was passed directly through the fiber splice by means of a syringe pump or capillary electrophoresis (CE) output.[7] This setup enabled the analysis of very small volumes of liquid, ~700 pL. Although this analysis volume is ideal for CE, the absorption path length is very short, which greatly reduces the absorption sensitivity. In turn, this lower sensitivity requires very small changes in ring-down time to be detected.

Another limitation of typical FLRDS arrangements is that the laser light is injected into the core through a bend in the fiber, resulting in very low coupling efficiencies ($\sim 10^{-8}$).[5] An alternative is to use a directional coupler to introduce light at a much higher and known efficiency ($\sim 10^{-3}$),[11] but this modification raises the complexity and cost of the system and introduces additional optical losses. Moreover, directional couplers are currently unavailable for visible wavelengths. These drawbacks can be avoided by measuring the absorption of the evanescent wave by an analyte positioned near the core/cladding interface; this is the approach used in the present study.

Over recent years, numerous forms of these fiber-loop systems have been described for various sensing applications.[12] In most cases, the evanescent wave from light in the fiber core is used to probe the sample through direct absorption[4, 13-14] or leaking caused by temperature,[15] pressure,[11, 16] or refractive index changes.[17] Because the evanescent wave ordinarily penetrates only a short distance into the cladding material of a typical optical fiber, significant modifications to the cladding or fiber structure are usually needed to extend the evanescent wave into the sampling region, thus creating a fiber-loop ring-down (FLRD) sensor. Examples of such alterations include tapering a region of the fiber,[13] physically or chemically removing a section of cladding,[18] and incorporating long-period gratings into the core.[19] These modifications introduce additional losses, adversely affecting the ring-down time and, ultimately, sensitivity. Furthermore, these changes can often be made only to small sections of an optical fiber (< 1 m), limiting effective light-sample interaction volume. The majority of FLRDS systems employ NIR lasers (~800 nm — ~1500 nm) to generate the probing radiation mainly because of the high transmittance of NIR radiation in optical fibers (> 99.5%) and

associated optics. Only a couple of examples of FLRDS with the use of visible lasers have been presented;[8, 20] in both cases, the systems were used in a direct absorption mode, compromising the selectivity of the device.

We have previously shown that chemical-sensing molecules can be immobilized in large sections of the plastic cladding of an optical fiber, while introducing minimal light loss.[21] Upon exposure of the chemically modified fiber to a specific analyte, the maximum absorption wavelength of the sensing molecule shifts, which changes the absorption of the evanescent wave of light traveling through the fiber core.[21-23] In the present study, this colorimetric, chemical sensing approach was merged with the FLRD method to expand the methods and applications of FLRD sensors. This proof-of-concept study used phenol red as the fiber-doping agent and was used as a sensor for ammonia.

A.2 Theory

In conventional CRDS, the relationship between absorbance, A, of a sample within the optical cavity and the ring-down times of an empty and filled cavity (τ_1 and τ_2, respectively) is described by Eq. (5). However, when a fiber-optic ring resonator is used in place of the mirrors, Eq. (3) must be modified to include additional losses,

$$\tau = \frac{L_F}{c_o\left[\alpha_c L_F - \ln(T)\right]} \tag{6}$$

where L_F is the length of the fiber, c_o is the speed of light within the core, $\alpha_c L_F$ is the absorption of light in the core material, and T is the transmission of the fiber splice.

In the current study, a portion of the existing fiber cladding was chemically modified with an analyte-responsive reagent. This approach for making chemical sensors for detection of species in air and water offers several advantages over other schemes in which the optical fiber is re-clad with a sensing agent.[21-22, 24] These advantages include (1) preserved mechanical stability of the modified fiber region,[22] (2) no induced optical losses that otherwise originate from the removed original cladding and a replaced region, and (3) a possibility of modification over extended lengths of the fiber, at least several tens of meters.[24]

When only a portion of the original optical fiber cladding is modified with a chemically sensitive reagent, no additional losses are introduced to the sensor otherwise associated with a replaced/removed cladding or a modified fiber. Thus, the chemical response of the FLRD sensor can be described as:

$$\tau = \frac{L_F}{c_o\left[\alpha_c L_F - \ln(T) + A_S\right]} \tag{7}$$

where A_S is the absorbance of the optical fiber with the chemically modified cladding at the probe wavelength over the modified fiber length L_S.

Previously, we showed that when light is launched into a multimode optical fiber, the distribution of the bound modes will reach a steady state[25] and that integration over all those modes ($x = 0 - 1$) will describe the sensor absorbance, A_S.[23]

$$A_S = -\log_{10} \int_0^1 \exp\left\{ -\frac{\alpha_S n_2 L_S x^2}{n_1 V \left[\left(1 - x^2\right)\left(1 - 2\Delta x^2\right) \right]^{1/2}} \right\} dx \qquad (8)$$

In equation 8, x is the relative mode index, n_1 and n_2 are the refractive indices of the fiber core and cladding, respectively, V is the waveguide parameter, Δ is the profile height parameter, and α_S is the bulk absorption coefficient of the chemically modified cladding.

Overall, Eqs. (7) and (8) describe the response of the colorimetric FLRD sensor based on a multimode step-index optical fiber with a chemically modified, original cladding. Again, this approach does not add scattering losses to Eq. 7 that are present when a fiber is tapered or its cladding replaced/removed. Equation 8 also illustrates that the effective path length of the chemical sensor is related to the properties of the employed waveguide structure and of the mode distribution in the fiber during the chemical measurement.

A.3 Experimental

A.3.1 Chemical Reagents and Materials

Phenol red was obtained from Aldrich (Milwaukee, WI). Solutions of phenol red were prepared in reagent-grade tetrahydrofuran (THF) purchased from commercial suppliers. For sensing, concentrated, reagent-grade NH_4OH and distilled, deionized water were used. Dry nitrogen was supplied from boil-off of a local liquid-nitrogen storage facility. Multimode plastic clad silica (PCS) fibers SPC 200/300/400N and SPC 200/300R were purchased from Fiberguide Industries (Sterling, NJ). Propylene glycol (Aldrich, Milwaukee, WI) was used to remove the fiber jacket, when necessary.

A.3.2 Fiber-Loop Ring-Down Setup

A diagram of the experimental system is given in Figure A.1. In all cases, the fiber was coiled onto a spool and the splice position was adjusted with an x-y-z translation stage (Model F1015, Newport Corporation, Irvine, CA). Pulses of 532 nm light from a 5 kHz, frequency-doubled Nd:YAG laser (10 mW average power, NG-151-100, JDS Uniphase, Milpitas, CA) were injected into the fiber through the splice point. Light scattered from the fiber core was detected at a different section of the fiber by means of a photomultiplier tube (PMT, R928, Hamamatsu Corporation). The output signal from the PMT was fed directly into a 50Ω terminal of a 500 MHz digital oscilloscope (TDS 520, Tektronix, Inc., Beaverton, OR). The FLRD trace was then transferred to a computer by a GPIB USB cable (GPIB-USB-B, National Instruments, Austin, TX) and recorded with an in-house written LabVIEW program.

A.3.3 FLRD Signal Processing

A typical ring-down trace is given in Figure A.2. In order to extract the ring-down time from the data trace, a different in-house written LabVIEW program was used. The peaks were identified and fit, by means of the least-squares method, to an exponential of the form,

$$y = y_o + A_1 \times e^{(-t/\tau)} \tag{9}$$

The first few peaks of each trace were discarded from the fit for the two following reasons: i) the first peak is generated when light is inefficiently backscattered into the loop, which then strikes the detector before the main injection pulse and ii) the PMT was

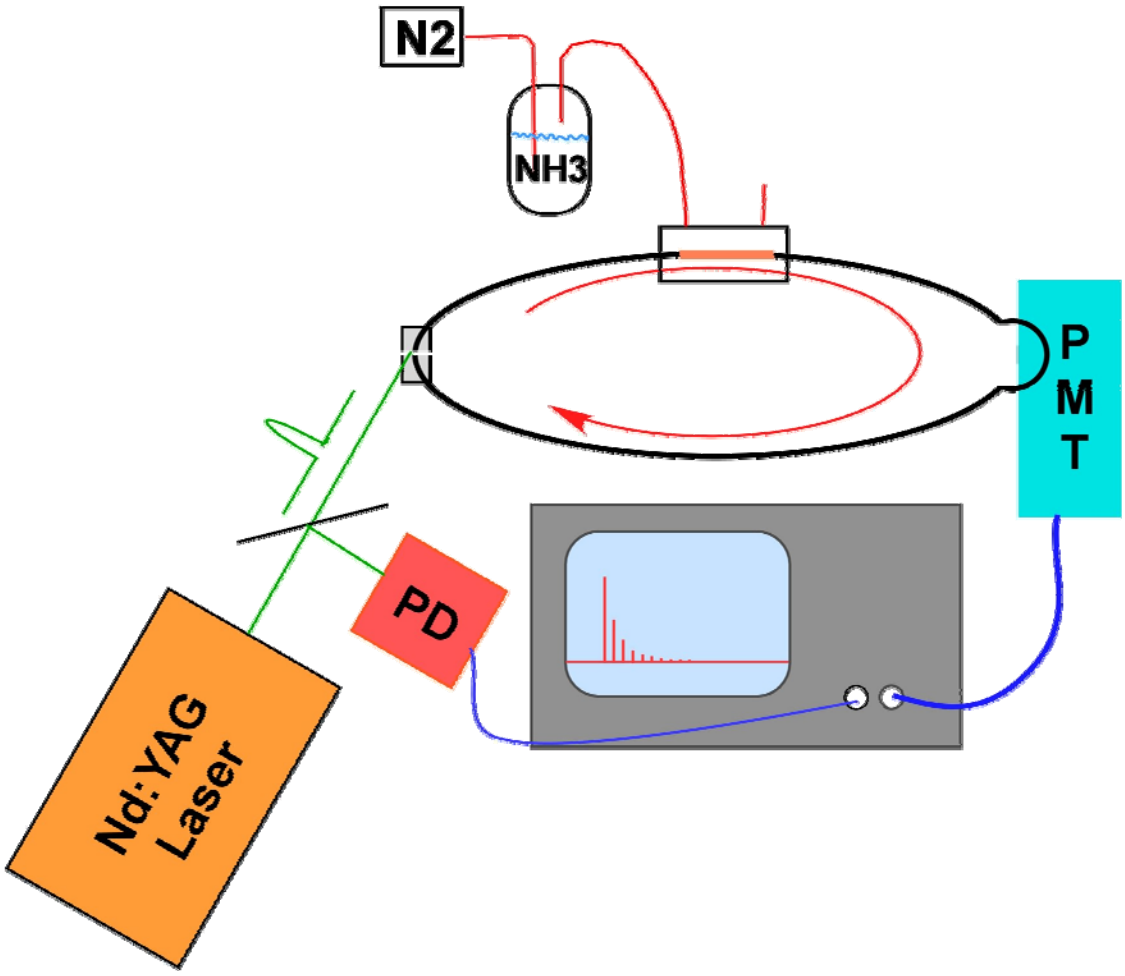

Figure A.1 Diagram of FLRD setup used in the present study. A pulse of 532 nm laser light from a frequency doubled Nd:YAG laser was coupled into the fiber by injection at the splice point. A photodiode (PD) was used to trigger the oscilloscope to accurately record the ring-down trace from the PMT.

either saturated or near saturation. After these considerations, the ring-down time, τ, was easily extracted. For time-based measurements, the time of the ring-down trace was recorded with each collected signal.

A.3.4 Modification of Existing Silicone Cladding

The protective nylon jacket was removed from an 8.5-m strand of SPC 200/300/400N fiber by immersing the fiber into boiling propylene glycol for ~5 min.[22] For ammonia sensing, 300 μL of a 0.1 mM solution of phenol red in THF was applied three times to a 7.5-cm section of the silicone cladding and allowed to dry. After the final application, the fiber was allowed to dry for about 30 min to allow the cladding to shrink back to its original dimensions. Finally, the fiber was rinsed with ethanol and THF to remove any unbound phenol red.

A.3.5 Ammonia Sensing

For gas-phase ammonia sensing, the modified section of fiber was placed into a small-volume (~6 mL) gas sample cell. Spatially averaged measurements of ammonia concentrations over the doped region were performed with the FLRD set-up shown in Figure A.1. Dry nitrogen was bubbled through a solution containing NH_4OH and H_2O. The resulting vapor was passed over the fiber in the gas sample cell. Special care was taken to ensure that the gas flow rate over the fiber, as well as relative humidity, were held constant throughout each experiment.

A.4 Results and Discussion

A typical ring-down trace from an un-doped, 8.7-m optical fiber is shown in Figure A.2. The calculated ring-down time from this trace was 206.4 ns, which corresponds to a loss of 0.863 dB per roundtrip. The manufacturer's listed spectral attenuation for this optical fiber, with the jacket intact, at 532 nm is ~0.025 dB/m, which indicates a significant portion of light is lost through other means, such as scattering at the splice point or from damaged cladding cause by the jacket-removal process. It is also interesting that the ring-down peaks were significantly wider (~ 11 ns) than the laser pulse width (~600 ps). In addition, the ring-down peaks continue to widen with each round-trip. This broadening is due to the multimode nature of the optical fiber. Higher-order modes trapped in the fiber take longer to traverse the loop than lower-order modes. Furthermore, the ring-down peak shapes also yield qualitative information about the mode structure contained within the fiber. The sharp rising edge followed by a decaying tail (cf. Figure A.2), indicates that lower-order modes comprise the majority of light surviving multiple passes.

To test the feasibility of a distributed colorimetric FLRD sensor operated at visible wavelengths, phenol red was used as the sensing agent for this model system. Phenol red has a well-characterized absorption-spectrum shift upon exposure to basic conditions; the absorption maximum moves from ~450 nm to ~560 nm,[21] making the 532-nm laser a suitable choice for these experiments. Another advantage of phenol red as an ammonia sensing agent, over other colorimetric dyes[26] such as nile red, is that it exhibits minimal fluorescence, in either the acidic or basic form, upon excitation at

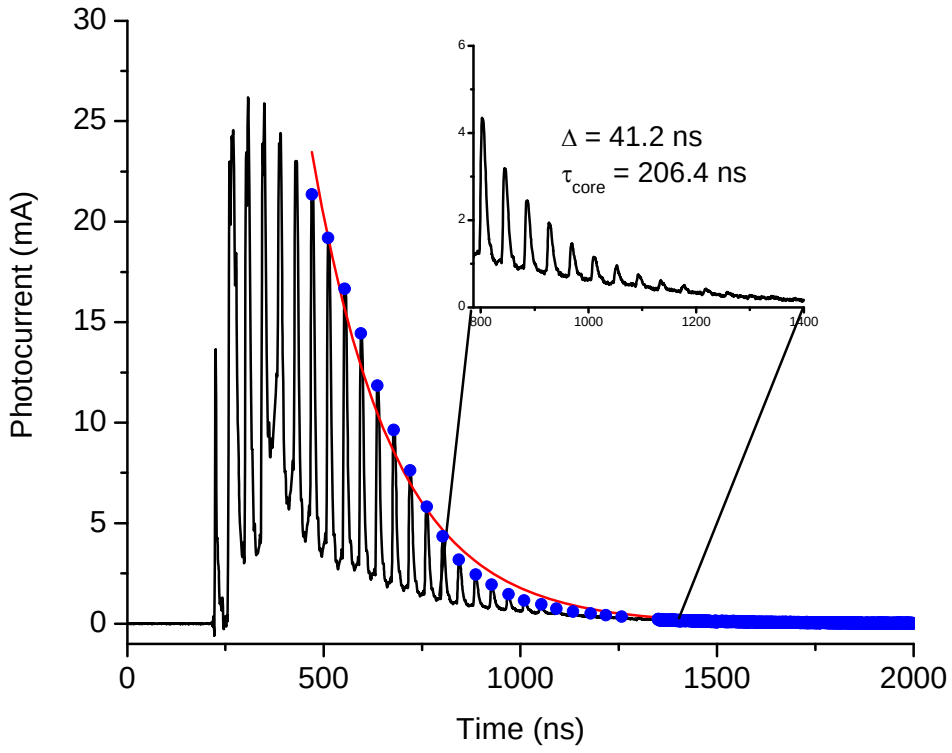

Figure A.2 Typical trace from the FLRD set-up. In fitting the peaks with an exponential curve, the first few were disregarded because of backscattered laser light or PMT saturation. The fiber length and effective path length were determined to be 8.7 m and 178.5 m, respectively, from the distance (Δ) between peaks (41.2 ns) and the number of detectable peaks (21). The path length corresponds to the total distance in the fiber and not to the path length through the cladding-modified section.

532 nm. Fluorescence from the sensing dye into the fiber core would introduce errors in the ring-down time.

Diffusion of the chemical sensing agent, phenol red, into the cladding was monitored in real time by measuring the ring-down time when the THF/phenol red solution was applied to the fiber (cf. Figure A.3). The ring-down time was constant until the solution was added to the fiber's silicone cladding, at which point τ began to decrease as the cladding swelled from the exposure to THF. The sudden drop in τ from 240 ns to 90 ns occurred when the THF completely evaporated and the sensing agent was fully incorporated into the cladding. Quickly washing the fiber with THF and ethanol removed crystalline phenol red that otherwise acted as a scattering agent and further reduced τ.

Upon initial exposure to ammonia vapor, the ring-down time surprisingly increased (Figure A.4). However, once the ammonia vapor was removed, the ring-down time lengthened yet again and the sensor behaved as expected to the ammonia vapor. Although the reason for this priming of the sensor is not yet understood, the same behavior was noted during earlier experiments involving the development of this fiber sensor in a conventional, evanescent-wave absorption mode.[21] It has also been previously shown that these sensors are stable over long periods of time even in harsh conditions, such as storage in solutions of high acidity or basicity.[22]

Because the ammonia vapor in these experiments was produced from an aqueous solution, the influence of relative humidity on the sensor response was determined (cf. Figure A.5). There was found to be a rise in ring-down time τ from ~140 ns to ~150 ns as the relative humidity was increased. The same trend was observed when a change in

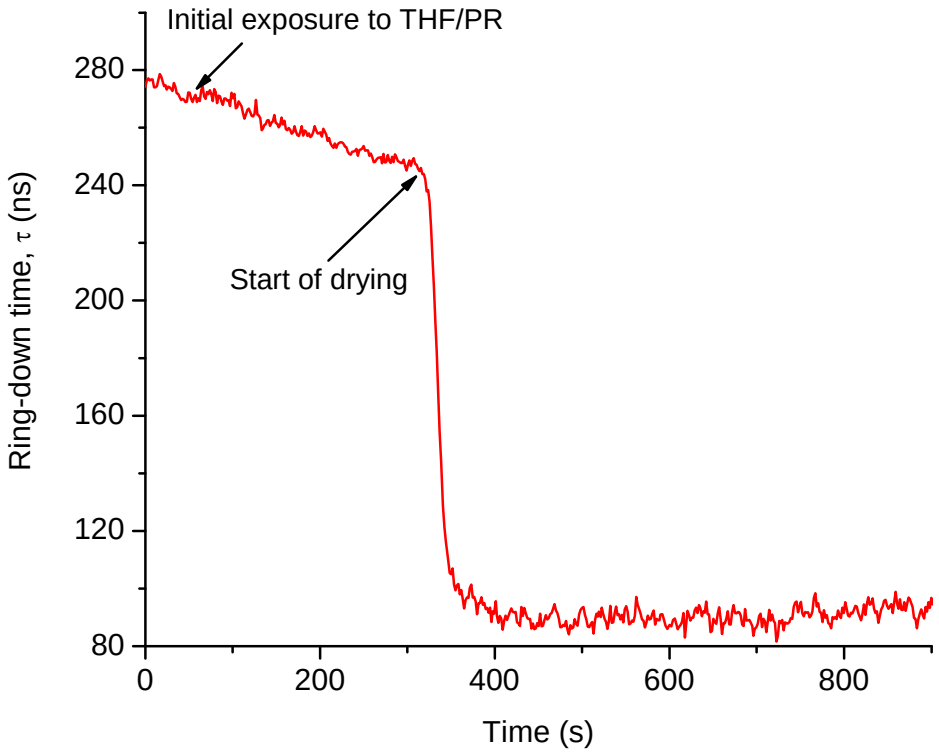

Figure A.3 Initial exposure of the optical fiber to a solution of THF and phenol red. Once the THF fully evaporates, there is a rapid, dramatic drop in the ring-down time due to evanescent wave absorption by phenol red at the core/cladding interface.

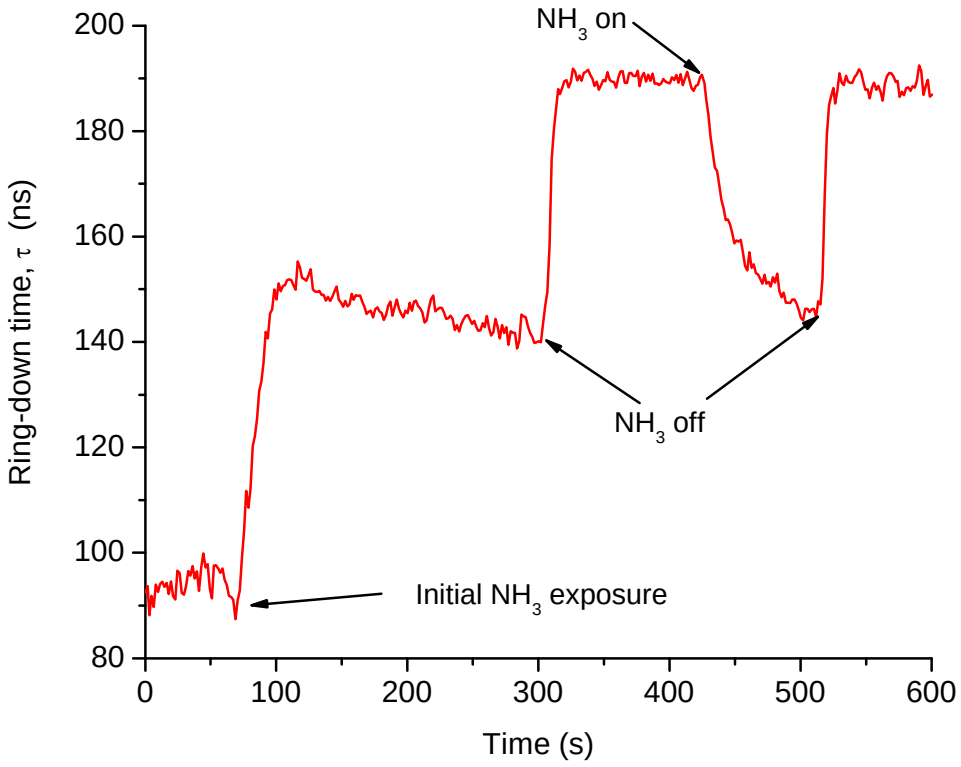

Figure A.4 Repeated exposure of the sensor to ammonia vapor after the cladding was doped with phenol red. The sensor required an initial priming with ammonia vapor before behaving as expected.

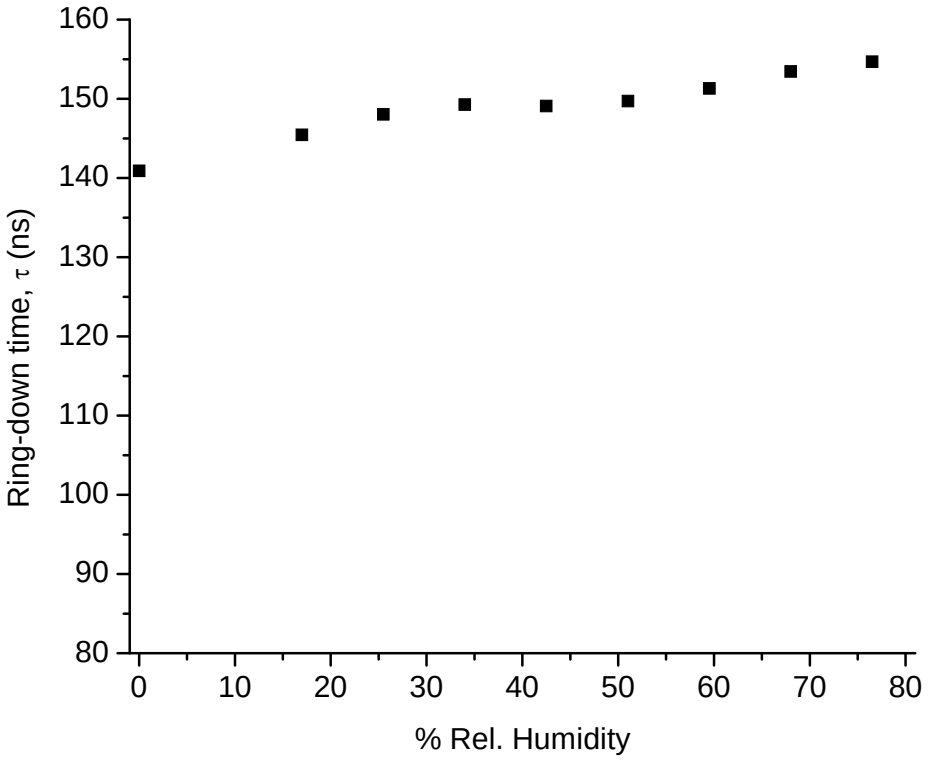

Figure A.5 Effect of relative humidity on ring-down time, τ. The increase in ring-down time is likely due to a change in the refractive index of the fiber cladding.

humidity was applied to an undoped section of the fiber. Therefore, this rise in ring-down time is likely due to a change in the refractive index ratio between the core and the cladding. The addition of water to the cladding would lower its refractive index, allowing more modes to be maintained within the core of the fiber, ultimately resulting in longer ring-down times. For this reason, the humidity and total gas flow were maintained at constant values for all subsequent studies with this sensor.

As a benchmark, use of the distributed colorimetric FLRD sensor was compared with its use in a conventional transmission mode. The transmission mode was implemented simply by breaking the fiber splice and placing a neutral density filter between the fiber end and the detector to measure the peak height of the laser pulse. A transmission-mode plot of the signal versus time for various concentrations of ammonia is shown in Figure A.6a, with the resulting calibration curve in Figure A.6b. Nonlinearity in the calibration curve was due to saturation of the sensing molecule, which occurred at a relatively low concentration because only a 6-cm section of the fiber was doped. Fitting the data with a sigmoidal function yielded a correlation coefficient of 0.988 and a limit of detection (LOD) of 2.1 ppm. When the transmission calibration curve is compared to one generated with the sensor used in FLRD mode (Figure A.7), the most important feature is that the same non-linearity exists in both operating modes. In addition, the measured absorbance values agree well. For the case of the sensor in FLRD mode, the correlation coefficient and LOD were 0.992 and 1.8 ppm, respectively. Although little, if any, improvement in LOD and sensitivity are seen with the presented form of FLRD sensor, this study demonstrates the feasibility of a colorimetric FLRD sensor with a chemically modified cladding. Of course, larger sections of cladding could

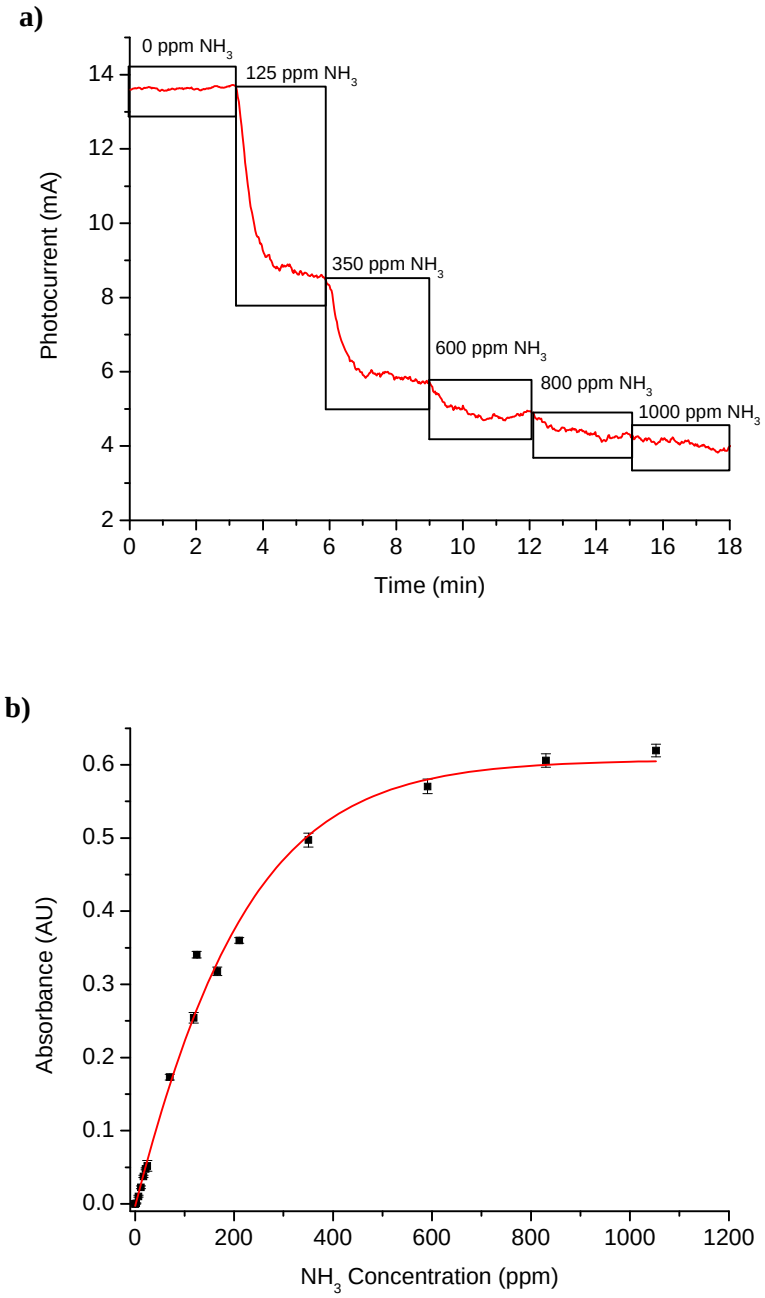

Figure A.6 a) Response of the phenol-red-doped sensor in transmission mode to different concentrations of NH_3. b) Calibration curve from data in part (a); correlation coefficient and LOD are 0.988 and 2.1 ppm, respectively.

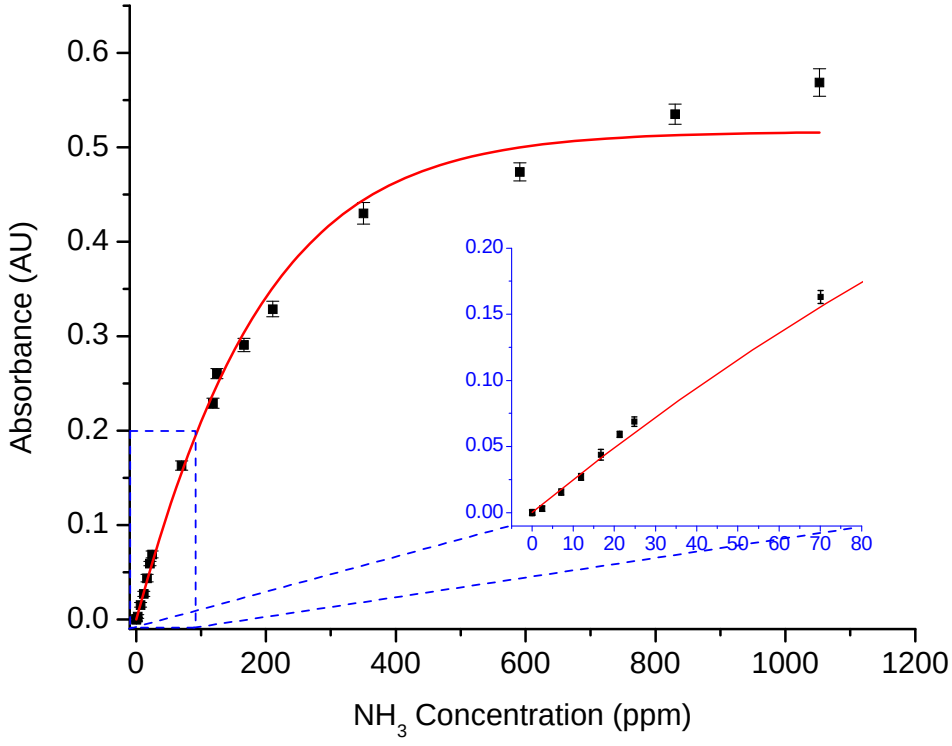

Figure A.7 Calibration curve for sensor in FLRD mode. Correlation coefficient and LOD for FLRD-mode are 0.992 and 1.8 ppm, respectively.

be doped to improve sensitivity, while introducing minimal scatter losses. However, only small sections were doped in this initial study to maintain the same fiber splice before, during, and after chemical modification.

The main reason for the limited sensitivity of the present sensor in the FLRD mode was fluctuation in light scattered from the fiber core with each pass of light circulating around the fiber. This problem might be overcome either by using a directional coupler or by incorporating a scattering agent into the cladding. Use of directional couplers would be an ideal option to improve not only light detection, but injection as well; however, directional couplers are fairly expensive and require more components for optical alignment as well as for splices. A much simpler and more cost-effective method would be to incorporate salts or fluorophores into the cladding for use as internal references. Although this approach would introduce additional losses into the fiber core, it has been found that most of the losses in FLRDS are from inefficient transmission at the splice.[7]

In this study, the applicability of distributed colorimetric sensors to the field of fiber-loop ring-down spectroscopy was exploited to overcome issues of selectivity observed with conventional FLRDS systems. Conversely, employing cavity ring-down principles to fiber-optic chemical sensing can reduce noise associated with short- and long-term fluctuations of the light source while increasing the interaction length between the light and the sensing dye. A full comparison between the FLRD distributed sensor described here with both conventional FLRDS and standard evanescent-wave absorption sensors is given in Table A.1. Ultimately, chemically modifying the silicone cladding of

Table A.1. Comparison of evanescent-wave absorption, conventional FLRDS, and the FLRD distributed sensor.

	Evanescent-wave absorption sensor	Conventional FLRDS	FLRD Distributed Sensor
Sensing region	Pathlength limited by recladded fiber length and propagating modes in the fiber.	Detection region between spliced fiber tips or short region of bare-core fiber.	Distributed sensing region along fiber length.
Optical quality of sensing region	Large scatter losses due to manual cladding removal and recladding with a sensing material.	Scatter losses from bare-core fiber or reflections from non-index matched liquids.	No additional scatter losses introduced by modification of fiber cladding.
Light injection approach	Simple illumination of fiber tip with NA-matching objective.	Complicated directional coupler or poor injection into bend in fiber.	Straightforward injection into the fiber splice.
Ring-down signal/noise enhancement	No	Yes	Yes
Intensity-independent readout	No	Yes	Yes

a fiber loop should drastically increase the interaction volume between the light and analyte over previously described FLRDS methods, without introducing additional losses induced by cladding removal or fiber tapering. Further, although lasers are commonly used in FLRDS, it is not essential to use a coherent light source. Inexpensive light sources, such as light-emitting diodes, could be employed as long as their light is efficiently coupled into the fiber loop and the source has a turn-off time significantly faster than the ring-down time. The result would be a sensitive, inexpensive, and selective chemical sensing system.

References

1. Busch, K. W.; Busch, M. A., *Cavity-Ringdown Spectroscopy*. American Chemical Society: 1999; Vol. 720, p 269.
2. Engeln, R.; von Helden, G.; van Roij, A. J. A.; Meijer, G. *J. Chem. Phys.* **1999**, *110*, 2732-2733.
3. Bahnev, B.; vanderSneppen, L.; Wiskerke, A. E.; Ariese, F.; Gooijer, C.; Ubachs, W. *Anal. Chem.* **2005**, *77*, 1188-1191.
4. Xu, S.; Sha, G.; Xie, J. *Rev. Sci. Instrum.* **2002**, *73*, 255-258.
5. Brown, R. S.; Kozin, I.; Tong, Z.; Oleschuk, R. D.; Loock, H. P. *J. Chem. Phys.* **2002**, *117*, 10444-10447.
6. Loock, H.-P. *Tr. Anal. Chem.* **2006**, *25*, 655-664.
7. Tong, Z. G.; Jakubinek, M.; Wright, A.; Gillies, A.; Loock, H. P. *Rev. Sci. Instrum.* **2003**, *74*, 4818-4826.
8. Waechter, H.; Bescherer, K.; Durr, C. J.; Oleschuk, R. D.; Loock, H. P. *Anal. Chem.* **2009**, *81*, 9048-9054.
9. Stewart, G.; Atherton, K.; Yu, H. B.; Culshaw, B. *Meas. Sci. Technol.* **2001**, *12*, 843-849.
10. Tarsa, P. B.; Wist, A. D.; Rabinowitz, P.; Lehmann, K. K. *Appl. Phys. Lett.* **2004**, *85*, 4523-4525.
11. Wang, C. J.; Scherrer, S. T. *Appl. Opt.* **2004**, *43*, 6458-6464.
12. Waechter, H.; Litman, J.; Cheung, A. H.; Barnes, J. A.; Loock, H. P. *Sensors* **2010**, *10*, 1716-1742.

13. Tarsa, P. B.; Rabinowitz, P.; Lehmann, K. K. *Chem. Phys. Lett.* **2004**, *383*, 297-303.

14. Jiang, M.; Zhang, W. G.; Zhang, Q.; Liu, Y. P.; Liu, B. *Optics Communications* **2010**, *283*, 249-253.

15. Wang, C. J.; Mbi, A. *Meas. Sci. Technol.* **2006**, *17*, 1741-1751.

16. Tarsa, P. B.; Brzozowski, D. M.; Rabinowitz, P.; Lehmann, K. K. *Opt. Lett.* **2004**, *29*, 1339-1341.

17. Barnes, J.; Dreher, M.; Plett, K.; Brown, R. S.; Crudden, C. M.; Loock, H. P. *Analyst* **2008**, *133*, 1541-1549.

18. von Lerber, T.; Sigrist, M. W. *Appl. Opt.* **2002**, *41*, 3567-3575.

19. Pu, S. A.; Gu, X. J. *Opt. Lett.* **2009**, *34*, 1774-1776.

20. Andachi, M.; Nakayama, T.; Kawasaki, M.; Kurokawa, S.; Loock, H. P. *Appl. Phys. B-Lasers Opt.* **2007**, *88*, 131-135.

21. Potyrailo, R. A.; Hieftje, G. M. *Appl. Spectrosc.* **1998**, *52*, 1092-1095.

22. Potyrailo, R. A.; Hieftje, G. M. *Fresenius. J. Anal. Chem.* **1999**, *364*, 32-40.

23. Potyrailo, R. A.; Ruddy, V. P.; Hieftje, G. M. *Appl. Opt.* **1996**, *35*, 4102-4111.

24. Potyrailo, R. A.; Hieftje, G. M. *Anal. Chem.* **1998**, *70*, 1453-1461.

25. Potyrailo, R. A.; Ruddy, V. P.; Hieftje, G. M. *Anal. Chem.* **1999**, *71*, 4956-4964.

26. Wolfbeis, O. S. *Anal. Chem.* **2006**, *78*, 3859-3873.

Jacob T. Shelley

Department of Chemistry • Indiana University • Bloomington, IN 47405
Phone: 812-855-7905 • Fax: 812-855-0958 • jtshelle@indiana.edu

1200 Rolling Ridge Way, Apt. 401, Bloomington, IN 47403
Phone: 505-660-1852

PERSONAL INFORMATION

Birth: March 4, 1984 – Albuquerque, NM
Citizen of the United States of America

EDUCATION

2005-2011 — Indiana University — Bloomington, IN
Ph.D. Candidate in Analytical Chemistry
Minor: Physical Chemistry/Spectroscopy
Research Advisor: Professor Gary M. Hieftje
Thesis Title: Development and Characterization of Plasma-based Sources for Ambient Desorption/Ionization Mass Spectrometry

Completion Date: May 31, 2011

2002-2005 — Northern Arizona University — Flagstaff, AZ
B.S. Chemistry (ACS Certified)
Minor: Mathematics

RESEARCH EXPERIENCE

2009-2010 — Purdue University — West Lafayette, IN
Research Assistant
Advisor: Professor R. Graham Cooks
Fundamentally compared plasma-based ionization sources for molecular mass spectrometry. Gained experience with ion source and ion trap MS development and maintenance. Worked collaboratively with other group members and with other research groups within the university.

2005-present — Indiana University — Bloomington, IN
Research Assistant
Advisor: Professor Gary M. Hieftje
Developed and characterized a novel ambient ionization source for MS. Developed a novel fiber-optic sensor based on fiber-loop ring-down

spectroscopy. Gained experience with time-of-flight MS, GC, laser use and maintenance, laser ablation, LabVIEW, electronics, and machining. Worked collaboratively with other group members and with other research groups within the university.

2005 — Los Alamos Nation Laboratory — Los Alamos, NM
Bioscience Division
Graduate Research Assistant
Mentors: Dr. Christy Ruggiero and Dr. Srinivas Iyer
Used mesoporous silica wafers as a means to perform matrix-free MALDI analyses. Developed metallomic analysis methods in gel electropherograms using XRF. Gained experience with numerous analytical and biochemical techniques (XRF, CE, MALDI, SDS-PAGE, and IEF).

2004-2005 — Northern Arizona University — Flagstaff, AZ
Undergraduate Research Assistant
Advisor: Dr. Diane Stearns
Determined metal-DNA adduct levels in CHO cells using ICP-OES. Performed elemental analysis of tattoo inks. Gained experience with using, managing, and maintaining ICP-OES.

2003-2005 — Los Alamos Nation Laboratory — Los Alamos, NM
Chemistry Division
Undergraduate Student Internship
Mentors: Dr. Christian Hassell and Dr. Cris Lewis
Built miniature Grimm-type interface glow discharge quadrupole mass spectrometer. Performed method development for ^{90}Sr detection. Gained experience with instrument development and different scintillation techniques.

2003 — Northern Arizona University — Flagstaff, AZ
Undergraduate Research Assistant
Supervisor: Professor Paul Torrence
Performed organic syntheses of precursors for potential herpes and smallpox vaccinations. Gained experience using HPLC and NMR.

TEACHING EXPERIENCE

2005-present — Indiana University — Bloomington, IN
Associate Instructor
Instructed freshman and sophomore undergraduates (C117), junior and senior undergraduate biochemistry majors (A316) and first and second year graduate students (C501, C566, C612). Responsible for preparing, administering, and grading both oral and written examinations as well as written lab reports.

C612, Spectrochemical Methods of Analysis, Spring 2009
C501, Chemical Instrumentation, Head Associate Instructor, Fall 2008
C566, Molecular Optical Spectroscopy, Spring 2008
C501, Chemical Instrumentation, Laboratory Associate Instructor, Fall 2007
C501, Chemical Instrumentation, Laboratory Associate Instructor, Fall 2006
A316, Bioanalytical Chemistry Laboratory, Spring 2006
C117, General Chemistry Laboratory, Fall 2005

2008	2008 Winter Conference on Plasma Spectrochemistry Time-of-Flight Mass Spectrometry For Elemental Analysis, Gary M. Hieftje and **Jacob T. Shelley**. Short course.	Temecula, CA
2010	2010 Winter Conference on Plasma Spectrochemistry Ambient Desorption/Ionization-Mass Spectrometry: From Fundamentals to Applications, **Jacob T. Shelley**. Short course.	Fort Meyers, FL

HONORS

2010	2010 FACSS Student Award	FACSS, Raleigh, NC
2009	G. M. Hieftje Research Group Award	Indiana University
2009	Center for Analytical Instrumentation Development Fellowship	Purdue University
2009	Associate Instructor Award	Indiana University
2008	Baxter Pharmaceutical Fellowship	Indiana University
2007	FACSS Student Poster Award	FACSS, Memphis, TN
2005	Senior Research Award	Northern Arizona University
2005	College of Engineering and Natural Sciences Symposium Award	Northern Arizona University

PROFESSIONAL ACTIVITIES

2004-Present	Society for Applied Spectroscopy
2004-Present	Alpha Chi Sigma chemistry fraternity
2007-Present	American Society for Mass Spectrometry
2004-2006	Student Affiliates of the American Chemical Society
2002-2005	American Chemical Society

PUBLICATIONS

Shelley, J. T.; Chan, G. C. Y.; Hieftje, G. M., Optical Characterization of the Flowing Atmospheric-Pressure Afterglow (FAPA) Ambient Ionization Source. *J. Am. Soc. Mass Spec.* **2011,** *Accepted.*

Shelley, J. T.; Hieftje, G. M., Ambient Mass Spectrometry: Approaching the Chemical Analysis of Things As They Are. *J. Anal. At. Spectrom.* **2011,** *Submitted.*

Shelley, J. T.; Wiley, J. S; Hieftje, G. M., Ultrasensitive Ambient Mass Spectrometric Analyses a Pin-to-Capillary Flowing Atmospheric-Pressure Afterglow Source. *Anal. Chem.* **2011,** *In Press.*

Gonzálvez, A.; **Shelley, J. T.**; Wiseman, J. M.; Armenta, S.; de la Guardia, M.; Hieftje, G. M., Direct Quantification of Veterinary Residues in Foodstuff Through Desorption Electrospray Ionization-Mass Spectrometry. *Analyst.* **2011,** *In Preparation.*

Chan, G. C. Y.; **Shelley, J. T.**; Wiley, J. S.; Jackson, A. U.; Engelhard, C.; Cooks, R. G.; Hieftje, G. M., Elucidation of Reaction Mechanisms Responsible for Afterglow Formation and Analyte Ionization in the Low-Temperature Plasma Probe Ambient Ionization Source. *Anal. Chem.* **2010,** 83, (10), 3675-3686.

Chan, G. C. Y.; **Shelley, J. T.**; Jackson, A. U.; Wiley, J. S.; Engelhard, C.; Cooks, R. G.; Hieftje, G. M., Spectroscopic Plasma Diagnostics on a Low-Temperature Plasma Probe for Ambient Mass Spectrometry. *J. Anal. At. Spectrom.* **2010,** *In Press*.

Shelley, J. T.; Hieftje, G. M., Fast transient analysis and first-stage collision-induced dissociation with the flowing atmospheric-pressure afterglow ionization source to improve analyte detection and identification. *Analyst.* **2010,** 135, (4), 682-687.

Shelley, J. T.; Potyrailo, R. A.; Ray, S. J.; Hieftje, G. M., Distributed, Colorimetric Fiber-Optic Sensor Based on Fiber-Loop Ring-Down Spectroscopy. *Rev. Sci. Inst.* **2010,** *Submitted*.

Shelley, J. T.; Hieftje, G. M., Ionization Matrix Effects in Plasma-Based Ambient Mass Spectrometry Sources. *J. Anal. At. Spectrom.* **2010,** 25, (1), 345-350.

Schilling, G. D.; **Shelley, J. T.**; Barnes, J. H.; Sperline, R. P.; Denton, M. B.; Barinaga, C. J.; Koppenaal, D. W.; Hieftje, G. M., Detection of Positive and Negative Ions from a Flowing Atmospheric Pressure Afterglow Using a Mattauch-Herzog Mass Spectrograph Equipped with a Faraday-Strip Array Detector. *J. Am. Soc. Mass. Spectrom.* **2010,** 21, (1), 97-103.

Shelley, J. T.; Wiley, J. S.; Chan, G. C. Y.; Schilling, G. D.; Ray, S. J.; Hieftje, G. M., Characterization of Direct-Current Atmospheric-Pressure Discharges Useful for Ambient Desorption/Ionization Mass Spectrometry. *J. Am. Soc. Mass. Spec.* **2009,** 20, (5), 837-844.

Schilling, G. D.; **Shelley, J. T.**; Broekaert, J. A. C.; Sperline, R. P.; Denton, M. B.; Barinaga, C. J.; Koppenaal, D. W.; Hieftje, G. M., Use of an ambient ionization flowing atmospheric-pressure afterglow source for elemental analysis through hydride generation. *J. Anal. At. Spectrom.* **2009,** 24, (1), 34-40.

Dattelbaum, A. M.; Hicks, R. K.; **Shelley, J.**; Koppisch, A. T.; Iyer, S., Surface assisted laser desorption-ionization mass spectrometry on patterned nanoporous silica thin films. *Microporous Mesoporous Mater.* **2008,** 114, (1-3), 193-200.

Shelley, J. T.; Ray, S. J.; Hieftje, G. M., Laser Ablation Coupled to a Flowing Atmospheric Pressure Afterglow for Ambient Mass Spectral Imaging. *Anal. Chem.* **2008**, 80, (21), 8308-8313.

Andrade, F. J.; **Shelley, J. T.**; Wetzel, W. C.; Webb, M. R.; Gamez, G.; Ray, S. J.; Hieftje, G. M., Atmospheric Pressure Chemical Ionization Source. Part II: Desorption-Ionization for the Direct Analysis of Solid Compounds. *Anal. Chem.* **2008,** 80, (8), 2654-2663.

Andrade, F. J.; **Shelley, J. T.**; Wetzel, W. C.; Webb, M. R.; Gamez, G.; Ray, S. J.; Hieftje, G. M., Atmospheric Pressure Chemical Ionization Source. Part I: Ionization of Compounds in the Gas Phase. *Anal. Chem.* **2008**, 80, (8), 2646-2653.

Koppisch, A. T.; Browder, C. C.; Moe, A. L.; **Shelley, J. T.**; Kinke, B. A.; Hersman, L. E.; Iyer, S.; Ruggiero, C. E., Petrobactin is the Primary Siderophore Synthesized by Bacillus Anthracis str. Sterne Under Conditions of Iron Starvation. *Biometals* **2005,** 18, (6), 577-585.

Stearns, D. M.; Yazzie, M.; Bradley, A. S.; Coryell, V. H.; **Shelley, J. T.**; Ashby, A.; Asplund, C. S.; Lantz, R. C., Uranyl Acetate Induces hprt Mutations and Uranium-DNA Adducts in Chinese Hamster Ovary EM9 Cells. *Mutagenesis* **2005,** 20, (6), 417-423.

PATENTS

Laser Ablation Flowing Atmospheric-Pressure Afterglow For Ambient Mass Spectrometry, Gary M. Hieftje, Francisco J. Andrade, Steven J. Ray, and **Jacob T. Shelley**, US Patent Application 2009/0272893, 2009.

Method and Apparatus for Ionization and Desorption Using Glow Discharge, Gary M. Hieftje, Steven J. Ray, Francisco J. Andrade, William C. Wetzel, Michael R. Webb, Gerardo Gamez, and **Jacob T. Shelley**, US Patent 7,893,408.

INVITED PRESENTATIONS

Flowing Atmospheric-Pressure Afterglow for Ultrasensitive, Direct Detection of Weaponized Chemicals in Complex Matrices, **Jacob T. Shelley**, Steve J. Ray, and Gary M. Hieftje, *To be presented at the 2011 Federation of Analytical Chemistry and Spectroscopy Societies Conference*, **Invited Lecture**, Reno, NV, October 2 – 7, 2011.

Investigations of Fundamental Processes and Ion Chemistry of the Flowing Atmospheric-Pressure Afterglow and Low-Temperature Plasma Probe Ambient Ionization Sources, **Jacob T. Shelley**, Joshua S. Wiley, Carsten Engelhard, Ayanna U. Jackson, R. Graham Cooks, and Gary M. Hieftje, *2010 Federation of Analytical Chemistry and Spectroscopy Societies Conference*, **Invited Lecture**, Raleigh, NC, October 17 – 21, 2010.

The Flowing Atmospheric-Pressure Afterglow (FAPA): A Glow Discharge for Ambient, Molecular Mass Spectrometry, **Jacob T. Shelley**, *Anorganische Und Metallorganische Chemie Minisymposium at ETH Zürich*, **Invited Lecture**, Zürich, Switzerland, May 19, 2010.

Ambient Desorption/Ionization Mass Spectrometry (ADI-MS): Plasma-based Tools and Methods, **Jacob T. Shelley**, Kevin P. Pfeuffer, and Gary M. Hieftje, *2009 Federation of Analytical Chemistry and Spectroscopy Societies Conference*, **Invited Lecture**, Louisville, KY, October 18 – 22, 2009.

The Flowing Atmospheric-Pressure Afterglow: A Glow Discharge for Molecular Mass Spectrometry, **Jacob T. Shelley**, Steven J. Ray, and Gary M. Hieftje, *2009 Gladnet Meeting,* **Invited Lecture,** Budapest, Hungary, September 1 – September 4, 2009.

Ambient Mass Spectrometry: Where CSI Becomes Analytical Reality, **Jacob T. Shelley**, Francisco J. Andrade, and Gary M. Hieftje, Northern Arizona University, **Invited Lecture**, Flagstaff, AZ, November 7th, 2008.

Fiber-Optic Chemical Sensing Using Cavity Ring-Down Principles, **Jacob T. Shelley**, Carsten Engelhard, Radislav A. Potyrailo, and Gary M. Hieftje, *2008 Federation of Analytical Chemistry and Spectroscopy Societies Conference*, **Invited Poster**, Reno, NV, September 28 – October 2, 2008.

Use of a Flowing Atmospheric-Pressure Afterglow Ionization Source for Sensitive Detection of Fast Transient Signals, **Jacob T. Shelley**, Steven J. Ray, and Gary M. Hieftje, *2008 Federation of Analytical Chemistry and Spectroscopy Societies Conference*, **Invited Poster**, Reno, NV, September 28 – October 2, 2008.

A Novel Cold Plasma Source for the Soft Ionization of Organic Molecules, **Jacob T. Shelley**, Francisco J. Andrade, Steven J. Ray, Joshua S. Wiley, and Gary M. Hieftje, *2007 Federation of Analytical Chemistry and Spectroscopy Societies Conference*, **Invited Lecture**, Memphis, TN, October 14-18, 2007.

FIRST-AUTHOR PRESENTATIONS

Developments and Novel Biological Applications of the Flowing Atmospheric-Pressure Afterglow Ambient Ionization Source, **Jacob T. Shelley**, Justin M. Wiseman, and Gary M. Hieftje, *Presented at the 2010 Pittsburgh Conference,* Orlando, FL, February 28 – March 5, 2010.

The Flowing Atmospheric-Pressure Afterglow (FAPA) Ionization Source: Fundamental Investigation and Novel Applications, **Jacob T. Shelley**, Kevin P. Pfeuffer, Steven J. Ray, and Gary M. Hieftje, *Presented at the 2010 Winter Conference on Plasma Spectrochemistry,* Fort Myers, FL, January 4 – January 9, 2010.

The Flowing Atmospheric-Pressure Afterglow: A Glow Discharge for Molecular Mass Spectrometry, **Jacob T. Shelley**, Steven J. Ray, and Gary M. Hieftje, *Colloquium Spectroscopicum Internationale XXXVI,* Budapest, Hungary, August 30 – September 3, 2009.

Plasma-based Ambient Desorption/Ionization Mass Spectrometry (ADI-MS): Investigations Into Desorption Characteristics and Competitive Ionization, **Jacob T. Shelley**, Kevin P. Pfeuffer, Steven J. Ray, and Gary M. Hieftje, *2009 American Society for Mass Spectrometry Conference on Mass Spectrometry*, Philadelphia, PA, May 31 – June 4, 2009.

Fast Transient and Structural Analysis Using the Flowing Atmospheric-Pressure Afterglow Ionization Source with a Time-of-Flight Mass Spectrometer, **Jacob T. Shelley**, Steven J. Ray, and Gary M. Hieftje, *2009 Pittsburgh Conference,* Chicago, IL, March 8 – 13, 2009.

Fundamental Properties of DC Atmospheric-Pressure Helium Discharges Used in Mass Spectrometry, **Jacob T. Shelley**, George C.-Y. Chan, Steven J. Ray, and Gary M. Hieftje, *2008 Federation of Analytical Chemistry and Spectroscopy Societies Conference*, Reno, NV, September 28 – October 2, 2008.

Coupling a Novel Atmospheric-Pressure Ionization Source with Laser Ablation to Perform Imaging Mass Spectrometry, **Jacob T. Shelley**, Steven J. Ray, Francisco J. Andrade, and Gary M. Hieftje, *2008 Pittsburgh Conference*, New Orleans, LA, March 2-7, 2008.

Novel Atmospheric-Pressure Glow Discharge for Ambient Mass Spectrometry (AMS), **Jacob T. Shelley**, Steven J. Ray, Francisco J. Andrade, and Gary M. Hieftje, *2008 Winter Conference on Plasma Spectrochemistry*, Temecula, CA, January 5-12, 2008.

Analyte Mapping of Solid Samples by Coupling Laser Ablation with an Atmospheric-Pressure Glow Discharge Ionization Source , **Jacob T. Shelley**, Francisco J. Andrade, Steven J. Ray, and Gary M. Hieftje, *Federation of Analytical Chemistry and Spectroscopy Societies Conference*, Memphis, TN, October 14-18, 2007.

Mass Spectral Imaging of Solid Samples Using a Novel Cold Plasma Ionization Source, **Jacob T. Shelley**, Steven J. Ray, Francisco J. Andrade, and Gary M. Hieftje, *Turkey Run Analytical Conference*, Marshall, IN, September 14-15, 2007.

Fiber Optic Chemical Sensing Using Fiber-Loop Ring-Down Spectroscopy. **Jacob T. Shelley**, Steven J. Ray, Radislav A. Potyrailo, and Gary M. Hieftje, *2007 Pittsburgh Conference*, Chicago, IL, February 25th, 2007.

Use of Fiber-Loop Ring-Down Spectroscopy in Fiber Optic Chemical Sensing. **Jacob T. Shelley**, Steven J. Ray, Radislav A. Potyrailo, and Gary M. Hieftje, *Turkey Run Analytical Conference*, Indianapolis, IN, October 6-7, 2006.

Laser Desorption-Ionization Mass Spectrometry on Mesoporous Silica Thin Films. **Jacob T. Shelley**, Andrew M. Dattelbaum, and Srinivas Iyer, *Los Alamos National Laboratory Student Research Symposium*, Los Alamos, NM, August 5, 2005.

Quantitation of Uranium-DNA Adducts via Inductively Coupled Plasma Optical Emission Spectroscopy (ICP-OES). **Jake T. Shelley**, Adam Ashby, and Diane M. Stearns, *Arizona-Nevada Academy of Sciences Annual Meeting*, Las Vegas, NV, April 9, 2005.

Measurement of Uranium-DNA Adducts by Inductively Coupled Plasma Optical Emission Spectroscopy (ICP-OES). **Jake T. Shelley**, Adam Ashby, and Diane M. Stearns, *2005 Pittsburgh Conference*, Orlando, FL, February 27 – March 4, 2005.